

Reduction of magnetic noise in PWM-supplied induction machines - low-noise design rules and multi-objective optimisation



Jean LE BESNERAIS

Laboratoire d'Electricité et d'Electronique de Puissance de Lille

Ecole Centrale de Lille

A thesis submitted for the degree of

Doctor of Philosophy in Electrical Engineering

20th of November, 2008

Rapporteurs	M. Gabsi, Professeur, ENS Cachan A. Miraoui, Professeur, Université de Technologie de Belfort Montbéliard
Jury	P. Brochet, Professeur, Ecole Centrale de Lille M. Hecquet, Professeur, Ecole Centrale de Lille V. Lanfranchi, Maître de Conférence, Université de Technologie de Compiègne G. Friedrich, Professeur, Université de Technologie de Compiègne M. Bekemans, Docteur Ingénieur, ALSTOM Transport A. Randria, Ingénieur, ALSTOM Transport

Ce travail est dédié à mes parents qui m'ont soutenu tout au long de mes études, aux enseignants qui m'ont particulièrement marqué, notamment Mr Varjabédian et Mr Desfontaines (Lycée Châtelet, Douai), Mr Mallet et Mr Sautet (Lycée Wallon, Valenciennes), et Mr De Vuyst (Ecole Centrale Paris), ainsi qu'à Elise, sans qui rien de cela n'aurait été possible — tout comme tant d'autres choses.

Remerciements

Les résultats de ce travail de thèse sont avant tout issus d'une dynamique favorable entre le laboratoire d'Electrotechnique et d'Electronique de Puissance de Lille (L2EP), le Laboratoire d'Electromécanique de Compiègne (LEC), et les entreprises ALSTOM et VIBRATEC, et je souhaiterais d'abord remercier l'ensemble des personnes qui ont contribué à cette synergie, et plus particulièrement Pascal Brochet, professeur à l'Ecole Centrale de Lille et directeur de l'équipe Optimisation du L2EP, et Michel Hecquet, professeur à l'Ecole Centrale de Lille, pour le montage de ce projet passionnant et fructueux. Je suis entré dans cette thèse en ayant de nombreuses idées reçues sur le génie électrique, alimentées par le peu de souvenirs qu'il me restait des travaux pratiques de classes préparatoires ; j'en ressors avec un véritable enthousiasme et un vif intérêt pour la discipline, dont les concepts et les problématiques de modélisation m'ont procuré une importante satisfaction intellectuelle – à tel point que j'espère, après deux ou trois ans d'expérience dans l'industrie, reprendre le métier de chercheur.

Je remercie également Pascal Brochet pour la confiance qu'il m'a accordée et la confortable indépendance qui en a résulté, et lui suis reconnaissant de m'avoir confié une charge d'enseignement et de conseil auprès des projets des élèves ingénieurs, qui fût une expérience humaine très enrichissante. Je le remercie aussi pour avoir su créer au sein de son équipe une ambiance chaleureuse, propice aux échanges tant personnels que scientifiques, et où travailler fût agréable. Je remercie au passage l'ensemble des membres de l'équipe (je pense en particulier à Frédéric Gillon, Stéphane Brisset et Xavier Margueron) pour leur accueil et leur accessibilité.

Je tiens à remercier Michel Hecquet pour le suivi et l'organisation de mon travail de thèse, et surtout pour son dynamisme, sa bonne humeur et son écoute. Ce fût un vrai plaisir de travailler avec lui, et j'espère que nous aurons encore à collaborer après la thèse pour la rédaction de nombreux articles.

Je remercie vivement Vincent Lanfranchi, maître de conférence à l'Université de Technologie de Compiègne (UTC), pour l'intérêt qu'il a porté à mon travail, pour son soutien et son immense réactivité, plus particulièrement lors de la rédaction d'articles et lors de la rédaction de thèse, ainsi que pour les nombreuses discussions techniques qu'il a soulevées, et les idées qu'il a initiées en vue de résoudre de multiples problèmes. Je le remercie également, ainsi que Guy Friedrich, professeur à

l'UTC et directeur du LEC, pour s'être associés de manière aussi active au projet, et nous avoir prêté leur matériel de laboratoire qui nous aura permis d'enrichir considérablement notre compréhension des phénomènes.

Je remercie aussi fortement Marc Bekemans (TCE Research Manager, ALSTOM-Charleroi), preuve vivante que l'on peut parfois faire plus de recherche en entreprise qu'en laboratoire, pour son suivi particulièrement technique, son profond sens physique et la pertinence de ses remarques qui ont donné naissance à une partie des développements plus théoriques de cette thèse. Si je poursuis ma carrière dans l'industrie, j'espère pouvoir concilier à sa manière de hautes responsabilités en Recherche et Développement, avec un niveau et une implication technique tout aussi importants. Je remercie au passage Anthony Leroy (ULB) dont le travail complémentaire sur le bruit des selfs et la psychoacoustique nous a été fort utile, tout comme les discussions qu'il a initiées. Je tiens également à remercier Sylvain Récorbet (ingénieur acoustique, ALSTOM-Tarbes) pour sa gestion efficace et agréable du projet PROSODIE, bien qu'il ait pris cette responsabilité alors que le projet avait déjà démarré.

Je remercie sincèrement la société VIBRATEC, notamment par le biais d'Eric Augis, de Grégory Lemaire et de Julien Berger, pour sa contribution dynamique et stimulante au projet, en dépit même d'un manque temporaire de moyens. Toutes nos rencontres ont été à la fois chaleureuses et riches en enseignements.

Je remercie également Andry Randria (Responsable Technique Nouveaux Projets R&D et Nouveaux Produits, ALSTOM-Ornans) pour la rapidité avec laquelle il a validé nos articles, et surtout pour avoir réussi à faire réaliser le premier des deux prototypes conçus lors de cette thèse avant la soutenance. Je remercie aussi les ingénieurs Johnny Bousada (ALSTOM-Charleroi), Eric Rigolier et Michel Scherer (ALSTOM-Ornans) pour leur disponibilité et leur collaboration, et Roger Gutknecht (ALSTOM-Ornans) qui m'a très efficacement assisté aux essais.

Je souhaiterais enfin remercier les anciens étudiants Laurent Leplat, Emmanuel Thibierge, Philippe Josse et Lyse Laurent (HEI) pour leurs travaux de TER effectués en 2005 et 2006, ainsi qu'Aymeric Ansel qui les a dirigés, dont les études sont souvent utilisées par des thésards sans pour autant être citées. Leur travail m'a permis de gagner un temps précieux sur la validation du modèle électrique.

Abstract

This thesis focuses on the reduction of the audible magnetic noise radiated by induction machines due to air-gap radial Maxwell forces in variable-speed traction application (e.g. subways and light-rail vehicles). It especially accounts for the interaction between the motor and its inverter, and aims at giving low magnetic noise rules which apply at the design stage of the motor.

In a first part, an overview of the electrical and vibro-acoustic modelling techniques of induction machines and their associated assumptions is done. A review of the existing low magnetic noise design rules is done, and the influence of the motor and inverter various design variables (slot combination, slot shapes, switching frequency, etc) is discussed. Finally, the optimisation works applied to the induction machines are reported, and especially those aiming at decreasing magnetic noise.

In a second part, a fully analytical model of the vibro-acoustic and electrical behaviour of the induction machine is established. The electromagnetic model, which aims at computing the motor traction characteristics (output torque, efficiency), and its radial air-gap flux density distribution responsible for audible magnetic noise, is detailed. Some simulation results are validated with finite element methods (FEM). Saturation, load and pulse-width modulation (PWM) effects are considered. An equivalent 2D ring model of the stator is adopted to compute its natural frequencies in the vibro-acoustic model, which is validated on different motors with tests and FEM. The vibrations of the stator stack and the sound power level are then validated with tests and boundary element method (BEM). The implementation in Matlab of this full model gave a fast and accurate simulation tool called DIVA.

In a third part, an exhaustive analytical description of the main magnetic forces is done. The exciting force harmonics are classified, and their characteristics (frequency and propagation direction, number of nodes, magnitude) are validated using experimental sonagrams and operational deflection shapes. On the ground on this analysis and DIVA simulations, some new low-noise design rules are inferred, especially on the slot numbers combination, the slot openings and the switching frequency.

The model is then coupled to a mixed variable constrained multi-objective optimisation algorithm, NSGA-II, in order to design a new low-noise motor achieving specified traction characteristics. Two rotor prototypes are designed to decrease the noise of a given industrialised motor. Some new switching frequency values are also proposed in order to decrease PWM noise.

Some tests are run on the first prototype, and up to a 15 dB decrease is observed at certain speeds on the total noise level (magnetic+aerodynamic) in no-load sinusoidal case, while DIVA simulations predicted a 20 dB reduction on magnetic noise only. In on-load case, improvements reach up to 10 dB. The new switching frequencies decrease PWM noise from 5 to 10 dB in the starting phase, in accordance with analytical predictions. Furthermore, this new prototype successfully reached specified output torque without increasing iron losses neither phase current.

Résumé

Cette thèse porte sur la réduction du bruit audible d'origine magnétique émis par les machines asynchrones alimentées par modulation de largeur d'impulsion (MLI), et plus particulièrement par les moteurs de traction ferroviaire pour des applications de type métro ou tramway. Ce bruit magnétique est supposé provenir des forces radiales de Maxwell présentes dans l'entrefer et à l'origine des vibrations du stator. Ce travail tient en particulier compte de l'interaction entre le moteur et l'onduleur, et cherche à établir des règles de conception silencieuses qui puissent s'appliquer dès le stade de conception.

Dans une première partie, une vue générale des travaux de modélisation vibro-acoustique des machines asynchrones et de leurs hypothèses est donnée. L'ensemble des règles de conception silencieuse existantes est présenté, et les effets des variables de conception du moteur (nombres et formes d'encoches, etc) et de l'onduleur (fréquence de découpe, etc) sur le bruit sont rapportés. Les travaux portant sur la conception optimale des machines asynchrones sont discutés, et plus particulièrement ceux s'intéressant au facteur acoustique.

En second lieu, un modèle analytique complet du comportement vibro-acoustique et électrique du moteur est établi. Le modèle électromagnétique, qui calcule les caractéristiques de traction du moteur (couple utile, rendement), ainsi que la distribution du flux radial d'entrefer à l'origine du bruit, est d'abord détaillé. Des résultats de simulation sont également présentés et validés par éléments finis ou par expérience. La saturation, la MLI et la charge sont pris en compte dans le modèle. Un modèle d'anneau équivalent est utilisé pour calculer les fréquences naturelles du stator, et il est validé sur différents moteurs par éléments finis et par tests. La détermination de l'amplitude des vibrations dynamiques du stator et de la puissance acoustique est enfin validée par tests et par éléments frontières. La programmation en Matlab de ce modèle complet a donné un outil de simulation rapide et précis nommé DIVA.

En troisième partie, une description analytique exhaustive des ondes principales de force magnétique est faite. Les harmoniques de force excitatrice sont classés,

et leurs caractéristiques (fréquence, sens de propagation, nombre de noeuds, amplitude) sont validées à l'aide de spectrogrammes expérimentaux et de déformées opérationnelles. A partir de cette analyse et de simulations avec DIVA, de nouvelles règles de conception silencieuse sont établies, qui portent en particulier sur les combinaisons d'encoche, l'ouverture des encoches, et la fréquence de découpe. Le modèle est ensuite couplé à un algorithme d'optimisation multi-objectif à variables mixtes et sous contraintes, NSGA-II, afin de concevoir un nouveau moteur à faible bruit magnétique respectant les caractéristiques de traction spécifiées (couple fonction de la vitesse). Deux prototypes de rotor sont conçus, et les simulations prévoient des gains significatifs (jusqu'à 20 dB de réduction du bruit magnétique en sinus à vide).

Des essais sont réalisés sur un premier prototype, et un gain de 15 dB est observé sur le bruit total (aérodynamique+magnétique) en fonctionnement sinus à vide. En charge, une réduction de 10 dB est encore observée. En régime MLI, les nouvelles fréquences de découpe proposées donnent un gain de 5 à 10 dB pendant le démarrage du moteur. Enfin, le nouveau moteur atteint le couple spécifié sans accroître les pertes ni le courant de phase.

Contents

List of figures	xx
Nomenclature	xxv
1 Introduction	1
1.1 Background	1
1.1.1 Noise of railway transport systems	1
1.1.1.1 Sources of noise	1
1.1.1.2 Acoustic norms	2
1.1.2 PROSODIE Project	3
1.2 Objectives	4
1.3 General approach	5
2 State of the art and orientation of the work	7
2.1 Electromagnetic and vibro-acoustic modelling	7
2.1.1 Electromagnetic forces modelling	7
2.1.1.1 Maxwell forces	9
2.1.1.2 Magnetostriction forces	12
2.1.1.3 Conclusion	14
2.1.1.3.1 Air-gap flux density modelling	14
2.1.1.3.2 Saturation modelling	15
2.1.2 Vibro-acoustic modelling	15
2.1.2.1 Static displacements	15
2.1.2.2 Natural frequencies and dynamic deflections	16
2.1.2.3 Radiation factor and sound power level	17
2.2 Noise reduction methods	18
2.2.1 Low-noise design rules	18
2.2.1.1 Design variables influence	18
2.2.1.1.1 Rotor and stator slot number combination	19
2.2.1.1.2 Rotor and stator slots shape	19
2.2.1.1.3 Skewing	20

2.2.1.1.4	Stator stack dimensions	20
2.2.1.1.5	Eccentricities	20
2.2.1.1.6	Manufacturing errors: tolerances, asymmetries	20
2.2.1.1.7	Materials	21
2.2.1.2	Mounting and coupling influences	21
2.2.1.3	Supply current influence	22
2.2.1.3.1	Supply frequency	22
2.2.1.3.2	PWM strategy	22
2.2.1.3.3	Switching frequency	24
2.2.1.3.4	Comparison between PWM noise and slotting noise	24
2.2.2	Active methods	24
2.2.2.1	Current injection methods	25
2.2.2.2	Piezo-electric methods	25
2.2.2.3	Other methods	25
2.3	Vibro-acoustic optimisation	25
2.4	Conclusion	26
2.4.1	Modelling assumptions	26
2.4.2	Position of the work	27
3	Electromagnetic and vibro-acoustic models	28
3.1	Electromagnetic model	28
3.1.1	Currents computation	29
3.1.1.1	Voltage computation	30
3.1.1.1.1	Method	30
3.1.1.1.2	Validation	30
3.1.1.2	Extended single phase equivalent circuit	30
3.1.1.2.1	Fundamental case	30
3.1.1.2.1.1	Expression	30
3.1.1.2.1.2	Saturation factor computation	32
3.1.1.2.2	Harmonic extension	33
3.1.1.3	Validations	34
3.1.1.3.1	No-load saturated sinusoidal case	34
3.1.1.3.2	On-load unsaturated sinusoidal case	34
3.1.1.3.3	No-load unsaturated PWM case	35
3.1.2	Magnetomotive forces computation	37
3.1.2.1	Stator magnetomotive force	37
3.1.2.2	Rotor magnetomotive force	39
3.1.3	Permeance computation	39
3.1.3.1	Expression	39

3.1.3.2	Skewed case	40
3.1.3.3	Saturated case	40
3.1.3.4	Eccentric case	42
3.1.3.4.1	Static eccentricity	42
3.1.3.4.2	Dynamic eccentricity	42
3.1.4	Air-gap radial flux density computation	43
3.1.4.1	Offload sinusoidal validations	44
3.1.4.1.1	Unsaturated case	44
3.1.4.1.2	Saturated case	45
3.1.4.2	On-load sinusoidal validations	45
3.1.5	Traction characteristics computation	46
3.1.5.1	Torque, power factor, efficiency expressions	46
3.1.5.2	Variable-speed characteristics	47
3.1.5.3	Validation	48
3.1.6	Instantaneous electromagnetic torque	48
3.2	Vibro-acoustic model	51
3.2.1	Natural frequencies computation	52
3.2.1.1	Expression	52
3.2.1.2	Effect of magnetic stiffness	53
3.2.1.3	Validation	54
3.2.2	Vibration computation	56
3.2.2.1	Expression	56
3.2.2.2	Experimental validation	58
3.2.2.2.1	Sinusoidal case	58
3.2.2.2.2	PWM case	59
3.2.3	Radiation factor computation	61
3.2.3.1	Expression	61
3.2.3.2	Validation	61
3.2.4	Sound power level computation	62
3.2.4.1	Expression	62
3.2.4.2	Validation	63
3.2.4.2.1	FEM/BEM simulations	63
3.2.4.2.2	Experiments	66
3.2.4.2.2.1	No-load sinusoidal case	66
3.2.4.2.2.2	No-load PWM case	66
3.3	Numerical considerations	70
3.3.1	Fourier versus time/space domain modelling	70
3.3.2	Computing tricks	72
3.3.3	Discretisation quality, spectral range and resolution	73

3.3.3.1	Time and space discretisation	73
3.3.3.2	Speed discretisation	73
3.3.3.3	Spectral resolution	74
3.3.3.4	Spectral range	74
3.3.3.5	Conclusion	74
4	Characterisation and reduction of noise	75
4.1	Analytical charaterisation of magnetic force lines	75
4.1.1	General method	75
4.1.2	Standing versus rotating waves	76
4.1.3	Expression of main magnetic lines orders and frequencies	78
4.1.3.1	General case	78
4.1.3.2	Sinusoidal case	82
4.1.3.2.1	Expression of main lines	82
4.1.3.2.2	Pure slotting force lines	83
4.1.3.2.2.1	Expression	83
4.1.3.2.2.2	Validation	83
4.1.3.2.2.3	Effect of current magnitude	86
4.1.3.2.3	Saturation force lines	87
4.1.3.2.3.1	Expression	87
4.1.3.2.3.2	Validation	87
4.1.3.2.3.3	Interaction with rotor skewing	87
4.1.3.2.4	Eccentricity force lines	90
4.1.3.2.5	Winding force lines	91
4.1.3.2.5.1	Expression	91
4.1.3.2.5.2	Validation	91
4.1.3.3	PWM case	92
4.1.3.3.1	Pure PWM force lines	93
4.1.3.3.1.1	Expression	93
4.1.3.3.1.2	Validation	95
4.1.3.3.1.3	Influence of current magnitude	95
4.1.3.3.1.4	Influence of phase angle	97
4.1.3.3.2	Slotting PWM force lines	99
4.1.3.3.2.1	Expression	99
4.1.3.3.2.2	Validation	100
4.1.4	Expression of main magnetic lines magnitude	102
4.1.5	Conclusion	104
4.2	Low-noise design rules	106
4.2.1	Slot combination	106

4.2.1.1	Exhaustive search	106
4.2.1.1.1	Realisation of the slot combination database	107
4.2.1.1.2	Application	108
4.2.1.2	Special slot numbers	110
4.2.2	Slot openings width	111
4.2.2.1	Optimal choice	111
4.2.2.2	Application	113
4.2.3	PWM supply	115
4.2.3.1	Psychoacoustic factors	115
4.2.3.2	Choice of the switching frequency	116
4.2.3.2.1	Pure PWM noise	116
4.2.3.2.2	Slotting PWM noise	117
4.2.3.3	Current injection method	118
4.3	Noise minimisation	120
4.3.1	Optimisation problem	120
4.3.1.1	Objectives	120
4.3.1.2	Design variables	120
4.3.1.3	Constraints	121
4.3.2	Optimisation method	122
4.3.3	Application	124
4.3.3.1	Rotor optimisation	125
4.3.3.2	PWM strategy optimisation	127
4.3.3.3	Experimental validation	128
4.3.3.3.1	Traction characteristics	128
4.3.3.3.2	No-load sinusoidal tests	129
4.3.3.3.3	On-load sinusoidal tests	130
4.3.3.3.4	No-load PWM tests	131
5	Conclusion, future work and prospects	134
5.1	Conclusion	134
5.2	Future work	136
5.3	Prospects	137
A		138
A.1	English/French electromechanical glossary	138
A.2	Motor parameters and main slotting vibrations	138
A.3	Winding matrix filling algorithm	141
A.4	DIVA/OPERA coupling	141

B	143
B.1 Mode shapes of a finite-length cylindrical shell	143
B.2 Green's function formalism	147
B.2.1 Rotating circumferential load wave on a circular cylindrical shell	147
B.2.2 Standing circumferential load wave on a circular cylindrical shell	150
C	152
C.1 Exhaustive magnetic force lines characteristics	152
C.2 Low order magnetic force lines characteristics	155
C.3 Low order magnetic force lines characteristics with sinusoidal supply and sinusoidal mmfs	158
C.4 Slot combination database of motor M1	160
References	178

List of Figures

1.1	IEC 60034-9 norm noise limit	3
1.2	IEC 60034-9 norm tonalities penalisation. ΔL is the average of the sound levels of the adjacent one-third octaves: the correction in dB must be added to the global sound power level in dBA.	3
2.1	Left: definition of dS surface and its normal and tangential directions. Right: definition of the local coordinate system defined by a magnetic field line (from (14)).	9
2.2	Direction of total Maxwell stress for different magnetic line directions.	9
2.3	Example of flux density lines distribution in an induction machine, in unsaturated case: the main part of the magnetic flux enters perpendicularly to tooth tips.	11
2.4	Simplified representation of a material flux density lines (left) and the resulting magnetostrictive effect (right).	13
2.5	Maxwell (left) and magnetostrictive (right) force fields in a 37 kW induction machine (15). Note that different scales have been used in both figures: as discussed in (15), the FEA representation of nodal forces can be misleading because tooth tips mesh is generally finer: few but long arrows can stand for the same pressure as numerous but short arrows.	13
2.6	Typical flux density versus magnetic field curve.	15
2.7	Illustration of the electromagnetic force decomposition in several sinusoidal force waves (spatial orders 0, 1 and 2). The magnitude, velocity, propagation direction of these elementary force waves are given by the 2D FFT of the air-gap electromagnetic pressure distribution.	16
2.8	A-weighting in function of frequency ($\text{dBA} = \text{dB} + \Delta L_a$) in the audible range 20 Hz to 20 kHz: the human's ear maximum sensitivity is reached around 2500 Hz.	22
3.1	DIVA models and their main input/output.	28
3.2	Simulink inverter model.	31
3.3	Comparison between experimental and simulated (DIVA) stator phase voltage in asynchronous mode on M1 motor ($U_0=6$ V, $f_c=1600$ Hz, $f_s=50$ Hz).	31

3.4	Fundamental single phase equivalent circuit	32
3.5	Left: mean flux line for saturation factor computation. Right: typical magnetising inductance curve in function of air-gap flux.	32
3.6	Multi-layer single phase equivalent circuit.	33
3.7	Experimental and simulated stator phase currents at several supply frequencies and supply voltages (motor M2, $s = 0.01\%$).	34
3.8	Experimental and simulated (DIVA) phase current as a function of slip on M3 motor ($U_0=810$ V, $f_s=150$ Hz). The nominal slip is 1.56 %.	35
3.9	Rotor current distributions among bars obtained with FEM (left) and DIVA (right) (motor M2, $f_s = 150$ Hz, $s = 1\%$).	35
3.10	Rotor bar current waveforms obtained with FEM (left) and DIVA (right) (motor M2, $f_s = 150$ Hz, $s = 1\%$). FEM spectrum abscissa is graduated in multiples of the supply frequency (harmonics 6 and 12 stand for $6f_s$ and $12f_s$ frequencies), whereas DIVA spectrum is directly graduated in Hz.	36
3.11	Experimental and simulated (DIVA) stator phase current on M5 motor (asynchronous PWM with $f_c=1280$ Hz, $U_0=30$ V, $f_s=5$ Hz, $s=0.01\%$).	36
3.12	Left: decomposition of a stator winding function (wf) in a sum of two turn functions (tf). Right: stator turn function of a single coil.	37
3.13	Motor M2 winding pattern, winding functions and resulting mmf in full-pitch case (left, $Y/sp_s=6/6$) and shorted-pitch case (right, $Y/sp_s=5/6$).	37
3.14	Motor M1 winding pattern, winding functions and resulting stator mmf.	38
3.15	Stator mmf distribution along the air-gap at $t=0$ (motor M2 to M4, 5/6 shorted-pitch winding cf. Fig. 3.13). The main space harmonics are here $11p = 33$ and $13p = 39$	38
3.16	Left: rotor turn function. Right: rotor mmf distribution along the air-gap at $t=0$ (motor M2). The main space harmonics are here $Z_r - p = 25$ and $Z_r + p = 31$	39
3.17	C_s function marking the location of stator slot openings on motor M2.	40
3.18	Permeance per unit area distribution along the air-gap (motor M2, $f_s = 50$ Hz) at $t=0$ (left) and in function of time at $\alpha_s=0$ (right).	40
3.19	Saturated permeance per unit area distribution along the air-gap (motor M2, $f_s = 50$ Hz) at $t=0$ (left) and in function of time at $\alpha_s=0$ (right).	41
3.20	Illustration of the air-gap radial flux density flattening due to even order saturation permeance waves.	42
3.21	Left: permeance per unit area distribution along the air-gap (motor M2, 5% static eccentricity, $f_s = 50$ Hz) at $t=0$. Right: permeance per unit area distribution in function of time (motor M2, 5% dynamic eccentricity, $f_s = 50$ Hz) at $\alpha_s=0$	42
3.22	Radial air-gap flux density distribution along the air-gap at $t=0$ (motor M2). The main space harmonics are here $Z_s - p = 33$ and $Z_s + p = 39$	43

3.23	Maxwell pressure, stator and rotor magnetomotive forces, and permeance distributions at $t=0$ (motor M2).	43
3.24	FEM and DIVA fundamental radial air-gap flux density as a function of phase voltage on M3 motor at $f_s = 150.2$ Hz (left) and M2 motor at $f_s = 50.11$ Hz (right) (no-load unsaturated case, $s = 10^{-4}$).	44
3.25	FEM and DIVA radial flux density distribution along the air-gap (left) and in function of time (right) (motor M3, sinusoidal no-load case, $s = 10^{-4}$, $f_s = 150.2$ Hz, $U_0 = 763$ V).	44
3.26	Approximated FEM and DIVA stator mmf (left) and permeance (right) distributions along the air-gap (motor M2, $f_s = 50.11$ Hz, $U_0 = 173.2$ V, $s = 10^{-4}$).	45
3.27	Left: FEM and DIVA main flux density saturation harmonic of spatial order $3p$ in function of the applied phase voltage on motor M2, after having fit the analytical model. Right: FEM and DIVA flux density distribution along the air-gap in saturated case.	46
3.28	DIVA and FEM radial flux density distribution along the air-gap in sinusoidal on-load case ($U_0 = 173.2$ V, $f_s = 50$ Hz, $s = 1\%$).	46
3.29	Phase current, air-gap flux E_0/f_s , output torque, output power, efficiency, phase voltage and slip in function of speed, obtained with ALSTOM simulation tool and DIVA (motor M5a). Friction losses have been experimentally determined and used both simulation tools.	49
3.30	Experimental and simulated (DIVA) power factor, output torque and output power as a function of slip on M3 motor ($U_0=810$ V, $f_s=150$ Hz).	50
3.31	Left: stator stack equivalent cylinder dimensions. Right: motor M5 stator stack and end-plates.	51
3.32	Deflection shapes of the first five stator circumferential modes ($m = 0$: breathing mode, $m = 1$: rotor bending mode, $m = 2$: elliptical mode, $m = 3$: 3-order elliptical mode, $m = 4$: 4-order elliptical mode).	54
3.33	Relative static displacement in function of R_{sy}/h_{sy} ratio for several modes. Doubling the relative static displacement increases the SWL at resonance of $10 \log_{10}(2^2) \approx 6$ dB.	58
3.34	Experimental and simulated vibratory spectrum obtained (motor M1, $s = 3\%$, $f_s = 75$ Hz, $U_0 = 6$ V).	59
3.35	Experimental (left) and simulated (right) acceleration spectrogram in sinusoidal case (motor M1, $f_s=12$ to 60 Hz). An uncertainty exists on the experimental supply frequency as no tachometer probe could be used.	60
3.36	Left: OMA deflection shape at 713 Hz (second bending mode, motor M1). Right: M1 motor test-bench.	60
3.37	Measured (left) and simulated (right) acceleration spectrogram in on-load asynchronous PWM case (motor M1, $f_c = 1600$ Hz, $f_s = 10$ to 80 Hz).	61

3.38	DIVA and FEM radiation efficiency under an exciting force wave of order 0 (left) and order 1 (right) (magnitude 250 N/m^2).	62
3.39	DIVA and FEM radiation efficiency under an exciting force wave of order 2 (left) and order 4 (right) (magnitude 250 N/m^2).	62
3.40	DIVA and FEM+BEM sound power level generated by a rotating force wave of order 2 (left) and 4 (right).	64
3.41	DIVA and FEM+BEM sound power level generated by a pulsating force wave of order 0, and a combination of a order 2 and 3 rotating force waves.	64
3.42	Study of the vibration response of symmetrical or asymmetrical cylinder subjected to a rotating force wave of order 4.	65
3.43	Experimental (left) and simulated (right) sonagram on motor M3 in sinusoidal no-load case. Note that experimental sonagram abscissa is time in seconds, as no tachometer prove was available, whereas simulated sonagram abscissa is f_s in Hz.	66
3.44	Experimental and simulated (DIVA) A-weighted SWL spectrum in asynchronous PWM case (motor M5, $f_s=5 \text{ Hz}$, $f_c=1280 \text{ Hz}$).	67
3.45	Schematic view of motor M5/M5a stator stack and welded plated with rods (the slot number and the slot shapes have been changed on purpose).	68
3.46	Experimental and simulated (DIVA) stator phase current magnitude spectrum at low frequencies (motor M5, $I_0 = 200 \text{ A}$, $f_s=5 \text{ Hz}$, $f_c=1280 \text{ Hz}$). The experimental supply frequency was slightly over-estimated, which explains why experimental and simulated current harmonics do not appear at exactly the same place. . . .	69
4.1	Illustration of different force waves types. The nodes of rotating waves travel along the air-gap, whereas standing waves ones stay at the same place.	77
4.2	Simulated SWL of a standing or rotating force wave of spatial order 4 and magnitude 250 N/m^2 . At resonance, there is exactly a 3dB difference.	78
4.3	Complex FFT of shorted-pitch motor M2 stator mmf in sinusoidal case ($f_s = 50 \text{ Hz}$).	80
4.4	Experimental and simulated (DIVA) acceleration spectrogram in sinusoidal case (motor M1, $f_s=12 \text{ to } 60 \text{ Hz}$).	84
4.5	Stator deflection of order 3 due to a slotting vibration (motor M1, sinusoidal case, $f_s = 50 \text{ Hz}$).	85
4.6	Pure slotting force waves on motor M1, and their propagation direction (c.c. r.: counter-clockwise rotation, c. r.: clockwise rotation). Grey deflection indicates a time anterior to black deflection.	85
4.7	Experimental (left) and simulated (right) sonagram on motor M2 in sinusoidal no-load case.	86

4.8	Order analysis of motor M5 in sinusoidal case. Saturation line of spatial order $m = -2$ and frequency $f_s(Z_r(1-s)/p+4) \approx 46f_R$ therefore appears at the order 46 abscissa.	88
4.9	Operational Deflection Shape of motor M5 near 600 Hz ($f_s \approx 30$ Hz i.e. 900 rpm). An elliptical deflection of the stator stack is observed.	88
4.10	Influence of rotor skewing on the sound pressure level in on-load sinusoidal case.	89
4.11	Operational Deflection Shape of motor M5 at 1138 Hz (maximal flux, PWM no-load case, $f_s \approx 50$ Hz - test by VIBRATEC).	89
4.12	3D shape of the saturation force harmonic of equation (4.22) due to rotor skewing.	90
4.13	Operational deflection shape at 942 Hz at two successive instants (motor M5, $f_s \approx 50$ Hz, sinusoidal case).	91
4.14	Left: stator mmf without the fundamental. Right: corresponding magnetic noise spectrum with stator modes contribution (motor M3, $f_s = 100$ Hz).	92
4.15	Experimental stator current harmonic groups magnitude in function of supply frequency (motor M5, asynchronous PWM with triangular carrier, $f_c = 1280$ Hz).	93
4.16	Complex FFT of shorted-pitch motor M2 stator mmf in asynchronous PWM case ($f_s = 50$ Hz, $f_c = 1280$ Hz).	94
4.17	Pure PWM vibration waves (motor M1, $f_c=4$ kHz), and their propagation direction (c.c. r.: counter-clockwise rotation, c. r.: clockwise rotation).	96
4.18	Measured spectrogram sweeping the switching frequency from 2.5 kHz to 10 kHz (motor M1, $f_s = 50$ Hz).	97
4.19	2D FFT of motor M5 magnetic radial force for $s \approx 1\%$ (left) and $s = 0$ (right) in on-load asynchronous PWM case ($f_c = 1280$ Hz, $f_s = 40$ Hz).	98
4.20	Evolution of the pure PWM acoustic line of frequency $2f_c = 2560$ Hz when progressively increasing the load at constant fundamental stator current.	99
4.21	Frequency shift of main slotting PWM lines of motor M1 during starting phase in PWM asynchronous case ($f_c = 1600$ Hz).	100
4.22	Experimental spectrogram measured on motor M1 from $f_s = 0$ to 70 Hz in PWM asynchronous case ($f_c = 1600$ Hz).	101
4.23	Slotting PWM vibration waves (motor M1, $f_c=4$ kHz), and their propagation direction (c.c. r.: counter-clockwise rotation, c. r.: clockwise rotation).	101
4.24	Experimental spectrogram measured on motor M1 from $f_c = 1$ to 6 kHz in PWM asynchronous case ($f_s = 50$ Hz).	102
4.25	Experimental spectrogram measured on motor M5 in asynchronous PWM no-load case ($f_c = 1280$ Hz).	102
4.26	Rotor slot number noise database for $Z_s = 27$, $p = 2$ (motor M1).	108
4.27	Rotor slot number noise database for $Z_s = 36$, $p = 2$ (motor M1).	108

4.28	Sound power level (dB) measured on motors M2 ($Z_r = 28$), M3 ($Z_r = 26$), M4 ($Z_r = 44$) which share the same stator, but with different rotor slot numbers, rotor slot shapes, and air-gap widths.	109
4.29	Magnitude of main slotting forces in function of stator and rotor slot opening widths b_s and b_r	110
4.30	Simulated sonagram of motor M6 in sinusoidal no-load case.	111
4.31	Rotor or stator slot opening smallest optimal value to cancel a slotting harmonic linked to integers k_r and k_s	112
4.32	A-weighted SWL spectrum at motor M7 mode number 4 resonance ($f_s = 44.2$ Hz), for the initial rotor slot opening value (left) and the optimal value (right). .	114
4.33	SWL radiated by the slotting lines associated to $k_{s0} = 3$ and $k_{r0} = 4$ in function of the rotor slot opening b_r varying from 0 to τ_r (motor M7). The three non zero minima correspond to the three b_r values of equation (4.48).	114
4.34	Simulated sound power level of motor M7 without current injection (no-load sinusoidal case, $f_s \approx 31$ Hz).	118
4.35	Simulated sound power level of motor M7 with current injection, cancelling the slotting force of frequency $f_s(4Z_r(1-s)/p+2)$ and order 4 (left), and cancelling the slotting force of frequency $f_s(4Z_r(1-s)/p-2)$ and order 4 (right).	118
4.36	Illustration of NSGA ranking method in case of two objectives f_1 and f_2 . Individual j is non-dominated by i if there exist $k \in [1, N]$ such as $f_k^j < f_k^i$, f_k^i denoting the k -th objective function of individual i	123
4.37	Final population (Pareto front) objectives 2-D projections (motor M6 optimisation).	126
4.38	Motor sections of different individuals.	126
4.39	DIVA simulation of magnetic noise emitted by industrial motor M5a and prototype M7 during starting phase (no-load sinusoidal case).	127
4.40	Rotor of prototype M7.	128
4.41	Experimental set-up.	129
4.42	Sound pressure level of prototype M7, compared to the industrialised motor M5a, and its skewed rotor version M5 (sinusoidal no-load case).	130
4.43	Sound pressure level of prototype M7, compared to the industrialised motor M5a, and its skewed rotor version M5 (sinusoidal on-load case).	131
4.44	Sound pressure level spectrum of prototype M7 (asynchronous 1280 Hz PWM no-load case).	132
4.45	Sound pressure level of prototype M7 during starting phase, using various switching frequencies (left: noise level in function of time, right: maximum and average noise levels from 10 to 50 Hz). The default asynchronous PWM switching frequency used on the industrialised motor M5a is 1280 Hz.	133

4.46	Illustration of the interference between main slotting lines (in black) and pure PWM lines (in blue), in asynchronous 1280 Hz PWM no-load case (left: $f_s = 35.43$ Hz, middle: $f_s = 35.55$ Hz, right: $f_s = 35.66$ Hz).	133
A.1	FEM model of motor M7 (OPERA software).	142
B.1	Modal base of a cylindrical shell (I).	144
B.2	Modal base of a cylindrical shell (II).	145
B.3	Modal base of a cylindrical shell (III).	146

Nomenclature

Roman Symbols

B_g	Radial air-gap flux density
b_r	Rotor slot opening width
b_s	Stator slot opening width
c_0	Speed of sound in air
D_f	Stator frame diameter
d_r^f	Rotor fictitious slot depth
d_s^f	Stator fictitious slot depth
D_{sh}	Rotor shaft diameter
D_{ri}	Rotor stack inner diameter
D_{si}	Stator stack inner diameter (bore diameter)
D_{ro}	Rotor stack outer diameter
D_{so}	Stator stack outer diameter
E_r	Rotor stack Young modulus in radial direction
E_s	Stator stack Young modulus in radial direction
E_{sh}	Rotor shaft Young modulus in radial direction
f_n^s	PWM n -th time harmonic of stator phase current ($f_0^s = 0, f_1^s = f_s$)
f_R	Rotor mechanical frequency ($= 2\pi\Omega_R$)
f_{max}	Maximum fundamental stator supply frequency
f_s	Fundamental stator supply frequency

g	Air-gap width
G	Number of generations
h_f	Stator frame width
h_{sy}	Stator yoke height
I_1^0	Stator fundamental phase current
I_2^0	Rotor branch fundamental current
i_r^b	Rotor b -th bar current
i_s^q	Stator q -th phase current
K_c	Carter slotting coefficient
K_s	Saturation coefficient
k_{w0}^s	Stator winding fundamental distribution factor
L_2^0	Rotor equivalent inductance (without skin effect)
L_f	Stator frame length
L_r	Rotor stack length
l_{rb}	Distance between rotor shaft bearings
L_s	Stator stack length
l_{sh}	Rotor shaft length
M	Number of objectives functions
m_s	Number of stator slots per pole and per phase
N	Number of design variables
n_l	Stator winding layers number
N_r^b	Winding function of b -th rotor bar
n_s	Number of turns in series per phase in stator winding
N_s^q	Winding function of q -th stator phase
N_{sp}	Number of angular discretisation steps per pole pair

N_{ti}	Number of time discretisation steps per electrical period
N_{trs}	Number of simulated rotor turns
p	Number of pole pairs
P_{fri}	Friction power losses
P_{IR}^{rt}	Rotor teeth iron power losses
P_{IR}^{ry}	Rotor yoke iron power losses
P_{IR}^r	Total rotor iron power losses
P_{IR}^{sy}	Stator yoke iron power losses
P_{IR}^{st}	Stator teeth iron power losses
P_J^r	Rotor Joule power losses
P_J^s	Stator Joule power losses
q_r	Number of stator phases
q_s	Number of stator phases
R_2^0	Rotor equivalent resistance (without skin effect)
R_g	Air-gap average radius ($= R_{si} - g/2 = R_{ro} + g/2$)
R_{ro}	Rotor stack outer radius
R_{si}	Stator inner radius ($= D_{si}/2$)
R_{sy}	Stator yoke (back core) mean radius ($= R_{so} - h_{sy}/2$)
s	Fundamental slip
sl_r	Rotor slotting ratio
sl_s	Stator slotting ratio
s_{mn}	Harmonic slip linked to stator current n -th time harmonic and mmf m -th space harmonic
sp_s	Number of stator slots per pole ($= Z_s/2/p$)
TF_r	Rotor turn function
TF_s	Stator turn function

Y	Stator coil pitch
Z_r	Rotor teeth number
Z_s	Stator teeth number

Greek Symbols

α_s	Angular position in stator steady frame (rad)
β_x	Coefficients ± 1 involved in flux density harmonics
δ_x	Coefficients ± 1 involved in radial force harmonics
ϵ_x	Coefficients ± 1 involved in permeance harmonics
η	Motor efficiency
η_x	Coefficients ± 1 involved in mmf harmonics
λ_{de}	Dynamic eccentricity degree
λ_{se}	Static eccentricity degree
λ_R	Motor rotation direction ($= \pm 1$)
μ_s	Stator stack Poisson ratio
ν_r	Rotor mmf space harmonics
ν_s	Stator mmf space harmonics
Ω_R	Rotor mechanical pulsation ($= (1 - s)\omega_s/p$)
ω_r	Rotor bar current fundamental pulsation ($= (1 - s)\omega_s$)
ω_s	Stator current fundamental pulsation ($= 2\pi f_s$)
ρ_r	Rotor stack mass per unit volume
ρ_s	Stator stack mass per unit volume
σ_m	Motor radiation efficiency of circumferential mode number m
τ_r	Rotor slot pitch ($= \pi D_{ro}/Z_r$)
τ_s	Stator slot pitch ($= \pi D_{si}/Z_s$)
ξ_m	Damping coefficient of mode m

Acronyms

BEM Boundary Element Method

DIVA Name of the simulation software (*D*imensionnement *V*ibroAcoustique)

DTC Direct Torque Control

EMA Experimental Modal Analysis

emf Electromotive force

FEA Finite Element Analysis

FEM Finite Element Method

FFT Fast Fourier Transform

GA Genetic Algorithm

mmf Magnetomotive force

NSGA Non-dominated Sorting Genetic Algorithm

ODS Operational deflection shapes

OMA Operational Modal Analysis

PFM Pulse Frequency Modulation

PWM Pulse-Width Modulation (regular sampling type)

RFPM Random Frequency Pulse-Width Modulation

RPPM Random Pulse-Position Modulation

RPWM Random Pulse-Width Modulation

RSF Random Switching Frequency

SEA Statistical Energy Analysis

SPEC Single Phase Equivalent Circuit

SPL Sound Pressure Level

SWL Sound Power Level

wf Winding function

ZVM Zero Vector Modulation

Chapter 1

Introduction

1.1 Background

As the urgency of a global sustainable development policy grows in public consciousness, searching for a sustainable mobility - safe, efficient, eco-friendly and human-friendly - is one of the current greatest scientific challenge.

Among the existent means of transportation, the electric railway system has many advantages: its engine does not emit any greenhouse gas and runs with electricity, on the cleanest sources of energy today, assuming that cleanliness does not apply to the management of long-term nuclear wastes.

Furthermore, noise has become a major factor in qualifying our environment quality: one third of the Europeans complains about noise (98). At same exposure level, the noise emitted by planes is more unpleasant than the one emitted by cars, whereas noise due to railway traffic, which concerns between 2 and 4 % of the european population, is generally less annoying than the car traffic one. The estimated cost of railway noise (through its effects on health, the building of noise-reducing infrastructures, the depreciation of lands, etc.) is inferior to the ones of road and air traffics.

However, light-rail vehicles often drive close to residents, alike subways in the aerial parts of their track, and the demand of higher transport capacity tends to place passengers closer to the engine. The noise requirements of operators have therefore become stricter, and low noise traction motors are now a key success factor for railway industries.

1.1.1 Noise of railway transport systems

1.1.1.1 Sources of noise

The sources of noise in railway transport systems are traditionally classified in three types:

- aerodynamic source (e.g. train turbulence and ventilation, motor fan)

- mechanical source (e.g. train wheel-rail squealing noise, motor bearings and gearbox)
- magnetic source (e.g. traction box transformers, inductances and rheostatic braking resistances, motor stator and cables)

Audible noise always has an aerodynamic origin, in the sense that it is produced by air vibrations occurring in the audible range [20 Hz, 20 kHz]. The magnetic source of noise is defined as audible noise coming from vibrations due to magnetic forces, and therefore stops as soon as the machine is current-free. However, bearings noise comes from the shaft rotation, which comes itself from the action of electromagnetic torque: mechanical noise could therefore be considered as a type of magnetic noise¹. Such a classification has no physical foundation, and was probably more guided by the different specialisations of engineers (aerodynamics, mechanics or electromagnetism).

The contribution of these three sources to the global sound power level, and the class of people exposed to noise, depend on the application (subway, light-rail vehicle, regional or high-speed train), on the traction motor topology (water-cooled or fan-cooled motor, self-ventilated or not, opened or closed enclosure) and type (synchronous permanent magnet motor, induction motor), and on speed. In starting phase, the aerodynamic source is generally low, and the current level is maximum in order to develop the maximum torque, leading to high magnitude magnetic forces. On the contrary, at high speed, the air-gap flux is lower, and aerodynamic noise generally covers magnetic noise. In both starting and braking phases, several PWM strategies are employed and significantly enrich the magnetic noise spectrum. The noise of high speed trains mainly affect residents, whereas the noise emitted by subways and light-rail vehicles can annoy both passengers (including the driver) and frontage residents, as traction and braking mainly occur in railway stations.

Magnetic noise generally occurs in traction machines at relatively high frequencies (500 Hz to 4 kHz, far from mechanical frequencies), and is often characterised by high tonalities: the total noise spectrum presents sharp peaks, creating an unpleasant sound which is penalised by acoustic norms. These tonalities are also characteristic of fan noise (*siren effect*).

1.1.1.2 Acoustic norms

The only current international acoustic norm on traction motors is the International Electrotechnical Commission standard IEC 60034-9 (Rotating electrical machines - Part 9: Noise limits). It specifies a total sound power level (SWL) limit in dBA² depending on speed, as shown in Fig. 1.1.

This norm also defines how to penalise the pure tones occurring in the one-third octave band spectrum (Fig. 1.2).

¹Magnetic noise is also sometimes called electrical noise, but the term of electromagnetic noise is reserved to the electromagnetic compatibility (EMC) field.

²The dBA is a SWL measure in dB weighted by human's ear sensitivity, see Fig. 2.8.

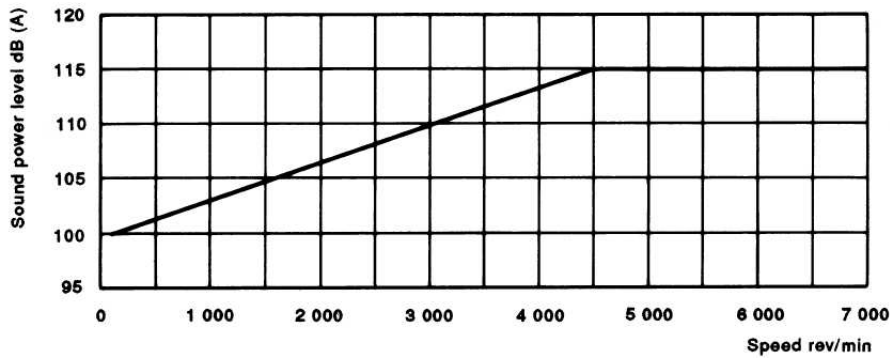


Figure 1.1: IEC 60034-9 norm noise limit

Decibel above average	Correction dB
$5 < \Delta L \leq 6$	3
$6 < \Delta L \leq 8$	4
$8 < \Delta L \leq 10$	5
$\Delta L > 10$	6

Figure 1.2: IEC 60034-9 norm tonalities penalisation. ΔL is the average of the sound levels of the adjacent one-third octaves: the correction in dB must be added to the global sound power level in dBA.

The noise level must be measured at no-load and under sinusoidal supply. These normalised test conditions are highly questionable, as it has been already pointed out by some authors (107), notably because pulse-width modulation (PWM) supply significantly changes the motor noise (see section 2.2.1.3): some operators have already reported some complaints coming from residents or passengers, even when the IEC norm was fulfilled. The prediction of the audible magnetic noise due to PWM is therefore especially important when designing a traction motor.

1.1.2 PROSODIE Project

This thesis work is a part of a larger project, called PROSODIE ("PROpulsion Silencieuse Optimisée et Dimensionnée pour l'Environnement"), which aims at understanding and predicting the audible magnetic noise emitted by inverter-fed traction motors, and by passive components such as inductors and transformers. Our work dealing with traction motors, which started in December 2005 and ended in September 2008, followed two main thesis works : *Vibro-acoustic dimensioning and sensitivity analysis of alternative current variable-speed machines* (3), and *Contribution to the study of acoustic noise generated by the association of an electrical machine and its static power converter - application to the induction machine* (81).

Besides the company ALSTOM-Transport and the laboratories L2EP and LEC, another important actor of the PROSODIE project is the company VIBRATEC, specialised in acoustic, vibration measurements and numerical simulation. They have performed three of the four test

campaigns run on ALSTOM motors (three more campaigns have been carried on our own in LEC laboratory), and performed several simulations with the mechanical finite element method (FEM) software Ideas, and the acoustic boundary element method (BEM) software Sysnoise.

1.2 Objectives

The main objective of this work is to build some models able to predict the audible magnetic SWL emitted by a squirrel-cage induction machine in function of the motor design variables (slot numbers, dimensions, ...) and its PWM strategy parameters (switching frequency, type of PWM strategy, ...). These models must also be able to compute the motor performances (output torque, efficiency) in order to help designing low-noise motors achieving some specified traction characteristics.

The simulation tool must be especially fast: firstly, it is necessary to calculate noise at variable speed (traction and breaking phases) in order to take into account resonance effects ; secondly, as induction motor design involves several conflicting objectives, the programme will be coupled to a multi-objective optimisation tool: if this task has to be handled by a 2 GHz laptop, the evaluation of one motor design must not last more than a few minutes. Therefore, the use of analytical models are favoured in this thesis, and FEM are only used as numerical validations besides experiments.

An underlying objective of this work is to break the limits of AIT-HAMMOUDA and HUBERT works (3; 81), comprising:

1. unsaturated hypothesis (linearity of voltage/current curve, and no saturation of the air-gap flux density shape) for both works
2. sinusoidal hypothesis (no inverter model) for AIT-HAMMOUDA work
3. off-load hypothesis (zero slip, no rotor currents, no output torque computation) for AIT-HAMMOUDA work
4. uncoupled mechanical structure and magnetic excitation for HUBERT work
5. prohibitive computing time (up to 10 mn per motor speed) for both works

The first simulation tool programmed by AIT-HAMMOUDA (referred as DIVA¹ 1.0, opposed to DIVA 2.0 which was developed during our work) also suffered from several computing limitations (shorted-pitch was not correctly taken into account, and fractional-slot modelling was not possible), and a lack of visualisation tools. Other problems came from the fact that all the electromagnetic air-gap distributions (windings and permeance) were calculated as Fourier series in the programme, giving low-accuracy and time-consuming results. This old version has therefore been completely reworked, and nothing remains of it in DIVA 2.0.

¹DIVA means *D*imensionnement *V*ibroAcoustique.

1.3 General approach

In a first part, a general overview of previous works is done (chapter 2). The different electromagnetic and vibro-acoustic models found in literature are presented, and the analytical models adopted in this thesis, as well as their underlying assumptions, are argued. The noise reduction methods seen during the bibliographic study are then detailed: they include low-noise design rules, based on the influence on magnetic noise of motor design variables, environment and supply current, and active methods such as current injection. Finally, the works dealing with induction machine optimal design are considered, especially when they include the vibro-acoustic factor.

In a second part, the analytical models chosen along the first part are exposed in depth (chapter 3), and at its stage of the computations, some simulation results with DIVA (2.0 will be omitted in the rest of the thesis) are presented and validated. The air-gap radial flux density computation is first presented and validated including load, PWM and saturation effects. The mechanical and acoustic analytical models are also presented and validated by FEM and/or tests on induction machines from 0.7 to 350 kW. Along this part, some experimental validations will be made on different motors, noted from M1 to M7, whose main characteristics are given in Appendix A.2 (note that M2, M3 and M4 share the same stator, as well as M5 and M7). Indeed, ALSTOM test-benches were not enough available and flexible to ensure all the test campaigns, and they required a high safety level which did permit all needed measurements. Moreover, ALSTOM experimental data was not necessarily gathered on the same motor. Validations have thus been carried on two main types of motors: the small power motor of LEC laboratory (M1), on which any PWM strategy could be implemented and any measurement could be carried, and the medium power motors of ALSTOM Transport (M2 to M6). More than a lack of coherence, this should be seen as the opportunity to validate the model implemented in this thesis on a very wide power range. Note that when ALSTOM motors are concerned, some data (drawings, noise levels) have been modified for confidentiality reasons.

In a third part, new methods to reduce magnetic noise annoyance at the design stage are investigated (chapter 4). The most important magnetic force waves are first analytically characterised in terms of frequency, number of nodes and propagation direction, and experimentally validated. On the ground of these analytical results, some noise reduction guidelines are established acting on the motor geometry (slot numbers, slot openings) and PWM strategy. Finally, a constrained multi-objective optimisation technique is presented and applied to an industrialised traction machine. To ensure the validity of these approaches, two low-noise motor prototypes for a subway application are designed. One of them is manufactured and successfully tested: it improves the noise level on the whole speed range, and noise reduction reaches 15 dBA in off-load sinusoidal case. Some changes are also proposed on the PWM strategy, and a 5 dBA

noise reduction is obtained.

In a last part (chapter 5.1), the conclusions of this thesis work are drawn. Some weaknesses of DIVA analytical models are then pointed out for future work, and some new research fields that could be investigated using DIVA are finally proposed.

More resources about this thesis work can be found on the internet at the following address:

`http://l2ep.univ-lille1.fr/pagesperso/lebesnerais/`

Chapter 2

State of the art and orientation of the work

In this chapter, an overview of the most important works seen during the bibliographic study are presented. As the thesis scope involves several fields of physics (electromagnetism, mechanics, acoustics) and mathematics (optimisation), an exhaustive list of all the references studied during these three years would be inappropriate: the more distinctive publications have been selected in terms of clearness, scientific rigour, synoptic view and pioneering work.

Modelling magnetic noise generation requires to model both the electromagnetic exciting force and the mechanical response of the excited structure (magnetic force / structure vibration transfer). Once the vibrations of this structure are known, an acoustic model is necessary to compute the sound power level radiated by the machine (air vibrations / SWL transfer). This first part details the different analytical models that were found in literature. The most appropriate ones to fulfil our goals (cf. section 1.2) are chosen, and all their assumptions are clarified.

2.1 Electromagnetic and vibro-acoustic modelling

2.1.1 Electromagnetic forces modelling

Magnetic forces occurring in electrical machines are traditionally classified in three types:

1. Maxwell forces (sometimes called reluctance forces)
2. Laplace forces
3. magnetostrictive forces

This classification, which is often reported in literature, is as ill-defined as the previous one on noise sources: indeed, as pointed out in (15), one must distinguish force distributions or densities, acting on differential volumes or surfaces of the machine, from total forces, which

are integrals of force distributions on some parts of the machine (e.g. conductors for Laplace forces). Moreover, Maxwell forces are often expressed from the definition of the Maxwell tensor, whose general definition already contains the Lorentz force.

Neglecting the electrical fields, the i -th component of the force density applying on a given volume element of the motor can be written under the form (133) :

$$f_i = [\mathbf{div}(\mathbf{Y})]_i + [\mathbf{j} \times \mathbf{B}]_i - \frac{1}{2} \sum_{j,k=1}^3 H_j H_k \partial_i \mu_{jk} - \frac{1}{2} [\mathbf{rot}(\mathbf{H} \times \mathbf{B})]_i + [\mathbf{div}(\mathbf{\Phi})]_i + [\mathbf{div}(\mathbf{\Psi})]_i \quad (2.1)$$

where f_i stands for the i -th ($i=1,2,3$ being the Cartesian coordinates in basis $(\mathbf{x}_1, \mathbf{x}_2, \mathbf{x}_3)$) component of force vector \mathbf{f} , and μ_{jk} is the magnetic permeability second order tensor (matrix) assuming the medium is anisotropic. The meaning of these six components is the following:

1. $\mathbf{Y} = \mathbf{C}(\mathcal{E})$ is the mechanical stress tensor, \mathbf{C} is the elasticity tensor and \mathcal{E} the strain tensor. In the linear case we have $y_{ij} = \sum_{k,l=1}^3 c_{ijkl} \epsilon_{kl}$ (Hooke's law).
2. $\mathbf{j} \times \mathbf{B}$ is the Lorentz force per unit volume which applies to a coil flowed by a current \mathbf{j} in an external flux density field \mathbf{B} (also called Laplace force in its integral form).
3. $-\frac{1}{2} H_j H_k \partial_i \mu_{jk}$ describes the force per unit volume caused by magnetic permeability inhomogeneities, assuming that it does not depend of the magnetic field intensity.
4. $-\frac{1}{2} [\mathbf{rot}(\mathbf{H} \times \mathbf{B})]_i$ represents a torque (133) which vanishes if \mathbf{H} and \mathbf{B} are colinear.
5. $\mathbf{\Phi}$ is the magnetostriction tensor, related to the strain dependence of the magnetic permeability.
6. $\mathbf{\Psi}$ is the thermal stress tensor.

Using the conservation of magnetic flux, the magnetic force densities number 2, 3 and 4 can be expressed by a magnetic tensor called Maxwell tensor (94):

$$T_{ij} = \frac{1}{2} (H_i B_j + H_j B_i - \sum_{k=1}^3 \delta_{ij} H_k B_k) \quad (2.2)$$

The extra-diagonal terms of this tensor stand for magnetic shear stresses, whereas the diagonal terms stand for magnetic normal stresses. All the magnetic stress present in an electrical machine parts, which vanishes when it is magnetic-field free (i.e. current-free in induction motors), either comes from Maxwell stress or magnetostrictive stress.

Focusing of these magnetic forces, the electromagnetic force density can be written as

$$\mathbf{f} = \mathbf{div}(\mathbf{T} + \mathbf{\Phi}) \quad (2.3)$$

2.1.1.1 Maxwell forces

Assuming that $\mathbf{B} = \mu\mathbf{H}$ (isotropic permeability), and taking a surface dS with normal direction \mathbf{x}_3 (Fig. 2.1), the magnetic stresses in its normal and tangential direction are given by

$$\sigma_t = T_{23} = \mu H_n H_t \quad \sigma_n = T_{33} = \frac{1}{2} \mu (H_n^2 - H_t^2) \quad (2.4)$$

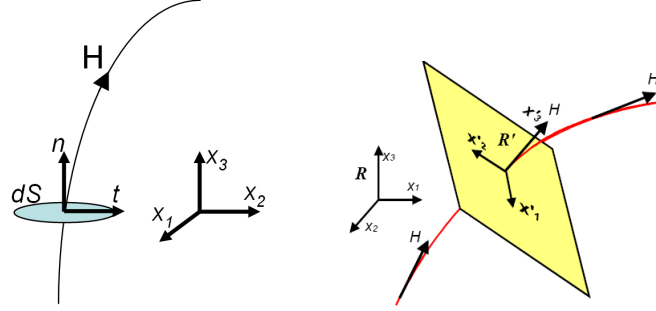


Figure 2.1: Left: definition of dS surface and its normal and tangential directions. Right: definition of the local coordinate system defined by a magnetic field line (from (14)).

In an induction machine, where cylindrical coordinates (r, θ, z) are more adapted, σ_n becomes σ_r and σ_t becomes σ_θ . The modulus of this stress is constant and independent of the surface orientation. It is given by

$$\sqrt{\sigma_t^2 + \sigma_n^2} = \frac{\mu}{2} |\mathbf{H}|^2 \quad (2.5)$$

which is the electromagnetic energy density (homogeneous to a pressure, which explains the use of the expression "Maxwell pressure") at that point. A geometrical interpretation of that magnetic stress is also reported in (14): the angle Δ between the magnetic force which applies to a given surface and its normal direction is twice the one between the local magnetic field line direction and the surface normal direction. As a consequence, when \mathbf{H} is perpendicular to a surface ($\Delta = 0$), the magnetic force seen by that surface is collinear to \mathbf{H} ; when \mathbf{H} is parallel to a surface ($\Delta = \pi/2$), the magnetic force is also perpendicular to the surface, but in opposite direction (see Fig. 2.2).

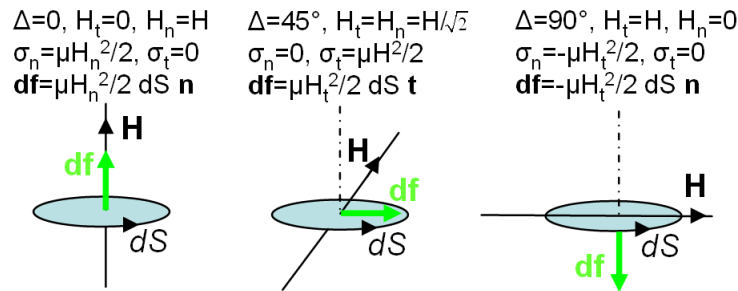


Figure 2.2: Direction of total Maxwell stress for different magnetic line directions.

If Maxwell tensor is expressed in the local coordinates defined by a given magnetic field line (cf. Fig. 2.1), it becomes

$$\mathbf{T} = \mu \begin{pmatrix} -\frac{1}{2}|\mathbf{H}|^2 & 0 & 0 \\ 0 & -\frac{1}{2}|\mathbf{H}|^2 & 0 \\ 0 & 0 & \frac{1}{2}|\mathbf{H}|^2 \end{pmatrix} \quad (2.6)$$

Two different stresses therefore occur in the perpendicular plane of the magnetic line, and in the direction of the magnetic line: the first one can be interpreted as an hydrostatic magnetic pressure, which tends to keep the magnetic field lines away from one another; the second one can be interpreted as a magnetic tension which tends to make magnetic field lines shorter (14). The first one also corresponds to the law of maximum flux, which "inflates" a deformable solenoid, while the second one corresponds to the law of minimal reluctance, which tenses the solenoid.

Expression (2.4) can also be found using the Ostrogradsky theorem (or divergence theorem) (15), which shows that the volume integral of the Maxwell stress divergence can be reduced to a surface integral enclosing the volume under consideration:

$$\mathbf{F} = \int_{\mathcal{V}} \mathbf{f} d\tau = \int_{\mathcal{S}/\mathcal{V} \subset \mathcal{S}} \mathbf{T} \cdot d\mathbf{S} \quad (2.7)$$

If we want to calculate the total Maxwell force which applies on the volume \mathcal{V} of the full stator, we can define a closed surface \mathcal{S} composed of a cylinder in the air-gap, another cylinder outside the motor, and two rings in the motor end-regions. Assuming that the magnetic field vanishes outside the machine, the surface integration over \mathcal{S} is reduced to a surface integration over the air-gap cylinder:

$$\mathbf{F}_{stator} = \int_{\theta=0}^{2\pi} \int_{z=0}^{L_s} \mathbf{T} \cdot \mathbf{u}_r r d\theta dz = \int_{\theta=0}^{2\pi} \int_{z=0}^{L_s} (\mu_0 H_r H_\theta \mathbf{u}_r + \frac{1}{2} \mu_0 (H_r^2 - H_\theta^2) \mathbf{u}_\theta) r d\theta dz \quad (2.8)$$

The Maxwell stress at the interface between the air-gap and the stator stack can therefore be expressed as

$$\sigma_n = \frac{1}{2} \mu_i (H_n^2 - H_t^2) - \frac{1}{2} \mu_0 (H_n'^2 - H_t'^2) \quad (2.9)$$

$$\sigma_t = \mu_i H_n H_t - \mu_0 H_n' H_t' \quad (2.10)$$

where μ_i stands for the magnetic permeability of iron, H stands for magnetic field values in the iron, whereas H' stand for magnetic field value in the air. Using the continuity laws of flux density and magnetic field, we have $H_t = H_t'$ and $B_n = B_n'$, so that

$$\sigma_n = \frac{H_t'^2}{2}(\mu_0 - \mu_i) + \frac{B_n'^2}{2}\left(\frac{1}{\mu_i} - \frac{1}{\mu_0}\right) = \frac{1}{2}(\mu_0\mu_i H_t'^2 + B_n'^2)\left(\frac{1}{\mu_i} - \frac{1}{\mu_0}\right) \quad (2.11)$$

$$\sigma_t = 0 \quad (2.12)$$

Maxwell stress at the interface between air-gap and stator iron (in front of stator teeth) is therefore a normal stress, in radial direction. Note that at this stage of the analysis, no assumption has been made on the fact that magnetic flux density lines radially enter in stator teeth. The property of a purely radial Maxwell stress at the interface is independent of the incidence angle of the flux density lines, and only comes from continuity laws.

This radial stress tends to pull stator towards rotor (law of minimal reluctance), it is a negative pressure which applies on the inner surface of the stator. As illustrated in Fig. 2.3, only a small amount of flux density lines enters in teeth sides. If the inner surface of stator slots had been included in the surface integration, we would have found some additional Maxwell forces acting on stator teeth sides in transverse direction. These tangential forces can play an important vibro-acoustic role in certain cases, e.g. in large turbines (64; 66; 124) where the teeth bending natural frequencies can be excited (their natural frequency computation is detailed for instance in (61)). In (134), some tangential tooth forces linked to PWM supply are also shown to be superior or equal to radial tooth forces in sinusoidal case. However, teeth radial compression is directly transmitted to the stator yoke and frame, and efficiently radiated in audible sound power level, whereas their bending is damped by windings and wedges, and badly transmitted to the stator frame: these tangential Maxwell forces will be neglected in this work.

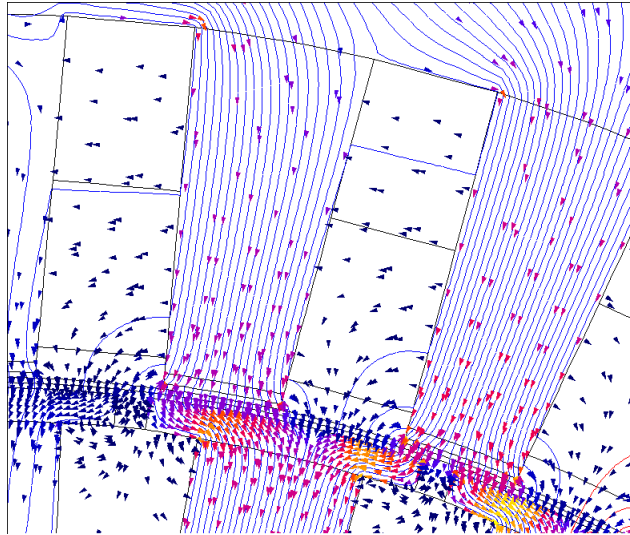


Figure 2.3: Example of flux density lines distribution in an induction machine, in unsaturated case: the main part of the magnetic flux enters perpendicularly to tooth tips.

As $\mu_0 \ll \mu_i$, the radial Maxwell stress can finally be approximated by

$$\sigma_n \approx -\frac{1}{2\mu_0}(\mu_0\mu_i H_t'^2 + B_n'^2) = -\frac{1}{2\mu_0}\left(\frac{\mu_i}{\mu_0}B_t'^2 + B_n'^2\right) \quad (2.13)$$

In non-saturated case, magnetic flux lines enter almost perpendicularly into the iron (cf. Fig. 2.3), so that $\mu_i B_t' \ll \mu_0 B_n'$, and a new approximation of σ_n can be made:

$$\sigma_n \approx -\frac{B_n'^2}{2\mu_0} \quad (2.14)$$

This negative radial pressure is here assumed to be the only significant source of audible magnetic noise in traction machines. In order to compute it analytically, the expression of the radial flux density B_n' at the outer surface of stator teeth is needed. As the air-gap is generally very thin, B_n' is approximated by the flux density value in the middle of the air-gap.

Expression (2.14) is only valid considering that stator iron has a linear characteristic. The effect of saturation will therefore have to be treated separately (see section 2.1.1.3.2).

Laplace forces are the integral expression of Maxwell forces on conductors, i.e. stator windings and rotor bars in an induction machine. They can produce high vibrations of the stator end-windings in both starting transient and steady state conditions (113). However, the stator slots flux density is too low to produce significant vibrations of the yoke, and stator conductors are wedged into slots. Acoustic noise due to Laplace forces is therefore neglected in this work.

2.1.1.2 Magnetostriction forces

The general phenomenon of magnetostriction in active materials comprise an isotropic phenomenon called *volume magnetostriction*, and an anisotropic phenomenon called *Joule and transverse magnetostriction* (15). Volume magnetostriction occurs in the iron at magnetic fields superior to 8 kA/m, but it can be neglected in the two-dimensional iron sheets of the stator stack: magnetostriction will therefore only refer to Joule and transverse magnetostriction in the following.

Magnetostriction is a magnetomagnetic phenomenon which stretches or shrinks a material in the magnetic field lines direction (Fig. 2.4), keeping its volume constant (15; 67). The elongation value for an electrical iron sheet can reach from 1 to 10 $\mu\text{m}/\text{m}$, which is also the order of magnitude of Maxwell relative displacements¹.

Magnetostrictive forces are defined as the force field which creates the same strain than the magnetostrictive stress. This stress is partly due to the overlapping of the dipoles electronic

¹Taking the magnitude $B_0^2/(2\mu_0)$ of the fundamental Maxwell force, which has a $2p$ spatial order and $2f_s$ frequency, gives for $B_0 = 1.5$ T on motor M5 an elongation of $Y_{2p\omega}^s \approx 310^{-6}$ (see equation (3.39)). Note that kind of comparison can be misleading as magnetic noise does not come from the low frequency fundamental magnetic vibration, but from some of its harmonics of higher frequencies and smaller magnitude (the same remark applies to magnetostrictive and Laplace forces).

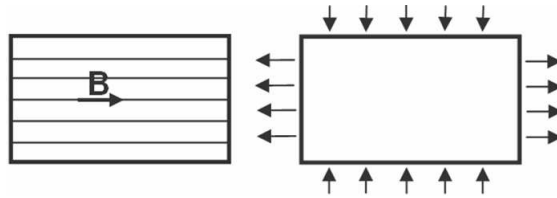


Figure 2.4: Simplified representation of a material flux density lines (left) and the resulting magnetostrictive effect (right).

clouds that compose the iron ferromagnetic material, when they naturally align with an external magnetic field. Another part of this stress is produced at a larger scale between different domains of the crystalline structure (11; 97). As Maxwell forces, magnetostrictive forces depend on the observation direction and are therefore properly represented by a tensor.

Magnetostrictive vibrations occur at same frequencies than Maxwell vibrations (97): it is therefore impossible to distinguish them on a vibration spectrum. Moreover, it is hard to quantify how much Maxwell efforts are greater than magnetostrictive efforts. It was shown in particular that it can depend on the deflection shape of the stator (97): magnetostrictive deflections can either limit or reinforce Maxwell deflections at a given frequency. An example of Maxwell and magnetostrictive force distributions is displayed in Fig. 2.5.

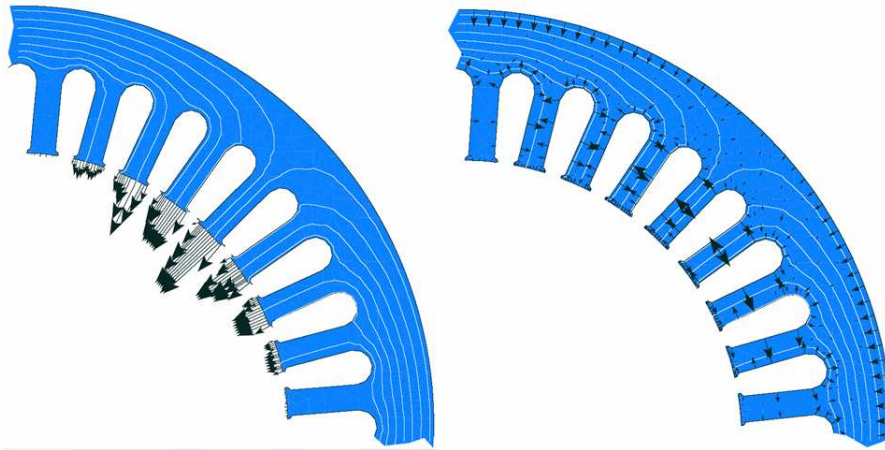


Figure 2.5: Maxwell (left) and magnetostrictive (right) force fields in a 37 kW induction machine (15). Note that different scales have been used in both figures: as discussed in (15), the FEA representation of nodal forces can be misleading because tooth tips mesh is generally finer: few but long arrows can stand for the same pressure as numerous but short arrows.

The relative importance of magnetostrictive and Maxwell forces strongly depends on the air-gap width, on the intrinsic magnetic properties of the iron (for instance, silicon-enriched materials limit magnetostriction (90)), and on the frequency range. Many studies were carried on different motors with different assumptions, leading to different conclusions.

As an example, a first study was made by BELMANS (19) who suggested that magnetostriction was negligible. Then, GARVEY (65) proposed a method to compute magnetostriction

effects, and its numerical application on a large machine showed that magnetostriction was negligible. Some other works (92) on a 2.2 kW motor showed that 10 to 30% of the magnitude of magnetic vibration lines were due to magnetostriction. The thesis work of LAFTMAN (97) concluded that magnetostrictive forces magnitude could be as high as Maxwell forces magnitude in mean power machines (50 kW), and suggested that magnetostriction could even make machines quieter. However, the comparison between Maxwell and magnetostriction is made on stator displacements magnitude, without considering the frequency factor: if magnetostriction is as high as Maxwell forces larger component occurring at two times the supply frequency, it can still be unsequential on the A-weighted sound power level. This is precisely the conclusion of a FEM-based work of DELAERE (49), who compared the vibration spectra induced by reluctance forces and magnetostriction on a 45 kW up to 2 kHz, and concluded that magnetostriction vibrations are considerably smaller than Maxwell ones, apart from the twice supply frequency component where both vibrations have same order of magnitude.

Given the complexity of the subject, we suggest to take the work of BELAHSEN (15), probably the most advanced in the domain, as a reference. His rigorous work suggested in particular that magnetostriction may only produce significant vibrations at frequencies inferior to 1500 Hz.

There exist different models of magnetostriction (15). The most commonly used model in FEM simulation (16; 47; 48; 49; 76; 77; 149) is the force-based one: magnetostrictive forces are assimilated as a thermal tensor whose characteristics are a function of magnetostriction coefficients. These coefficients are obtained by experiments made on iron sheets (7; 39).

Magnetostrictive effects will be neglected in this thesis. We will see thereafter that magnetostriction modelling is not necessary to satisfyingly explain the acoustic behaviour of ALSTOM traction machines studied along this thesis.

2.1.1.3 Conclusion

The only electromagnetic forces that are assumed to play a significant role in acoustic noise radiation are air-gap radial Maxwell forces, which depend on the air-gap radial flux density.

2.1.1.3.1 Air-gap flux density modelling

There are two main analytical methods able to determine the air-gap radial flux density distribution. The first one consists in decomposing the flux density as the product of a permeance function and magnetomotive forces (mmf), the latter being decomposed in current and winding functions (wf) (33; 68). The second method consists in analytically solving the electromagnetic field equations in a simplified geometry by applying conformal transformations (125; 132). However, the latter does not take into account iron saturation yet, and some progress is needed to make it a viable design option to other analytical models and FEA.

The permeance/winding function decomposition is therefore adopted in this thesis.

2.1.1.3.2 Saturation modelling

Saturation of stator and rotor iron sheets (see $B(H)$ curve in Fig. 2.6) has several influences on our electromagnetic model. Firstly, it decreases the magnetising inductance, which also increases stator and rotor currents. This effect can be modelled by introducing in the electrical circuit a dependence of the magnetising inductance with respect to the saturation level, quantified by the saturation factor (31; 108). Secondly, the top of the air-gap flux density distribution cannot increase proportionally to the applied current, given the saturation of the $B(H)$ curve in the active parts and the magnetic flux conservation: the flux density distribution in the air-gap is therefore flattened. This way, saturation changes the electromagnetic force spectrum, and can have a strong influence on magnetic noise.

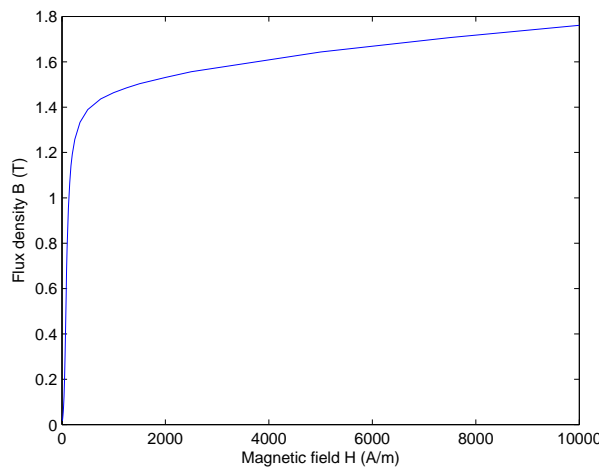


Figure 2.6: Typical flux density versus magnetic field curve.

This second effect is taken into account by adding a saturation permeance wave (62; 112). It can be also modelled more precisely by introducing a local saturation factor, varying along the air-gap (118). These two methods are well adapted to the permeance/fmm decomposition of the radial flux density distribution, but the former is adopted in this thesis as it requires less computations.

Furthermore, saturation of the tooth tips tends to widen the effective slot openings, and increase the average length of flux density lines entering the slots. As a first approximation, these effects will not be included in the permeance computation.

2.1.2 Vibro-acoustic modelling

2.1.2.1 Static displacements

Although the rotor is also subjected to Maxwell forces, its radial vibrations are damped by the air-gap and cannot make meaningfully vibrate the stator stack. Of course, axial rotor vibrations can be transmitted to the end-plates, but they are generally too small to relevantly participate

to the global sound power level, especially when the rotor is not skewed (skewing introduces an axial dependence of Maxwell forces, which have then a non-zero axial component). In addition, the end-plates area is much smaller than the stator frame one on ALSTOM motors: at same vibration level, the SPL radiation difference between an end-shield and the frame or stator stack is approximately

$$\Delta L_w = 10 \log \left(\frac{L_f}{D_f} \right) \approx 6 \text{ dB} \quad (2.15)$$

It is thus assumed that magnetic noise mainly comes from Maxwell radial forces excitation of the mechanical structure composed of stator stack (teeth and yoke) and frame.

In order to compute the vibrations of that structure, its static deflections must first be determined. This can be done by decomposing the electromagnetic force in Fourier series, and modelling the structure as an equivalent ring subjected to several sinusoidally distributed loads. Let us notice that if the total Maxwell force distribution pull stator teeth towards the rotor, it is not necessarily the case for its Fourier harmonics whose sign can change along the air-gap (see Fig. 2.7 where the spatial orders¹ 0, 1 and 2 are showed). In that simplified case of sinusoidal force waves, some analytical expressions of stator ring deflections can be established (87; 145; 166).

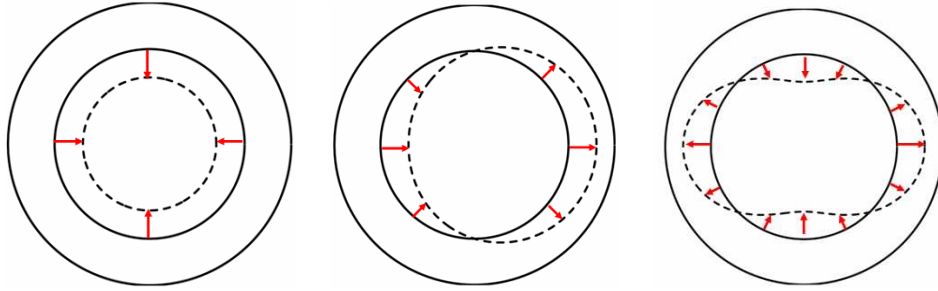


Figure 2.7: Illustration of the electromagnetic force decomposition in several sinusoidal force waves (spatial orders 0, 1 and 2). The magnitude, velocity, propagation direction of these elementary force waves are given by the 2D FFT of the air-gap electromagnetic pressure distribution.

2.1.2.2 Natural frequencies and dynamic deflections

Dynamic deflections are then obtained by modelling the dynamic response of the structure as a second order filter. Its damping factors cannot be analytically modelled, however some

¹The spatial modes are here defined as the spatial frequencies coming from the two dimensional Fast Fourier Transform of distributions which depend on time and on the mechanical angle α_s , not the electrical angle. As an example, the fundamental stator mmf has a spatial order p . One must also distinguish the orders of the exciting forces from the modes of the excited structure.

experimental laws have already been established on induction machines (166), showing that they lie between 1 and 4 % (TIMAR also proposed an average value of 2 % (145)), and linearly increase with the natural frequency. The analytical determination of these natural frequencies has been widely investigated (69; 104; 139; 151; 162), considering for instance the effects of teeth, frame (121), end-shields (167), windings (121), laminations (164), boundary conditions (159) and motor length (158).

Let us remark that this way of modelling the dynamic behaviour of the mechanical structure assumes that a resonance occur if and only if there is a matching between both the spatial order of the force wave and the mode number of the cylinder, and between the electrical frequency of the force wave and the cylinder mode natural frequency. This two conditions are also found when exactly solving the equations of the cylinder surface movement under a sinusoidal load, using Green's function method (139) (see Appendix B.2.2). Green's function method can be considered as another analytical method, which allows to directly express the cylinder surface deflection in function of the applied load. It has two advantages: its clear, compact formalism, and the use of the load expression in the time and space domain, which avoids a computationally expensive Fourier development. However, this useful formalism was found lately during the thesis, and the first analytical model of stator deflections has been adopted.

It is also noteworthy that as soon as Maxwell forces are supposed to be radial and independent of the motor axial direction (case of non-skewed and long enough motors), the calculation of natural frequencies involving longitudinal modes (e.g. modes id. 3 and 4 in Table) is useless. In this work, motor natural frequencies are calculated by modelling the stator and frame structure as an equivalent 2D ring.

The total stator deflection is then obtained by summing the dynamic deflections associated to each force harmonic. Indeed, modelling the vibratory behaviour of stator ring as a system of masses and springs leads to the following linear differential equation (152):

$$\mathbf{M}\mathbf{x}'' + \mathbf{C}\mathbf{x}' + \mathbf{K}\mathbf{x} = \mathbf{F} \quad (2.16)$$

where \mathbf{M} is the mass matrix, \mathbf{C} is the damping matrix, \mathbf{K} is the stiffness matrix, \mathbf{F} is the exciting force vector and \mathbf{x} is the stator deflection vector.

2.1.2.3 Radiation factor and sound power level

The sound power level radiated by the motor can then be determined by summing the vibrational powers associated to each mode, weighted by the modal radiation factor, which represents the ability of the structure to radiate a given spatial mode. The analytical computation of the radiation factor can be hard, even when modelling the stator frame as a finite-length cylindrical shell (159): according to the motor shape and the aimed accuracy, several analytical models can be used. The simplest ones are plane radiator, infinite-length cylindrical or pulsating sphere models (146; 166; 168). There exist more elaborate models, integrating the finite-length of

the motor and its boundary conditions (157; 159; 160). Let us notice that the use of a 3D radiation factor model is not incompatible with a 2D natural frequency model as soon as a modal-averaged radiation efficiency is used in the sound power level expression (157). Moreover, acoustic measurements are only able to estimate the modal-averaged radiation factor.

An alternative to this deterministic model of sound power level computation is the Statistical Energy Analysis (SEA) method (50; 110), which is especially adapted for complex structures involving several dynamical couplings. However, that method relies on the coupling loss factors involved in the system: if some theoretical expressions of these coupling factors exist in simple cases, and an experimental database have been built, the relevance of such technique in motor noise prediction is still to be proved (163).

2.2 Noise reduction methods

Noise reduction techniques are usually qualified as active or passive. Active noise control methods (also called anti-noise or noise-cancelling methods) are active in the sense that they use sound or vibration data from the motor in a closed control loop: they usually determine the vibration waves frequency, magnitude and phase in order to destructively interfere with them, by the aid of an additional vibration wave of same magnitude and frequency, but with opposite phase. Active techniques are generally expensive as they involve electromechanical devices and control loops; they are used once the motor is built and proves to be particularly noisy. On the contrary, passive devices such as dampers (shock and vibration absorbers) are low-cost, and can be planned at the design stage of the motor. In this chapter, this kind of passive methods will not be considered, but the acoustic influence of the motor and supply strategy design variables are looked over, as well as the resulting low-noise design guidelines. As pointed out in the introduction, there is still a leeway to decrease magnetic noise radiation at the design stage, and some new guidelines will be proposed in this work (see section 4.2).

2.2.1 Low-noise design rules

2.2.1.1 Design variables influence

The influence of motor geometrical characteristics on magnetic noise has been widely studied, the first work being the one of FRITZ in 1921. If a full vibro-acoustic model of the induction machine involves more than a hundred variables, the most influential ones on noise have already been identified using a sensitivity analysis tool (3; 20): they comprise rotor and stator slot opening widths, rotor and stator slot numbers, the stator outer diameter and height of yoke, and the air-gap width.

2.2.1.1.1 Rotor and stator slot number combination

The air-gap flux density distribution is modulated by the stator and rotor slots (see Fig. 3.24), so the electromagnetic force is directly linked to the stator and rotor teeth numbers. More precisely, when developing in 2D Fourier series its distribution which depends on time t and angular position α_s , its time frequencies depends on Z_r and p (due to rotor rotation), whereas its spatial orders (corresponding to the spatial frequencies) depend on Z_r , Z_s and p (145). Therefore, the choice of discrete parameters Z_r and Z_s directly influences the matching between the exciting frequencies and motor natural frequencies, and strongly affects magnetic noise level.

Many different empirical rules for choosing the quietest slot numbers combinations have been elaborated early (96). TIMAR has listed most of them in his book (145), and other lists can be found in (18; 51; 69; 88). However, some of these rules are contradictory, as they never take into account the motor specific natural frequencies neither its specific speed range. Moreover, some of them were established in order to decrease torque pulsations, although they do not necessarily generate magnetic noise: torque ripple is a function of the air-gap tangential flux density distribution, whereas magnetic noise due to radial Maxwell forces only depends on its radial component as seen in section 2.1.1.1.

An exhaustive experimental study of rotor slot number influence for $Z_s = 36$, $p = 2$ and $p = 3$ has been carried by HIROTSUKA (78), and compared to an analytical development of Maxwell force harmonics. However, if the natural frequencies of the motor are specified in the paper, their associated mode shapes are not mentioned and therefore not compared to the electromagnetic force spatial orders. In addition, the analysis is carried at a fixed supply frequency ($f_s = 60$ Hz), and cannot take into account resonance effects.

HUANG (80) successfully proposed some redesigns of noisy induction motors on the base of the analytical expression of Maxwell force harmonics, but still without considering the motor natural frequencies and the variable-speed effects.

Finally, KOBAYASHI (95) studied by FEM and experiments the vibro-acoustic behaviour of three different rotors, and correctly considered the variable-speed factor and the spatial orders of the Maxwell force. However, FEM computations are too much computationally greedy to be used during an optimisation process.

2.2.1.1.2 Rotor and stator slots shape

Stator and rotor slot openings considerably affect radiated noise. Decreasing them reduces the variation of permeance, and thus the magnitude of reluctance forces, lowering the noise (127). Nevertheless, closed rotor slots dramatically increase leakage flux (69). In a same way, the variation of permeance can be lowered by reducing the mean length of flux density lines entering into the slots.

These effects were studied for example by SALON (135) with FEM simulations. His work also concluded that if smaller openings decrease Maxwell force waves magnitude, they increase

saturation force waves magnitude. Indeed, saturation of the tooth tips tends to increase the effective slot opening width, and the mean length of flux density lines in the slot. Other studies on the rotor and stator slot shapes led to similar conclusions (43; 126).

2.2.1.1.3 Skewing

Skewing the rotor is a widely-used technique for lowering magnetic noise and vibrations. It consists in cancelling a given space harmonic of the air-gap flux density by properly choosing a biasing angle of rotor slots (116; 120). Stator skewing is rarely used as it makes windings manufacturing harder. As the main flux density space harmonics involved in Maxwell force distribution are $Z_s + p$ and $Z_s - p$ (see for instance Fig. 3.22), the corresponding optimal skewing angles of the rotor are given by $Z_s/(Z_s + p)$ and $Z_s/(Z_s - p)$ stator slot pitch. Usually, these two harmonics are both reduced by choosing a one ($Z_s/(Z_s \pm p) \approx 1$) stator slot pitch skewing of the rotor.

As seen in section 2.1.2, skewing also increases axial electromagnetic forces, and is therefore not recommended for large machines. It can also create high saturation levels in loaded case (31).

2.2.1.1.4 Stator stack dimensions

Apart from the obvious influence of the stator dimensions on its natural frequencies, the outer diameter to height of yoke ratio sizes the ability of the stator structure to transmit vibrations: the larger is the stator diameter and the thinner is its yoke, the more it plays the role of a sound box (28; 81) (see Fig. 3.33).

The stator and frame dimensions also affect the motor radiation efficiency: the longer is the motor and the smaller is its diameter, the less it radiates vibrational power into sound power (69).

2.2.1.1.5 Eccentricities

Static and dynamic eccentricities modify the electromagnetic forces by acting on the air-gap permeance (145). Static eccentricity appears at the manufacturing stage of the motor, and modify the spatial harmonics of Maxwell forces. It has been studied in particular by DELAERE (46). The effect of dynamic eccentricity, which modifies both the frequencies and spatial orders of reluctance forces, has been studied for instance by DORRELL (54). Both eccentricities introduce odd spatial orders in the exciting force spectrum, and especially some order 1 which can excite the rotor bending mode.

2.2.1.1.6 Manufacturing errors: tolerances, asymmetries

LO (109) showed that manufacturing errors could result in significant differences in noise radiation. More generally, the effect of geometrical asymmetries has been examined by CHANG

and YACAMINI (40), who concluded the importance to build the most symmetric machines, and especially a perfectly symmetric winding.

2.2.1.1.7 Materials

The works of VERMA and BALAN (152) especially showed the importance of the amount of "damping materials" present in the motor. These materials (mainly lamination, windings and insulation) allow to damping the vibrational power through viscous and coulombian phenomena.

Stator radial vibrations magnitude are inversely proportional to stator stack radial stiffness. Laminations, which aim at reducing the core Foucault losses, decrease the stator axial stiffness and increases its number of resonances in the audible range (152). The axial clamping pressure due to struss rods increases the stator axial stiffness: consequently, the motor tends to exhibit purely radial vibrations (164). This property comforts the choice in this thesis of a purely radial model of the electromagnetic forces, and a 2D cylinder model for natural frequencies computation.

Let us finally notice that the use of soft magnetic alloys help reducing magnetostrictive effects (90). The change of the intrinsic material properties could also possibly reduce Maxwell vibrations by the aid of opposite magnetostrictive vibrations (11; 97).

2.2.1.2 Mounting and coupling influences

Vibro-acoustic tests are often carried in no-load case on a test-bench: therefore, the motor is not in its normal running conditions, coupled to the load and mounted on the bogie. Whether test-bench acoustic measurements are significantly affected by motor mounting and coupling or not (at same magnetic excitation) is thus an important question.

On the one hand, loading the motor increases its stiffness and can therefore lower the noise (169)¹; on the other hand, loading changes the Maxwell forces spectrum (rotor mmf harmonics combine with permeance harmonics and give new flux density harmonics, and rotor harmonic fields induce in stator windings new harmonics (150)²), shifts all Maxwell forces frequencies by a larger slip, and increases the number of the structure natural frequencies, which can either lead to more or less noise... Coupling, as a mechanical effect, only influences the lowest part of the magnetic acoustic spectrum, and may therefore have a stronger influence on magnetic noise at lower speed as magnetic forces frequencies are proportional to the supply frequency (162).

Mounting the motor also increases its stiffness, and changes its natural frequencies, but it also adds damping to the system (169) which can possibly reduce noise.

¹The effect of stiffness itself is not that simple to predict: an infinitely rigid body do not move, and therefore transmits all the vibrations to its environment, which can creates structure-borne noise.

²This effect of multiple armature reaction will not be considered in this thesis, assuming that stator harmonic currents induced by rotor harmonic fields are too low to have a significant vibro-acoustic effect.

2.2.1.3 Supply current influence

2.2.1.3.1 Supply frequency

As it was underlined by the work of TIMAR and LAI (146), the noise level of a sinusoidally-fed induction motor increases with speed, as magnetic vibrations are proportional to the square of the exciting force frequency, which is itself proportional to the supply frequency. Moreover, in starting phase, increasing the supply frequency moves the magnetic noise frequencies in a higher sensitivity zone of the human's ear (see Fig. 2.8), which naturally heightens the dBA level even if no resonance is encountered.

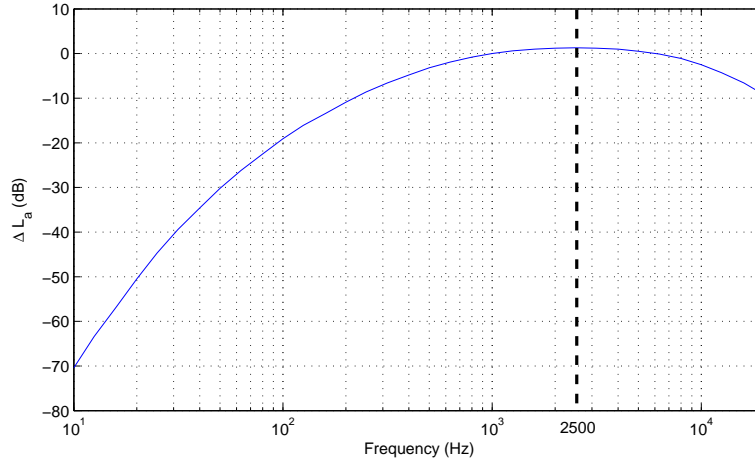


Figure 2.8: A-weighting in function of frequency ($\text{dBA} = \text{dB} + \Delta L_a$) in the audible range 20 Hz to 20 kHz: the human's ear maximum sensitivity is reached around 2500 Hz.

2.2.1.3.2 PWM strategy

The inverter voltage time harmonics generate additional current frequencies besides the fundamental supply frequency, which modifies the air-gap flux density distribution spectrum and consequently magnetic noise spectrum. This new harmonic content depends on two main parameters: the applied PWM strategy, which can be a function of the supply frequency, and the switching frequency.

In traction machines, during starting phase, the following strategies are generally applied:

1. asynchronous
2. synchronous
3. angle-calculated
4. full wave

Asynchronous and synchronous strategies are obtained with regular sampling PWM, where commuting angles are determined by intersecting a symmetrical triangular carrier with a sinusoidal modulating signal. In angle-calculated strategies and full wave mode, the commuting angles are precomputed by optimisation of several criteria (e.g. elimination of harmonics rejected to the catenary, and low frequency torque pulsations).

The vibro-acoustic influence of the supply strategy was first studied by TIMAR (144). Since this work, some authors tried to link in a general way the supply current shape or distortion rate to noise radiation (52; 84; 143; 165), or tested different PWM strategies (32; 100; 138; 161).

The strategies that were studied the most in terms of acoustic effects are spread-spectrum methods, which consists in spreading the current spectrum, creating more harmonics but with lower magnitude. They are widely applied in electromagnetic interference (EMI) field at higher frequencies (147). These techniques are usually separated in deterministic and non-deterministic ones, or scalar and vectorial ones. However, they all can be brought down to a natural sampling scalar PWM whose parameters are varied in a deterministic or way or not (101). These parameters are the modulating magnitude, the triangular carrier slope, and the carrier frequency. A classical deterministic spread-spectrum technique is for instance the Pulse Frequency Modulation (PFM) method, which consists in sinusoidally modulating the carrier frequency (141). A complete review of random strategies (RPWM) has been done by STANKOVIC (140), whose article also deals with the analytical prediction of RPWM voltage spectrum. All these techniques keep the fundamental current unchanged, and so for motor fundamental performances. When the PWM parameters remain unchanged on average, motor and inverter harmonic losses might also be unchanged.

Spread-spectrum techniques can lower noise annoyances due to a given current harmonic by reducing its magnitude, but increase the probability to meet a resonance by spreading the exciting forces spectrum. In addition, it has been reported in (93; 102) that random strategies could result in a bad sound quality. Psycho-acoustic factors are still missing to describe the quality of non-stationary sounds such as noise radiation of a random PWM fed motor (170).

Consequently, the experiments which aim at qualifying the PWM strategies acoustic properties may again differ according to the motor natural frequencies and PWM switching frequency, all the more when they are only carried at a single supply frequency. ERTAN (56) and STEMMER (141) experimented that PFM was quieter than PWM. BOYS successfully tested the noise mitigation properties of random switching frequency method (RSF) (35). In LO work (109), SVM was as noisy as symmetrical regular sampling PWM. XU studied the Direct Torque Control strategy and experimented that it was not quieter than RFPWM. NA (119) experimented the effect of RPPM. Random slope PWM has been studied by LIAW (106) and HABETLER (71). Other authors have studied mixed random techniques (1).

2.2.1.3.3 Switching frequency

Independently of the supply strategy, the switching frequency plays a major role in noise generation (18; 19; 111; 156): as it determines the frequencies at which the groups of current harmonics appear, a high switching strategy can push them out of the ear's sensitivity (cf. Fig. 2.8) (70). However, this method dramatically increases the switches stress and the inverter losses, and is therefore inapplicable to traction chains.

2.2.1.3.4 Comparison between PWM noise and slotting noise

It is important to notice that compared to the sinusoidal case, the PWM does not excite some new modes of the stator structure, and only adds new Maxwell forces frequencies (112). In a motor fed with an ideal frequency inverter, Maxwell forces only create some so-called slotting harmonics ¹, whose frequencies are proportional to the supply frequency (145):

$$f_{\text{slotting}} = f_s(k_r(1-s)\frac{Z_r}{p} \pm 0, 2) = Z_r f_R \pm 0, 2f_s \quad k_r \in \mathbb{N}^* \quad (2.17)$$

When feeding the motor with PWM, these harmonics remain, but some new harmonics appear. These new harmonics are pure PWM harmonics, of spatial order 0 or $2p$, or combination between slotting and PWM harmonics (109): a noisy motor in sinusoidal case will remain noisy when PWM-fed. The definition, the origin and the expression of slotting lines, pure PWM lines and combination between slotting and PWM lines will be treated in section 4.1.

PWM noise and slotting noise can be hardly compared in general case, as they strongly depend on the motor natural frequencies, speed range and inverter switching frequency. However, PWM noise generally dominates the overall noise radiated by the machine in starting phase (161): when the supply frequency is close to 0, slotting frequencies are too low to be heard, whereas asynchronous PWM lines occur at higher frequencies, generally in the ear's most sensitive frequency range (cf. Fig. 2.8) for traction motors.

2.2.2 Active methods

After having detailed the influence of motor and supply strategy variables on noise, in order to reach low noise levels at the motor design stage, a short review of noise reduction active methods is presented.

¹Indeed, the absence of rotor and stator slots would reduce the reluctivity changes in the air-gap, and Maxwell forces harmonics. More precisely, a smooth air-gap sinusoidally-fed machine only creates two Maxwell force harmonics of same magnitude: a DC component of spatial order 0 and frequency 0, and an AC component of mode $2p$ and frequency $2f_s$ (29). In traction induction machines, $f_s < 200$ Hz: these harmonics have therefore relatively low frequencies, and do not size the A-weighted total SWL. Moreover, they cannot resonate with the stator structure as 0 and $2p$ natural frequencies reach a few kHz (see section 4.1). However, they can play an important role in structure-borne noise problems.

2.2.2.1 Current injection methods

A first active method consists in adding a magnitude and phase-controlled current harmonic in the PWM sinusoidal modulating (99). This additional current harmonic creates two magnetic force waves (as Maxwell forces are a quadratic function of the air-gap flux density), one of which is chosen to destructively interfere with the magnetic force wave identified as noisy (17; 38; 44). However, this method is only applicable when noise comes from a slotting harmonic of order 0 or $2p$, which supposes that PWM noise is negligible compared to slotting noise. Unfortunately, traction motors have all 2 or 3 pole pairs, and their magnetic noise usually comes from slotting harmonics of order 2, which makes current injection technique inapplicable. Moreover, one must be sure that the second additional force does not resonate with the stator structure. Finally, as the injected current is added to the inverter modulating wave, the PWM switching frequency f_c must be much higher than the injected frequency: as magnetic noise harmful frequencies lie between 1 and 4 kHz, f_c must be of a few kHz, which is inconceivable in traction application.

Some other methods consists in adding a secondary winding to the machine (41; 82), and controlling in a same way the injected current.

2.2.2.2 Piezo-electric methods

Another class of active methods consists in creating noise-canceling vibration waves at the stator surface by the aid of piezo-electrical devices. In electrical engineering, it has been especially applied to synchronous reluctance machines (63; 117).

2.2.2.3 Other methods

Programmed PWM techniques allow to avoid switching frequency values that create high noise levels (55). In a similar way, KIM (91) experimented an active construction of the random switching frequency distribution. HASHEMI (72) also proposed an active control of the switching frequency in order to avoid resonances during starting and breaking phase.

2.3 Vibro-acoustic optimisation

Induction machine design is a multidisciplinary problem involving electrical, mechanical, thermal and acoustic aspects, and the analytical equations that rule these numerous models cannot be inverted. In that case, optimisation methods can help reaching some given technical specifications, and finding designs that even overcome the objectives.

NURDIN (123) makes an excellent history of the use of optimisation techniques in electrical engineering from 1964 to 1990. Previous works have used the optimisation techniques of non-linear programming techniques (4) such as boundary search along active constraints (9) and Han-Powell methods (60; 79), univariant search (5; 6; 130), Hooke-Jeeves method (58), and sequential quadratic programming (137).

These techniques can be classified according the following criteria:

- convergence to a global or local minimum
- accuracy
- convergence rate
- robustness
- constraints handling
- necessity to start from a feasible design (synthesis)
- multi-objective handling
- mixed variable handling (i.e. continuous, discrete and integer variables)
- use of decision making tools

As time-consuming FEM simulations are often necessary when evaluating the induction machine objectives, special efforts have been made in order to reduce the optimisation time. These techniques comprise surrogate models based on neural networks (83), kriging techniques (103), or experimental designs (154), and space mapping (12).

Evolutionary algorithms such as multi-objective genetic algorithms (89), niching genetic algorithms (42), particle swarms (13) and simulated annealing (131), are widely used in the most recent works.

To our knowledge, the only article that treated the optimal design of an induction machine including the acoustic criterion is the one of HADJ AMOR (5). The optimisation technique that he used, univariant search, does not handle several objectives, and converges to a local minimum. He compared the optimal designs obtained by noise minimisation and cost minimisation, and tried to define the cost of 1 dB in the neighbourhood of the optimal solution.

2.4 Conclusion

2.4.1 Modelling assumptions

The chosen analytical models are based on the following assumptions:

1. magnetic noise mainly comes from the radial component of the air-gap Maxwell forces, which are supposed to be independent the motor axial direction
2. magnetic noise is mainly radiated by the motor outer frame (or stator stack if the motor only has end-shields)

3. motor structure natural frequencies are computed using an equivalent 2D ring
4. motor radiation factor is close from the one of a sphere or an infinite-length cylinder

Some improvements of these assumptions are proposed all along the thesis.

2.4.2 Position of the work

As seen in this first chapter, several investigations aiming at modelling and reducing the electromagnetic noise emitted by induction machines suffer some too strong hypothesis or fast assertions. They comprise in particular:

1. generalising some laws based on experimental results carried at nominal speed, on a particular motor
2. minimising noise at a given speed, without considering resonance effects
3. studying the exciting force without considering its interaction with the mechanical structure
4. ignoring the exciting force harmonics spatial orders
5. minimising noise without taking into account PWM or saturation effects, though they can dominate magnetic noise

Consequently, a simulation tool able to predict the magnetic SWL radiated by a given motor with a reasonable error has not been implemented yet; no publication explicitly compares an experimental vibration or acoustic spectrum to a simulated one with similar accuracy. Moreover, a mixed-variable global multi-objective constrained optimisation technique has never been applied to induction motors, and even less with the noise criterion. We will see in section 3.3 that some numerical problems may have prevented some works from successfully building a fast and accurate simulation tool, and coupling it to some optimisation algorithms.

The magnetic noise issue is therefore far to be sorted out, and the use of active techniques to solve magnetic noise problems is probably premature in railway traction machines since a lot of progress seems to be possible in the analytical modelling, simulation and optimisation of audible magnetic noise: the potential noise reduction at the design stage has not been fully used yet.

Chapter 3

Electromagnetic and vibro-acoustic models

In this chapter are detailed the analytical models used in DIVA. They comprise an electromagnetic model, which computes the air-gap flux density distribution and the motor traction characteristics, a mechanical model which computes the dynamic vibrations of the stator stack, and an acoustic model which determines the SWL radiated by the stator (Fig. 3.1).

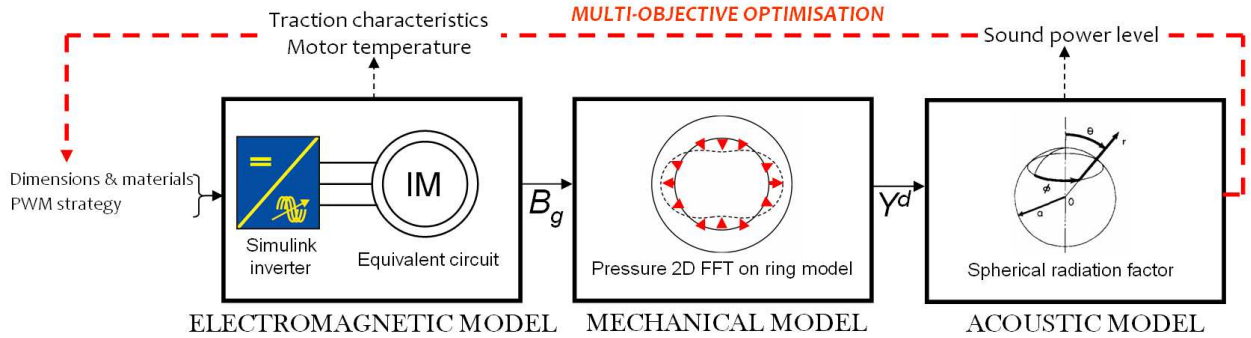


Figure 3.1: DIVA models and their main input/output.

3.1 Electromagnetic model

The electromagnetic part of the model computes the radial air-gap flux density distribution $B_g(t, \alpha_s)$, which gives the expression of air-gap radial Maxwell forces as seen in section 2.1.1.1. It also computes the motor performances (output torque, efficiency, etc) implied in the optimization process (see section 4.3.2).

By applying the Ampere's law to a properly chosen closed path in the induction machine

(33), one finds that the air-gap radial distribution can be written under the form

$$B_g(t, \alpha_s) = \Lambda(t, \alpha_s) \left(\underbrace{\sum_{b=1}^{Z_r} i_r^b(t) N_r^b(t, \alpha_s)}_{f_{mm}^r} + \underbrace{\sum_{q=1}^{q_s} i_s^q(t) N_s^q(\alpha_s)}_{f_{mm}^s} \right) \quad (3.1)$$

where Λ is the local air-gap permeance per unit area (the inverse of reluctance), and rotor and stator mmf are decomposed as the product of current (i_q^s or i_b^r) and winding functions (N_s^q or N_r^b).

Equation (3.1) can be viewed as a local and magnetic equivalent of Ohm's law: the air-gap radial magnetic flux plays the role of the electrical current, the inverse of permeance (the reluctance) stands for the electrical resistance, and the total magnetomotive force for voltage. The electromagnetic model first performs stator and rotor currents computation, which must be determined from the knowledge of supply voltages (electrical coupling circuit). Then, winding functions are computed according to the windings type (shorted-pitch, fractional-slot), and the permeance distribution is evaluated taking into account eccentricities and saturation effects.

Along this section, the time and/or space harmonic content of various functions are presented: they will be analytically detailed and discussed in section 4.1.

3.1.1 Currents computation

In transient state, stator and rotor currents can be computed by numerically solving the equations (see for instance (2; 115))

$$\mathbf{V} = \mathbf{R}\mathbf{I} + \frac{d\varphi}{dt} \quad (3.2)$$

$$\varphi = \mathbf{L}\mathbf{I} \quad (3.3)$$

where \mathbf{V} is the voltage vector, \mathbf{R} is the resistance matrix, \mathbf{I} is the current vector, \mathbf{L} is the inductance matrix, and φ is the flux vector. In order to evaluate the magnetic noise level radiated by a motor during its starting or braking phase, one can consider that the steady state is reached as soon as the motor speed variation characteristic time τ_{mec} is much larger than the characteristic time-scale of the motor circuit:

$$\tau_{mec} \gg \max(L_{1,2}^0/R_{1,2}^0) \approx 0.01s \quad \text{for motor M5} \quad (3.4)$$

A steady state interpretation of the equations (3.2) ($d/dt = j\omega_s$) leads to an equivalent electrical circuit similar to a transformer one (136). An excellent review of the equivalent circuit models can be found in HUBERT thesis (81). He established an equivalent circuit including time harmonics induced by stator mmf space harmonics in rotor bar currents, and time harmonics due to PWM supply, whose resolution can be formalised in a convenient matrix inversion.

An other method of currents computation (qualified as semi-analytical), consists in locally expressing the equations (3.2) and creating a so-called permeance or reluctance network (2; 128), which is also referred to an equivalent magnetic circuit (142). The network equations can be formalised with matrices, and fastly solved numerically. Permeance network method has also the advantage to take into account local saturation effects.

However, in this thesis, an equivalent circuit modelling is used following the works of AIT HAMMOUDA (3) and HUBERT (81). Local saturation effects will be included by modifying the permeance function. Since this equivalent circuit takes the phase voltage spectrum as an input, voltage computation must be validated first.

3.1.1.1 Voltage computation

3.1.1.1.1 Method

Phase voltage depend on the applied PWM strategy (asynchronous, synchronous, angle-calculated, full-wave, random strategies). For asynchronous, synchronous, full-wave and RSF strategies, a PWM inverter Simulink model has been elaborated in DIVA (see Fig. 3.2). The possibility to add a third harmonic voltage (at frequency $3f_s$, in order to increase the fundamental voltage component without over-modulating) has been also included. A direct vectorised implementation of sinus/triangle intersecting PWM is also available in DIVA for faster computations than the Simulink model; it is used in particular during optimisations.

In angle-calculated mode, the phase voltage waveform is built from an Excel sheet commuting angles table.

3.1.1.1.2 Validation

Simulated and experimental supply voltage have been compared for different strategies. In Fig. 3.3 is for instance displayed the asynchronous PWM experimental and simulated phase voltage spectra on motor M1 ($f_c = 1600$ Hz, $f_s = 50$ Hz). We can see that in this particular case, there are some slight difference on the voltage harmonics magnitude: the motor M1 PWM is generated on the ground of a numerical modulating (tabulated sinusoid which is scanned more or less quickly according to the supply frequency), whereas simulated PWM is generated from the Simulink sinusoidal modulating with a much higher number of discretising points.

3.1.1.2 Extended single phase equivalent circuit

3.1.1.2.1 Fundamental case

3.1.1.2.1.1 Expression

The classical single phase equivalent circuit (SPEC, see FIG. 3.4) allows to compute fundamental currents and motor performances.

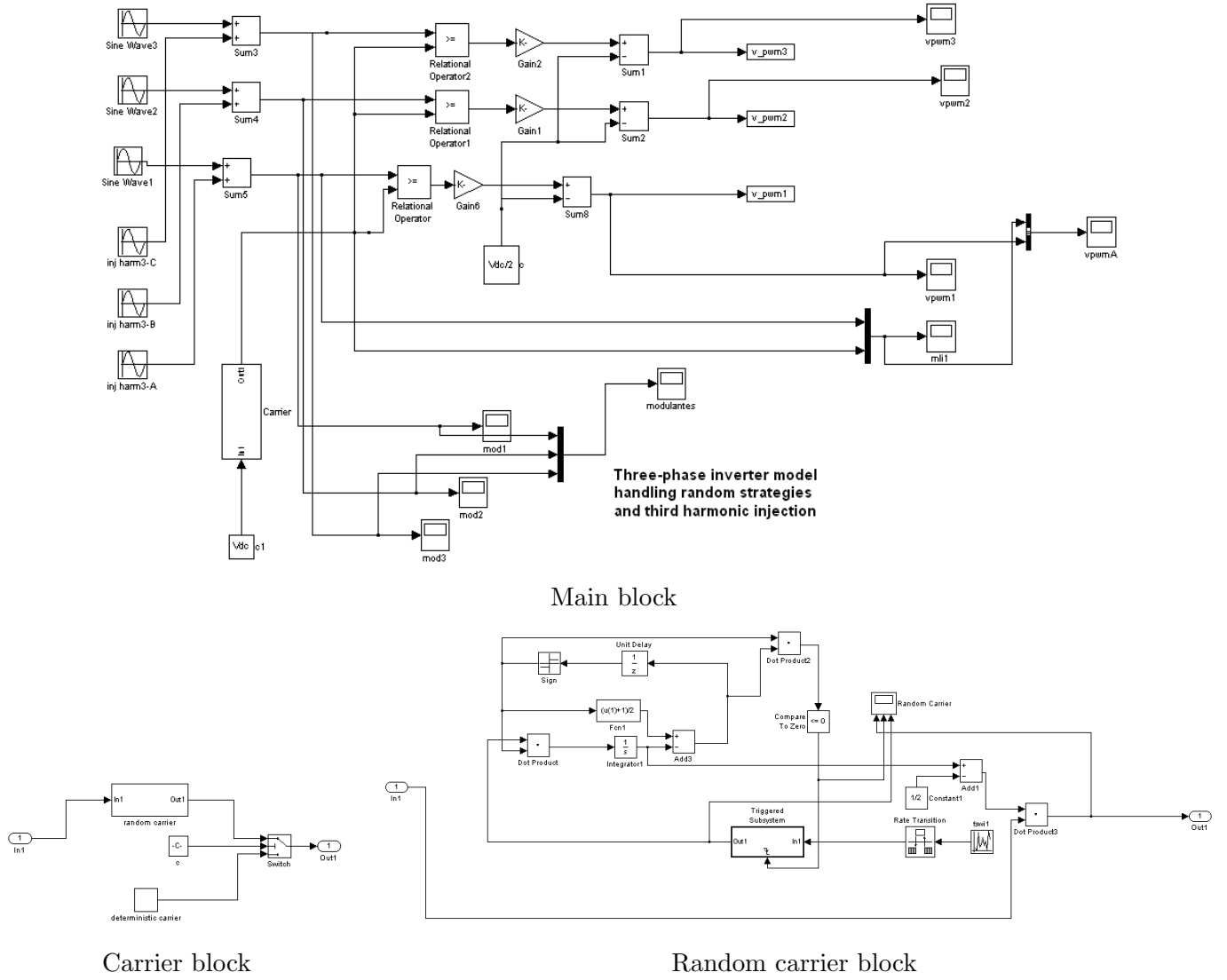


Figure 3.2: Simulink inverter model.

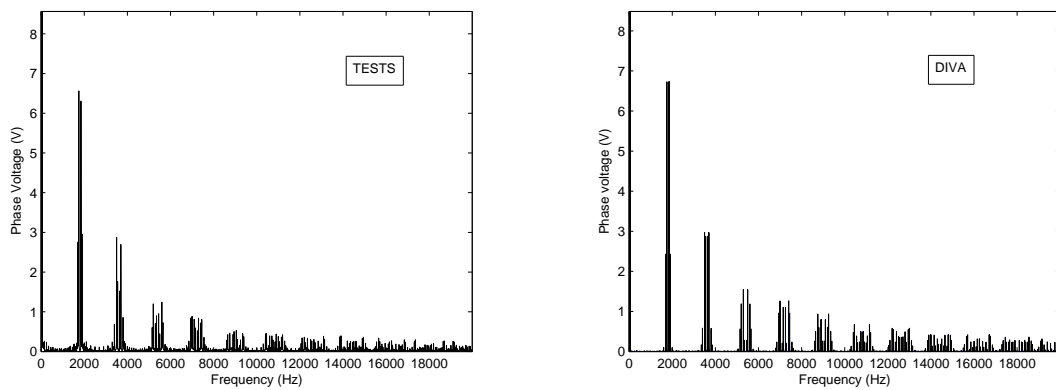


Figure 3.3: Comparison between experimental and simulated (DIVA) stator phase voltage in asynchronous mode on M1 motor ($U_0=6$ V, $f_c=1600$ Hz, $f_s=50$ Hz).

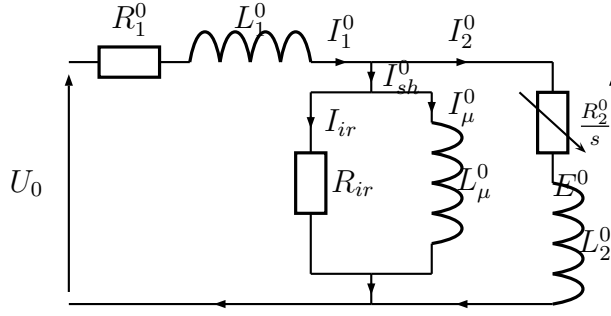


Figure 3.4: Fundamental single phase equivalent circuit

The analytical expression of the circuit elements can be found for instance in (34; 81; 108). The iron losses resistance R_{ir} in the shunt branch is a function of fundamental iron losses, which are computed according to a model described in section 3.1.5.

3.1.1.2.1.2 Saturation factor computation

As explained in the overview (cf. section 2.1.1.3.2), the saturation model of DIVA does not account for local saturation phenomena, but models the magnetisation inductance L_μ^0 decrease with saturation through the computation of a global saturation factor.

The saturation factor computation relies on the evaluation the total mmf along an equivalent flux line (see Fig. 3.5). Along this path are computed stator and rotor back cores mmf F_{sy} and F_{ry} , stator and rotor teeth mmf F_{tr} and F_{ts} , and the air-gap mmf F_g . The total mmf is therefore $2F_g + 2F_{st} + 2F_{rt} + F_{sy} + F_{ry}$, and the saturation factor is defined as:

$$K_s = \frac{F_g + (2F_{st} + 2F_{rt} + F_{sy} + F_{ry})}{F_g} \quad (3.5)$$

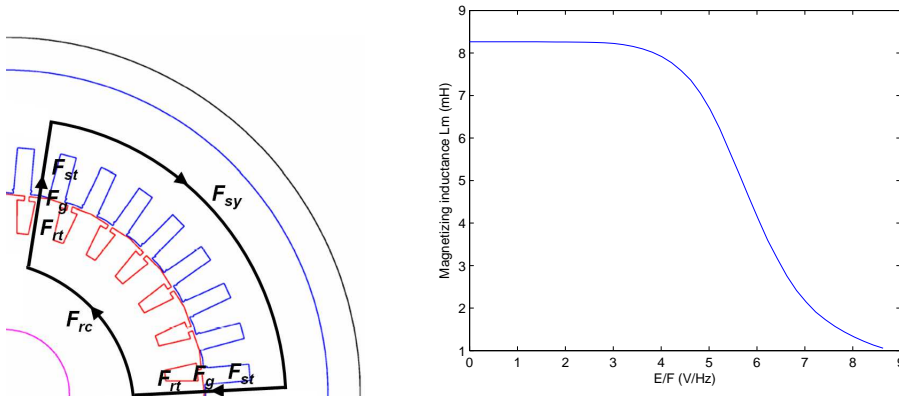


Figure 3.5: Left: mean flux line for saturation factor computation. Right: typical magnetising inductance curve in function of air-gap flux.

To evaluate these different parts mmfs, the peak flux densities B_i are first computed using the flux conservation law. The teeth peak flux densities are determined by dividing the teeth in three different sections. The $B(H)$ curve (cf. Fig. 2.6) is then used to compute the magnetic fields H_i , and each mmf F_i is finally computed as

$$F_i = H_i l_i \quad (3.6)$$

where l_i is the mean flux line length in part i . Since F_g is proportional to the air-gap width g , the saturation factor represents the air-gap enlargement in saturated case from g to $K_s g$: when the active materials are saturated, their magnetic permeability tends to be closer to the air one, so the air-gap is artificially enlarged (from the magnetic point of view). The magnetisation inductance is inversely proportional to the air-gap width, so saturation tends to make it decrease. At the beginning of the simulation, the saturation database is built by computing K_s as a function of the air-gap flux E_0/f_s . The magnetising inductance L_μ^0 (cf. Fig. 3.4) is also computed as a function of the air-gap flux (see Fig. 3.5).

More details on the saturation factor computation can be found in (31; 108).

3.1.1.2.2 Harmonic extension

The fundamental circuit does take into account PWM voltage time harmonics, and the space harmonics coming from the stator stepped mmf distribution, which induce rotor bars harmonic currents. Therefore, an extended multilevel equivalent circuit is computed in DIVA following the model proposed by HUBERT (81) (see Fig. 3.6). This model resolution is expressed as a simple matrix inversion for each time harmonic (28):

$$\mathbf{Z}^n \cdot \mathbf{I}^n = \mathbf{U}^n \quad (3.7)$$

where the matrix \mathbf{Z}^n has n lines (number of time harmonics) and m columns (number of space harmonics of stator mmf induced in rotor currents). For instance, the component R_2^n/s_{mn} of this extended circuit corresponds to the R_2^0/s component of the fundamental circuit (cf. Fig. 3.4). The resistances R_1^n and R_2^n , as well as the reactances X_1^n and X_2^{mn} , are modified to

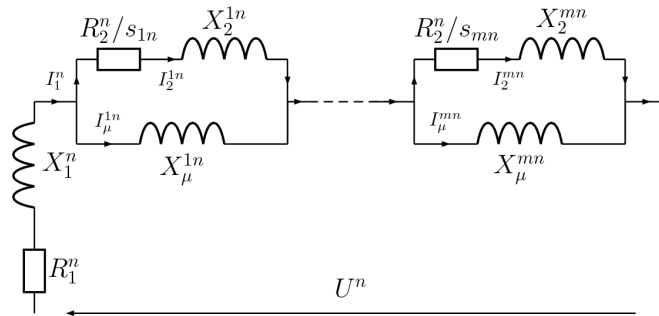


Figure 3.6: Multi-layer single phase equivalent circuit.

account for skin effect (114). s_{mn} represents the slip between the fundamental rotor mmf field (pulsation Ω_R) and an harmonic stator mmf field due to a n -th PWM time harmonic and a m -th winding space harmonic (pulsation Ω_S):

$$s_{mn} = \frac{\Omega_S - \Omega_R}{\Omega_S} = 1 - \frac{(1-s)\omega_s/p}{\pm\omega_n/m} \quad (3.8)$$

where the ± 1 factor accounts for the stator field propagation direction (1 for forward direction, which is the one of the fundamental field, -1 otherwise). If $m = p$ and $n = 0$, we can see that s_{mn} equals the fundamental slip s .

3.1.1.3 Validations

3.1.1.3.1 No-load saturated sinusoidal case

The saturation factor computation has been validated by comparing the phase current obtained with DIVA to the experimental phase current measured at different saturation levels (Fig. 3.7).

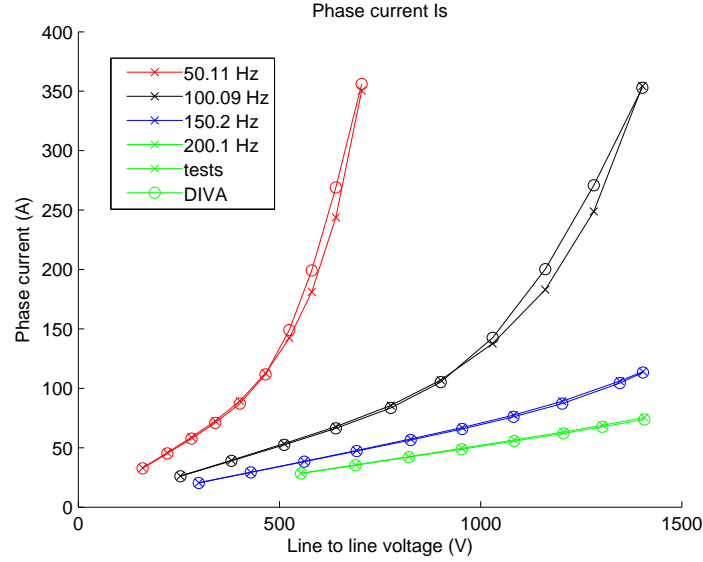


Figure 3.7: Experimental and simulated stator phase currents at several supply frequencies and supply voltages (motor M2, $s = 0.01\%$).

3.1.1.3.2 On-load unsaturated sinusoidal case

Simulated and experimental stator phase current in function of slip are compared in Fig. 3.8. If there is a 10 % maximal error, the trends are well respected and the nominal phase current is close from experiments.

The current distribution among rotor bars has been favourably compared to FEM simulations (see Fig. 3.9). We can see that the rotor instantaneous current is sinusoidally distributed over rotor bars.

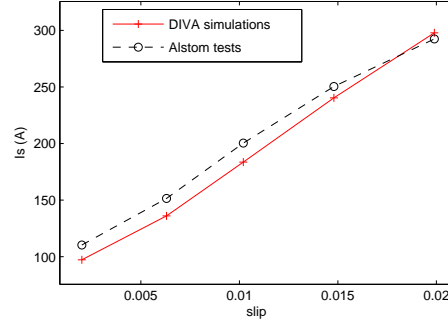


Figure 3.8: Experimental and simulated (DIVA) phase current as a function of slip on M3 motor ($U_0=810$ V, $f_s = 150$ Hz). The nominal slip is 1.56 %.

The frequency and magnitude of rotor current harmonics induced by stator mmf space harmonics have been also qualitatively validated using FEM (Fig. 3.10): we can see that the harmonics of spatial order $\nu_s = 7p$ and $\nu_s = -11p$ coming from stator mmf (see Fig. 3.15) creates the main rotor current harmonics at frequencies $|1 - (1 - s)\nu_s/p|f_s = 11.89f_s = 1783.5$ Hz and $5.93f_s = 889.5$ Hz.

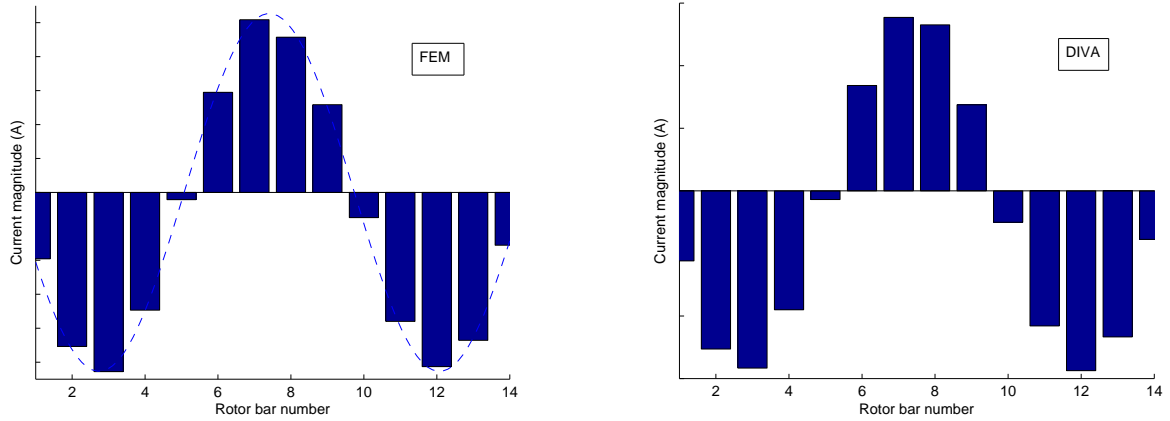


Figure 3.9: Rotor current distributions among bars obtained with FEM (left) and DIVA (right) (motor M2, $f_s = 150$ Hz, $s = 1\%$).

3.1.1.3.3 No-load unsaturated PWM case

PWM phase current has been validated on different machines with different PWM strategies. As an example, Fig. 3.11 compares the harmonic distributions of experimental and simulated phase current in an asynchronous case, and the main current harmonics magnitude are displayed in Table 3.1. Note that motor M5 has a skewed rotor, and tends to saturate a lot ($K_s=1.4$ in starting phase).

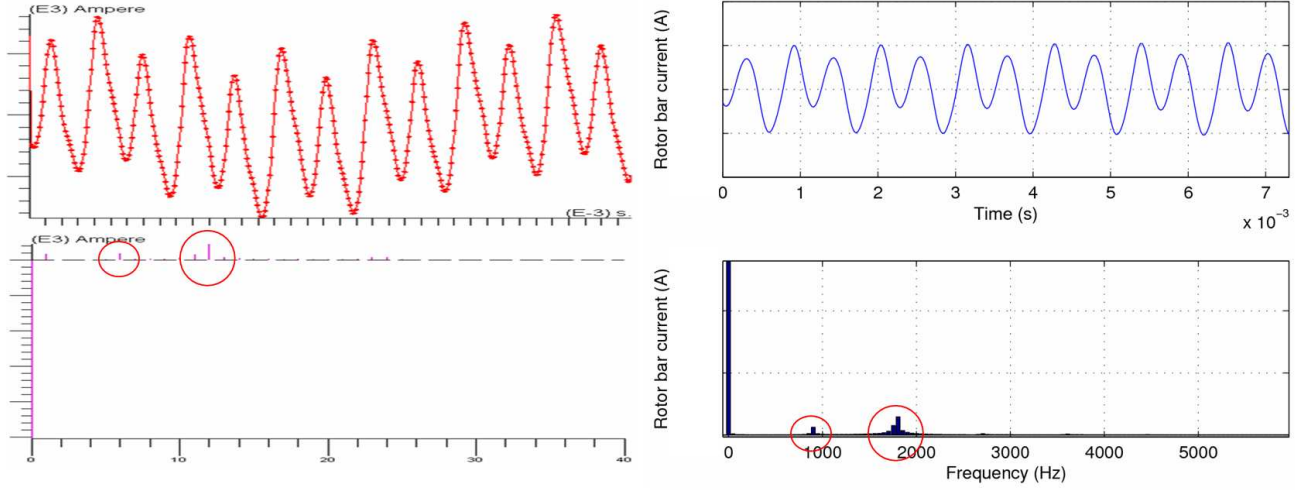


Figure 3.10: Rotor bar current waveforms obtained with FEM (left) and Diva (right) (motor M2, $f_s = 150$ Hz, $s = 1\%$). FEM spectrum abscissa is graduated in multiples of the supply frequency (harmonics 6 and 12 stand for $6f_s$ and $12f_s$ frequencies), whereas Diva spectrum is directly graduated in Hz.

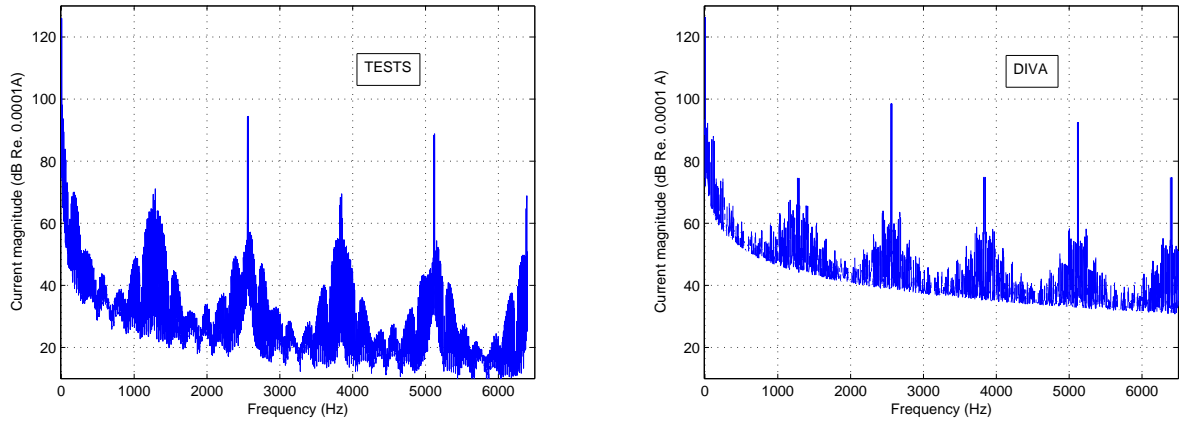


Figure 3.11: Experimental and simulated (DIVA) stator phase current on M5 motor (asynchronous PWM with $f_c = 1280$ Hz, $U_0 = 30$ V, $f_s = 5$ Hz, $s = 0.01\%$).

Frequency	f_s	$f_c - f_s$	$f_c + f_s$	$2f_c - f_s$	$2f_c + f_s$	$3f_c - f_s$	$3f_c + f_s$	$4f_c - f_s$	$4f_c + f_s$
Tests	199.8	0.234	0.359	5.16	5.28	0.261	0.298	2.62	2.75
DIVA	200.6	0.24	0.245	4.75	4.5	0.206	0.202	2.74	2.81

Table 3.1: Stator current harmonics magnitude on motor M5 (asynchronous regular sampling PWM with $f_c = 1280$ Hz, $U_0 = 30$ V, $f_s = 5$ Hz, $s = 0.01\%$).

3.1.2 Magnetomotive forces computation

3.1.2.1 Stator magnetomotive force

The stator winding function N_s^q represents the number of turns associated to the q -th phase current at angle α_s . It can be decomposed in a sum of piecewise linear turn functions (tf) weighted by the current sign as illustrated in Fig. 3.12 (81). The stator turn functions comprise a linear rise in front of stator slots (86). Such a decomposition enables to model any type of winding: it is therefore especially useful for the description of shorted-pitch winding (Fig. 3.13) and fractional-slot winding, which have a fractional number of slot per pole and per phase (Fig. 3.14).

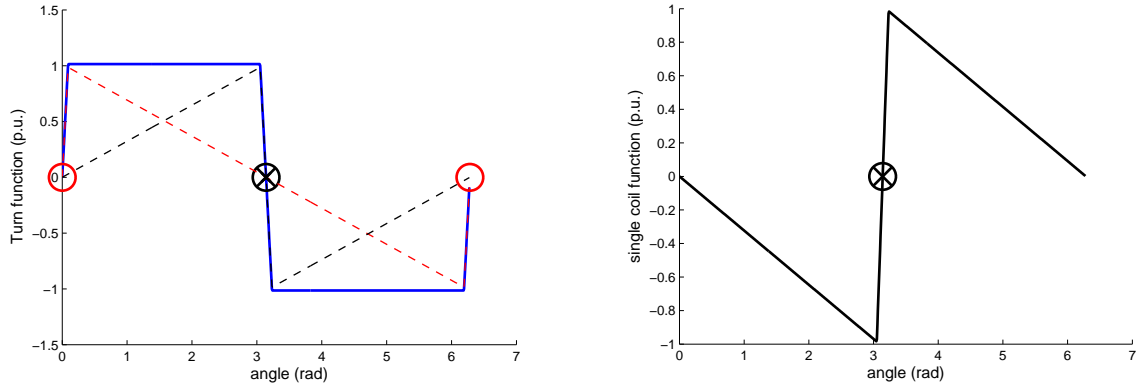


Figure 3.12: Left: decomposition of a stator winding function (wf) in a sum of two turn functions (tf). Right: stator turn function of a single coil.

More precisely, any stator winding can be represented in a single matrix \mathbf{M}_w of size (Z_s, q_s) which contains for each phase the number of cumulated turns under each stator tooth. For shorted-pitch windings, this matrix can be built following the algorithm detailed in appendix

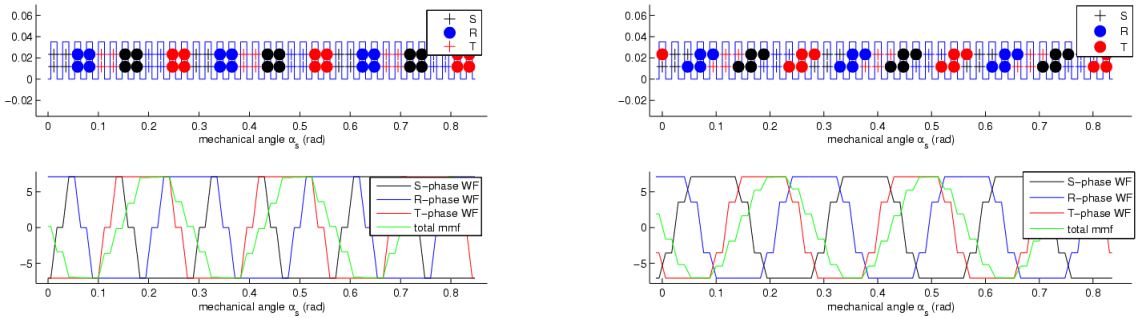


Figure 3.13: Motor M2 winding pattern, winding functions and resulting mmf in full-pitch case (left, $Y/sp_s=6/6$) and shorted-pitch case (right, $Y/sp_s=5/6$).

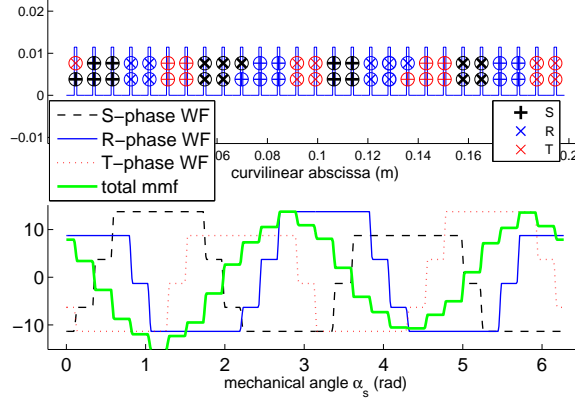


Figure 3.14: Motor M1 winding pattern, winding functions and resulting stator mmf.

A.3. The winding function of the q -th phase is then obtained as:

$$N_s^q(\alpha_s) = \sum_{i=1}^{Z_s} \mathbf{M}_w(i, q) TF_s(\alpha_s - (i-1) \frac{2\pi}{Z_s}) \quad (3.9)$$

where $TF_s(\alpha_s)$ is the turn function associated to one stator coil placed at $\alpha_s = 0$ (cf. Fig. 3.12). The total stator mmf is then obtained as:

$$f_{mm}^s(t, \alpha_s) = \sum_{q=1}^{q_s} i_s^q(t) N_s^q(\alpha_s) \quad (3.10)$$

The typical stepped distribution of stator mmf along the air-gap, and its corresponding space harmonics $\nu_s = p(2q_s h_s \pm 1)$ ($h_s \in \mathbb{N}$), is represented in Fig. 3.15 for a shorted-pitch integral winding.

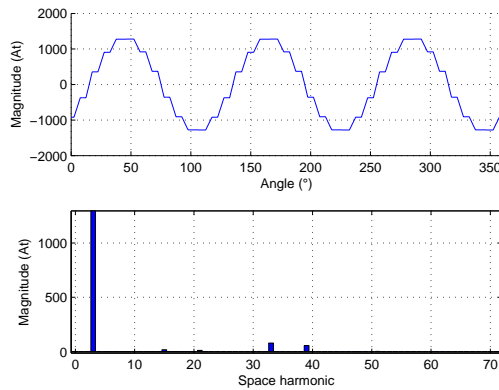


Figure 3.15: Stator mmf distribution along the air-gap at $t=0$ (motor M2 to M4, 5/6 shorted-pitch winding cf. Fig. 3.13). The main space harmonics are here $11p = 33$ and $13p = 39$.

3.1.2.2 Rotor magnetomotive force

Rotor mmf is computed using the same principle (74; 85): its equivalent Z_r -phase winding is decomposed as a sum of turn functions TF_r (see Fig. 3.16) such as

$$N_r^b(t, \alpha_s) = TF_r(\alpha_s - (b-1)\frac{2\pi}{Z_r} + \lambda_R \omega_r t) \quad (3.11)$$

The obtained rotor mmf distribution is displayed in Fig. 3.16, with its space harmonic content.

3.1.3 Permeance computation

3.1.3.1 Expression

The permeance distribution is given by

$$\Lambda(t, \alpha_s) = \frac{\mu_0}{g_{fic}(t, \alpha_s)} \quad (3.12)$$

where g_{fic} is the fictitious air-gap width (i.e. the magnetic width of the air-gap): it stands for the mean flux density lines length along the air-gap. The mean flux lines entering the slots are computed using some fictitious slot depths d_s^f and d_r^f which are proportional to the slot openings, as suggested in (36):

$$g_{fic}(t, \alpha_s) = g + d_s^f C_s(\alpha_s) + d_r^f C_r(t, \alpha_s) \quad (3.13)$$

where $d_s^f = b_s/5$, $d_r^f = b_r/5$, and C_s and C_r functions mark the stator and rotor slot openings locations (see Fig. 3.17). Note that these fictitious slot depths do not depend on the real slot depth, but on the slot opening width: for closed slots, $d_s^f = 0$.

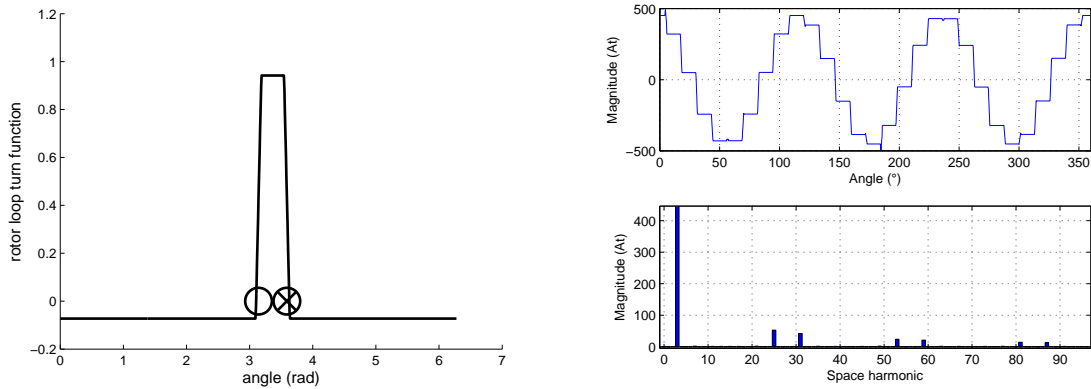


Figure 3.16: Left: rotor turn function. Right: rotor mmf distribution along the air-gap at $t=0$ (motor M2). The main space harmonics are here $Z_r - p = 25$ and $Z_r + p = 31$.

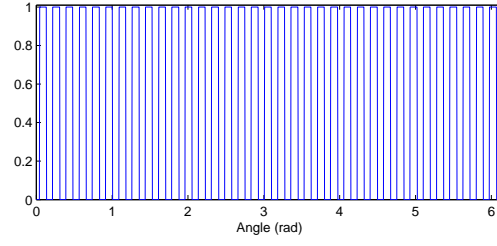


Figure 3.17: C_s function marking the location of stator slot openings on motor M2.

The typical distribution of permeance in space and time is presented in Fig. 3.18. We can see that the main space harmonics are here $Z_s = 36$ and $3Z_s = 108$, whereas frequencies are proportional to $Z_r f_R$ (the time harmonics location is similar to the one of a Z_r blades fan).

3.1.3.2 Skewed case

Rotor skew can be modelled by computing the averaged permeance along the axial direction:

$$\Lambda_{skew}(t, \alpha_s) = \frac{1}{n} \sum_{k=1}^n \Lambda \left(t, \alpha_s - \alpha_{sk} \left(-L_r/2 + \frac{k-1}{n-1} L_r \right) \right) \quad (3.14)$$

where n is the number of slices in the axial direction, and $\alpha_{sk}(z)$ is the rotor skew angle at height $z \in [-L_r/2, L_r/2]$.

3.1.3.3 Saturated case

As explained in the first chapter, we have chosen to take into account the saturation influence on the flux density distribution by modifying the permeance function, adding the new harmonics

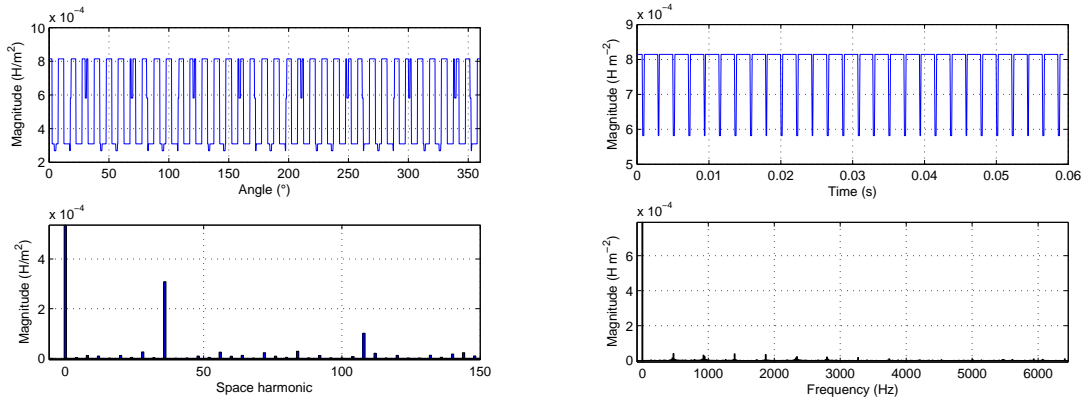


Figure 3.18: Permeance per unit area distribution along the air-gap (motor M2, $f_s = 50$ Hz) at $t=0$ (left) and in function of time at $\alpha_s=0$ (right).

(62; 112; 118; 150) that flatten the air-gap flux density distribution:

$$\Lambda_{sat}(t, \alpha_s) = \Lambda(t, \alpha_s) + \sum_{k_a=1}^{\infty} \Lambda_{k_a} \cos(2k_a \omega_s t + 2pk_a \alpha_s + \phi_a) \quad (3.15)$$

We can see that these saturated permeance harmonics rotate as same speed as the fundamental flux density ($2k_a \omega_s / (2k_a p) = \omega_s / p$). The main saturation permeance wave ($k_a=1$) has the magnitude (62; 112)

$$\Lambda_1 = \frac{\mu_0}{gK_c K_s} \frac{2A_{sat}}{1 + A_{sat}} \quad A_{sat} = \frac{F_{st} + F_{rt}}{F_g + F_{sy} + F_{ry}} \quad (3.16)$$

where K_c is the Carter coefficient, i.e. the ratio between the peak air-gap sinusoidal flux density in an ideal machine with a non-slotted air-gap and sinusoidal mmf, and the effective peak flux density of a slotted machine with a stepped mmf (31). This ratio can be expressed as:

$$K_c = \frac{\tau_s}{\tau_s - b_s / (5g + b_s)} \frac{\tau_r}{\tau_r - b_r / (5g + b_r)} \quad (3.17)$$

where $\tau_r = \pi D_{ro} / Z_r$ and $\tau_s = \pi D_{si} / Z_s$ are rotor and stator slot pitches.

If there is no saturation of the tooth tips ($F_{st} = F_{rt} = 0$), we can see that $A_{sat} = 0$ and $\Lambda_1 = 0$ which shows that this permeance saturation harmonic account for the teeth saturation effect on the flux density distribution. Fig. 3.19 shows how the permeance distribution is modified by saturation harmonics: we can see that a space harmonics of order $2p = 6$ appears besides the unsaturated permeance harmonics of Fig. 3.18. Combined with the fundamental flux of order p , this saturation permeance wave gives an additional flux density wave of order $3p$ which flattens the flux density distribution (cf. Fig. 3.20).

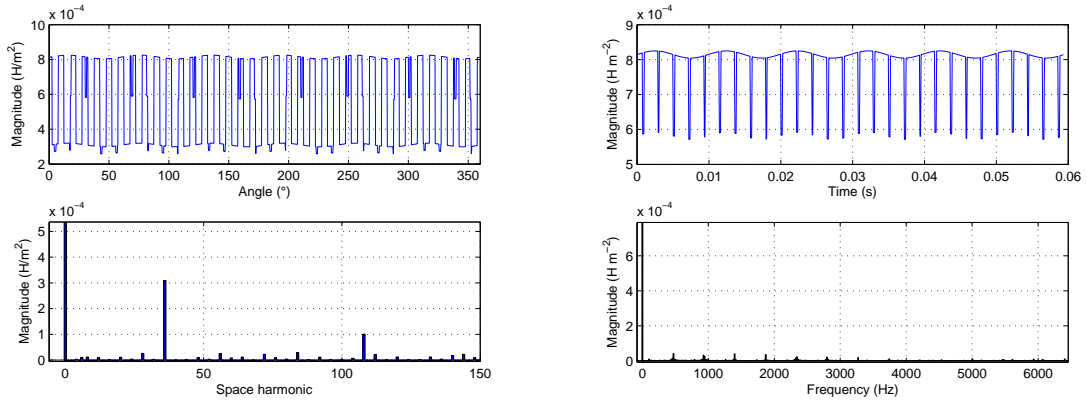


Figure 3.19: Saturated permeance per unit area distribution along the air-gap (motor M2, $f_s = 50$ Hz) at $t=0$ (left) and in function of time at $\alpha_s=0$ (right).

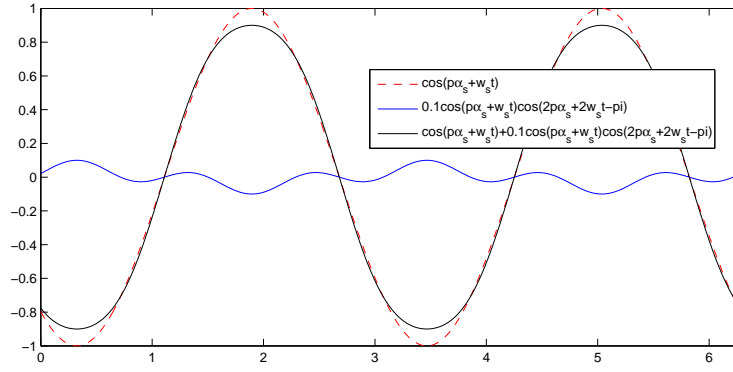


Figure 3.20: Illustration of the air-gap radial flux density flattening due to even order saturation permeance waves.

3.1.3.4 Eccentric case

3.1.3.4.1 Static eccentricity

To take into account static eccentricity, the fictitious air-gap width must be modulated following

$$g_{fic}(t, \alpha_s) = (g + d_s^f C_s(\alpha_s) + d_r^f C_r(t, \alpha_s)) (1 - \lambda_{se} \cos(\alpha_s)) \quad (3.18)$$

The resulting permeance distribution is displayed in Fig. 3.21.

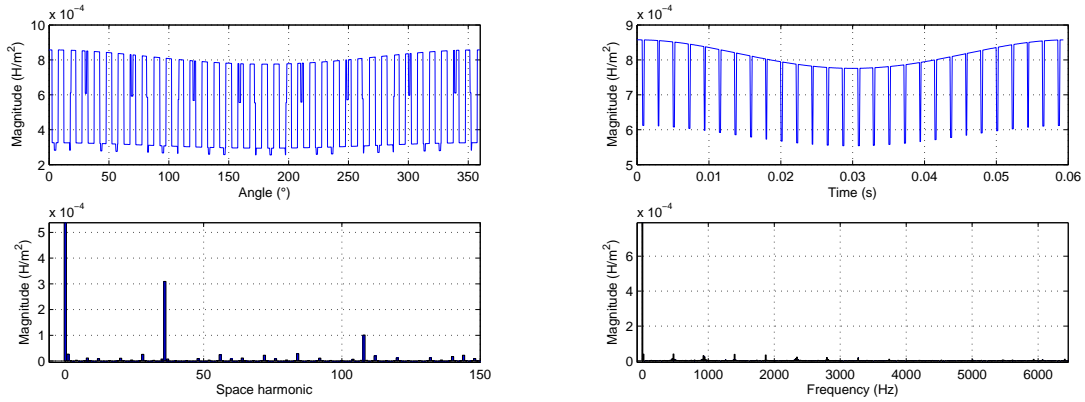


Figure 3.21: Left: permeance per unit area distribution along the air-gap (motor M2, 5% static eccentricity, $f_s = 50$ Hz) at $t=0$. Right: permeance per unit area distribution in function of time (motor M2, 5% dynamic eccentricity, $f_s = 50$ Hz) at $\alpha_s=0$.

3.1.3.4.2 Dynamic eccentricity

For dynamic eccentricity, the fictitious air-gap width is expressed as

$$g_{fic}(t, \alpha_s) = (g + d_s^f C_s(\alpha_s) + d_r^f C_r(t, \alpha_s)) (1 - \lambda_{de} \cos(\alpha_s - \Omega_R t)) \quad (3.19)$$

The resulting permeance distribution in time is displayed in Fig. 3.21.

3.1.4 Air-gap radial flux density computation

The air-gap radial flux density distribution is computed as the product of permeance and total mmf. Its typical shape and harmonic content are displayed in Fig. 3.22.

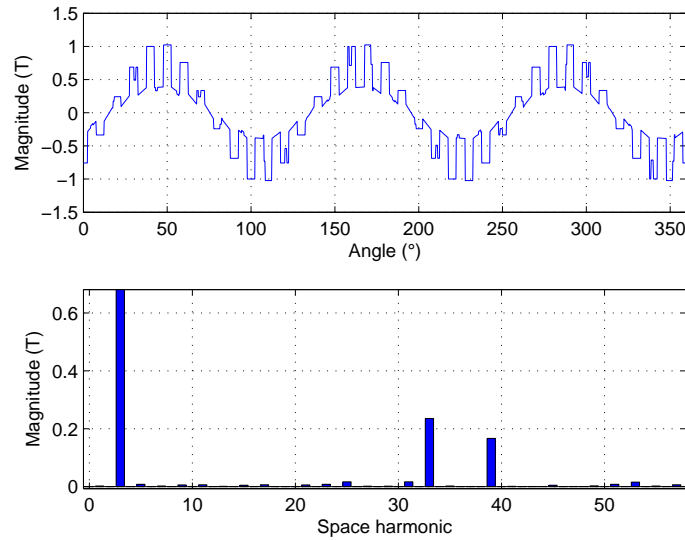


Figure 3.22: Radial air-gap flux density distribution along the air-gap at $t=0$ (motor M2). The main space harmonics are here $Z_s - p = 33$ and $Z_s + p = 39$.

We can see that the main space harmonics are $Z_s - p = 33$ and $Z_s + p = 39$: they do not come from stator mmf but from permeance. The distribution of the Maxwell pressure along the air-gap is

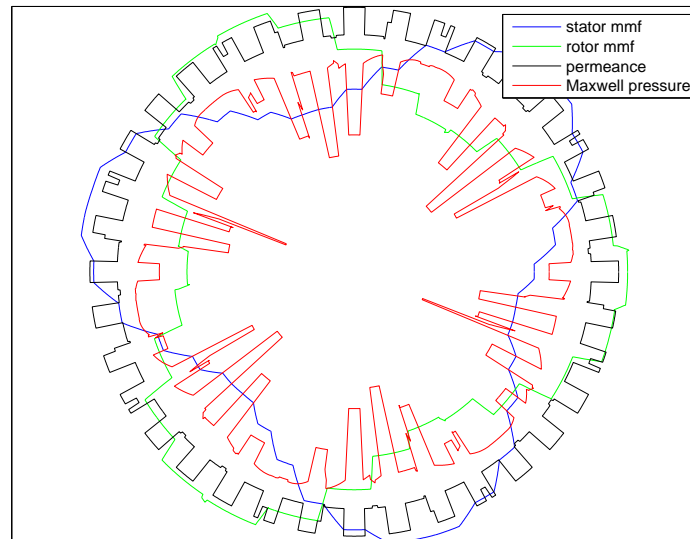


Figure 3.23: Maxwell pressure, stator and rotor magnetomotive forces, and permeance distributions at $t=0$ (motor M2).

3.1.4.1 Offload sinusoidal validations

3.1.4.1.1 Unsaturated case

The fundamental radial air-gap flux density value has been validated with FEM at different phase voltages on two different motors (Fig. 3.24).

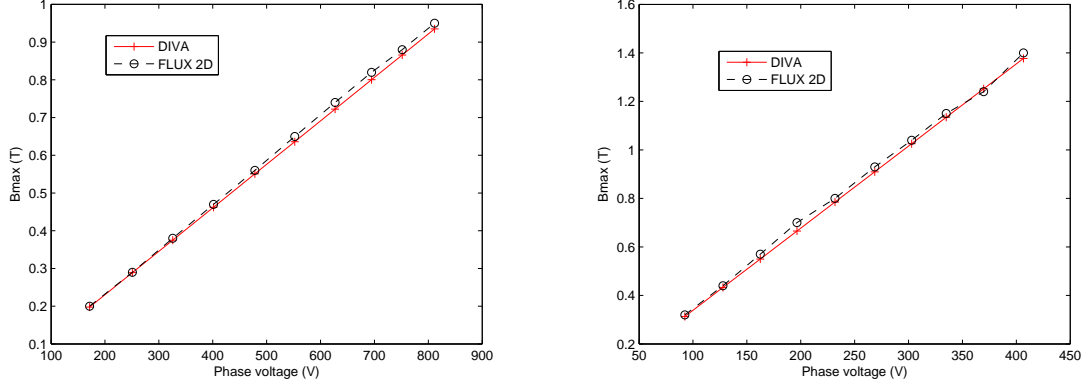


Figure 3.24: FEM and DIVA fundamental radial air-gap flux density as a function of phase voltage on M3 motor at $f_s = 150.2$ Hz (left) and M2 motor at $f_s = 50.11$ Hz (right) (no-load unsaturated case, $s = 10^{-4}$).

The flux distribution has been successfully compared with FEM simulations at different supply frequencies on two different motors (Fig. 3.25).

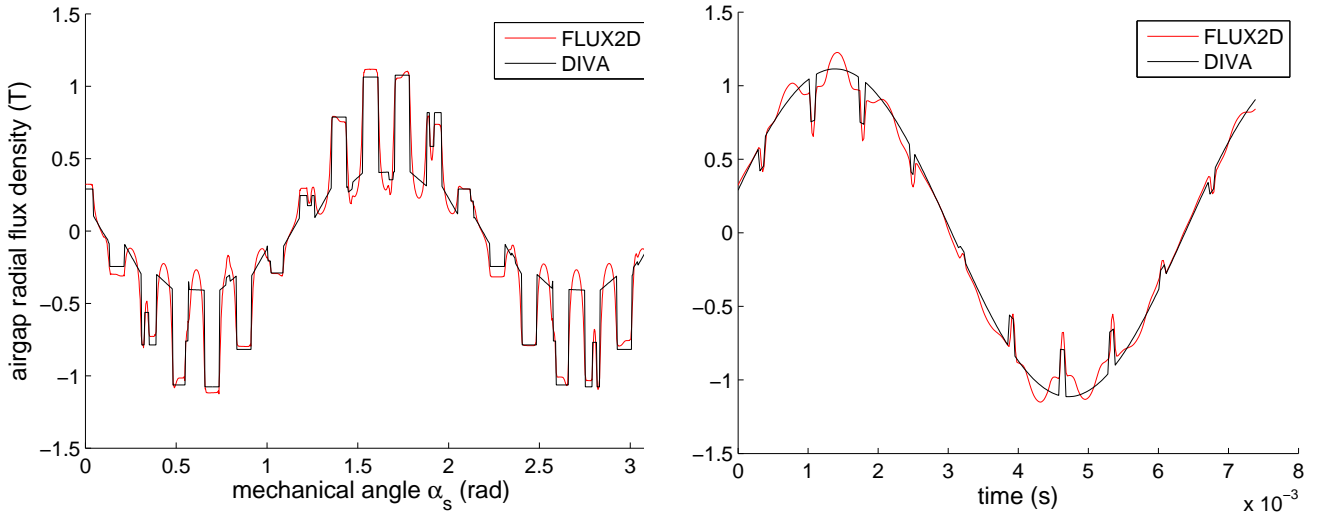


Figure 3.25: FEM and DIVA radial flux density distribution along the air-gap (left) and in function of time (right) (motor M3, sinusoidal no-load case, $s = 10^{-4}$, $f_s = 150.2$ Hz, $U_0 = 763$ V).

To get an idea of the mmf distribution computed by FEM, the FEM flux density distribution has been divided by DIVA permeance distribution. In a same way, the FEM flux distribution has been divided by DIVA mmf in order to have an approximation of the FEM permeance distribution. These results are displayed in Fig. 3.26.

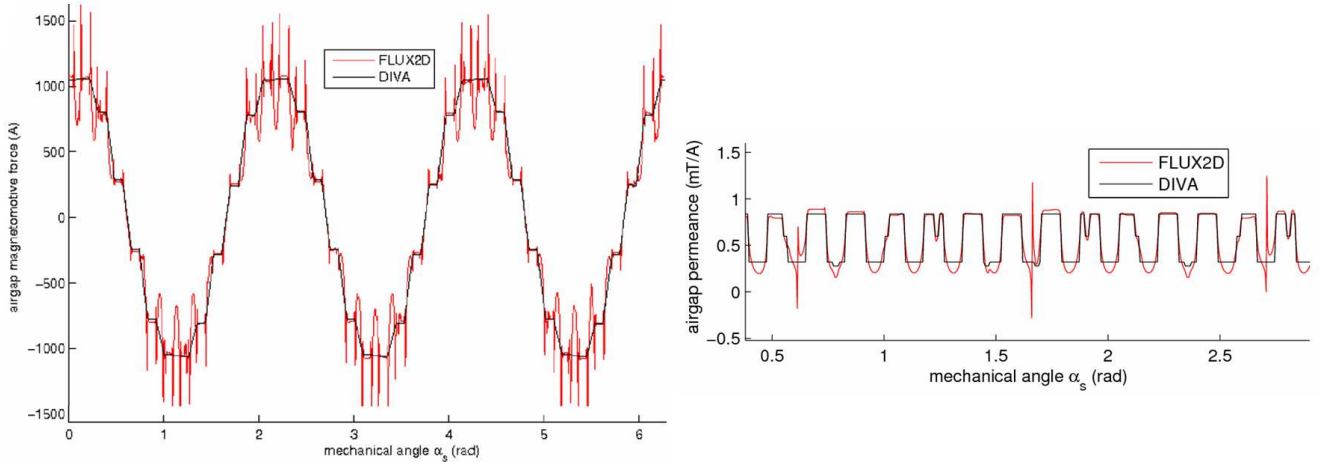


Figure 3.26: Approximated FEM and DIVA stator mmf (left) and permeance (right) distributions along the air-gap (motor M2, $f_s = 50.11$ Hz, $U_0 = 173.2$ V, $s = 10^{-4}$).

3.1.4.1.2 Saturated case

Some FEM simulations have been run on M2 motor at different saturation levels, and the magnitude of the main flux density harmonic due to saturation has been compared to DIVA. However, saturated flux density harmonics computed by DIVA were too large, although their evolution with the saturation level was the same as in FEM: a fitting coefficient ($\approx 1/6$) has therefore been multiplied to the analytical expression of the saturation permeance waves magnitude (cf. (3.16)). This kind of fit is usually used in analytical models ; it will be shown in next chapter that it gives a good approximation of saturation acoustic lines appearing on motor M5a and M3.

The resulting simulated flux density harmonics due to saturated permeance (cf. section 3.1.3.3), as well as the saturated air-gap flux-density distribution, are displayed and compared to FEM in Fig. 3.27.

3.1.4.2 On-load sinusoidal validations

The on-load flux density distribution has also been favourably compared to FEM (Fig. 3.28). However, the phase angle between rotor and stator mmf computed by DIVA in the equivalent electrical circuit did not correspond to the one of FEM simulations, and consequently, the fundamental electromagnetic torque was neither the same. This might come from some different values of the equivalent circuit rotor components. The phase angle of DIVA rotor mmf has therefore been shifted in order to have the same electromagnetic torque level, and compare the air-gap flux density distributions assuming that the phase angle between mmfs was correct.

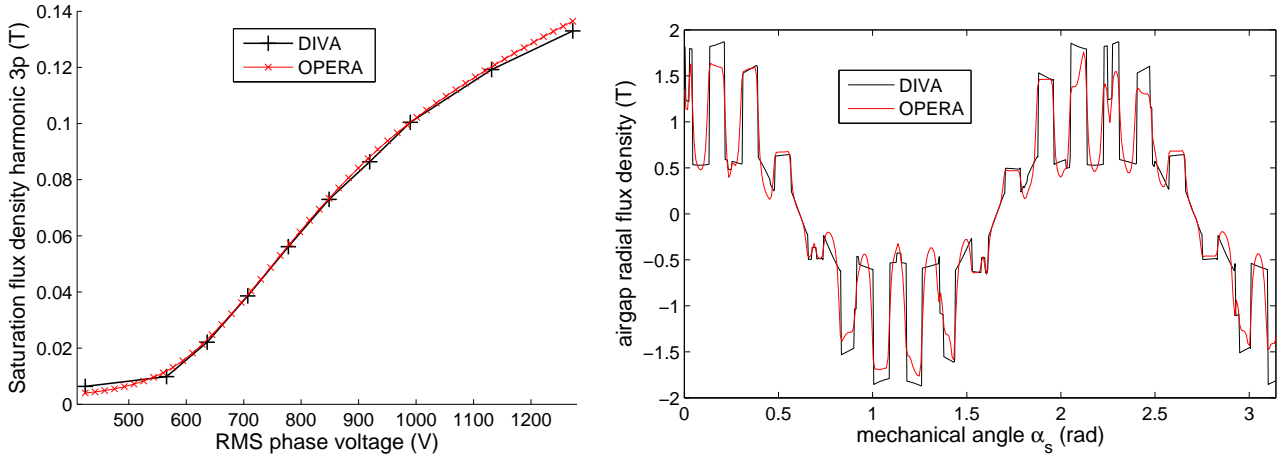


Figure 3.27: Left: FEM and DIVA main flux density saturation harmonic of spatial order $3p$ in function of the applied phase voltage on motor M2, after having fit the analytical model. Right: FEM and DIVA flux density distribution along the air-gap in saturated case.

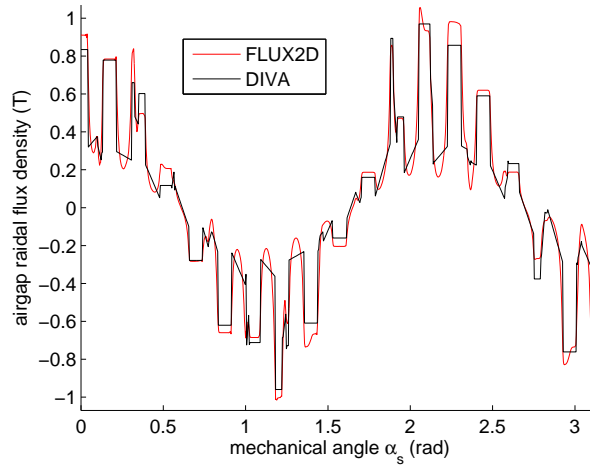


Figure 3.28: DIVA and FEM radial flux density distribution along the air-gap in sinusoidal on-load case ($U_0 = 173.2$ V, $f_s = 50$ Hz, $s = 1\%$).

3.1.5 Traction characteristics computation

3.1.5.1 Torque, power factor, efficiency expressions

The iron losses model is based on a Steinmetz/Bertotti formulation, whose coefficients were adapted to FEM simulations at several supply frequencies and voltages (Loss Surface Model of FLUX2D software). Its elaboration is detailed in (59).

The friction losses model is expressed as a cubic function of the mechanical speed N_0

$$P_{fri} = \alpha N_0 + \beta N_0^3 \quad (3.20)$$

where α and β are determined from experiments. As an example, for motor M5, we have $\alpha = 0.167$ and $\beta = 8.33 \cdot 10^{-8}$.

The efficiency η is given by the ratio between input and output powers:

$$\eta = \frac{P_{out}}{P_{in}} = \frac{P_{mec} - P_{IR}^r - P_{fri}}{P_{em} + P_{IR}^{sy} + P_{IR}^{st} + P_J^s} \quad (3.21)$$

where $P_{em} = P_J^r/s$ is the air-gap electromagnetic power, P_J^r and P_J^s are the rotor and stator Joule power losses, $P_{mec} = (1-s)P_{em}$ is the mechanical air-gap power, P_{IR}^r represents the total rotor iron power losses, P_{IR}^{sy} and P_{IR}^{st} the stator yoke and teeth iron power losses.

The output torque in traction phase is computed as:

$$T_{out} = \frac{P_{out}}{\Omega_R} \quad (3.22)$$

The power factor pf_0 in sinusoidal case is expressed as

$$pf_0 = \frac{\Re(Z_0)}{|Z_0|} \quad (3.23)$$

where Z_0 is the total complex impedance of the fundamental circuit (cf. Fig. 3.4).

3.1.5.2 Variable-speed characteristics

The traction motor has a torque/speed curve to fulfil (see Fig. 3.29) which is sized according to the track profile and the train load. Given a motor design, one must check that it can reach the aimed output torque with a sufficiently high efficiency, reasonable heating and current densities in stator winding and rotor bars. The traction phase is therefore discretised in several speeds, at which phase current, efficiency, output power and torque are computed. The torque/speed curve is decomposed in two domains: a first phase at constant and maximal air-gap flux ($E_0/f_s = \Phi_{max}$ for $N_0 < N_{mains}$), and a second phase at constant phase voltage ($U_0 = U_{max}$ for $N_0 \geq N_{mains}$), where the output torque is an hyberbola ($T_{out}N_0 = \text{cstt}$).

At each speed N_0 , the supply frequency is first approximated with a null slip ($f_s \approx N_0 p/60$). During the first phase, the emf $E_0 = \Phi_{max} f_s$ is imposed, and the slip is computed by iterations on the equivalent circuit in order to reach the specified output torque T_{out}^{spe} at speed N_0 . The fundamental circuit of Fig. 3.4 indeed defines an equation $T_{out} = h_1(U_0, f_s)$, but as U_0 is an unknown, the output torque is expressed as a function of the air-gap flux by the equation $T_{out} = h_2(\Phi_{max}, f_s)$. An iterative root search algorithm is then performed on the function $f_s \mapsto h_2(\Phi_{max}, f_s) - T_{out}^{spe}$. At the end of the iterations, the actual slip is computed as $s = 1 - pN_0/(60f_s)$. Once the supply frequency and the slip are known, the phase voltage is determined solving the whole equivalent circuit, i.e. computing $U_0 = g(\Phi_{max}, f_s)$.

During the second phase, the phase voltage is kept at its last value U_{max} , and the slip is computed in the same way by finding the root of the equation $f_s \mapsto h_3(U_{max}, f_s) - T_{out}^{spe}$. As the input phase voltage is known, the full equivalent circuit is then simply solved computing $\mathbf{I} = \mathbf{Z}^{-1}\mathbf{U}$.

3.1.5.3 Validation

All the traction characteristics have been checked by comparing DIVA results to ALSTOM simulation tool (Fig. 3.29). Power factor, output torque and power have been validated with test at different slip values (Fig. 3.30).

3.1.6 Instantaneous electromagnetic torque

The instantaneous electromagnetic torque is computed in DIVA in order to be able to compute torque pulsations. It can be expressed as

$$T_e = -\frac{\partial W_m}{\partial \Theta}|_{i=cst} \quad (3.24)$$

where $\partial/\partial\Theta$ represents an infinitesimal virtual rotation of the rotor, and W_m is the total magnetic energy contained in the air-gap:

$$\begin{aligned} W &= \int_0^{L_1} \int_0^{2\pi} \int_{R_{re}}^{R_{re}+g} \frac{B_g(t, \alpha_s)^2}{2\mu_0} dz r d\alpha_s dr = \frac{L_1((R_{re}+g)^2 - R_{re}^2)}{4\mu_0} \int_0^{2\pi} B_g(t, \alpha_s)^2 d\alpha_s \\ &\approx \frac{L_1 R_{re} g}{2\mu_0} \int_0^{2\pi} B_g(t, \alpha_s)^2 d\alpha_s \end{aligned} \quad (3.25)$$

The electromagnetic torque is therefore given by

$$T_e = -\frac{L_1 R_{re} g}{2\mu_0} \int_0^{2\pi} \frac{\partial B_g^2}{\partial \Theta}|_{i=cst} d\alpha_s \quad (3.26)$$

We have

$$\frac{\partial B_g^2}{\partial \Theta}|_{i=cst} = 2\Lambda \frac{\partial \Lambda}{\partial \Theta} f_{mm}^2 + \Lambda^2 \left(2f_{mm} \frac{\partial f_{mm}^r}{\partial \Theta}|_{i=cst} \right) \quad (3.27)$$

as

$$\frac{\partial f_{mm}^s(t, \alpha_s)}{\partial \Theta}|_{i=cst} = \sum_{q=1}^3 i_q^s(t) \underbrace{\frac{\partial N_q^s(\alpha_s)}{\partial \Theta}}_{=0} = 0 \quad (3.28)$$

Rotor mmf derivative can be obtained as (assuming $\lambda_R = 1$)

$$\frac{\partial f_{mm}^r(t, \alpha_s)}{\partial \Theta}|_{i=cst} = \frac{\partial f_{mm}^r(t, \alpha_s)}{\partial \alpha_s} \quad (3.29)$$

while permeance derivative is obtained as

$$\frac{\partial \Lambda(t, \alpha_s)}{\partial \Theta} = \frac{\partial \Lambda(t, \alpha_s)}{\Omega_R \partial t} \quad (3.30)$$

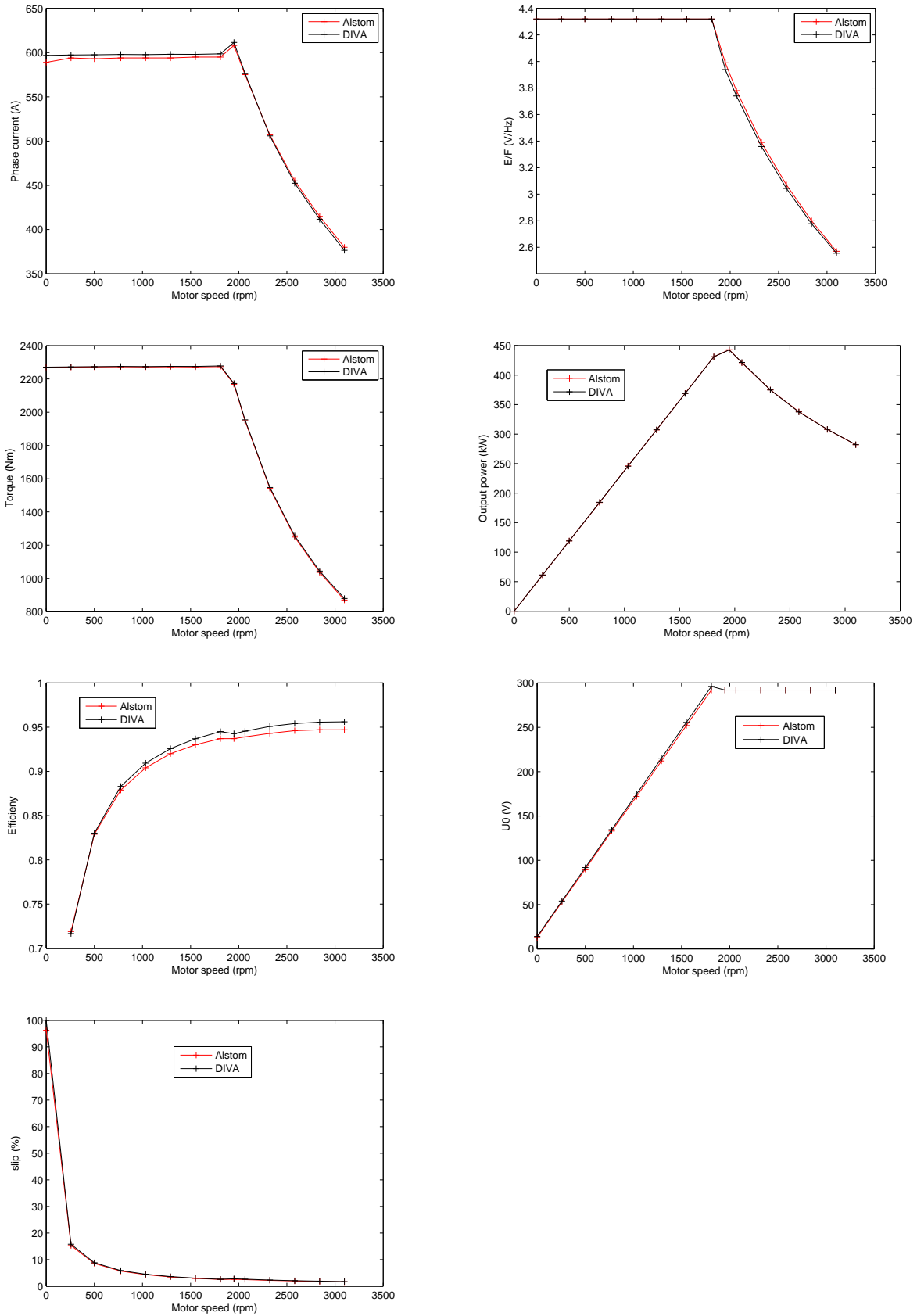


Figure 3.29: Phase current, air-gap flux E_0/f_s , output torque, output power, efficiency, phase voltage and slip in function of speed, obtained with ALSTOM simulation tool and DIVA (motor M5a). Friction losses have been experimentally determined and used both simulation tools.

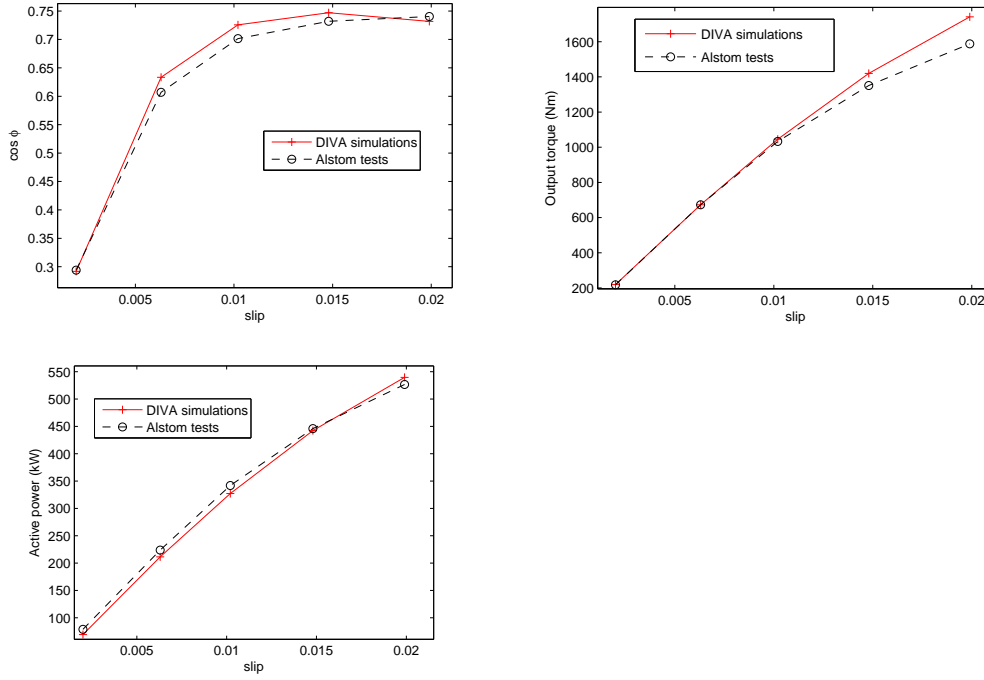


Figure 3.30: Experimental and simulated (DIVA) power factor, output torque and output power as a function of slip on M3 motor ($U_0=810$ V, $f_s=150$ Hz).

The electromagnetic torque can then be decomposed in a reluctant torque T_{rel} (which is null if there is no reluctance variation along the air-gap) and a fundamental electromagnetic torque T_{emf} (which is null when $s = 0$):

$$T_e = \underbrace{-\frac{L_1 R_{reg}}{\Omega_R \mu_0} \int_0^{2\pi} \Lambda(t, \alpha_s) f_{mm}^2(t, \alpha_s) \frac{\partial \Lambda(t, \alpha_s)}{\partial t} d\alpha_s}_{T_{rel}} + \underbrace{-\frac{L_1 R_{reg}}{\mu_0} \int_0^{2\pi} \Lambda^2(t, \alpha_s) f_{mm}(t, \alpha_s) \frac{\partial f_{mm}^r(t, \alpha_s)}{\partial \alpha_s} d\alpha_s}_{T_{emf}} \quad (3.31)$$

We therefore have in no-load case $-\frac{\partial W_m}{\partial \Theta}|_{i=cst} = T_{rel}$, where W_m is the total air-gap electromagnetic energy, which is also the volume integral of Maxwell pressure in the air-gap. Therefore, a relatively strong correlation between magnetic noise and torque pulsations should not be surprising. However, whether magnetic noise generally increases or decreases with higher torque pulsations is still to be investigated. If DIVA can calculate these torque pulsations, we did not have enough time to validate their computation.

3.2 Vibro-acoustic model

Before looking for some analytical models of the stator vibro-acoustic behaviour, it is important to characterise the geometry of the equivalent cylinders of ALSTOM motor ranges. The dimensions of the stator stack (without teeth and frame, see Fig. 3.31) are given in Table 3.2. Two characteristic frequencies have been computed: the ring frequency f_{rg} , which is the breathing mode natural frequency (without modifying the stator mass density to account for teeth and winding mass, as it is done in section 3.2.1), and the critical frequency f_{ct} :

$$f_{rg} = \frac{1}{2\pi a} \sqrt{\frac{E_s}{\rho_s}} \quad f_{ct} = \frac{c_0}{2\pi h} \sqrt{\frac{12\rho_s(1 - \mu_s^2)}{E_s}} \quad (3.32)$$

where c_0 is the speed of sound waves in the air, and μ_s is the stator stack Poisson ratio. f_{rg} is also the frequency at which the wavelength of the shell extensional waves equal the shell circumference, whereas f_{ct} is the frequency at which the acoustic wavelength in the air is the same as in the stator.

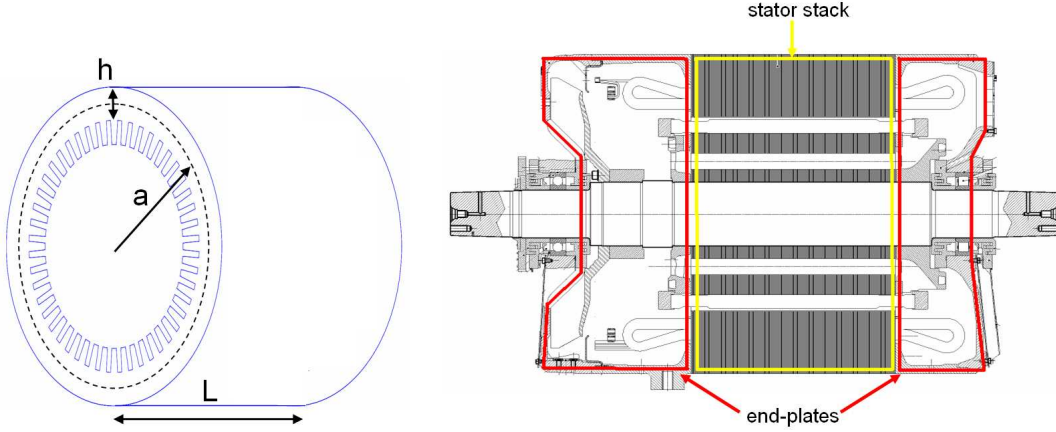


Figure 3.31: Left: stator stack equivalent cylinder dimensions. Right: motor M5 stator stack and end-plates.

We can see that all the studied motors have a critical frequency f_{ct} which is inferior to the ring frequency f_{rg} , which shows that all the stator stacks behave like acoustically thick shells (159)¹. An important consequence of that property is that the cylinder radiation efficiency strongly depends on the excitation type (57), and on its length L contrary to acoustically thin shells.

The end-plates have also a significant vibro-acoustic role (167), as their total length can be as high as the stator stack length on ALSTOM motors (cas of motor M5, cf. Fig. 3.31). However, we will see that they can be neglected to estimate the stator natural frequencies. During the experiments run on motor M5, measurements showed that the end-plates radial

¹A shell can be thin ($h \ll a$) but acoustically thick.

Motor name	h/a	L/a	h/L	f_0 (Hz)	f_{ct} (Hz)	Application
M1	0.1895	1.6842	0.1125	17330	1316	LEC test-bench
M2-M4	0.23606	<u>1.8158</u>	0.13	3370	334	Regional train
M5	0.23401	1.3818	0.1693	2872	291	Subway
M6	0.31299	1.2431	<u>0.2518</u>	3033	<u>205</u>	Subway
X	<u>0.33557</u>	1.4765	0.2272	<u>4217</u>	<u>1257</u>	High-speed train
X	<u>0.14874</u>	1.2652	<u>0.1175</u>	2067	375	High-speed train
X	0.17359	1.28	0.1356	<u>1853</u>	377	Intercity train
X	0.22703	1.2613	0.18	2365	238	Locomotive
X	0.23048	<u>1.1524</u>	0.2	2378	248	Regional train
X	0.20952	1.5928	0.1315	2761	284	Commuter train
X	0.23201	1.7621	0.1317	3750	391	Light-rail vehicle
X	0.22281	1.3263	0.168	3274	380	Subway

Table 3.2: Parameters of the equivalent cylinders representing ALSTOM motor ranges (cf. Fig. 3.31). The extremal values encountered in ALSTOM motors have been underlined. f_0 is the breathing mode natural frequency and f_{ct} is the critical frequency.

vibrations could be as high as the stator stack radial vibrations. The end-plates length is therefore not neglected in the radiation factor and in the sound power level computations.

3.2.1 Natural frequencies computation

3.2.1.1 Expression

Two main analytical models have been successfully experimented: the one used by HUBERT (81) (method $m1$), which uses corrective coefficient to take into account the third dimension, and the one described by GIERAS (69) (method $m2$).

This last method computes the breathing mode natural frequency F_0 as:

$$f_0 = \frac{1}{2\pi a} \sqrt{\frac{E_s}{K_{fs} \Delta_m \rho_s}} \quad (3.33)$$

where K_{fs} is the stator stacking factor, $a = (D_{so} + h_f - h_{sy})/2$ is the stator mean radius taking into account the frame width h_f , and Δ_m is the mass increase due to winding and teeth:

$$\Delta_m = 1 + \frac{W_{st} + W_{sw}}{W_f + W_{sy}} \quad (3.34)$$

where W_{st} , W_{sw} , W_f and W_{sy} respectively stand for the mass of stator teeth, winding, frame and yoke.

The natural frequency f_1 of the rotor first bending mode will have to be determined (see section 3.2.2.1), it is computed modelling the rotor as a beam loaded with a ring. When the rotor is symmetrically supported by the bearings, this frequency can be approximated by (112)

$$f_1 = \frac{1}{2\pi} \sqrt{\frac{K}{M}} \quad K = \frac{3\pi}{4} \frac{E_r D_{sh}^4}{l_{rb}^3} \quad M = \rho_r \pi L_r (D_{ro}^2 - D_{sh}^2)/4 + \rho_{sh} \pi l_{sh} D_{sh}^2/8 \quad (3.35)$$

where l_{rb} is the distance between the two bearings that support the rotor shaft of length l_{sh} , diameter D_{sh} and mass density ρ_{sh} .

For modes $m > 1$, f_m is computed as

$$f_m = K_m f_0 \frac{h}{2\sqrt{3}a} \frac{m(m^2 - 1)}{\sqrt{m^2 + 1}} \quad (3.36)$$

where $h = h_{sy} + h_f$, and K_m is a corrective coefficient whose expression can be found in (8; 69; 112).

3.2.1.2 Effect of magnetic stiffness

Besides the effects on natural frequencies of temperature, boundary conditions, frame, and manufacturing errors which have already been studied, BEKEMANS (14) suggested that the magnetic flux in the induction machine acts on the stator and rotor coupling like a magnetic spring, and could change the stator natural frequencies. He showed that the distribution of the air-gap magnetic lines can be interpreted as the result of a balance between a magnetic tension (due to Maxwell forces), which tends to reduce the magnetic lines length (law of minimal reluctance), and an hydrostatic magnetic pressure, which tends to keep the magnetic lines far from one another. When slightly moving the stator inner surface away from this balanced position, the interaction between stator and rotor can be approximated at first order by a magnetic spring of stiffness $2B_0^2/(\mu_0 g)$, B_0 being the fundamental air-gap flux density.

The natural frequencies expression of a circular cylindrical shell with an additional spring have been established, and computations showed that magnetic stiffness should reduce the elliptical mode natural frequency of only a few %. This fact has been validated experimentally by carrying two experimental modal analysis, one on a current-free motor and the other one on a motor supplied with maximum current. The second analysis has been done as fast as possible so that the motor remained cool, and results were not affected by the temperature change. In agreement with analytical computations, no significant shift was observed on the stator elliptical mode near 600 Hz, which shows that the effect of magnitude stiffness can be neglected.

3.2.1.3 Validation

A first validation was done on motor M1, using some FEM and test results carried by HUBERT, namely the hammer shock method and the sinus method ¹. Another experimental test was done using an operational modal analysis (OMA²). These results are presented in Table 3.3, and the OMA modal deflection shapes are also shown in Fig. 3.32. We can see that the analytical method *m1* is slightly more adapted to the small motor M1.

(m, n)	2-D FEM	Hammer Method	Sinus Method	DIVA- <i>m1</i>	DIVA- <i>m2</i>	OMA
(0,0)	14656	OR	OR	14860	15465	14400
(1,0)	ND	1200	1273	1234	1234	1148
(2,0)	2364	2400	2423	2485	2270	2345
(3,0)	6473	6100	6210	6415	6420	6370
(4,0)	11898	11700	OR	12065	12310	11790

Table 3.3: Stator natural frequencies computation (Hz) of motor M1 using different methods. OR: Out of Range, ND: Non Definite.

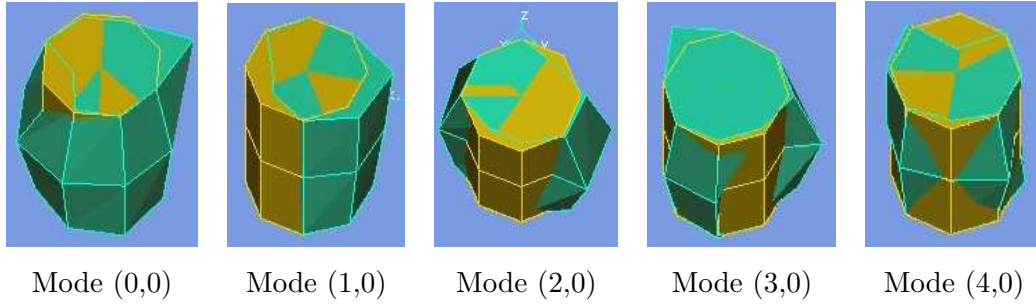


Figure 3.32: Deflection shapes of the first five stator circumferential modes ($m = 0$: breathing mode, $m = 1$: rotor bending mode, $m = 2$: elliptical mode, $m = 3$: 3-order elliptical mode, $m = 4$: 4-order elliptical mode).

Another validation was carried on ALSTOM motor M5 using three different 3D FEM models, all simulated in free-free boundary conditions:

1. plate model of the equivalent cylindrical shell, i.e. with a modified mass density accounting for teeth and winding

¹This method consists in feeding the motor with a variable high-frequency current, and determining at which frequency noise peaks occur.

²In an experimental modal analysis, an external excitation (hammer shock for instance) is used to determine the natural frequencies of the structure. In an operational model analysis (OMA), the internal excitation of the structure is used as an excitation force to determine the natural frequencies. An OMA is therefore relevant for structures with wide-band internal excitation forces. In our case, the internal forces are Maxwell forces, and OMA measurements are done by starting the motor in PWM mode from $f_s = 0$ to $f_s = 80$ Hz in order to produce the widest and richest exciting spectrum.

2. solid model of the equivalent cylindrical shell, i.e. with a modified mass density accounting for teeth and winding
3. real geometry of the motor whose material properties were fitted to experiments

An experimental modal analysis (EMA) was also carried on the stator alone and on the whole motor (stator + end-plates + rotor). All these results are displayed in Table 3.4, where the damping factors appear in parenthesis. On this application, we can see that analytical methods $m1$ and $m2$ are both close to FEM results. Some longitudinal modes natural frequencies have been also computed using $m2$ method, although there are not used in DIVA as Maxwell forces are assumed to be independent of the axial direction, and the results are close to solid-based FEM results.

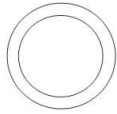
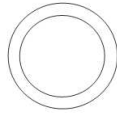
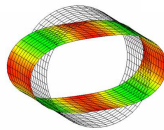
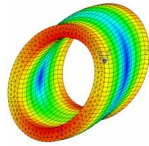



Method	DIVA- $m1$	DIVA- $m2$	FEM plate	FEM solid	EMA stator	EMA full	FEM fitted
(m,n)							
(0,0)	2870	2890	2830	2870	OR	OR	OR
(2,0)	595	526(1.2)	516	580	584+670(0.92)	606(0.8)	582+730
(2,1)	X	820	573	800	513(1.3)+651	537+892	876
(3,0)	1535	1490	1410	1570	1402	NI	1252
(3,1)	X	2020	1520	1930	1260	NI	NI
(4,0)	2885	2850	2590	2840	1955	OR	OR
(4,1)	X	3500	2720	3240	1454	OR	OR

Table 3.4: Stator natural frequencies computation (Hz) and damping coefficient (between parenthesis, in %) of motor M5 using different methods. OR: Out of Range, NI: Not Identified.

The influence of frame and fixations has already been studied in AIT-HAMMOUDA thesis (3) on ALSTOM motor M2, which has a totally different architecture than motor M5: the stator stack is totally enclosed in a frame as it is a water-cooled motor. He used three 2D FEM models of the motor real geometry: model A of the stator stack, model B of the stator stack and frame, and model C of the stator stack, frame and fixations. These FEM results in free-free conditions are recalled and compared with DIVA 2.0 in Table 3.5. We can see that the breathing mode natural frequency is decreased by 10 % due to fixations. Moreover, it is close from the 4 lobes mode natural frequency like on motor M5 (cf. Table 3.4). DIVA results were obtained without accounting for the frame width in the equivalent cylindrical model, which explains why its results are closer to FEM model B than A.

Methods $m1$ and $m2$ give similar results on traction motors, and behave well for both self-ventilated motors, where the stator stack is apparent and the end-plates are thick, and

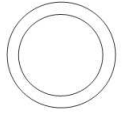
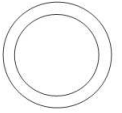
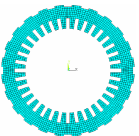
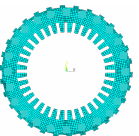
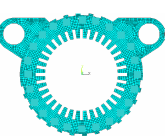
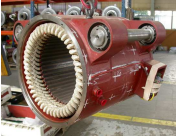
Method	DIVA- <i>m1</i>	DIVA- <i>m2</i>	FEM A	FEM B	FEM C	EMA full stator
(m,n)						
(0,0)	3453(2.5)	3681(2.6)	3648	3642	3353	3283(1.5)
(2,0)	719(1.3)	673(1.27)	555	699	710+758	616(2.16)+731(2.22)
(3,0)	1857(1.8)	1904(1.72)	1487	1831	1797+1934	1406(1.47)+1622(2.1)+1769(1.16)
(4,0)	3493(2.5)	3651(2.28)	2666	3200	3560+4015	3106(0.96)+3383(0.88)

Table 3.5: Stator natural frequencies computation (Hz) and damping coefficient (in parenthesis, in %) of motor M2 using DIVA and FEM (Ansys).

water-cooled motors, where the stator stack is totally enclosed in a frame. Let us remind that a 15 % relative error on the natural frequency computation is still acceptable in order to avoid variable speed resonances: as the exciting magnetic force frequency is proportional to the supply frequency, it gives a 15 % relative error on the speed at which the resonance occurs. Method *m1* is the default method used in DIVA.

3.2.2 Vibration computation

3.2.2.1 Expression

The magnetic pressure $B_g^2/(2\mu_0)$ is first decomposed in 2D Fourier series to obtain a set of sinusoidal force waves of complex magnitude $P_{m\omega}$, spatial order m and pulsation ω (cf. the forces waves illustrated in Fig. 2.7). The static displacements under each sinusoidal load are then computed. Static displacement associated to order 0 is (87)

$$Y_{0\omega}^s = P_{0\omega} \frac{R_{sy} R_{si}}{E_c h_{sy}} \quad (3.37)$$

$Y_{1\omega}^s$ is generated by the force per unit area $P_{1\omega}$: as seen in Fig. 2.7, it generates a rigid body motion of the stator. From the rotor point of view, where Maxwell forces also apply¹, this motion excites its first bending mode. This rotor deflection can be modelled as a simply supported beam loaded with pressure $P_{1\omega}$:

$$Y_{1\omega}^s = P_{1\omega} \frac{4R_{si} l_{sh}^3 L_r}{3E_{sh} D_{sh}^4} \quad (3.38)$$

¹We can show that the total force acting on the rotor is also given by the surface integration of Maxwell stress over an air-gap cylinder. The expression $B_g^2/2/\mu_0$ is therefore also valid to approximate the effect of radial Maxwell forces on the rotor. The bending deflection of the rotor can therefore be computed from the 1 order space harmonic of σ_n . All the other force harmonics are supposed not to produce any rotor deflection, as its radial stiffness is much greater than the stator one.

Note that this deflection only exists if some odd spatial orders are generated by the magnetic force distribution. If its distribution in the air-gap is totally symmetric, only even orders exist. In fact, since the radial force distribution is a quadratic function of the flux density, it has an even number of pole pairs ($2p$) and the only way to break the symmetry is to have an odd number of rotor or stator slots, or eccentricities.

Notice that in equation (3.38), $Y_{1\omega}^s$ holds for rotor deflection, although it will be used to compute the sound power level radiated by the stator. This very strong hypothesis implicitly done in (112) assumes that the bending deflection of the rotor is totally transferred to the stator, i.e. that an infinite stiffness coupling exists between rotor and stator. This coupling is not a mechanical one, through bearings and end-shields, but a magnetic one: if a rotor bending deflection exists, it creates an eccentricity which locally enlarges and reduces the air-gap width. Consequently, Maxwell forces which apply on the stator are locally reduced (as the air-gap flux density is inversely proportional to the air-gap reluctance i.e. the air-gap width) and enlarged, which also creates a kind of bending deflection of the stator. This dynamic coupling between rotor and stator bending deflection is therefore complex, and this model is rather rough; fortunately, ALSTOM motors do not have any eccentricities, and have even slot numbers, so this special bending mode has not a great influence on acoustic noise.

For orders $m \geq 2$, static deflections are expressed as

$$Y_{m\omega}^s = P_{m\omega} \frac{12R_{si}R_{sy}^3}{E_s h_{sy}^3 (m^2 - 1)^2} \quad (3.39)$$

If we compare the static displacements of order $m > 1$ to the zero-th order one, we get

$$\frac{Y_{m\omega}^s}{Y_{0\omega}^s} \propto \frac{P_{m\omega}}{P_{0\omega}} \frac{1}{(m^2 - 1)^2} \frac{R_{sy}^2}{h_{sy}^2} \quad (3.40)$$

The ratio R_{sy}/h_{sy} therefore sizes the ability of the motor to generate high displacements of order $m > 1$. Moreover, the higher is the spatial order, the lower is the displacement. This ratio has been plotted for different orders in Fig. 3.33.

Dynamic deflections $Y_{m\omega}^d$, which account for resonance effects, are computed as

$$Y_{m\omega}^d = Y_{m\omega}^s [(1 - f^2/f_m^2)^2 + 4\xi_m^2 f^2/f_m^2]^{-1/2} \quad (3.41)$$

where ξ_m is the modal damping coefficient associated to the m -th flexural mode, and f_m is the m -th mode natural frequency. As a first approximation, ξ_m can be computed using the experimental law established by (166)

$$2\pi\xi_m = 2.76 \times 10^{-5} f_m + 0.062 \quad (3.42)$$

If this law gives the right order of magnitude (between 1 % to 3 % for mode $m = 0, 2$ and 4, while TIMAR suggested an average of 2% (145)), it was established on small power motors (10 kW) compared to ALSTOM motors. Moreover, the increase of damping with frequency is

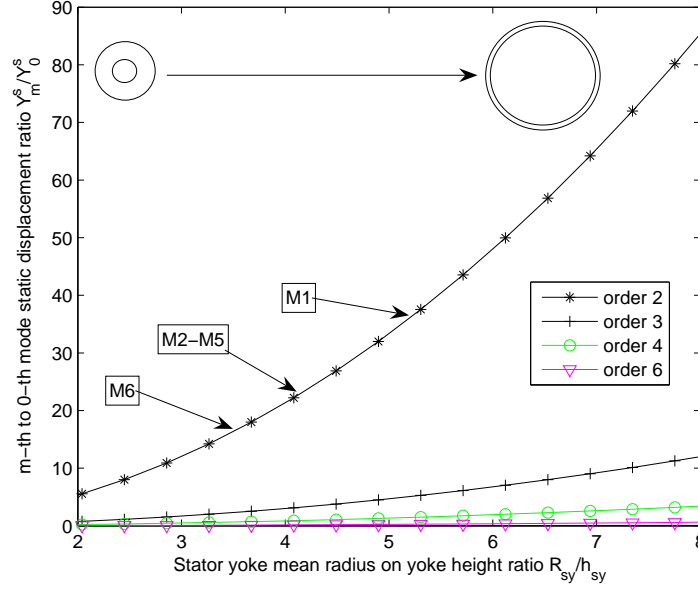


Figure 3.33: Relative static displacement in function of R_{sy}/h_{sy} ratio for several modes. Doubling the relative static displacement increases the SWL at resonance of $10 \log_{10}(2^2) \approx 6$ dB.

not that physical: at low frequencies, global modes appear, involving more damping, whereas at high frequencies, the damping is expected to be the one of the stator core (which is higher to the one of a steel core because of insulated laminations). This more physical behaviour is indeed observed during tests (cf. Table 3.5).

Experiments have shown that the damping coefficient was slightly over-estimated on motor M5 elliptical mode (1.2 % against 0.8 % experimentally, cf. Fig. 3.4). Note that the determination of damping coefficient has a great influence on the SWL level: at resonance,

$$\Delta L_w = 20 \log_{10}(\xi'/\xi) \quad (3.43)$$

which gives in our case $20 \log_{10}(1.2/0.8) \approx 3.5$ dB.

3.2.2.2 Experimental validation

3.2.2.2.1 Sinusoidal case

Some acceleration measurements have been done on motor M1 at fixed supply frequency (Fig. 3.34) and variable speed (spectrogram¹ Fig. 3.35). This spectrogram, as well as all the other ones presented in that thesis, is run at constant flux ($U_0/f_s = \text{cstt} \approx E_0/f_s$) in order to keep a constant magnetic excitation during starting phase.

In Fig. 3.34, we can see that in the lowest part of the spectrum, a high difference exists between DIVA and tests: it is mainly due to mechanical vibrations which are not modelled in

¹In a spectrogram or a sonagram, time or motor speed are reported in abscissa, frequencies are reported in ordinates, and the sound or vibration level is indicated with a colour gradient.

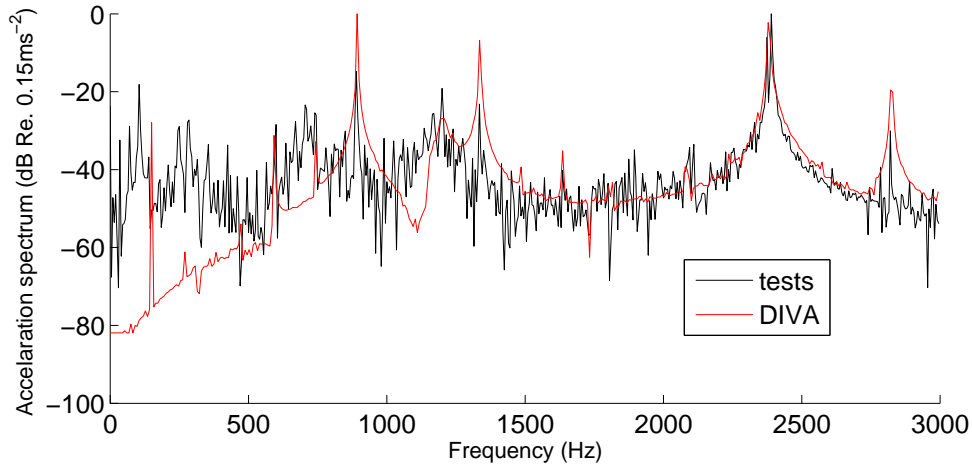


Figure 3.34: Experimental and simulated vibratory spectrum obtained (motor M1, $s = 3\%$, $f_s = 75$ Hz, $U_0 = 6$ V).

DIVA. At high frequencies (≤ 500 Hz), simulated acceleration spectrum compares favourably with experimental spectrum.

In the spectrogram of Fig. 3.35, run from 12 to 60 Hz, the parts that are amplified independently of motor speed (vertical lines) stand for the motor natural frequencies. In the experimental spectrogram, two main natural frequencies show up at 700 Hz and 1100 Hz. The latter is the bending mode identified in the OMA (Fig. 3.32) and modelled analytically in section 3.2.2.1. In fact, the OMA showed that the first natural frequency around 700 Hz is another bending mode (Fig. 3.36). These two modes are especially amplified on motor M1 because it is not clamped at both ends (see the motor photography in Fig. 3.36). The experimental spectrogram also contains three lines that are not proportional to the supply frequency because they do not start at the origin, when $f_s = 0$: these harmonics which are not present in simulations are generated by the DSP card interrupting frequency, which creates an artificial PWM effect at $f_c = 1500$ Hz (the effect of PWM will be detailed in next chapter).

We can see that in DIVA spectrogram, the mode 2 natural frequency around 2400 Hz is more amplified than in tests. However, the experimental response of a given natural frequency on a spectrogram highly depends on the position of the accelerometer (nodes or anti-nodes of the mode).

In both figures, we can see that the main slotting magnetic vibration lines are well predicted by DIVA. These vibration lines will be identified lately on the ground of the analytical work of section 4.1.3.2.2.2: the idea of this chapter is to show that there is a good agreement between tests and simulation, without detailing the theoretical origin of the vibration or acoustic lines.

3.2.2.2.2 PWM case

Fig. 3.37 shows the comparison between a measured and simulated spectrograms on motor M1 supplied with 1600 Hz asynchronous PWM. The measurement conditions are identical to Fig.

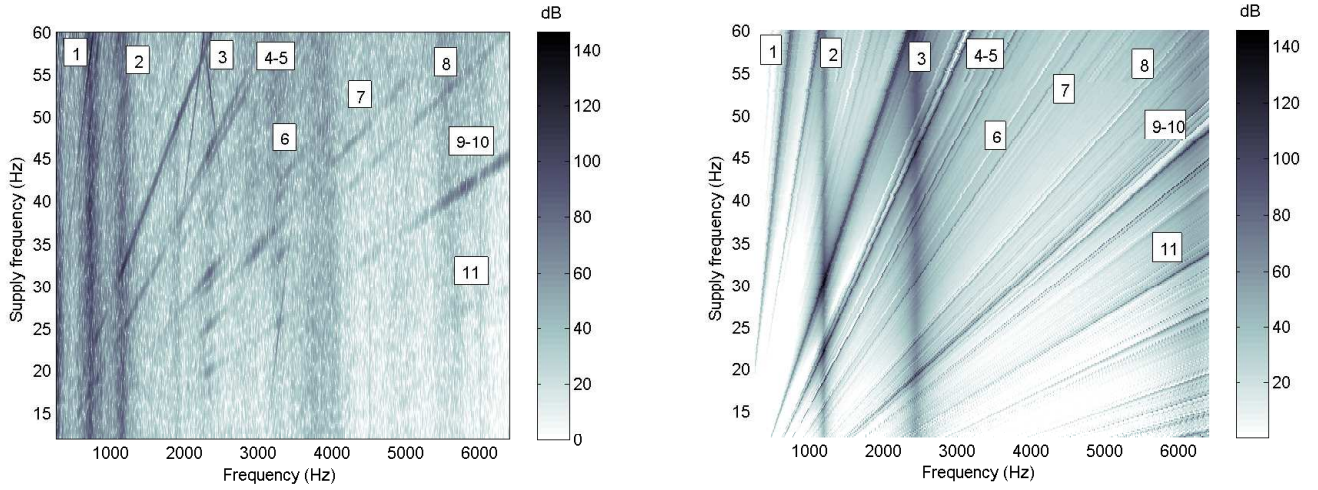


Figure 3.35: Experimental (left) and simulated (right) acceleration spectrogram in sinusoidal case (motor M1, $f_s=12$ to 60 Hz). An uncertainty exists on the experimental supply frequency as no tachometer probe could be used.

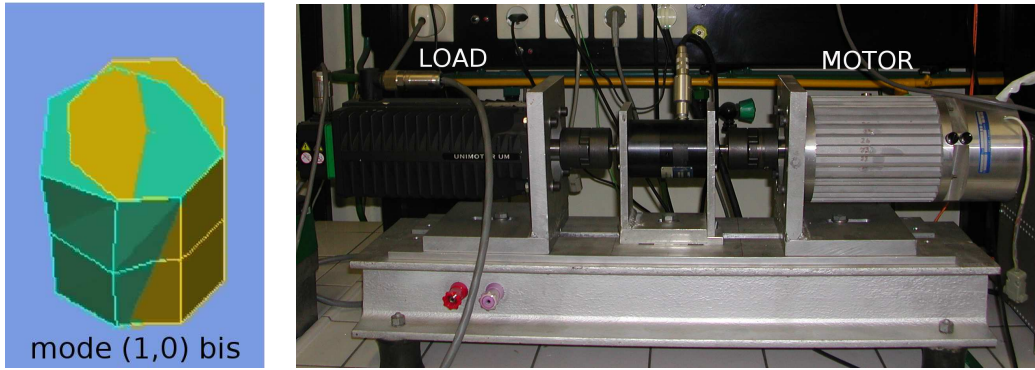


Figure 3.36: Left: OMA deflection shape at 713 Hz (second bending mode, motor M1). Right: M1 motor test-bench.

3.35. We can see that the main resonance, due to some slotting PWM vibrations that meet the stator elliptical mode near 2400 Hz as it will be explained in section 4.1.3.3.2, is correctly predicted by DIVA.

DIVA simulation has been run imposing a sinusoidal stator mmf, which explains that some lines are missing compared to the sinusoidal case of Fig. 3.35. This change has been done because contrary to an integral winding mmf, the fractional-slot winding mmf of motor M1 contains an odd order space harmonic $\nu_s = 1$: this relatively large odd order space harmonic creates a high number pure PWM vibrations of spatial order $p - \nu_s = 2 - 1 = 1$ (see section 4.1.3.3.1) which are all transmitted to the rotor in the model (cf. section 3.2.2.1 where the modelling assumptions of 1-order vibrations have been criticised), creating vibrations of unrealistically large magnitude.

We can see that a few lines of the spectrogram take negative frequency values at low speed. These non-physical vibrations may come from numerical problems that are still unidentified.

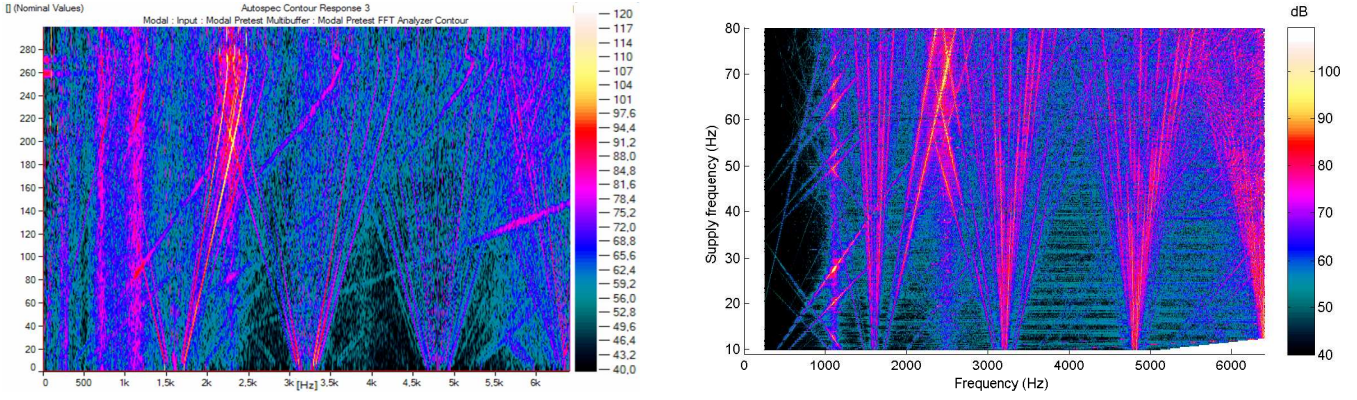


Figure 3.37: Measured (left) and simulated (right) acceleration spectrogram in on-load asynchronous PWM case (motor M1, $f_c = 1600$ Hz, $f_s = 10$ to 80 Hz).

3.2.3 Radiation factor computation

3.2.3.1 Expression

Since all ALSTOM stators are quite short (they fulfil the condition $1 < L/a < 4$, even when including in L the total length of the end-plates), the analytical model that has been used as a first approximation is the pulsating sphere one rather than the infinite cylinder one (146). Contrary to the infinite length cylinder model, this model depends on the cylinder length, which is coherent with the fact that ALSTOM stators have been identified as acoustically thick cylindrical shells.

The radiation factor of a sphere of radius R is expressed as:

$$\sigma_m(f) = \Re \left(\frac{\sum_{i=0}^m \frac{(m+i)!}{(m-i)!} \frac{m!}{i!} \left(\frac{4j\pi R}{\lambda} \right)^{m-i}}{\sum_{i=0}^m \frac{(m+i)!}{(m-i)!} \frac{m!}{i!} \left(\frac{4j\pi R}{\lambda} \right)^{m-i} \left(1 + \frac{2j\pi R+i}{\lambda} \right)} \right) \quad (3.44)$$

where $j = \sqrt{-1}$ and $\lambda = c_0/f$ is the wavelength in the air. The equivalent sphere radius is computed as $R = \max(a, L/2)$.

3.2.3.2 Validation

Some FEM simulations have been carried to compute the radiation efficiency of a motor equivalent cylinder under some typical magnetic excitation, that is to say rotating or standing waves of order 0, 2 and 4 (see section 4.1.2).

The radiation efficiency of the equivalent cylinder of motor M5 ($h = 5.25$ cm, $a = 44.75$ cm, $L = 31$ cm) has been computed by FEM with the model used in section 3.2.1.3. The full modal base decomposition of that cylinder is presented in Appendix B.1.

Its radiation efficiency has been computed using different excitation force waves (Fig. 3.38 and 3.39). We can see that the cut-off frequency is correct, and that the pulsating sphere model is accurate enough (a 20% error on the radiation efficiency gives a $10 \log(1/0.8) \approx 1$ dB error

on the SWL). Some small numerical noise appears at high frequencies in BEM results because the acoustic mesh is not enough fine at these frequencies.

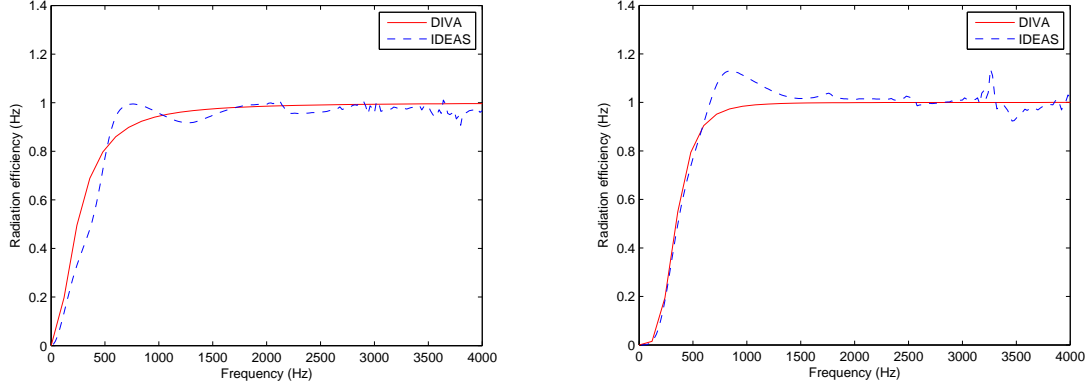


Figure 3.38: DIVA and FEM radiation efficiency under an exciting force wave of order 0 (left) and order 1 (right) (magnitude 250 N/m²).

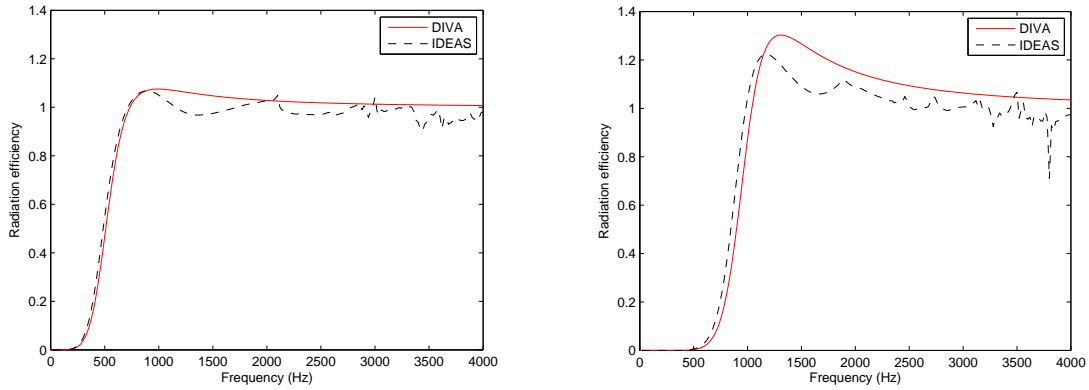


Figure 3.39: DIVA and FEM radiation efficiency under an exciting force wave of order 2 (left) and order 4 (right) (magnitude 250 N/m²).

3.2.4 Sound power level computation

3.2.4.1 Expression

Sound power radiated by vibrations of mode m and frequency f is

$$W_m(f) = \frac{1}{2} \rho_0 c_0 S_c \sigma_m(f) < \overline{v_{m\omega}^2} > \quad (3.45)$$

where S_c is the stator outer surface, ρ_0 the air density, and σ_m the modal radiation efficiency. σ_m is approximated using either its pulsating sphere expression or its infinite cylinder expression according to stator dimensions (146) – on ALSTOM motors, the pulsating sphere model is

always used. The $1/2$ factor in (3.45) takes into account backward and forward-travelling vibration waves.

Sound power level at frequency f is

$$L_w(f) = 10 \log_{10} \left(\sum_m W_m(f) / W_0 \right), \quad W_0 = 10^{-12} W \quad (3.46)$$

A-weighted total sound power level is finally obtained as

$$L_{wA} = 10 \log_{10} \left(\sum_f 10^{0.1(L_w(f) + \Delta L_A(f))} \right) \quad (3.47)$$

where $\Delta L_A(f)$ weight is a function of human's ear sensitivity (cf. Fig. 2.8). Note that the acoustic power loss is totally insignificant compared to other motor losses (friction and thermal losses): a 120 dBA sound power level only represents a power of 1 W.

3.2.4.2 Validation

3.2.4.2.1 FEM/BEM simulations

Some numerical simulations have been done by coupling the FEM software IDEAS output (vibration velocity field on the equivalent cylinder surface) to the boundary element method (BEM) software SYSNOISE. Some magnetic force waves have been applied to a FEM plate model of DIVA equivalent cylinder (motor M5), and the velocity field at the stator surface has been then injected in SYSNOISE acoustic mesh to compute the associated SWL. A frequency sweep has been realised in order to capture the resonance effects.

For instance, Fig. 3.40 presents the FEM/BEM results of the acoustic noise radiated by the cylinder under a rotating force wave of order 2, whose electrical frequency varies from 240 to 4000 Hz (its rotation frequency therefore goes from 120 to 2000 turn per second). DIVA results are very close to numerical results, even for a rotating force of order 4. Note that IDEAS cylinder natural frequencies were imposed in DIVA (cf. Table 3.4), as well as a 1 % damping, in order to focus on the accuracy of SWL computation.

The behaviour of DIVA model has been also tested when the stator is submitted to a standing force wave of order 0, and to a mix of different force waves (Fig. 3.41). The comparison with FEM software IDEAS is again very good.

A rotating force of order m therefore only resonates with the cylinder circumferential mode of same number. Even a rotating force wave of order 2 does not excite the circumferential mode $m = 4$. At resonance, the stator deflection visualised in IDEAS software has exactly the same shape as the exciting force. These two facts can be analytically proved using the Green's function formalism (139) (see appendix B.2). This is contrary to the experimental conclusions of VERMA and BALAN (151), who studied the vibration response of a stator submitted to magnetic forces of different spatial orders using special windings, and concluded that a four-pole excitation force could resonate with the stator two-pole mode. A first explanation comes

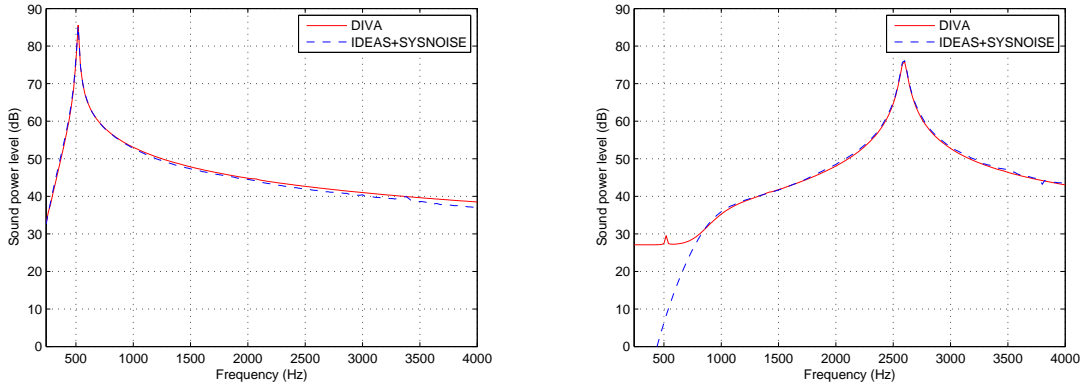


Figure 3.40: DIVA and FEM+BEM sound power level generated by a rotating force wave of order 2 (left) and 4 (right).

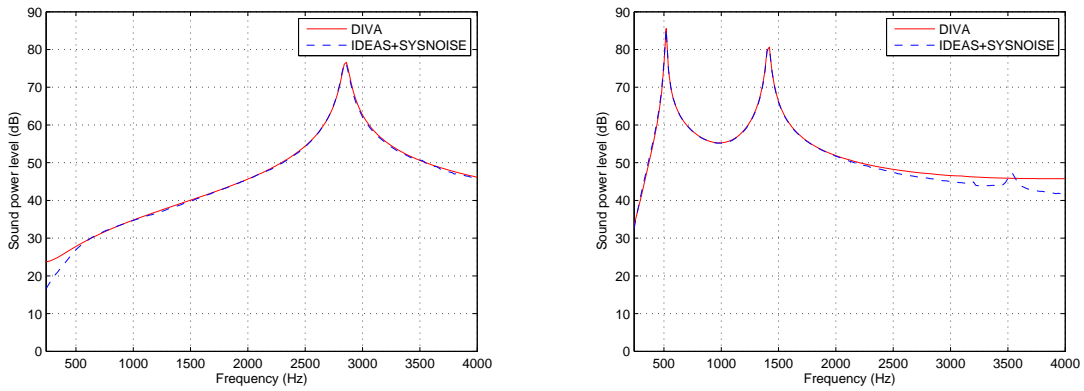


Figure 3.41: DIVA and FEM+BEM sound power level generated by a pulsating force wave of order 0, and a combination of a order 2 and 3 rotating force waves.

form the real motor geometrical asymmetries: if an asymmetry is introduced in the FEM cylinder model, the rotating force wave of order 4 is indeed able to appropriate the elliptical mode of the cylinder, and the mode number 4 natural frequency is doubled (see Fig. 3.42 study). Another explanation comes from the difference between the simulated force (a pure sinusoidal wave taking positive and negative values) and the experimental force (a rectified quasi-sinusoidal wave which only takes positive values, and contains other space harmonics than the fundamental due to the imperfections of the winding). These two explanations are actually similar, as they apply either on the "purity" of the excited structure modes, or on the "purity" of the exciting force orders. These asymmetries are not taken into account in DIVA analytical model, but they only create secondary resonances.

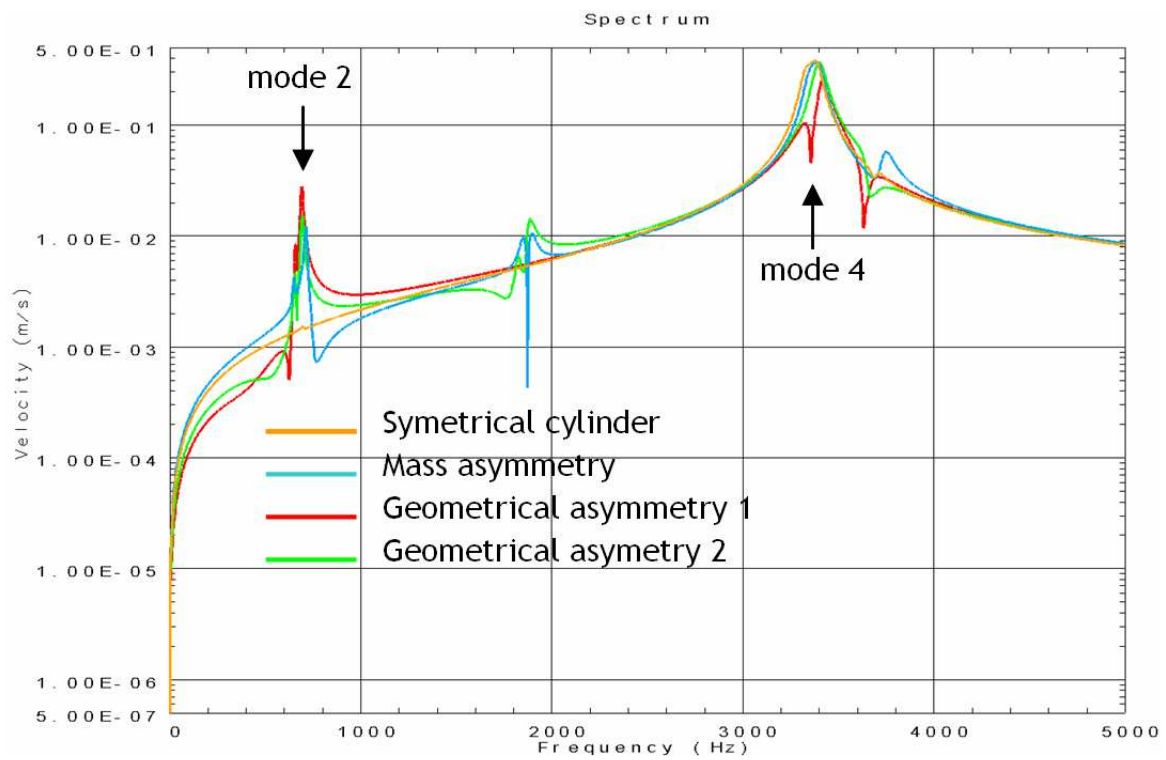


Figure 3.42: Study of the vibration response of symmetrical or asymmetrical cylinder subjected to a rotating force wave of order 4.

3.2.4.2.2 Experiments

3.2.4.2.2.1 No-load sinusoidal case

Fig. 3.43 shows an experimental and simulated sonagram of the water-cooled M3 motor run from 0 to 200 Hz. We can see that the main natural frequencies (vertical line) near 720 Hz, which corresponds to the stator elliptical mode (cf. section 3.2.1.3), is correctly predicted by DIVA. The main magnetic lines are also well predicted, as the resonance near 50 Hz. The origin of all these acoustic lines (winding, slotting and saturation harmonics) is detailed in section 4.1.3.2.

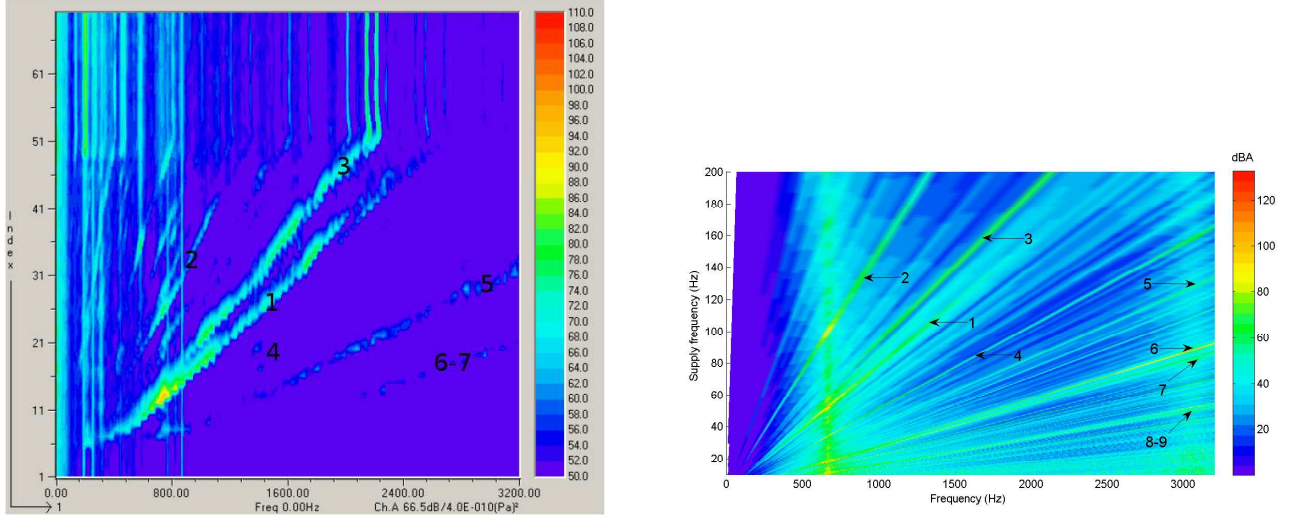


Figure 3.43: Experimental (left) and simulated (right) sonagram on motor M3 in sinusoidal no-load case. Note that experimental sonagram abscissa is time in seconds, as no tachometer prove was available, whereas simulated sonagram abscissa is f_s in Hz.

3.2.4.2.2.2 No-load PWM case

Fig. 3.44 shows the comparison between experimental and simulated acoustic spectra on motor M5 at low speed (150 rpm i.e. $f_s=5$ Hz), in asynchronous mode (1280 Hz switching frequency). At this speed, the slotting lines have very low frequencies (inferior to 1000 Hz), and noise due to PWM dominates. These slotting lines are overestimated by DIVA: motor M5 has skewed rotor, which was not simulated in this case.

DIVA correctly predicts the frequencies of the PWM main lines (groups 1, 2 and 3) and secondary lines (groups 4a, 4b, 5a, 5b, 6a, 6b), but on certain lines, some difference of 10 dBA can be observed between test and simulation. As seen in section 3.1.1.3.3, PWM currents are correctly estimated by DIVA, so it does not come from the calculation of the exciting force. These gaps probably come from a difference in damping coefficient: some of PWM lines excite 0 and 4 stator modes, as it will be experienced in section 4.3.3.3.4, which makes damping more important (cf. equation (3.43)). Besides that, the stator stack of motor M5 and M5a is far

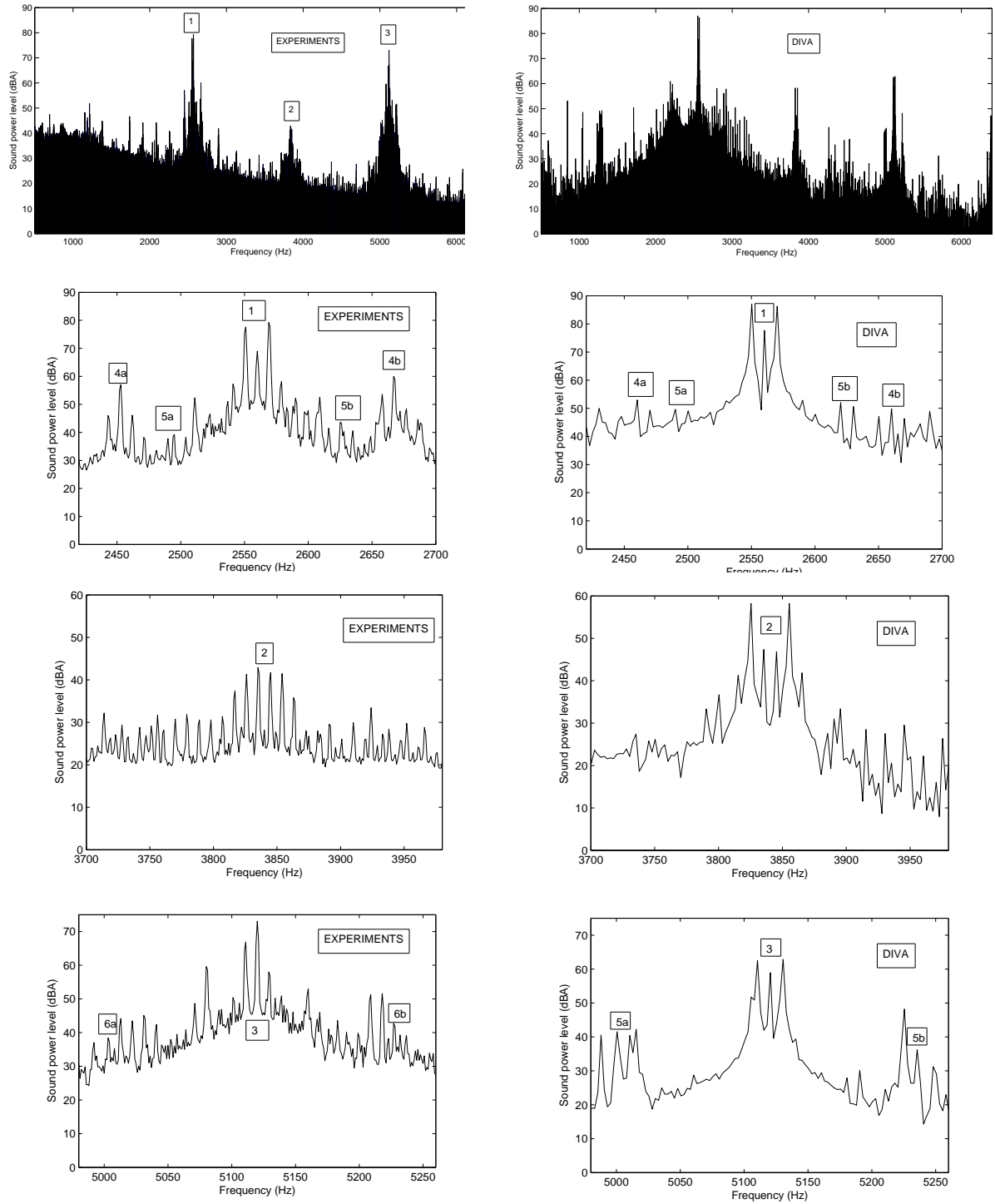


Figure 3.44: Experimental and simulated (DIVA) A-weighted SWL spectrum in asynchronous PWM case (motor M5, $f_s=5$ Hz, $f_c=1280$ Hz).

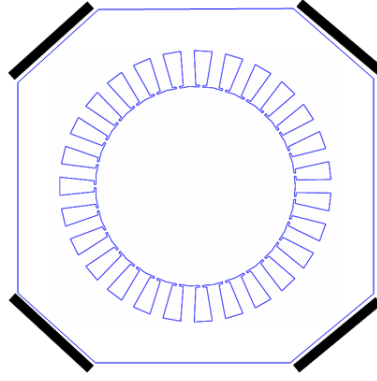


Figure 3.45: Schematic view of motor M5/M5a stator stack and welded plated with rods (the slot number and the slot shapes have been changed on purpose).

from being circular as illustrated in Fig. 3.45. Four metallic plates with struss rods are welded along the four corners of the stator stack and to the end-plates in order to stiffen the whole structure in its axial direction. The effect of the octagonal stack and bars may strongly change the static deflections of order 0 and 4, which leads to different acoustic radiation.

DIVA spectrum contain less harmonics than the experimental one. This fact has a numerical origin (see section 3.3), and a physical origin: simulated current contain far less low frequency harmonics than the experimental one (Fig. 3.46). For instance, a large component at $3f_s$ due to current unbalance is not present in DIVA. Some components $2f_s$, $4f_s$, etc., probably due to commutation dead time, are also missing in DIVA. The harmonics of the form $(6k \pm 1)f_s$ are present in both simulations, but their magnitude are sometimes very different: the way the PWM pattern is generated in the real motor has not been investigated, but may differ from the way is it generated with Simulink. These magnitude deviations could also come from some deviations in the third harmonic injection process.

These additional harmonics create new pure PWM lines. For instance, the component $4f_s$ creates some harmonics at $4f_c \pm 2 \times 4f_s$ i.e. 5080 Hz and 5160 Hz in our example. These lines around group number 3 are missing in DIVA simulation.

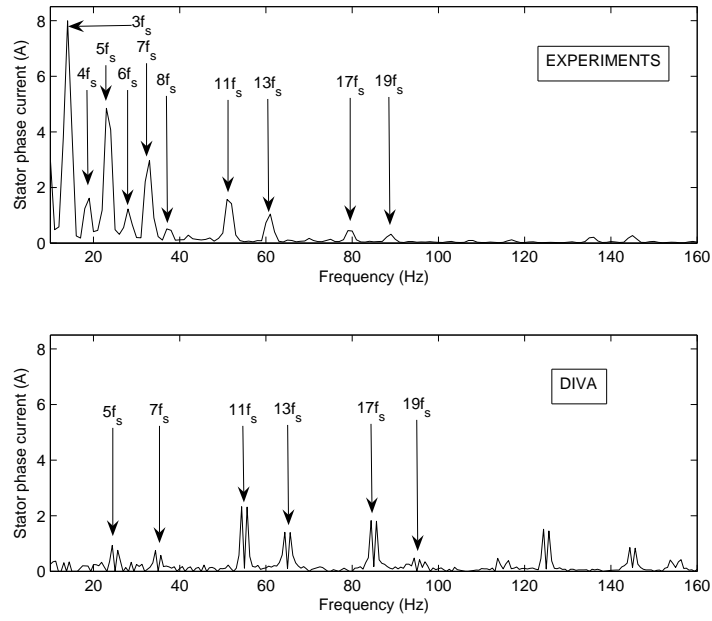


Figure 3.46: Experimental and simulated (DIVA) stator phase current magnitude spectrum at low frequencies (motor M5, $I_0 = 200$ A, $f_s = 5$ Hz, $f_c = 1280$ Hz). The experimental supply frequency was slightly over-estimated, which explains why experimental and simulated current harmonics do not appear at exactly the same place.

3.3 Numerical considerations

If all the models of DIVA were established decades ago, but their numerical simulation arises several computing and numerical difficulties which have prevented some researches from reaching a good agreement between experimental and measured noise or vibration spectrum, and from carrying some optimisations including the noise objective function.

3.3.1 Fourier versus time/space domain modelling

DIVA simulations last a few seconds on a 1 Gb RAM and 2.13 GHz laptop (computation of all the electrical output, and of magnetic noise radiation at a given speed). This time varies from 2 s when the motor is sinusoidally-fed in no-load case (no rotor mmf to compute), to 40 s when the motor is PWM-fed in on-load case. The number of space harmonics to include in the extended equivalent circuit also influences the computing time. A low supply frequency or a high switching frequency also strongly impacts the computing time in PWM case.

This relatively low computing time was achieved by several ways. First, the literature often presents the magnetic forces expression in its Fourier development, as it will be done in section 4.1.3, which usually results in very large expressions like $\sum_{n=1}^{\infty} \sum_{k_s=1}^{\infty} \sum_{k_r=1}^{\infty} \sum_{k_a=1}^{\infty} \sum_{h_s=1}^{\infty} \sum_{h_r=1}^{\infty}$. They are useful to identify the frequencies and spatial orders of magnetic force harmonics, but when the model has to be implemented, using the Fourier series developments leads to time-consuming and inaccurate results, as the infinite summations must be truncated. Moreover, the Fourier series development of stator and rotor mmf are often limited to the winding nature, and cannot be adapted to fractional-slot windings for instance. Several works made that mistake, and were then unable to fully use the potentialities of their software.

This point was already raised in the thesis of BEKEMANS (14), who noticed that these infinite Fourier harmonics contain some redundant information as they only account for the discrete property of the air-gap flux density (stepped mmf and permeance functions). He therefore proposed a full formalism for the computation of magnetic forces and electromagnetic torque based on a vectorial description of the air-gap flux density along the air-gap. His model does account for linear rise of mmf across slots as done in DIVA (86), and assumes that the permeance is uniform. Consequently, the stator magnetic field is given by

$$\mathbf{H}(t) = \frac{1}{g} \mathbf{N} \mathbf{I}(t) \quad (3.48)$$

where \mathbf{N} of size (Z_s, q_s) is the matrix of "cumulated turns under each teeth" for each phase (winding functions described in section 3.1.2), and \mathbf{I} is a vector of size $(q_s, 1)$ representing the stator instantaneous currents in each phase. This vectorial formalism led to promising geometrical interpretations.

HUBERT (81) has adopted a Fourier series approach in both time and space domains, but with a winding function decomposition, and an adapted matrix formalism which should have

speeded up the computation of Fourier harmonics. Moreover, as the mechanical model is based on the Fourier description of the magnetic forces, performing the FFT on vectors at the beginning of the simulation avoids the time-consuming computation of the final FFT of the force distribution in time and space domains. He expressed the stator magnetic flux density as

$$\hat{\mathbf{B}} = \hat{\mathbf{A}}\hat{\mathbf{F}}_{\text{mm}}^T, \quad \hat{\mathbf{F}}_{\text{mm}} = \frac{1}{2}\hat{\mathbf{w}}\hat{\mathbf{i}}^T \quad (3.49)$$

where $\hat{\mathbf{w}}$ is the stator winding functions space harmonics matrix, $\hat{\mathbf{i}}$ is the stator currents time harmonics matrix, $\hat{\mathbf{A}}$ is the permeance space and time harmonics matrix. The force harmonics are then computed as

$$\hat{\mathbf{F}} = \frac{1}{2\mu_0}\hat{\mathbf{B}}\hat{\mathbf{B}}^T \quad (3.50)$$

The matrix $\hat{\mathbf{F}}$ of magnetic force space and time harmonics can then be directly used as an input of the mechanical model. However, this matrix formulation did not help decreasing the high computing time due to the large number of space harmonics necessary for an accurate description of slotting effects.

These different works show that a Fourier series description of temporal currents is relevant: storing and manipulating a vector of n_t time steps describing a sinusoidal current takes more memory and computing time than using its Fourier development, which is reduced in that case to a $3 \times n_h$ matrix (3 for the magnitude, phase and frequency, n_h for the number of current harmonics) whereas the temporal vector must have $n_t \gg f_n/f_s$ elements¹. This assumes that a kind of "compression algorithm" removes the null components from FFT vectors, which is actually done in DIVA. Of course, when the complexity of the PWM current time waveform is increased to extremes, none of the components of the FFT vector is negligible, and the time description is equivalent to the Fourier description. Moreover, when computing the magnetic noise in the electrical steady state, the use of the equivalent circuit imposes a time harmonic description of the supply phase voltage (cf. section 3.1.1).

On the contrary, the stator winding distributions along the air-gap must clearly be coded in the space domain, since their stepped waveform would result in a high number of space harmonics to achieve a reasonable accuracy. This direct implementation also allows to easily model fractional-slot windings, as done in this thesis work for motor M1. The permeance distribution along the air-gap has also a stepped shape, but it changes with time as the rotor rotates. The time/space domains description of the permeance distribution is also better: its results in faster computations, it can be coded in a vectorial way in a few lines, and it can easily include eccentricities effect.

¹This effect is particularly striking when considering a single high frequency current harmonic at $f_n \gg f_s$. In that case, the FFT matrix has $2 \times 3 = 6$ components (fundamental and harmonic currents) whereas the temporal vector has $n_t \gg f_n/f_s \gg 1$ elements.

Since a Simulink PWM model is used, with a time domain voltage output, DIVA uses both the time and Fourier domain description of voltage and currents. However, the winding functions and the permeance distributions are all coded in the time and space domains. Once that the magnetic force distribution is computed as a function of time and air-gap angle, a FFT is performed and force harmonics are injected into the mechanical model. This FFT computation could be however avoided using the Green's function formalism, which directly expresses the vibration velocity in time and space domain as a function of the exciting force in time and space domain (see appendix B.2).

DIVA also use a matrix formalism, which can be seen as an extension of the one presented in (3.48) with only Z_s discretisation points along the air-gap, under each stator tooth. The matrix \mathbf{F}_{mms} containing stator mmf space and time values is computed in DIVA as

$$\mathbf{F}_{\text{mms}} = \mathbf{I}_s [\mathbf{w}_s^1 \quad \dots \quad \mathbf{w}_s^{q_s}] \quad (3.51)$$

where \mathbf{I}_s is the stator current matrix of size (pN_{ti}, q_s) , and \mathbf{w}_s^q is the q -th phase winding function vector of size $(pN_{sp}, 1)$, N_{sp} being the number of angular discretisation steps along the air-gap under one pole pair, and N_{ti} being the number of discretisation time steps per electrical period.

3.3.2 Computing tricks

To achieve a low computation time, several computing tricks are used. Firstly, in the case of even slot numbers, the stator flux density is symmetrical with respect to π , which divides by two the number of angular points to consider. Secondly, calculations that do not change with motor speed (e.g. geometrical quantities, magnetisation properties, radiation factor, unsaturated permeance distribution, etc) are computed once at the lowest speed and stored for the rest of computations. Finally, only the rotor bar number 1 winding function TF_r is computed at $t=0$ s, its evolution with time being obtained as

$$N_r^1(t, \alpha_s) = TF_r(\alpha_s - \Omega_R t) \quad (3.52)$$

while the other bar winding functions are obtained with

$$N_r^b(t, \alpha_s) = N_r^1 \left(t, \alpha_s - (b-1) \frac{2\pi}{Z_r} \right) \quad (3.53)$$

Both rotations are done by permuting the values of the first rotor bar winding function TF_r which is stored in a vector $\mathbf{TF}_r = (TF_r^j)_{j=1..pN_{sp}}$ of size $(1, pN_{sp})$. That permutation is done finding at time t the index k such as

$$k = \text{mod} \left(E((Z_r - b + 1)/Z_r - \Omega_R t) pN_{sp}, pN_{sp} \right) \quad (3.54)$$

where $\text{mod}(x, n)$ means x modulo n , and E stand for the floor function. The winding function of bar b at time t is then given by the vector

$$[TF_r^{k+1} \quad \dots \quad TF_r^{pN_{sp}}, TF_r^1 \quad \dots \quad TF_r^k] \quad (3.55)$$

if $k \geq 0$, and otherwise

$$[TF_r^1 \quad \dots \quad TF_r^{-k}, TF_r^{-k+1} \quad \dots \quad TF_r^{pN_{sp}}] \quad (3.56)$$

We can see that for $k = 0$, $b = 1$ and $t = 0$, and the initial \mathbf{TF}_r vector is found. This method is only applicable when the number of angular steps is sufficient. More precisely, it must fulfill

$$N_{sp} > \frac{N_{ti}}{1 - s} \quad (3.57)$$

In high slip on-load case, and especially when f_s is close to 0, this method therefore requires a very high number of angular discretisation steps.

3.3.3 Discretisation quality, spectral range and resolution

3.3.3.1 Time and space discretisation

The number of angular steps N_{sp} can be intuitively sized considering that the permeance distribution must be discretised enough in order to capture the smallest angular variation, given by $\min(b_s, b_r)/(2\pi R_g)$. The following inequality must therefore be respected:

$$N_{sp} \gg \frac{2\pi R_g}{p \min(b_s, b_r)} \quad (3.58)$$

The same consideration for the number of time steps N_{ti} leads to

$$N_{ti} \gg \frac{2\pi R_g(1 - s)}{pb_r} \quad (3.59)$$

In practice, a factor 2 or 3 is suitable in both criteria. Note that the use of powers of 2 for N_{ti} and N_{sp} (e.g. $N_{ti} = N_{sp} = 2^9$) speeds up the Fast Fourier Transform algorithm.

3.3.3.2 Speed discretisation

The speed discretisation step Δf_s must be chosen in order to correctly account for resonance phenomena. As the structure dynamic response is modelled by a second order filter (cf. equation (3.41)), the minimum value of Δf_s can be sized considering the 3 dB bandwidth:

$$\Delta f_s < \min_m 2\xi_m f_m \quad (3.60)$$

Experimentally, $\xi_m \geq 0.8\%$ (cf. section 3.2.1.3) and $f_m \geq 250$ Hz on ALSTOM motors, so that condition (3.60) is satisfied with $\Delta f_s \leq 4$ Hz.

3.3.3.3 Spectral resolution

At each speed, p electric periods (i.e. p/f_s seconds) are simulated, which nearly represents one rotor turn. Simulating pN_{trs} electric periods, i.e. nearly N_{trs} rotor turns, radial forces are computed until final time pN_{trs}/f_s , leading to the following spectral resolution:

$$\Delta F = \frac{f_s}{pN_{trs}} \quad (3.61)$$

Thus, ΔF line spacing worsens with speed, and the number of simulated rotor turns N_{trs} must be progressively increased during starting phase in order to keep an estimation of the sound power level enough accurate.

3.3.3.4 Spectral range

According to Shannon theorem, if each electric period $1/f_s$ is discretised with N_{ti} time steps, the maximal spectrum frequency F_{max} is given by

$$F_{max} = f_s N_{ti} / 2 \quad (3.62)$$

In sinusoidal case, F_{max} must be sized according to the most important natural frequencies of the motor (orders 0, 2 and 4). In PWM case, F_{max} must be greater than f_0 and f_{2p} in order to account for pure PWM resonances at it will be seen in section 4.1.3.3.1, and greater than $2f_c + 2f_{max}$ in order to account for the first PWM current harmonics in asynchronous case. Therefore, the following inequality must be respected:

$$F_{max} = \frac{N_{ti}}{2} f_s > \max(f_0, f_4, f_{2p}, 2f_c) \Rightarrow N_{ti} > \frac{2}{f_s} \max(f_0, f_4, f_{2p}, 2f_c + 2f_{max}) \quad (3.63)$$

In PWM case, at low supply frequency and relatively high switching frequency, the number of necessary time steps N_{ti} can dramatically increase. For instance, for $f_s = 5$ Hz, $f_c = 1280$ Hz and $f_{max} = 105$ Hz (motor M5), N_{ti} must be approximately superior to 2050 to account for PWM lines around $4f_c$ (cf. Fig. 3.44). For a 5% slip, equation (3.57) imposes $N_{sp} \geq 2160$. Consequently, the magnetic forces matrix of size $(pN_{ti}, pN_{sp}) = (4100, 4320)$ takes a memory of $4100 \times 4320 \times 8 = 141696000$ bytes, that is to say 141.696 Mb.

3.3.3.5 Conclusion

The computing time therefore increases at both high speed (equation (3.61)) and low speed (equation (3.63) and (3.57)). In on-load PWM case, at very low supply frequencies, the computation can turn to be impossible due to memory limitations.

Chapter 4

Characterisation and reduction of noise

As it was pointed out in the introduction, this thesis work is attached to explore the possibilities of magnetic noise reduction at the design stage. Consequently, this chapter firstly aims at determining all the potentially harmful radial force waves in terms of frequency, number of nodes (spatial order), and propagation direction, including the interacting effects of PWM, saturation, and load. These analytical expression can also be useful to check and interpret DIVA simulation results.

To achieve this goal, a Fourier-based method is presented and validated by visualising the stator operational deflection shapes (ODS¹). From this analytical work, some novel low-noise design rules are proposed. Some simulations are also carried to find the quietest slot number combinations. Besides these methods, the simulation tool DIVA is coupled to an evolutionary multi-objective method in order to find quiet, efficient and light motor designs.

4.1 Analytical characterisation of magnetic force lines

4.1.1 General method

As the noise spectrum lines have the same position in frequency that the vibration spectrum, and since the vibration spectrum lines have the same frequency position as in the exciting force spectrum, we will focus on the force spectrum, keeping in mind that high spatial orders are quickly negligible when transmitted as vibrations (cf. section 3.2.2.1), and that the A-weighting curve makes the very low and high frequencies inaudible (cf. Fig. 2.8). Decomposing the magnetic radial force F_{rad} in Fourier series, we get:

$$F_{rad}(t, \alpha_s) = \sum_{m,n} A_{mn} \cos(m\alpha_s + 2\pi f_n t + \phi_{mn}) = \sum_{m,n} A_{mn} \{(m, f_n)\} = \{(m_i, f_i)\}_{i \in I} \quad (4.1)$$

¹An operational deflection shape allows to visualising the animation of the stator deflection at a given frequency.

where (m_i, f_i) stands for a travelling wave (also called progressive wave) with $2m_i$ nodes, whose velocity is given by $2\pi f_i/m_i$. This wave has a propagation direction: it goes in the direction of the decreasing α_s (clockwise direction, referred as backward direction) if $f_i m_i \leq 0$, and in the anti-clockwise or forward direction if $f_i m_i \geq 0$. The information of the propagation direction can therefore be either carried by negative frequencies, or negative spatial orders. In this thesis, the negative spatial orders convention is used.

The radial force spectrum (m_i, f_i) comes from the interaction of currents spectra, magnetomotive forces spectra and permeance spectrum. These spectra can be found using the Fourier series development of permeance and mmf distributions.

In order to analytically find these spectra, the following trigonometric properties will be used:

$$\{(m_i, f_i)\}_{i \in I} + \{(m_j, f_j)\}_{j \in J} = \{(m_i, f_i)\}_{i \in I \cup J} \quad (4.2)$$

$$\begin{aligned} \{(m_i, f_i)\}_{i \in I} \times \{(m_j, f_j)\}_{j \in J} &= \sum_{i,j} \{(m_i, f_i)\} \times \{(m_j, f_j)\} \\ &= \sum_{i,j} \{(m_i + m_j, f_i + f_j), (m_i - m_j, f_i - f_j)\} \\ &= \sum_{i,j} \{(m_i + \eta_{ij} m_j, f_i + \eta_{ij} f_j)\}_{\eta_{ij} = \pm 1} \\ &= \{(m_i + \eta_{ij} m_j, f_i + \eta_{ij} f_j)\}_{i \in I, j \in J, \eta_{ij} = \pm 1} \end{aligned} \quad (4.3)$$

This last relation expresses the interaction of two travelling waves. The notation $\{(m_i \pm m_j, f_i \pm f_j)\}$ is not used because after several wave interactions, the expressions of the force waves contain several \pm which do not allow any more to associate a given frequency to its corresponding spatial order.

Note that this formalism has the main drawback to occult phase and magnitude information. In particular, two force lines of same magnitude, same spatial order and same frequency but with a π phase angle can destructively interfere. The case of two force waves (m, f) and $(m, -f)$ that come from the same harmonics interactions, and therefore have the same magnitude, will be considered with special care (see example of section 4.1.3.3.1.4).

4.1.2 Standing versus rotating waves

A second drawback of Fourier development is to occult the wave type: if two rotating forces waves (m, f) and $(m, -f)$ exist together with same magnitude and phase angle, they create a standing (also called pulsating) force wave which have the particularity to have null speed nodes (Fig. 4.1).

Let's compare the sound power level generated by a rotating vibration wave v_r of order $q > 0$ to a pulsating vibration wave v_p of same order and same magnitude. The vibration waves

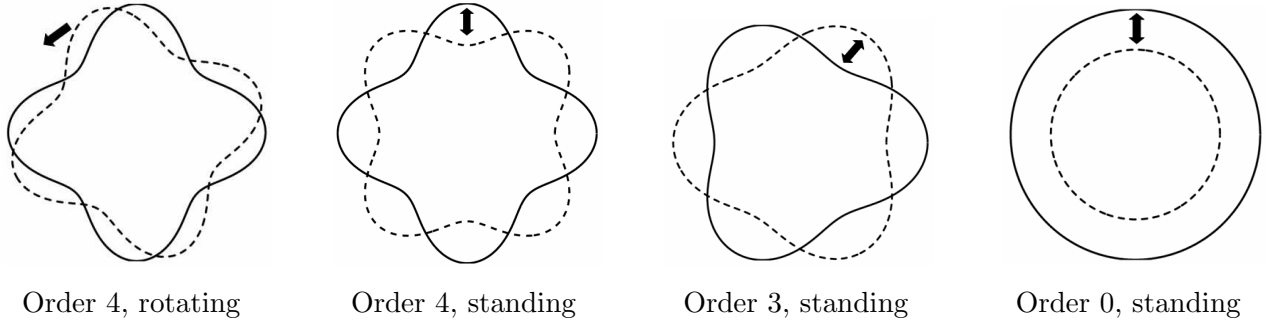


Figure 4.1: Illustration of different force waves types. The nodes of rotating waves travel along the air-gap, whereas standing waves ones stay at the same place.

can be expressed as

$$v_p = V_q \cos(q\Omega t) \cos(q\theta) \quad (4.4)$$

$$v_r = V_q \cos(q\Omega t - q\theta) \quad (4.5)$$

The corresponding radiated powers are

$$W_r \propto \overline{v_r^2} = \frac{1}{T} \int_0^T \frac{1}{2\pi} \int_0^{2\pi} v_r^2(t, \theta) dt d\theta = \frac{V_q^2}{2} \quad (4.6)$$

and

$$W_p \propto \overline{v_p^2} = \frac{1}{T} \int_0^T \frac{1}{2\pi} \int_0^{2\pi} v_p^2(t, \theta) dt d\theta = \frac{V_q^2}{4} (1 - \text{sinc}(2q\Omega T)) \quad (4.7)$$

Therefore, at resonance, a rotating vibration wave generates a SWL L_r^{max} 3 dB higher than a standing vibration wave SWL L_p^{max} :

$$L_r^{max} = L_p^{max} + 10 \log_{10}(2) = L_p^{max} + 3 \text{ dB} \quad (4.8)$$

This conclusion can be explained by the fact that in the standing case, some of the stator frame points do not move at all (nodes) and therefore do not contribute to pressure waves. This fact has been checked with both DIVA and SYSNOISE (see Fig. 4.2). Rotating waves are therefore more dangerous than standing ones in term of acoustic noise level.

In the case $q = 0$, the conclusion is of course different because no distinction can be made between the rotating and standing waves:

$$v_r = v_p = V_0 \cos(2\pi ft) \Rightarrow L_r^{max} = L_p^{max} \quad (4.9)$$

Another important property is that the stator vibration wave has exactly the same shape as the exciting force: a stator subjected to a standing force of order 4 has a standing deflection of order 4, and a stator subjected to a rotating force of order 2 has a rotating elliptical deflection. This can be proved analytically using the Green's function (139) (see Appendix B.2).

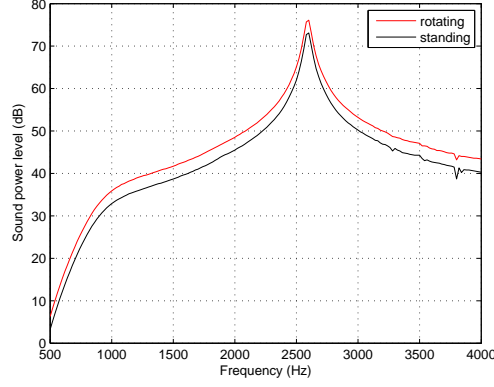


Figure 4.2: Simulated SWL of a standing or rotating force wave of spatial order 4 and magnitude 250 N/m^2 . At resonance, there is exactly a 3dB difference.

4.1.3 Expression of main magnetic lines orders and frequencies

A given flux density harmonic B_h can be written in a schematic form as

$$B_h = (1 + K_{se})(1 + K_{de})(P_0 + P_s + P_r + P_{sr} + P_a) ((N_0^s + N_h^s)(i_0^s + i_n^s) + (N_0^r + N_h^r)(i_0^r + i_n^r)) \quad (4.10)$$

where $N_0^{s/r}$ are the fundamental stator/rotor winding functions, and $N_h^{s/r}$ the corresponding winding space harmonics, $i_0^{s/r}$ are the fundamental stator/rotor currents, and $i_n^{s/r}$ the corresponding PWM time harmonics, P_0 is the fundamental permeance, and $P_{s,r,sr}$ the slotting permeance harmonics, P_a the saturation permeance harmonics, and K_{de} and K_{se} stand for dynamic and eccentricity harmonics.

The air-gap flux density therefore contains $2 \times 5 \times 8 = 96$ different types of harmonics, which result in $96^2 = 9216$ magnetic force harmonics. All these harmonics (which are accounted for in DIVA simulations) cannot be exhaustively expressed: consequently, some very low magnitude force harmonics (e.g. $P_a P_h N_h^s N_h^r i_n^s i_n^r$) will be implicitly ignored in that section. Since a low magnitude force harmonic can become significant at resonance, the border between negligible and not negligible harmonics has to be drawn subjectively. The validity of that subjective border is of course prone to experience: if a spectrogram contains a line which cannot be explained on the base of the following developments, the expressions of lower magnitude force harmonics will have to be explored.

4.1.3.1 General case

In this part are detailed the expressions of Maxwell radial magnetic force harmonics in the general case, i.e. considering PWM, load, saturation and eccentricities effect

With the rules of section 4.1.1, one can easily find that the permeance waves have the spectrum of Table 4.1 (36; 75). P_0 represent the permeance DC component, P_s , P_r and P_{sr}

Name/Amplitude	Spatial orders	Frequencies	Comments
P_s	$\epsilon_s k_s Z_s$	0	$k_s \geq 1$, stator slotting
P_r	$k_r Z_r$	$k_r Z_r f_R$	$k_r \geq 1$, rotor slotting
P_{sr}	$k_s Z_s + \epsilon_{sr} k_r Z_r$	$k_r Z_r f_R$	stator and rotor slotting interaction
P_a	$2k_a p$	$2k_a f_s$	$k_a \geq 1$, saturation
P_0	0	0	mean value
K_{se}	$\epsilon_{se} k_{se}$	0	$k_{se} \geq 1$, static eccentricity
K_{de}	k_{de}	$-k_{de} f_R$	$k_{de} \geq 1$, dynamic eccentricity

Table 4.1: Permeance harmonic groups orders and frequencies. The fundamental flux density wave is supposed to rotate in forward direction ($\lambda_R = 1$), its expression is therefore (p, f_s) .

represent the stator and rotor slotting permeance harmonics, P_a represents the saturation permeance harmonics, and K_{se} and K_{de} represent static and dynamic eccentricities harmonics (which have to be multiplied to the other permeance harmonics). These orders and frequencies can be found in the simulation results of permeance distribution plotted in Fig. 3.18 and 3.19.

To obtain the stator magnetomotive forces spectra, the stator current spectrum $(0, f_n^s)$ has to be multiplied to the stator winding functions. The summation on the q_s stator phases cancel some of the spatial harmonics of the winding function. A careful analysis (28) gives the stator harmonics F_s presented in Table 4.2. In a same way, the rotor current spectrum $(0, f_{m\nu_s}^s)$ (representing the rotor harmonic currents induced by the space harmonic ν_s and the time harmonic f_n^s coming from stator winding function and current) has to be multiplied by the rotor winding function, which gives the harmonics displayed in Table 4.2. These space harmonics can be observed in simulation results displayed in Fig. 3.15 and 3.16.

Name/Amplitude	Spatial orders	Frequencies	Comments
F_s	$\nu_s = p(2q_s h_s + \eta_s)$	$\eta_s f_n^s$	$h_s \geq 0$, stator mmf
F_r	$\nu_r = p(h_r Z_r / p + \eta_r)$	$\nu_r f_R + \eta_r f_{\nu_s n}^r$	$h_r \geq 0$, rotor mmf

Table 4.2: Stator and rotor mmf harmonics orders and frequencies.

Note that when $h_{s/r} = 0$ (fundamental mmf waves of order $\nu_s = \nu_r = p$), we have necessarily $\eta_{s/r} = 1$. η_s and η_r give the propagation direction of the mmf harmonics due to a winding space harmonic. These propagation directions can be visualised on the complex FFT of the mmf distribution. For instance, in Fig. 4.3, we can see that the fundamental mmf wave is $(p, -f_s)$ (it would have been (p, f_s) if the rotor turned in the opposite direction), and the harmonic mmf due to stator winding space harmonic $5p$ is $(-5p, -f_s) = (5p, f_s)$, and therefore rotates in the opposite direction of the fundamental mmf wave. The spectrum is symmetrical with respect to 0 because the stator mmf is real.

The air-gap flux density harmonics are obtained by combining the permeance and mmf harmonics one with another. The resulting spectrum is presented in Table 4.3 where coefficients

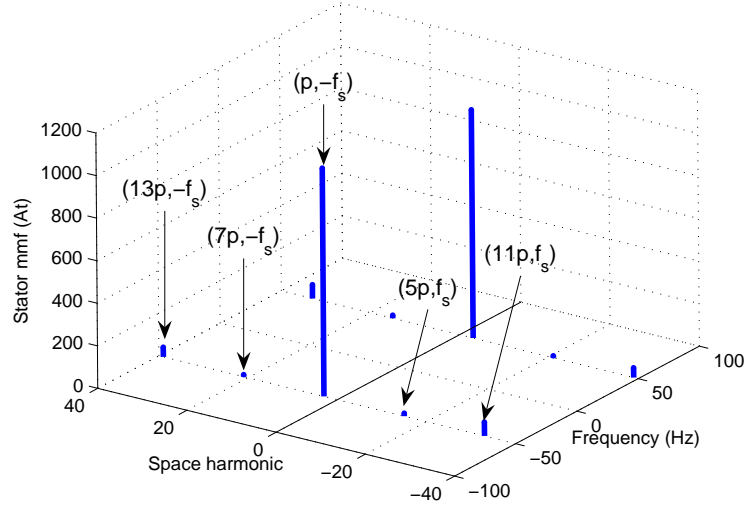


Figure 4.3: Complex FFT of shorted-pitch motor M2 stator mmf in sinusoidal case ($f_s = 50$ Hz).

β_x stand for some ± 1 factors resulting from the multiplication of a mmf harmonic with a permeance harmonic.

Name/Amplitude	Spatial orders	Frequencies	Comments
$B_1 = P_s F_s$	$\epsilon_s k_s Z_s + \beta_{ss} \nu_s$	$\beta_{ss} \eta_s f_n^s$	
$B_2 = P_s F_r$	$\epsilon_s k_s Z_s + \beta_{sr} \nu_r$	$\beta_{sr} (\nu_r f_R + \eta_r f_{\nu_s n}^r)$	
$B_3 = P_r F_s$	$k_r Z_r + \beta_{rs} \nu_s$	$k_r Z_r f_R + \beta_{rs} \eta_s f_n^s$	
$B_4 = P_r F_r$	$k_r Z_r + \beta_{rr} \nu_r$	$(k_r Z_r + \beta_{rr} \nu_r) f_R + \beta_{rr} \eta_r f_{\nu_s n}^r$	
$B_5 = P_{sr} F_s$	$k_s Z_s + \epsilon_{sr} k_r Z_r + \beta_{is} \nu_s$	$\epsilon_{sr} k_r Z_r f_R + \beta_{is} \eta_s f_n^s$	
$B_6 = P_{sr} F_r$	$k_s Z_s + \epsilon_{sr} k_r Z_r + \beta_{ir} \nu_r$	$(\epsilon_{sr} k_r Z_r + \beta_{ir} \nu_r) f_R + \beta_{ir} \eta_r f_{\nu_s n}^r$	
$B_7 = P_a F_s$	$2k_a p + \beta_{as} \nu_s$	$2k_a f_s + \beta_{as} \eta_s f_n^s$	
$B_8 = P_a F_r$	$2k_a p + \beta_{ar} \nu_r$	$2k_a f_s + \beta_{ar} (\nu_r f_R + \eta_r f_{\nu_s n}^r)$	
$B_9 = P_0 F_s$	ν_s	$\eta_s f_n^s$	
$B_{10} = P_0 F_r$	ν_r	$\nu_r f_R + \eta_r f_{\nu_s n}^r$	
$B_{11} = P_s F_s K_{se}$	$\epsilon_s k_s Z_s + \beta_{ss} \nu_s + \beta_{ses} \epsilon_{se} k_{se}$	$\beta_{ss} \eta_s f_n^s$	
$B_{12} = P_s F_s K_{de}$	$\epsilon_s k_s Z_s + \beta_{ss} \nu_s + \beta_{des} k_{de}$	$\beta_{ss} \eta_s f_n^s - \beta_{des} k_{de} f_R$	
$B_{13} = P_r F_s K_{se}$	$k_r Z_r + \beta_{rs} \nu_s + \beta_{ser} \epsilon_{se} k_{se}$	$k_r Z_r f_R + \beta_{rs} \eta_s f_n^s$	
$B_{14} = P_r F_s K_{de}$	$k_r Z_r + \beta_{rs} \nu_s + \beta_{der} k_{de}$	$(k_r Z_r - \beta_{der} k_{de}) f_R + \beta_{rs} \eta_s f_n^s$	
$B_{15} = P_a F_s K_{se}$	$2k_a p + \beta_{as} \nu_s + \beta_{sea} \epsilon_{se} k_{se}$	$2k_a f_s + \beta_{as} \eta_s f_n^s$	
$B_{16} = P_a F_s K_{de}$	$2k_a p + \beta_{as} \nu_s + \beta_{dea} k_{de}$	$2k_a f_s + \beta_{as} \eta_s f_n^s - \beta_{dea} k_{de} f_R$	

Table 4.3: Flux density harmonics orders and frequencies.

In order to find the whole radial force spectrum, all the flux density lines are then multiplied one to each other. The obtained force spectrum is exhaustively detailed in Table C.1 of the

appendix, where the notation F_{ij} means the force harmonic coming from the multiplication of flux harmonics B_i and B_j , and δ_x letters are used to represent the ± 1 factors involved in flux harmonic multiplication. The redundant force lines (e.g. $P_s F_s P_r F_r$ and $P_r F_s P_s F_r$) have been removed, and the lines associated to particularly high spatial orders are ticked. Using that table, it is important to keep in mind that $\nu_{s/r}$ is a function of $\eta_{s/r}$: for instance, taking the mmf harmonic $\nu_s = 5p$ implies $\eta_s = -1$. The spatial orders and frequencies expressions can take either negative or positive values, according to the propagation direction of the vibration wave. Finally, it is important to remember that each line of this table do not represent one force harmonics, but an infinite group of harmonics (k_r , k_s , k_a , f_n^s , etc. take an infinite number of different values). The force harmonics can sorted by magnitude using the following inequalities :

$$\begin{aligned}
 P_0 &\gg P_s, P_r, P_{sr} \\
 P_a &\ll P_s, P_r \\
 P_{sr} &\ll P_s, P_r \\
 F_r &\ll F_s
 \end{aligned} \tag{4.11}$$

With the Fourier series development, one can also show that (28):

$$\begin{aligned}
 F_s &\propto 1/\nu_s^2 \\
 F_r &\propto 1/\nu_r \\
 P_s &\propto 1/k_s \\
 P_r &\propto 1/k_r \\
 P_{sr} &\propto 1/(k_s k_r)
 \end{aligned} \tag{4.12}$$

Moreover, the largest force line are always given by $\nu_s = \nu_r = p$ (mmf fundamentals), $k_r = k_s = 1$, and $f_n^s = f_s$. For saturation and eccentricities harmonics, the highest magnitude is obtained with $k_a = 1$ and $k_{se} = k_{de} = 1$. Let's finally remind that the deflection magnitude due to a force line of order m is proportional to $1/m^4$ (for $m \geq 2$).

All the expressions of Table C.1 can be used in the case of a fractional-slot winding by replacing the stator winding space harmonics ν_s by the right ones (see (155)) for the analytical expression of fractional slot winding space harmonics). In a same way, these expressions can be adapted to different rotors (wounded rotors for instance) by changing the harmonics ν_r , and to any PWM strategy by changing the current harmonics f_n^s .

In next sections, some assumptions are going to be made in order to classify these force harmonics and express their frequency and order in simple analytical forms. High order force harmonics of Table C.1 are neglected as they do not generate high deflections (cf. equation (3.38)). The force harmonics that will be considered are therefore summed up in the appendix Table C.2.

4.1.3.2 Sinusoidal case

4.1.3.2.1 Expression of main lines

In this first part, the motor is assumed to be fed with sinusoidal currents ($f_n^s = f_s$). Considering that mmfs are also sinusoidal ($\nu_s = \nu_r = p$, and consequently $f_{\nu_s n}^r = s f_s$), removing static force harmonics (0, 0) and low magnitude harmonics (e.g. $P_{sr} F_r P_{sr} F_r$), we obtain Table C.3 force harmonics. In that table, low frequency (≤ 400 Hz) force harmonics have been ticked. Indeed, traction machines that we here consider are supplied with a maximum frequency $f_{max} = 200$ Hz: the force lines that are inferior to $2f_s$ are then necessarily inferior to 400 Hz. Even if a resonance could occur at this frequency, at maximum speed it is assumed that the aerodynamic noise dominates magnetic noise, so these force lines are excluded from the following acoustic analysis. These low-frequency lines should be taken into account in a structure-borne noise study, since low frequency vibration can be transmitted for example to the motor case and resonate with some larger systems with lower natural frequencies.

It is noteworthy that for all harmonics (apart from eccentricity ones), the parity of the sinusoidal case magnetic forces spatial orders \overline{m}^1 are all given by:

$$\overline{m} = \overline{k_r Z_r} - \overline{k_s Z_s} \quad (4.13)$$

On medium power machines, Z_r is often even to avoid a strong magnetic unbalance of the rotor (10). Moreover, if the stator is wound with an integral winding, Z_s must be proportional to $2pq_s$, which imposes that Z_s is also even. For motors M2 to M5, we therefore have $\overline{m} = 0$, which means that all magnetic force harmonics have even spatial orders (excluding eccentricity harmonics). In particular, the rotor bending mode cannot be excited if there is no eccentricity. On the contrary, small power M1 has a fractional-slot winding with an odd number of stator teeth, and an odd number of rotor slots: some odd modes of the motor can therefore be excited (23; 28).

Among these force harmonics, excluding the low frequency ones, we can make distinction between:

1. pure slotting lines, from the combination of fundamental mmf and permeance slotting harmonics ($F_{13}, F_{14}, F_{15}, F_{16}, F_{24}, F_{35}, F_{55}, F_{59}, F_{510}$)

¹By definition, \overline{m} equals 0 if m is even, and 1 if m is odd.

2. saturation lines, from the combination of a saturated permeance wave, a fundamental mmf and some slotting permeance harmonics (F_{57})
3. eccentricity lines, from the combination of slotting permeance waves, fundamental mmf and eccentricity harmonics (F_{113}, F_{114})

Another type of force harmonics is obtained by combining a space harmonics of stator mmf ($\nu_s \neq p$), combining it with a of fundamental mmf, and some permeance slotting harmonics. This particular lines, whose magnitude can be decreased by a proper choice of the coil-pitch, are here called winding force harmonics.

4.1.3.2.2 Pure slotting force lines

4.1.3.2.2.1 Expression

Pure slotting lines have always the same frequency and spatial order form which are summed up in Table 4.4. The highest ones are F_{13} family as they do not involve rotor mmf.

	Frequency f	Spatial order m
F_{slot}^-	$f_s(k_r Z_r(1-s)/p-2)$	$k_r Z_r - k_s Z_s - 2p$
F_{slot}^0	$f_s(k_r Z_r(1-s)/p)$	$k_r Z_r - k_s Z_s$
F_{slot}^+	$f_s(k_r Z_r(1-s)/p+2)$	$k_r Z_r - k_s Z_s + 2p$

Table 4.4: Pure slotting force lines expression.

4.1.3.2.2.2 Validation

The expression of the slotting force harmonics can be validated using the spectrogram of Fig. 4.4, which was already showed as a validation of the vibration model (cf. section 3.2.2.2.1). The characteristics of the main vibrations appearing in this spectrogram are detailed in Table 4.5 (these expressions can be easily found using the Table 4.4, or the line F_{13} of Table C.3).

Only one vibration cannot be explained using the slotting lines expressions: it is line nb. 2, a winding force harmonic which will be analysed later in section 4.1.3.2.5. We can see in that spectrogram that the main resonances come from line nb. 3 of order 1 with the bending mode natural frequency near 1100 Hz, and the line nb. 10 of of order 3 with the mode 3 of the stator near 6000 Hz (for motor M1 natural frequencies determination, cf. section 3.2.1.3). Using the analytical expressions of Table 4.5, one could easily predict at which speed f_s^1 and f_s^3 these resonances would occur:

$$f_s^1 = \frac{f_1}{4Z_r(1-s)/p-2} \approx 30\text{Hz} \quad f_s^3 = \frac{f_3}{13Z_r(1-s)/p} \approx 49\text{Hz} \quad (4.14)$$

Line nb. 1 is a very large magnetic magnetic line of order 2 because it is obtained with $k_r = k_s = 1$. However, the elliptical mode natural frequency of the stator is too high (2400

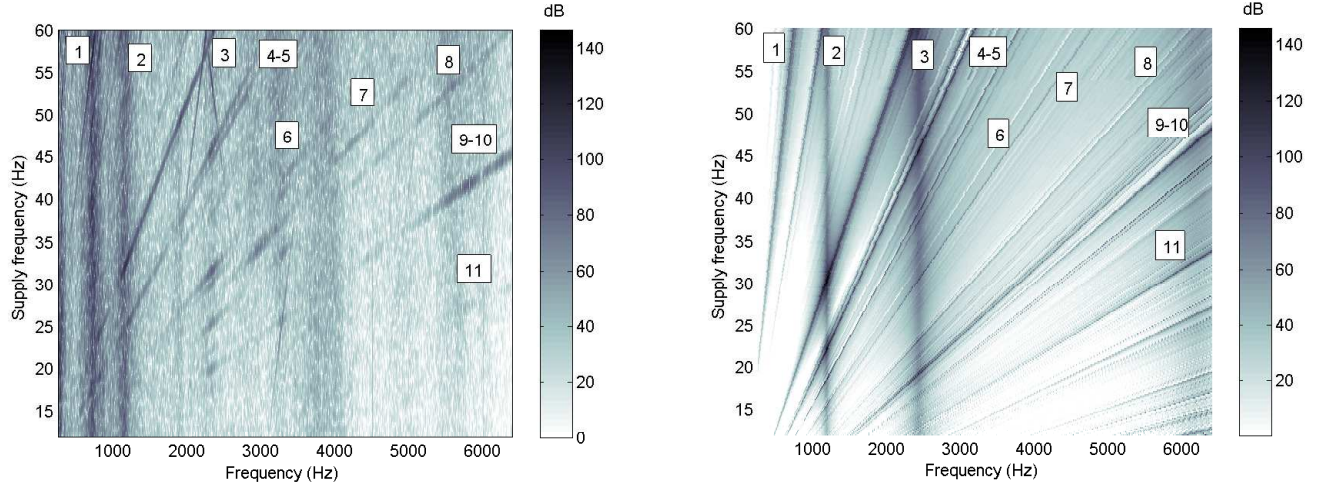


Figure 4.4: Experimental and simulated (DIVA) acceleration spectrogram in sinusoidal case (motor M1, $f_s=12$ to 60 Hz).

nb.	k_s	k_r	β_{ss}	β_{rs}	Frequency f	Spatial order m
1	1	1	-1	1	$f_s(Z_r(1-s)/p+2)$	-2
3	3	4	1	-1	$f_s(4Z_r(1-s)/p-2)$	-1
4	4	5	± 1	± 1	$f_s(5Z_r(1-s)/p)$	-3
5	4	5	-1	1	$f_s(5Z_r(1-s)/p+2)$	1
6	6	8	1	-1	$f_s(8Z_r(1-s)/p-2)$	2
7	7	9	± 1	± 1	$f_s(9Z_r(1-s)/p)$	0
8	8	10	-1	1	$f_s(10Z_r(1-s)/p+2)$	-2
9	10	13	1	-1	$f_s(13Z_r(1-s)/p-2)$	-1
10	10	13	± 1	± 1	$f_s(13Z_r(1-s)/p)$	3
11	14	18	± 1	± 1	$f_s(18Z_r(1-s)/p)$	0

Table 4.5: Characterisation of motor M1 ($Z_s = 27$, $Z_r = 21$, $p = 2$) pure slotting vibration lines.

Hz) to be excited during starting phase. The resonance of line nb. 10 with the stator mode 3 has been checked by visualising the stator deflection at this frequency with the Operational Deflection Shape tool of Pulse Labshop software (Fig. 4.5).

Another characteristic which is important to validate is the propagation direction of the force waves. This validation has been done with an Operational Deflection Shape (Fig. 4.6). For instance, Table 4.5 shows that line nb. 1 has a spatial order of -2, whereas line nb. 6 has a 2 spatial order: these two slotting vibrations should therefore have opposite propagation directions, which can be observed in the ODS of Fig. 4.6.

In a same way, the expressions of pure slotting lines occurring on motor M3 have been computed in Table 4.6. The sonograms of Fig. 4.7 already showed in section 3.2.4.2.2.1 shows

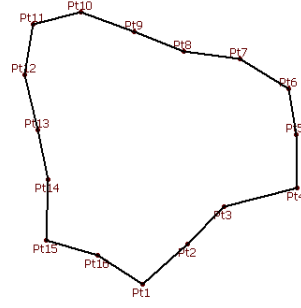


Figure 4.5: Stator deflection of order 3 due to a slotting vibration (motor M1, sinusoidal case, $f_s = 50$ Hz).

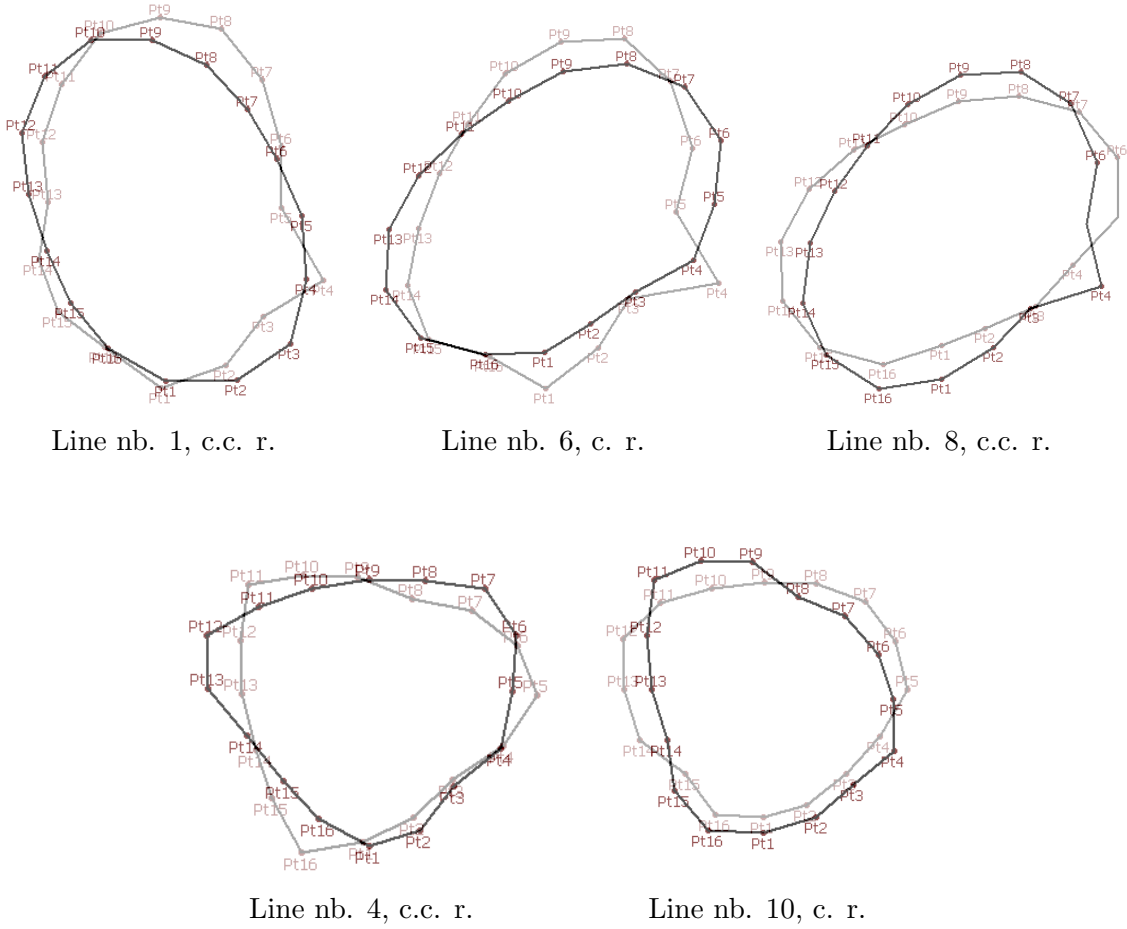


Figure 4.6: Pure slotting force waves on motor M1, and their propagation direction (c.c. r.: counter-clockwise rotation, c. r.: clockwise rotation). Grey deflection indicates a time anterior to black deflection.

that all the slotting lines are well predicted. Line number 1 is a saturation line that is detailed in section 4.1.3.2.3, and line number 2 is a winding line that is detailed in section 4.1.3.2.5.

nb.	k_s	k_r	β_{ss}	β_{rs}	Frequency f	Spatial order m
3	1	1	-1	1	$f_s Z_r(1-s)/p$	4
4	2	3	-1	1	$f_s(3Z_r(1-s)/p-2)$	0
5	3	4	-1	1	$4f_s Z_r(1-s)/p$	4
6	3	4	-1	1	$f_s(4Z_r(1-s)/p+2)$	-2
7	5	7	-1	1	$7f_s Z_r(1-s)/p$	-2
8	5	7	-1	1	$f_s(7Z_r(1-s)/p-2)$	4

Table 4.6: Characterisation of motor M2 ($Z_s = 36$, $Z_r = 26$, $p = 3$) pure slotting vibration lines.

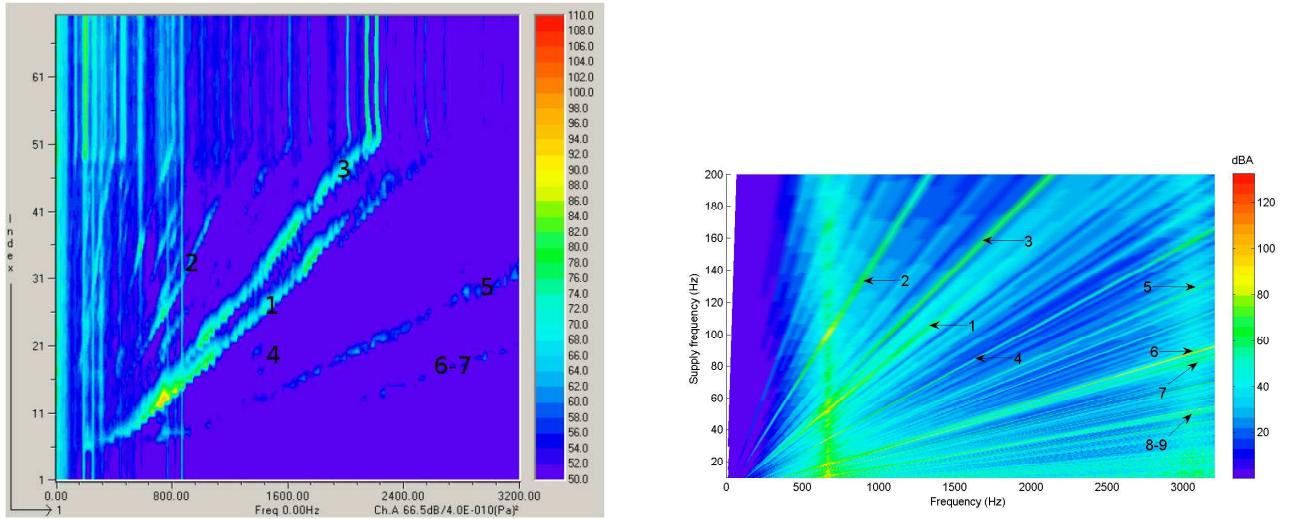


Figure 4.7: Experimental (left) and simulated (right) sonagram on motor M2 in sinusoidal no-load case.

These expressions have also been checked by analysing some spectrograms measured on other motors.

4.1.3.2.2.3 Effect of current magnitude

As the slotting force is proportional to the stator fundamental current I_1^0 , the effect of a current change from I_1^0 to $I_1^{0'}$ on the slotting noise level is given by

$$\Delta L_w^{slot} = 40 \log_{10} \left(\frac{I_1^{0'}}{I_1^0} \right) \quad (4.15)$$

If the current is twice higher, slotting noise should therefore increase of 12 dB independently of the spatial orders of magnetic forces.

4.1.3.2.3 Saturation force lines

4.1.3.2.3.1 Expression

The highest group of saturation lines is given by F_{57} , their expressions are summed up in Table 4.7. We can see that saturation lines can occur at exactly the same frequencies than some pure slotting lines, but with a different spatial order. The frequency expression $f_s(Z_r(1-s)/p \pm 4)$ is however characteristic of a saturation phenomenon.

	Frequency f	Spatial order m
F_{sat}^-	$f_s(k_r Z_r(1-s)/p - 2(1+k_a))$	$k_r Z_r - k_s Z_s - 2p(1+k_a)$
F_{sat}^0	$f_s(k_r Z_r(1-s)/p \pm 2k_a)$	$k_r Z_r - k_s Z_s \pm 2pk_a$
F_{sat}^+	$f_s(k_r Z_r(1-s)/p + 2(1+k_a))$	$k_r Z_r - k_s Z_s + 2p(1+k_a)$

Table 4.7: Saturation force lines expression.

4.1.3.2.3.2 Validation

The frequency and spatial order of this line has been validated on M5 motor ($Z_r = 38$, $Z_s = 48$, $p = 2$). Table 4.7 shows that a saturation force line of order $Z_r - Z_s + 4p = -2$ and frequency $f_s(k_r Z_r(1-s)/p + 4)$ exists in this motor. As its elliptical mode natural frequency f_2 is around 600 Hz (cf. 3.4), a resonance can occur around 30 Hz. This resonance was observed during tests, as shown in the order analysis¹ of Fig. 4.8 where the line $46f_R \approx 23f_s \approx f_s(Z_r(1-s)/p + 4)$ is responsible for two resonances. An Operational Deflection Shape analysis confirmed the spatial order 2 of that saturation line (see Fig. 4.9).

A noisy saturation vibration was also observed on motor M3. Indeed, Table 4.7 shows that for $k_r = k_s = 1$, a saturation force line of spatial order $2 = Z_r - Z_s - 4p$ occurs at frequency $f_s(Z_r(1-s)/p + 4)$. As the elliptical mode of the stator is near 600 Hz like in motor M5, a resonance will appear near $f_2/(Z_r/p + 4) \approx 50$ Hz. This resonance can be clearly observed in both experiments and simulation (cf. line number 1 in the sonagrams of Fig. 4.7).

4.1.3.2.3.3 Interaction with rotor skewing

Some old tests on motor M5 and M5a showed, as expected, that skewing a rotor improved the noise level in sinusoidal no-load case ; however, it increased noise in on-load case: in Fig. 4.10,

¹An order analysis is similar to a sonagram: time or supply frequency is displayed in ordinates, but the sampling frequency used for FFT analysis is not constant, it is proportional to speed. This way, a vibration line of frequency kf_s appears as a vertical line in an order analysis at abscissa k , and the evolution of an given line in function of speed is captured more easily. Coefficient k is called the order of the vibration line, but it has nothing to do with the spatial order of the vibration wave. Natural frequencies, which appear as vertical lines in the sonagram, appear as hyperbolas in an order analysis. Note that the order analysis is only interesting in no-load case: if slip varies with time, magnetic force lines frequencies are not proportional any more to speed, and they do not appear as vertical lines in the order analysis.

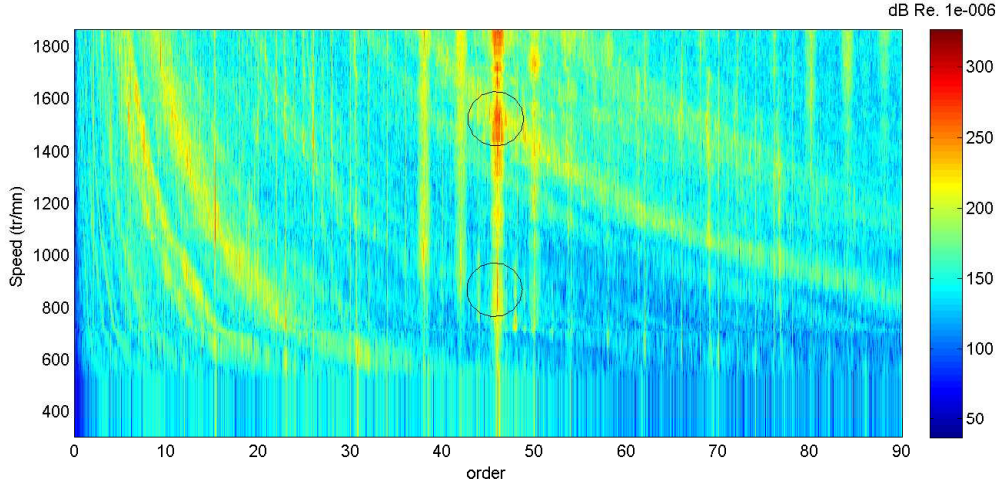


Figure 4.8: Order analysis of motor M5 in sinusoidal case. Saturation line of spatial order $m = -2$ and frequency $f_s(Z_r(1-s)/p + 4) \approx 46f_R$ therefore appears at the order 46 abscissa.

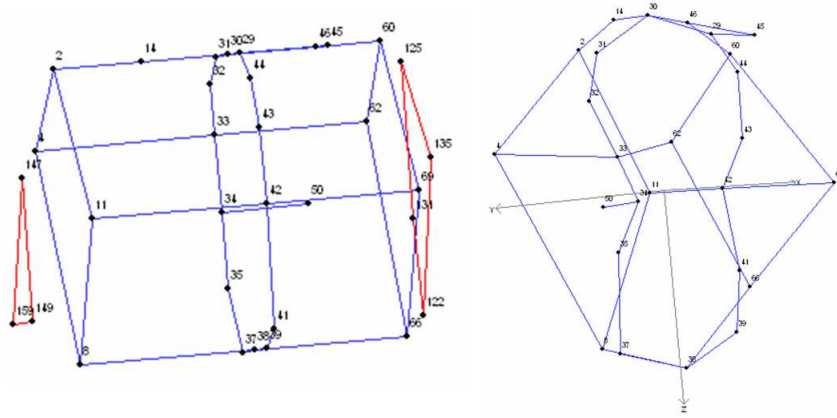


Figure 4.9: Operational Deflection Shape of motor M5 near 600 Hz ($f_s \approx 30$ Hz i.e. 900 rpm). An elliptical deflection of the stator stack is observed.

a strong resonance occurs near 50 Hz with the skewed rotor.

Analysing the sonagrams, it was found that the resonance was caused by the saturation line of order 2 and frequency $f_s(Z_r(1-s)/p + 4)$ identified in previous section, with a mode near 1150 Hz. An Operational Deflection Shape showed that this mode was a bending mode of the frame, which is not a pure bending as it involves the end-plates, and a strong coupling between rotor and stator (Fig. 4.11). A similar mode at this frequency was also found in the mechanical FEM analysis of the motor real geometry elaborated by VIBRATEC.

It is therefore assumed that the combination between saturation and skewing gave a magnetic force varying along the axial motor direction, making it able to excite some longitudinal modes of the motor. This assumption has been comforted with the following analytical work.

The slotting permeance harmonic P_{sr} involved in the saturation force can be expressed for

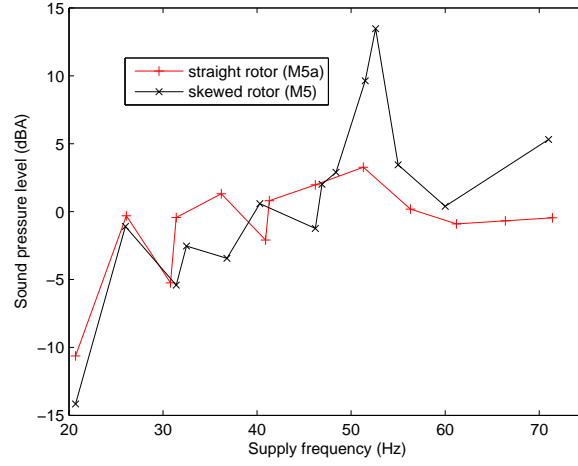


Figure 4.10: Influence of rotor skewing on the sound pressure level in on-load sinusoidal case.

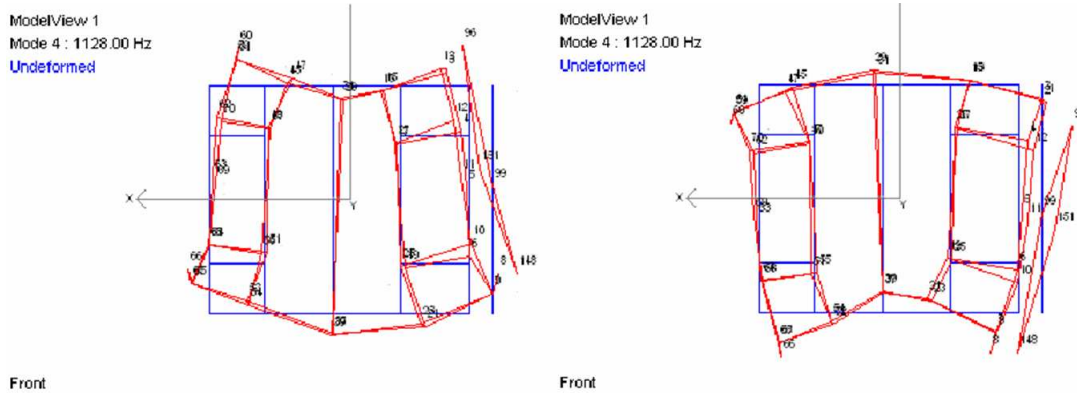


Figure 4.11: Operational Deflection Shape of motor M5 at 1138 Hz (maximal flux, PWM no-load case, $f_s \approx 50$ Hz - test by VIBRATEC).

a skewed rotor as

$$P_{sr}(t, \alpha_s, z) \propto \cos \left((Z_s - Z_r)\alpha_s - Z_r\omega_R \left(t - \frac{\alpha_{sk}(z)}{\omega_R} \right) \right) \quad (4.16)$$

where the skew angle α_{sk} is given for a one slot pitch skew by

$$\alpha_{sk}(z) = \frac{\pi z}{Z_r L_r}, \quad z \in [-L_r/2, L_r/2] \quad (4.17)$$

The first order saturation permeance harmonic P_a can be written as

$$P_a(t, \alpha_s) \propto \cos(2p\alpha_s + 2\omega_s t - \pi) \quad (4.18)$$

while the fundamental stator mmf F_s is

$$F_s(t, \alpha_s) \propto \cos(p\alpha_s + \omega_s t) \quad (4.19)$$

The combination between F_s and P_a gives rise to a flux density harmonic B_1 such as

$$B_1(t, \alpha_s) \propto \cos(3p\alpha_s + 3\omega_s t - \pi) \quad (4.20)$$

while the combination between F_s and P_{sr} gives rise to a flux density harmonic B_2 such as

$$B_2(t, \alpha_s, z) \propto \cos\left((Z_s - Z_r - p)\alpha_s - Z_r\omega_R\left(t - \frac{\alpha_{sk}(z)}{\omega_R}\right) - \omega_s t\right) \quad (4.21)$$

Finally, the multiplication of B_1 and B_2 gives in particular a force harmonic F_{sat} of the form

$$F_{sat}(t, \alpha_s, z) \propto \cos\left((Z_s - Z_r - 3p)\alpha_s - Z_r\omega_R\left(t - \frac{\alpha_{sk}(z)}{\omega_R}\right) - 4\omega_s t + \pi\right) \quad (4.22)$$

The 3D shape
this kind of force

. We can see that
ng.

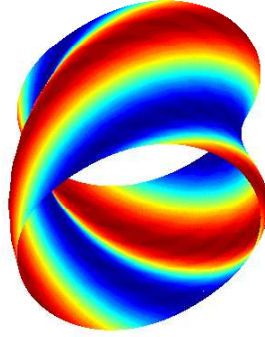


Figure 4.12: 3D shape of the saturation force harmonic of equation (4.22) due to rotor skewing.

4.1.3.2.4 Eccentricity force lines

Dynamic eccentricity lines are showed in Table 4.8 (static eccentricity lines are obtained by setting $k_{de} = 0$ in the frequencies expression). We can see that the main dynamic eccentricity harmonics ($k_{de} = 1$) do not overlap with pure slotting harmonics. The highest eccentricity lines are given by F_{113} and F_{114} .

	Frequency f	Spatial order m
F_{de}^-	$f_s(k_r Z_r(1-s)/p - 2 \pm k_{de}(1-s)/p)$	$k_r Z_r - k_s Z_s - 2p \pm k_{de}$
F_{de}^0	$f_s(k_r Z_r(1-s)/p \pm k_{de}(1-s)/p)$	$k_r Z_r - k_s Z_s \pm k_{de}$
F_{de}^+	$f_s(k_r Z_r(1-s)/p + 2 \pm k_{de}(1-s)/p)$	$k_r Z_r - k_s Z_s + 2p \pm k_{de}$

Table 4.8: Eccentricity lines expression.

These eccentricity lines characteristics have not been validated, and their influence on noise has not been investigated as ALSTOM motors are balanced, and do not have much eccentricity.

4.1.3.2.5 Winding force lines

4.1.3.2.5.1 Expression

If a fundamental mmf is combined with a space harmonic mmf, and with slotting permeance harmonics, we get from F_{13} group the so-called winding harmonics. Their expressions are summed up in Table 4.9.

	Frequency f	Spatial order m
F_w^-	$f_s(k_r Z_r(1-s)/p - 1 - \eta_s)$	$k_r Z_r - k_s Z_s - p - \nu_s(\eta_s)$
F_w^0	$f_s(k_r Z_r(1-s)/p - 1 + \eta_s)$	$k_r Z_r - k_s Z_s - p + \nu_s(\eta_s)$
F_w^0	$f_s(k_r Z_r(1-s)/p + 1 - \eta_s)$	$k_r Z_r - k_s Z_s + p - \nu_s(\eta_s)$
F_w^+	$f_s(k_r Z_r(1-s)/p + 1 + \eta_s)$	$k_r Z_r - k_s Z_s + p + \nu_s(\eta_s)$

Table 4.9: Winding force lines expression.

4.1.3.2.5.2 Validation

In the motor M1 spectrograms (Fig. 4.4), the line number 2 expression could not be identified as a pure slotting line. It is actually a winding harmonic of frequency $f_s(2Z_r/p - 2)$, which has been checked using DIVA by computing a spectrogram with a sinusoidal mmf.

In the same way, the line number 2 expression of motor M3 sonagram (Fig. 4.7) could not be characterised as a slotting line: it is a winding harmonic of order $-2 = Z_r - Z_s - p + 5p$ ($k_r = k_s = 1$, $\eta_s = -1$, $h_s = 1$) and frequency $f_s(Z_r(1-s)/p - 2)$, which resonates with the mode number 2 of the stator near $f_s = 100$ Hz. Another winding line of spatial order $2 = Z_r - Z_s - p + 7p$ and frequency $f_s Z_r(1-s)/p$ exists, and was observed in an operational deflection shape (Fig. 4.13).

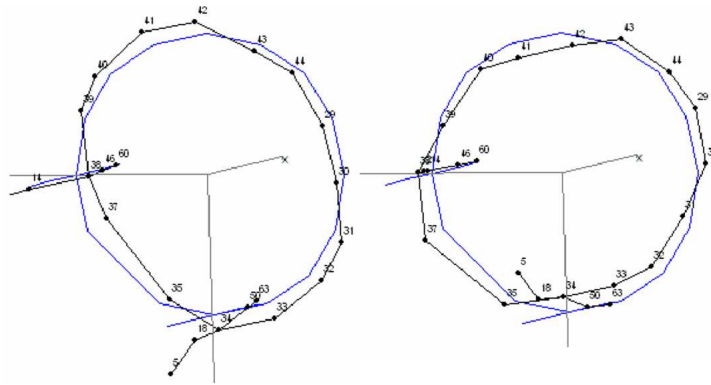


Figure 4.13: Operational deflection shape at 942 Hz at two successive instants (motor M5, $f_s \approx 50$ Hz, sinusoidal case).

The analytical expressions of Table 4.9 have exhaustively been checked with DIVA simulations. Motor M3 magnetic noise spectrum has been computed removing the fundamental

mmf wave of order p , and forcing the permeance to be constant (smooth air-gap) in order to obtain only the effect of winding forces in the noise spectrum. All the simulated acoustic lines frequencies and spatial orders¹ can be found using Table 4.9, which shows that the analytical expressions of winding lines are correct. Fig. 4.14 shows DIVA noise spectrum of winding lines, and Table 4.10 presents their characteristics (frequency and spatial order).

Line nb.	k_r	k_s	ν_s	Frequency f	Spatial order m
1	1	1	$5p$	$f_s(Z_r(1-s)/p - 2) = 666$ Hz	2
2	2	1	$7p, 5p$	$2f_s Z_r(1-s)/p = 1733$ Hz	-2
3	2	2	$7p$	$f_s(2Z_r(1-s)/p + 2) = 1933$ Hz	4
4	3	3	$11p$	$f_s(3Z_r(1-s)/p - 2) = 2400$ Hz	0
5	3	3	$11p, 13p$	$3f_s Z_r(1-s)/p = 2600$ Hz	6
6	4	4	$11p$	$4f_s Z_r(1-s)/p = 3466$ Hz	-4
7	4	2	$11p$	$f_s(4Z_r(1-s)/p + 2) = 3666$ Hz	2
8	5	4	$7p$	$5f_s Z_r(1-s)/p = 4333$ Hz	4
9	7	6	$7p$	$7f_s Z_r(1-s)/p = 6066$ Hz	2

Table 4.10: Expression of motor M3 main winding lines.

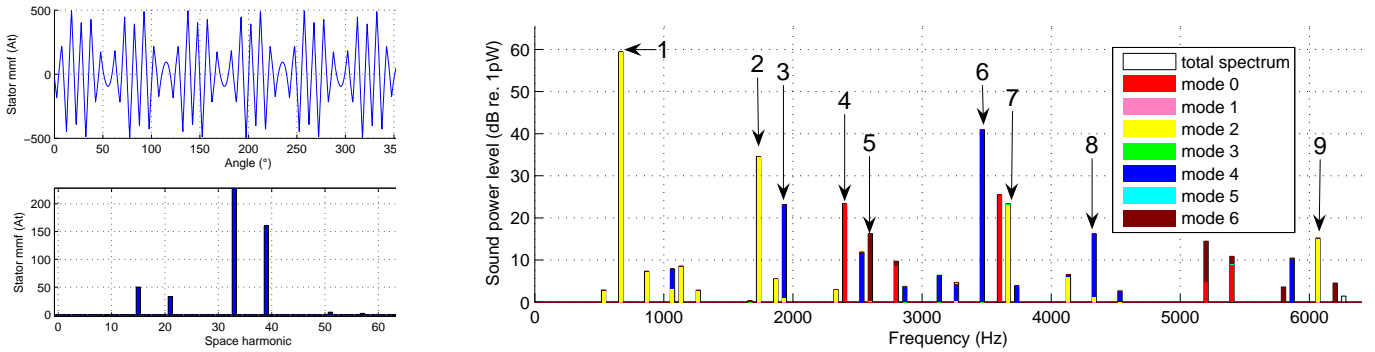


Figure 4.14: Left: stator mmf without the fundamental. Right: corresponding magnetic noise spectrum with stator modes contribution (motor M3, $f_s = 100$ Hz).

These winding force lines magnitude can be reduced by a proper choose of the coil pitch (25). However, their magnitude is much smaller than the one of pure slotting lines (their ratio is the one of the stator mmf fundamental magnitude with its space harmonic), and in on-load case the effect of the coil pitch is hardly visible on the noise spectrum.

4.1.3.3 PWM case

Considering the effect of PWM, the main force lines can be classified in two types:

¹DIVA visualisation tools comprise a noise spectrum where lines are coloured according to the spatial orders of the magnetic forces that contribute to its noise level.

	Frequency f	Spatial order m
F_{pwm}^-	$f_s - \eta_s f_n^s$	0
F_{pwm}^+	$f_s + \eta_s f_n^s$	$2p$

Table 4.11: Pure PWM force lines expression.

1. pure PWM force lines, which come from the combination between a mmf PWM harmonic, a fundamental mmf, and mean permeances (F_{99} , F_{910} and F_{1010}), which were neglected in sinusoidal case because of their low frequency)
2. PWM slotting force lines, which come from the combination between a mmf PWM harmonic, a fundamental mmf, and some slotting permeance harmonics (F_{99} and F_{910})

4.1.3.3.1 Pure PWM force lines

4.1.3.3.1.1 Expression

The main pure PWM lines, obtained by combining a stator fundamental mmf with a PWM harmonic mmf, are summed up in Table 4.11.

In the case of an interseptive PWM with triangular carrier, the harmonics f_n^s can be written as (148):

$$f_n^s = n_1 f_s \pm n_2 f_c \quad \text{where } n_1 \text{ and } n_2 \text{ have an opposite parity} \quad (4.23)$$

where f_c is the chopping frequency. The current harmonics of highest magnitude depend on the carrier type, and on the modulation index. As an example, the main group of current harmonics of motor M1 is $f_c \pm f_s$ and $f_c \pm 2f_s$ due to a forward saw-tooth carrier shape, while it is $2f_c \pm f_s$ on motor M5 on which a classical triangular carrier is used. Furthermore, the magnitude of current harmonics depends on speed (see Fig. 4.15 and (148)): in starting phase, the group $2f_c \pm f_s$ dominates on motor M5, whereas at maximum speed, it is the group $f_c \pm 2f_s$.

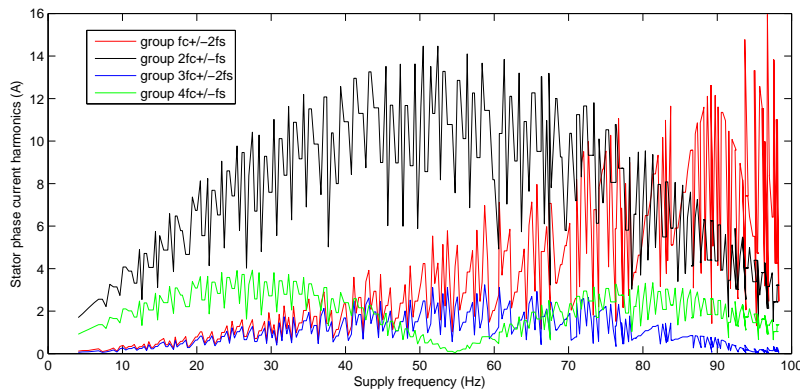


Figure 4.15: Experimental stator current harmonic groups magnitude in function of supply frequency (motor M5, asynchronous PWM with triangular carrier, $f_c = 1280$ Hz).

However, PWM magnetic noise is only annoying at low speed when the aerodynamic noise is lower. In the asynchronous case with a triangular carrier, the noisiest PWM lines can therefore be characterised by Table 4.12.

	Group 1 ($2f_c \pm f_s$)		Group 3 ($4f_c \pm f_s$)		Group 0 ($f_c \pm 2f_s$)		Group 2 ($3f_c \pm 2f_s$)	
	m	f	m	f	m	f	m	f
F_{pwm}^+	$2f_c - 2f_s$	$-2p$	$4f_c - 2f_s$	$-2p$	$f_c + f_s$	$-2p$	$3f_c + f_s$	$-2p$
F_{pwm}^-	$2f_c$	0	$4f_c$	0	$f_c + 3f_s$	0	$3f_c + 3f_s$	0
F_{pwm}^-	$2f_c$	0	$4f_c$	0	$f_c - 3f_s$	0	$3f_c - 3f_s$	0
F_{pwm}^+	$2f_c + 2f_s$	$2p$	$4f_c + 2f_s$	$2p$	$f_c - f_s$	$2p$	$3f_c - f_s$	$2p$

Table 4.12: Highest pure PWM force lines expression (frequency f , spatial order m) in asynchronous case (triangular carrier, case of motor M2 to M7). Groups 0 to 3 stand for current harmonics groups identified in Fig 4.15.

The expressions of these lines are obtained by replacing $\eta_s f_n^s$ of Table 4.11 by the corresponding current harmonics. One must be aware of the propagation direction of the mmf waves η_s : in the same way that the propagation direction of a space harmonic mmf depends on the space harmonic number (cf. Table 4.2 and Fig. 4.3), the travelling direction of a time harmonic mmf depends on the frequency (see Fig. 4.16).

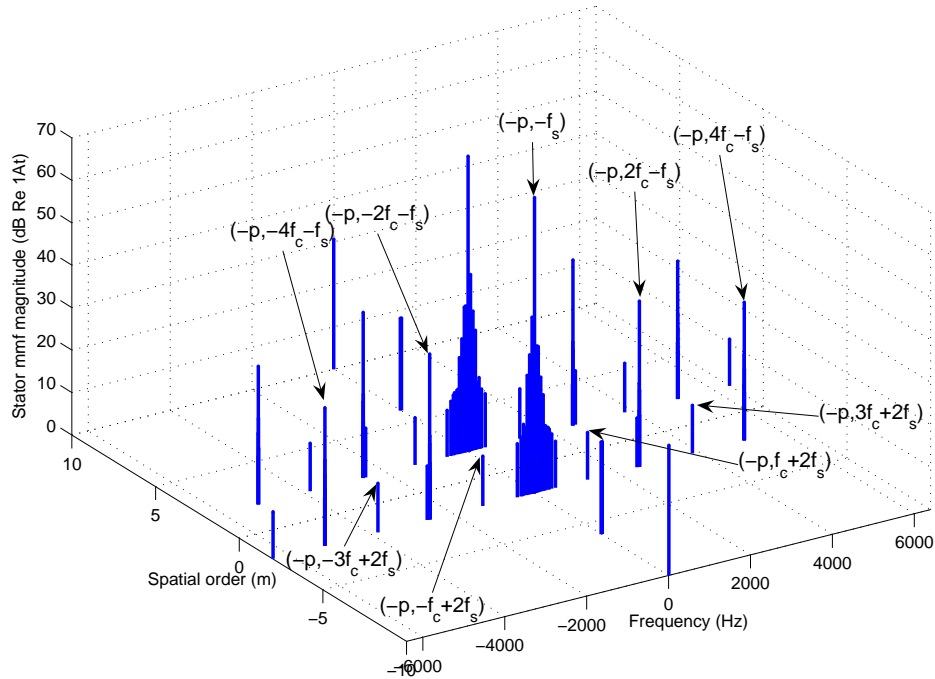


Figure 4.16: Complex FFT of shorted-pitch motor M2 stator mmf in asynchronous PWM case ($f_s = 50$ Hz, $f_c = 1280$ Hz).

For instance, to find the PWM force lines associated to the group 1 of current harmonics of frequencies $2f_c \pm f_s$, the PWM harmonic stator mmf F_s to take are $(-p, -2f_c - f_s) = (p, 2f_c + f_s)$ and $(-p, 2f_c - f_s) = (p, -2f_c + f_s)$.

In the case of a triangular carrier, the highest pure PWM lines are therefore centred around twice the switching frequency. It is different for a saw-tooth carrier as (case of motor M1), where the main asynchronous PWM current harmonic group is centred around the the switching frequency at frequencies $f_c \pm f_s$ and $f_c \pm 3f_s$ (see Table 4.13).

	Group 1 ($f_c \pm f_s$)		Group 2 ($f_c \pm 2f_s$)	
	m	f	m	f
F_{pwm}^+	$f_c - 2f_s$	$-2p$	$f_c - f_s$	$2p$
F_{pwm}^-	f_c	0	$f_c - 3f_s$	0
F_{pwm}^-	f_c	0	$f_c + 3f_s$	0
F_{pwm}^+	$f_c + 2f_s$	$2p$	$f_c + f_s$	$-2p$

Table 4.13: Highest pure PWM force lines expression (frequency f , spatial order m) in asynchronous PWM case (saw-tooth carrier, case of motor M1). Groups 1 and 2 stand for main PWM current harmonics at frequencies $f_c \pm 1, 2f_s$.

4.1.3.3.1.2 Validation

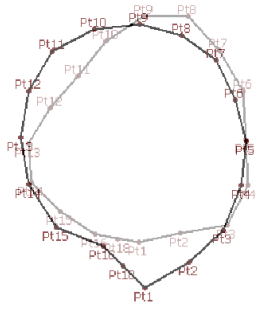
All the harmonic groups of Table 4.12 were observed in the experimental data of motor M5 which has been presented in the previous chapter. As an example, in Fig. 3.44, the three lines number 1 around $2f_c = 2580$ Hz correspond to the group number 1 of PWM force lines characterised in Table 4.12. In a same way, the four lines number 2 around $3f_c = 3840$ Hz correspond to the group number 2 of PWM force lines, and the three lines number 3 around $4f_c = 5120$ He correspond to the group number 3.

The spatial orders, frequency and propagation direction of various pure PWM lines have also been checked on motor M1 during an ODS analysis (29) (Fig. 4.17). For instance, the vibration waves of Table 4.13 at $f_c \pm f_s$ have a spatial order of 4, and should rotate in opposite directions, which can be observed in Fig. 4.17.

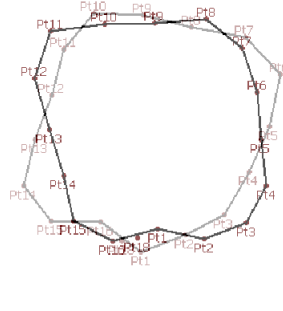
The fact that pure PWM vibration lines have only 0 or $2p$ spatial orders has also been checked by measuring a spectrogram at fixed supply frequency, but sweeping the switching frequency from 2.5 kHz to 10 kHz in order to see if the 0 and 4 circumferential modes around 11kHz and 14 kHz excited (see Fig. 4.18).

4.1.3.3.1.3 Influence of current magnitude

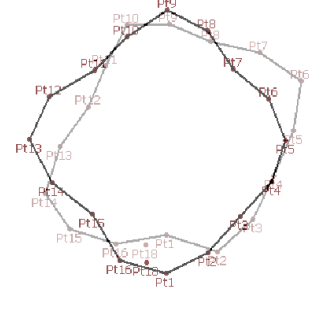
As the pure PWM force harmonics are proportional to the stator fundamental current I_1^0 and a stator harmonic current I_1^n , the effect of a current change from I_1^0 to $I_1^{0'}$ on the pure PWM



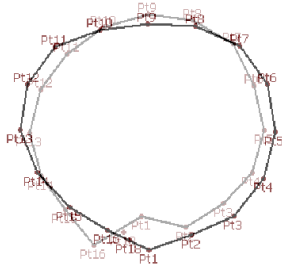
$$f = f_c - 3f_s, m = 0$$



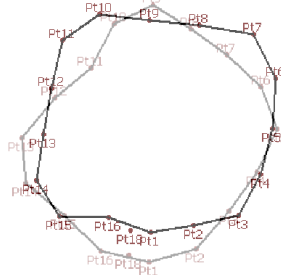
$$f = f_c - 2f_s, m = -2p, \text{c.c. r.}$$



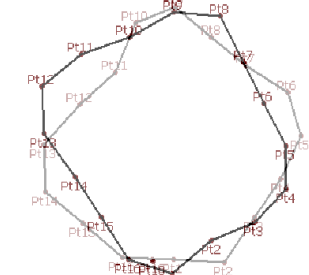
$$f = f_c - f_s, m = 2p, \text{c. r.}$$



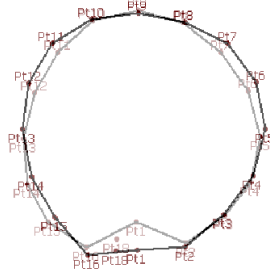
$$f = f_c, m = 0$$



$$f = f_c + f_s, m = -2p, \text{c.c. r.}$$



$$f = f_c + 2f_s, m = 2p, \text{c. r.}$$



$$f = f_c + 3f_s, m = 0$$

Figure 4.17: Pure PWM vibration waves (motor M1, $f_c=4$ kHz), and their propagation direction (c.c. r.: counter-clockwise rotation, c. r.: clockwise rotation).

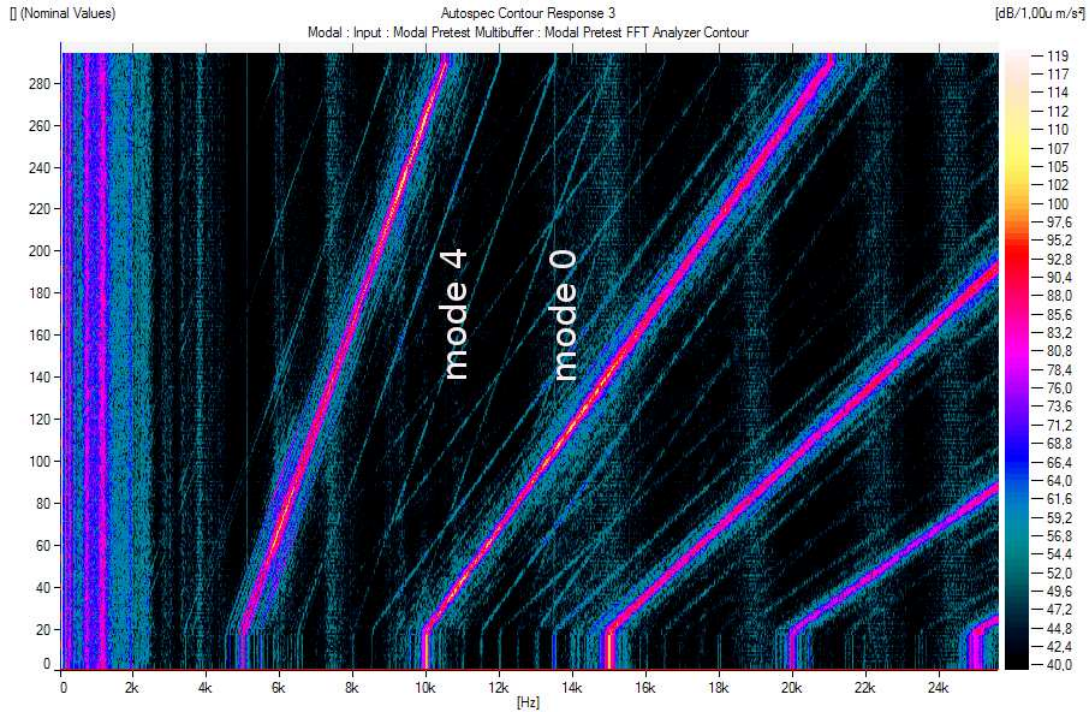


Figure 4.18: Measured spectrogram sweeping the switching frequency from 2.5 kHz to 10 kHz (motor M1, $f_s = 50$ Hz).

noise is given by

$$\Delta L_w^{pwm} = 20 \log_{10} \left(\frac{I_1^{0'}}{I_1^0} \right) \quad (4.24)$$

A harmonic current change from I_1^n to $I_1^{n'}$ causes a noise change of

$$\Delta L_w^{pwm} = 20 \log_{10} \left(\frac{I_1^{n'}}{I_1^n} \right) \quad (4.25)$$

These expressions are useful when post-processing some experimental data in order to properly compare two spectrograms, or remove the effect of a current magnitude change as done in next section.

4.1.3.3.1.4 Influence of phase angle

The phase angle of fundamental current has a high influence on the pure PWM vibration line magnitude at frequency $2f_c$ in the case of a triangular carrier, and f_c in the case of a sawtooth carrier. Indeed, in the example of motor M5, this vibration results from the addition of two vibration waves (cf. Table 4.12), each one resulting from the interaction of the fundamental current and a PWM current harmonic at frequency $2f_c + f_s$ or $2f_c - f_s$. In the electrical equivalent circuit, PWM current harmonics phase angle do not depend on fundamental slip (when considering high frequency harmonics, the resistance R_2^n/s_{mn} is close to R_2^n as $s_{mn} \approx 1$). On the contrary, the fundamental current phase angle highly depends on slip s . This fact

is illustrated by simulations of Fig. 4.19, where the magnitude of the force line at twice the switching frequency significantly changes with slip.

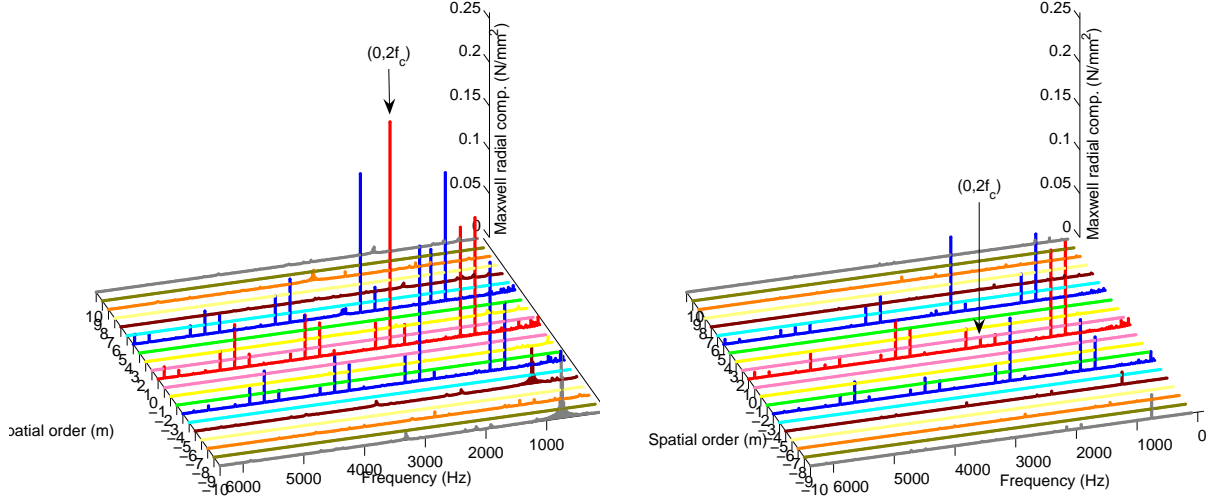


Figure 4.19: 2D FFT of motor M5 magnetic radial force for $s \approx 1\%$ (left) and $s = 0$ (right) in on-load asynchronous PWM case ($f_c = 1280$ Hz, $f_s = 40$ Hz).

This fact was confirmed during experiments. The sound pressure level has been measured varying the output torque from 200 to 2000 Nm near $f_s = 40$ Hz (as slip varies, the speed slightly changed from 1290 rpm to 1230 rpm). As a consequence, the phase current increased from 180 to 600 A, whereas the PWM current harmonics magnitude at $2f_c \pm f_s$ frequencies remained unchanged. According to equation (4.24), the sound pressure level of line $2f_c$ should have increase with the increasing current I_1^0 : on the contrary, it decreased of 2 dB. However, this noise level must be corrected in order to delete the effect of the increasing fundamental current magnitude, by computing

$$L'_p(t) = L_p(t) - 20 \log_{10} \left(\frac{I_1^0(t)}{I_1^0(0)} \right) \quad (4.26)$$

where L'_p is the sound pressure level of the PWM line assuming that the fundamental phase current I_1^0 remains constant, and L_p is the measured sound pressure level evolution with time, when progressively increasing the load. The graph of L'_p is displayed in Fig. 4.20: we can see that a 25 dB change occurs.

This fact shows that independently of the stator current spectrum, the load can have a great influence on PWM noise through the stator current harmonics phase angles. It was already known that the ICE norm is not realistic enough as it applies in sinusoidal no-load case, although PWM noise clearly dominates slotting noise at low speeds ; it is now also clear that acoustic measurements in PWM no-load case are not representative of the motor acoustic noise radiation in its real running conditions.

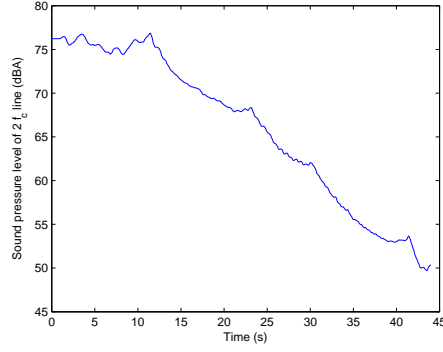


Figure 4.20: Evolution of the pure PWM acoustic line of frequency $2f_c = 2560$ Hz when progressively increasing the load at constant fundamental stator current.

Noise limits should therefore be specified in on-load PWM conditions, following the motor traction characteristics in order to "simulate" during the acoustic measurements the motor real starting phase conditions speed by speed.

4.1.3.3.2 Slotting PWM force lines

4.1.3.3.2.1 Expression

The same analysis was carried the lines resulting from the combination of a PWM harmonic mmf wave (p, f_n^s) , with the fundamental stator mmf wave (p, f_s) and the slotting permeance harmonics $P_s P_r$ (29). This group of force lines, that we here call slotting PWM lines, is characterised in Table 4.14.

	Frequency f	Spatial order m
$F_{slotpwm}^-$	$f_s(k_r Z_r(1-s)/p - 1) - \eta_s f_n^s$	$k_r Z_r - k_s Z_s - 2p$
$F_{slotpwm}$	$f_s(k_r Z_r(1-s)/p \pm 1) + \pm \eta_s f_n^s$	$k_r Z_r - k_s Z_s$
$F_{slotpwm}^+$	$f_s(k_r Z_r(1-s)/p + 1) + \eta_s f_n^s$	$k_r Z_r - k_s Z_s + 2p$

Table 4.14: Slotting PWM force lines expression.

Table 4.15 shows the expression of motor M1 main slotting PWM lines of order 2, $F_{slotpwm}^+$, due to stator current harmonics $f_c \pm f_s$ and $f_c \pm 2f_s$ with $k_r = k_s = 1$. We can see that these slotting PWM lines have the same spatial orders than the pure slotting lines, but occur at higher frequencies. On motor M1, an important slotting line of order 2 has been previously characterised, and it was shown that it was not noisy as the motor elliptical mode was much higher in frequency, near 2400 Hz. When feeding the motor with PWM, according to the switching frequency, the slotting PWM lines of Table 4.15 can easily resonate with the stator in starting phase.

In Fig. 4.21 are displayed the evolution of these slotting PWM lines running the motor M1 from 0 to 80 Hz for a switching frequency of 1600 Hz. We can see that if the motor

Frequency f	Spatial order m
$f_c - f_s(Z_r(1-s)/p + 2)$	2
$f_c - f_s(Z_r(1-s)/p + 1)$	2
$f_c + f_s(Z_r(1-s)/p + 1)$	-2
$f_c + f_s(Z_r(1-s)/p + 2)$	-2

Table 4.15: Characterisation of some M1 motor slotting PWM force lines.

elliptical mode lies between 600 and 2600 Hz, which is the case, the slotting PWM harmonics will be noisy. This resonance was clearly experimented during the tests run on motor M1 (see spectrogram of Fig. 4.22).

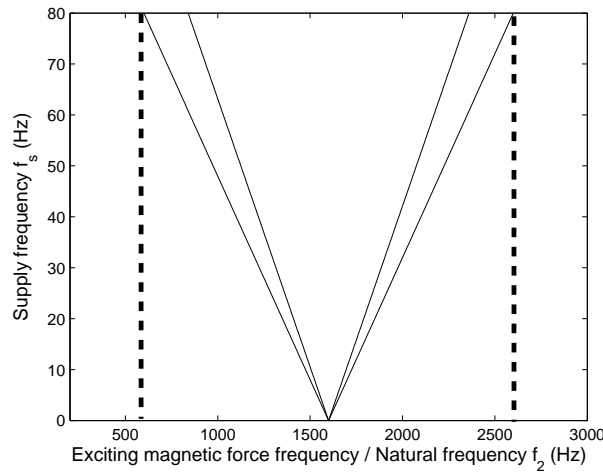


Figure 4.21: Frequency shift of main slotting PWM lines of motor M1 during starting phase in PWM asynchronous case ($f_c = 1600$ Hz).

4.1.3.3.2 Validation

In order to check the validity of slotting PWM lines expression of Table 4.15, and ODS has been run on motor M1. Results are displayed in Fig. 4.23: the spatial order, the frequency and the propagation direction of the vibration waves all match the analytical predictions.

Some spectrograms have also been measured at fixed supply frequency, changing the switching frequency from 1 to 6 kHz in order to identify the vibration lines that were linked to the PWM supply. Results are displayed in Fig. 4.24, where the four slotting PWM vibration lines of Table 4.15 appear, and resonate with the elliptical mode of the stator near 2400 Hz. The pure PWM lines in the middle of the slotting PWM lines can also be observed.

Some slotting PWM lines have also been observed during motor M5 tests. The first group of slotting PWM harmonics, given for $f_n^s = 2f_c \pm f_s$, is presented in Table 4.16.

These groups of lines clearly appear in experiments (cf. groups number 4a and 4b in Fig. 3.44, and lines in spectrogram of Fig. 4.25).

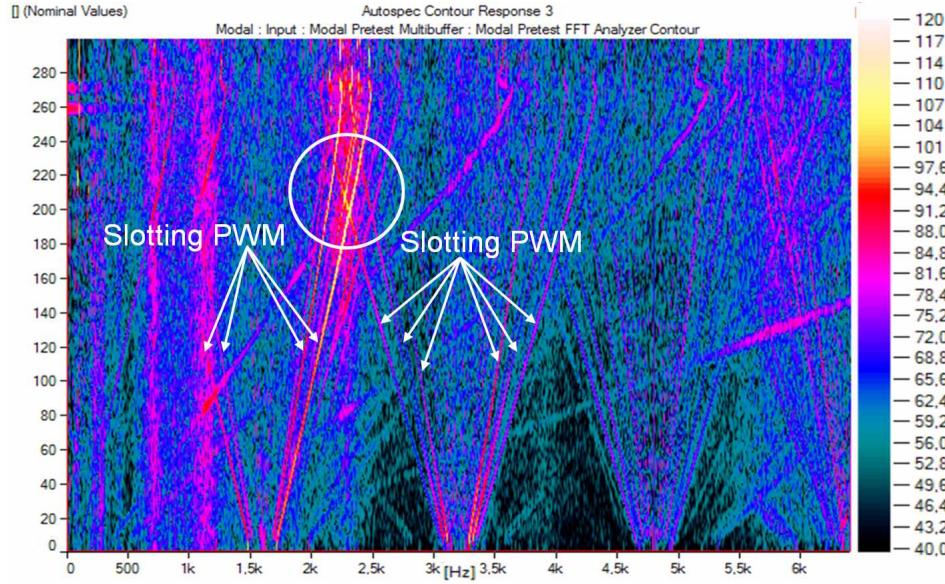


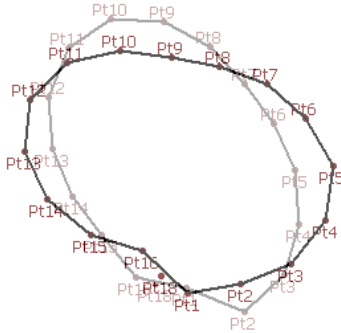
Figure 4.22: Experimental spectrogram measured on motor M1 from $f_s = 0$ to 70 Hz in PWM asynchronous case ($f_c = 1600$ Hz).



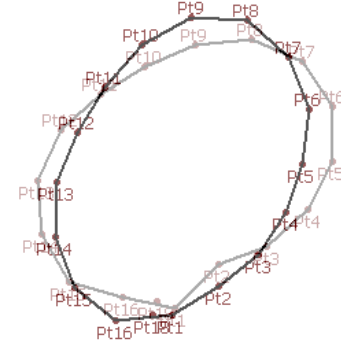
$$f = f_c - f_s(Z_r(1-s)/p + 2), m = 2, \text{ c. c. r.}$$



$$f = f_c - f_s(Z_r(1-s)/p + 1), m = 2, \text{ c. c. r.}$$



$$f = f_c + f_s(Z_r(1-s)/p - 1), m = -2, \text{ c. r.}$$



$$f = f_c + f_s(Z_r(1-s)/p + 2), m = -2, \text{ c. r.}$$

Figure 4.23: Slotting PWM vibration waves (motor M1, $f_c=4$ kHz), and their propagation direction (c.c. r.: counter-clockwise rotation, c. r.: clockwise rotation).

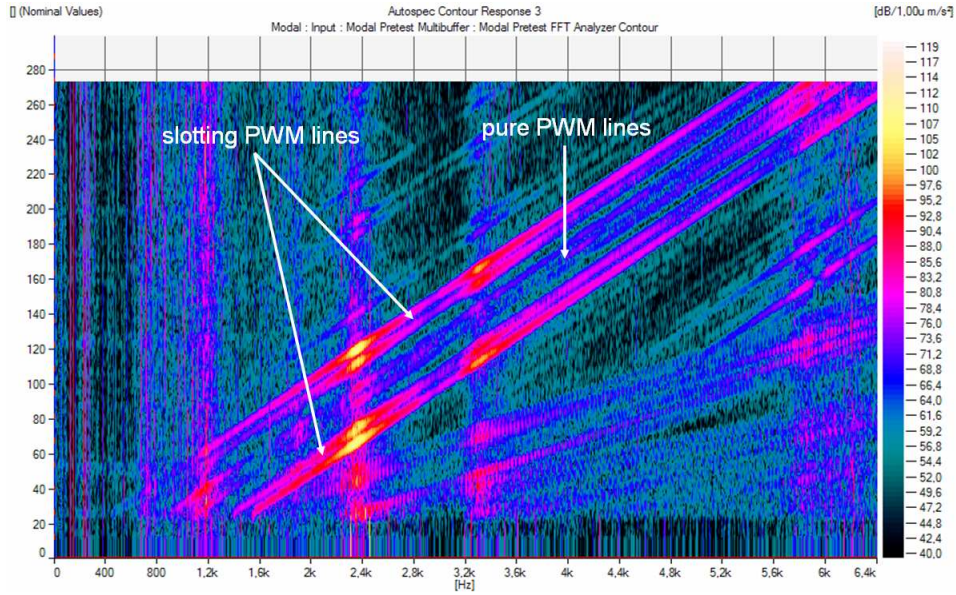


Figure 4.24: Experimental spectrogram measured on motor M1 from $f_c = 1$ to 6 kHz in PWM asynchronous case ($f_s = 50$ Hz).

Frequency f	Spatial order m
$2f_c \pm f_s(Z_r(1-s)/p - 3)$	$Z_s - Z_r + 2p$
$2f_c \pm f_s(Z_r(1-s)/p - 1)$	$Z_s - Z_r$
$2f_c \pm f_s(Z_r(1-s)/p + 1)$	$Z_s - Z_r$
$2f_c \pm f_s(Z_r(1-s)/p + 3)$	$Z_s - Z_r - 2p$

Table 4.16: Characterisation of some M5 motor slotting PWM force lines.

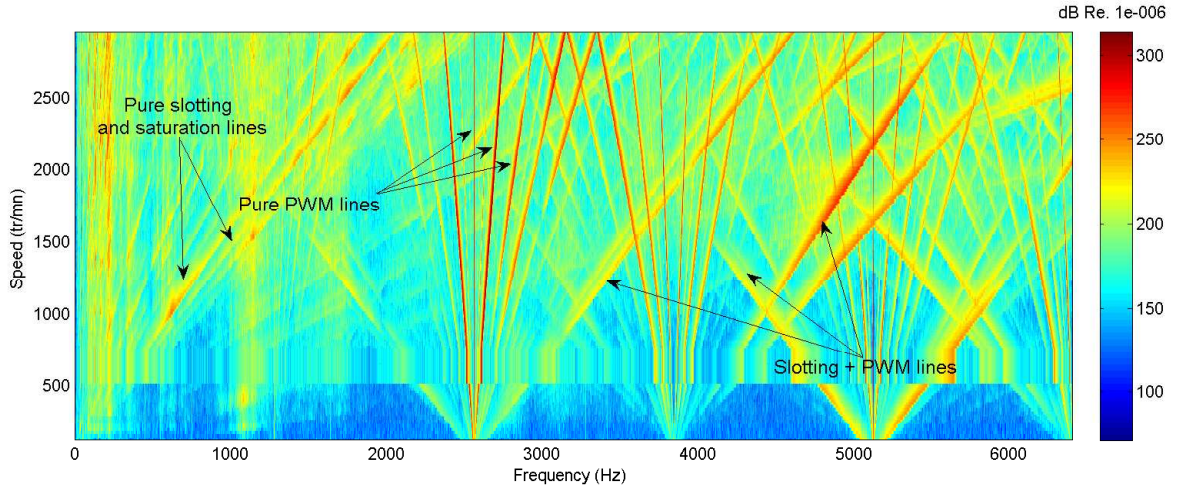


Figure 4.25: Experimental spectrogram measured on motor M5 in asynchronous PWM no-load case ($f_c = 1280$ Hz).

4.1.4 Expression of main magnetic lines magnitude

In this part are detailed the expressions of the magnitude of main magnetic lines identified in previous section (slotting, PWM and slotting PWM). Such expressions are useful to determine

whether pure PWM noise is greater than slotting noise (in term of magnitude, independently of their spatial order).

The pure slotting force line F_{13} magnitude (cf. Table C.3) is given by

$$F_{slot} = \frac{P_s P_r I_1^{02} N_s^2}{2\mu_0} \quad (4.27)$$

where N_s is the magnitude of the fundamental stator mmf wave divided by stator phase current magnitude. N_s can be expressed analytically with

$$N_s = \frac{q_s n_s k_{w0}^s}{\pi p} \quad (4.28)$$

where k_{w0}^s is the fundamental stator winding distribution factor, n_s the number of turns in series per phase, and q_s the number of stator phases. P_s and P_r can also be expressed analytically from the Fourier transform of permeance function (36):

$$P_r = 2 \frac{\mu_0}{K_s} A^r \frac{\sin(\pi s l_r k_{r0})}{2k_{r0}} \quad P_s = 2 \frac{\mu_0}{K_s} A^s \frac{\sin(\pi s l_s k_{s0})}{2k_{s0}} \quad (4.29)$$

assuming that the pure slotting line is linked to the terms k_{s0} and k_{r0} of the permeance Fourier series development. The coefficients A^s and A^r are given by

$$A^s = \frac{2d_s^f}{\pi g_M g^r} \left(1 + \left(1 + \frac{g_M}{g} \right) \frac{d_r^f s l_r}{g^s} \right) \quad A^r = \frac{2d_r^f}{\pi g_M g^s} \left(1 + \left(1 + \frac{g_M}{g} \right) \frac{d_s^f s l_s}{g^r} \right) \quad (4.30)$$

where

$$g_M = g + d_s^f + d_r^f \quad g^s = g + d_s^f \quad g^r = g + d_r^f \quad (4.31)$$

The slotting ratios $s l_s$ and $s l_r$ are given by

$$s l_s = 1 - \frac{b_s}{\tau_s} \quad s l_r = 1 - \frac{b_r}{\tau_r} \quad (4.32)$$

The pure PWM force lines magnitude is

$$F_{pwm} = \frac{P_0^2 I_n I_1^0 N_s^2}{2\mu_0} \quad (4.33)$$

where

$$P_0 = \frac{\mu_0}{g_M K_s} \left(1 + \frac{d_s^f s l_s}{g^r} + \frac{d_r^f s l_r}{g^s} + \left(1 + \frac{g_M}{g} \right) \frac{d_s^f s l_s}{g^r} \frac{d_r^f s l_r}{g^s} \right) \quad (4.34)$$

The term P_0 follows the inequality

$$\frac{\mu_0}{g_M K_s} < P_0 < \frac{\mu_0}{g K_s} \quad (4.35)$$

Therefore, a slotting force harmonic is equivalent in terms of magnitude to a pure PWM force harmonic generated by the harmonic current I_n such as

$$I_n = I_s \frac{P_s P_r}{P_0^2} \quad (4.36)$$

It is also the order of magnitude of the current harmonic to be added in the stator current spectrum in order to cancel the slotting harmonic force in the active noise reduction method (38). Equation (4.36) helps converting a slot ripple into a current ripple, in order to compare both effects. The comparison is distorted by the fact that P_s and P_r terms depend on k_{r0} and k_{s0} which define the slotting force spatial order, and might be different from pure PWM force spatial orders 0 and $2p$. To address this problem, we can imagine that the motor has the same number of stator and rotor slots ($Z_r = Z_s$): this way, the main slotting lines given for $k_{r0} = k_{s0} = 1$ have necessarily orders 0 and $2p$, and the ratio F_{slot}/F_{pwm} gives a good idea of the respective roles of slotting and PWM forces in noise radiation. This comparison only holds for asynchronous mode, because slotting noise can dominate at medium speed (otherwise, magnetic slotting lines have too low frequencies, resulting in a low dBA level).

The slotting PWM force line magnitude is given by

$$F_{slotpwm} = \frac{P_s P_r I_n I_1^0 N_s^2}{2\mu_0} \ll F_{slot}, F_{pwm} \quad (4.37)$$

As an illustration, these magnitudes have been computed for motors M1 and M5, taking for I_n value the largest PWM current harmonic magnitude. The results are displayed in Table 4.17. We can see motor M5 PWM forces magnitude increase from 5 Hz to 50 Hz, because the $2f_c \pm f_s$ current harmonics magnitude with frequency (cf. Fig. 4.15), while the current fundamental remains the same at the beginning of the starting phase (constant flux). Interpreting that table, one must keep in mind that the static deflections magnitude associated to these exciting forces magnitude change according to their spatial orders. As an example, in motor M1 which was proven to be noisy due to slotting PWM lines when $f_c = 1600$ Hz (cf. section 4.1.3.3.2), slotting PWM static deflections of order 2 are nearly 40 times more amplified than pure PWM static deflections of order 0, independently of the exciting force magnitude.

	M1 ($f_s = 50$ Hz)	M5 ($f_s = 50$ Hz)	M5 ($f_s = 5$ Hz)
F_{pwm}	31.0 10^3	61.1 10^3	20.7 10^3
F_{slot}	4.6 10^3	23.7 10^3	23.7 10^3
$F_{slotpwm}$	0.5 10^3	2.3 10^3	0.8 10^3

Table 4.17: Qualitative comparison between different magnetic pressures (N/m²) occurring in motors M1 ($f_c = 1600$ Hz) and M5 ($f_c = 1280$ Hz) in asynchronous PWM case.

4.1.5 Conclusion

A general method has been established in order to analytically derive the frequency, the spatial order, the propagation direction and the magnitude of any magnetic force line coming from the combination of slotting harmonics, saturation harmonics, stator and rotor mmf harmonics, PWM harmonics and eccentricities harmonics. The main magnetic lines (low spatial order, high

magnitude and frequency superior to 400 Hz) characteristics have been detailed and validated using operational deflection shapes, spectrograms and numerical simulations using DIVA which has been extensively validated in previous chapter.

This analytical work can be used to quickly interpret sonagrams and diagnose magnetic problems, but also to infer some low noise design rules as it is going to be done.

4.2 Low-noise design rules

As explained in the introduction, this thesis aims at reducing magnetic noise and vibrations at the design stage, through a better understanding of the noise generation process. Once the main magnetic vibration lines have been analytically derived in terms of frequency, spatial order but also magnitude, some rules to design quieter machines can be inferred (26).

Three main approaches are possible:

1. acting on the response magnitude of the excited structure (e.g. by acting on the motor radiation factor, on its ratio height of yoke to diameter, or by imposing the exciting force to have high spatial orders as done in section 4.2.1)
2. acting on the exciting force magnitude (e.g. by cancelling the slotting force magnitude by a proper choice of the slot openings as done in section 4.2.2, or spreading the PWM forces spectrum as done in section 4.2.3.1)
3. acting on the match between exciting force frequencies and orders and excited structure modes (e.g. by properly choosing the switching frequency as done in section 4.2.3.2, and by properly choosing the rotor slot number)

To reduce magnetic noise in sinusoidal case (slotting and saturation vibrations), the main levers are the number of rotor and stator teeth, and the slot opening widths. In PWM case (pure PWM vibrations), the main levers are the switching frequency value and the type of PWM strategy.

These three approaches can be explored at the same time using an optimisation algorithm, which will be done in section 4.3.

4.2.1 Slot combination

4.2.1.1 Exhaustive search

As seen in section 2.2.1.1.1, many attempts have been made in order to find the slot number combinations leading to low magnetic noise and vibrations ¹. Such rules have however two drawbacks: they do not account for the motor natural frequencies neither its speed range, and they are continuous (e.g. $0.75Z_s \leq Z_r < Z_s$) although the discrete nature of slot numbers implies some discontinuous resonance phenomena.

If some rules can be established, they highly depend on the stator natural frequencies. For instance, motor M1 slot number combination leads to a high magnitude force line of order

¹These rules have been used by some engineers although JORDAN pointed out since 1952 that there were no absolutely good slot combinations, and that the choice should be made "in the knowledge of the magnetic force waves components, the mechanical behaviour of the machine structure and the radiation properties of the machine surface" (166).

2 (cf. section 4.1.3.2.2) which is not noisy at all since the stator elliptical mode has a high natural frequency (near 2400 Hz, cf. section 3.2.1.3). However, using these slot numbers on motor M5 whose elliptical mode is near 600 Hz would have generated a strong resonance near $f_s = f_2/(Z_r/p + 2) \approx 50$ Hz.

Nevertheless, some rules can still be established on specific motor ranges, by making a distinction between small power motors like M1, and medium power motors like M2 to M5. If a new motor is built with similar power, its diameter will be also similar, and its natural frequencies will not shift very much. As noise is evaluated at variable-speed, and magnetic noise is more annoying at low to medium speed, where the magnetic excitation is held constant because the air-gap flux is constant, an error on the natural frequency computation simply shifts the resonance without changing its noise level. The application of the same slot combination rules is then still relevant.

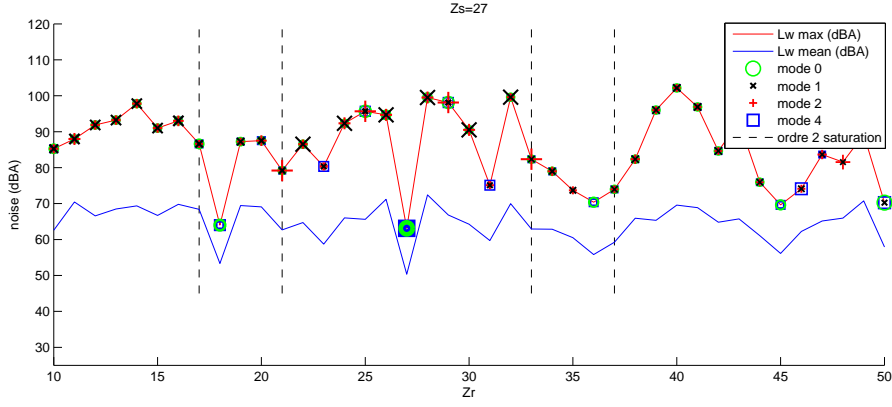
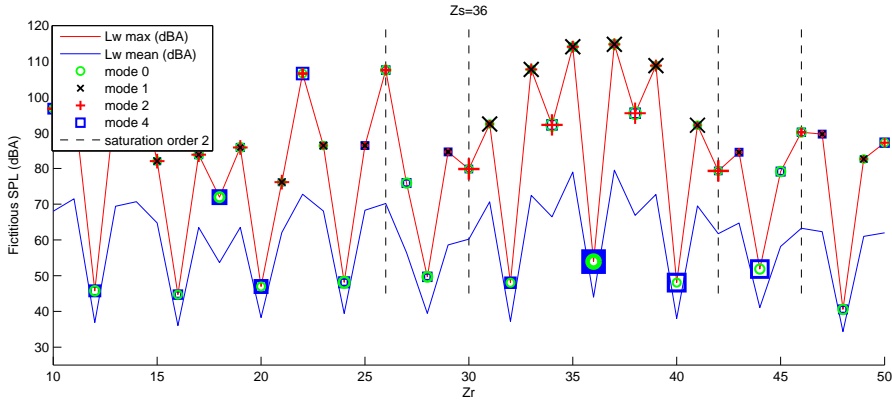
4.2.1.1.1 Realisation of the slot combination database

As DIVA simulation tool is very fast (a few seconds for noise computation at a given speed), all the slot number combinations can exhaustively be tested at variable-speed. A virtual motor has been therefore defined by averaging an ALSTOM motor range, and all the even combinations of Z_s and Z_r have been simulated from 0 to 3500 rpm and for $p = 2$ and $p = 3$, with sinusoidal supply and sinusoidal mmf in order to experiment pure slotting noise. The same analysis has been done on motor M1, but including the odd slot numbers, and running the motor from 0 to 3000 rpm.

In all cases, the stator current has been forced to keep the same peak value, in order to have a magnetic excitation of constant magnitude ($I_1^0 I_1^0 = \text{cstt}$). As seen in equation 4.29, the slotting permeance harmonics magnitude depend on fictitious slot depth $d_{s,r}^f \propto b_{s,r}$ and slotting ratios $sl_{s,r}$. The fictitious slot depths have therefore been forced to a constant value, and the product $Z_r b_r$ and $Z_s b_s$ have also been forced to be constant in order to have a constant slotting ratio (otherwise, increasing the number of slots would have reduced the slot openings, and reduce the magnetic force lines magnitude). This way, the values of the computed average noise and maximum noise levels during starting phase only reflect the effect of the slot combination on the coincidence between the exciting magnetic spatial orders and the stator modes.

An example of the database obtained on motor M1 is displayed in Fig. 4.26 for $Z_s = 27$, $p = 2$, and in Fig. 4.27 for $Z_s = 36$, $p = 2$. In this graphs, the excited modes and their relative magnitude in noise radiation are displayed for each choice of rotor slot number. We can see that mode number 1 is always excited for $Z_s = 27$ as it is an odd slot number, but is only excited for odd Z_r when $Z_s = 36$. The rotor slot numbers that create a main saturation vibration wave of order 2 are been also emphasised in the graphs.

The quietest rotor slot number for $Z_s = 27$, $p = 2$ is therefore $Z_r = 18$ ($Z_r = Z_s$ should be avoided at its creates high synchronous torque pulsations). For $Z_s = 36$, $p = 2$, we can see


 Figure 4.26: Rotor slot number noise database for $Z_s = 27$, $p = 2$ (motor M1).

 Figure 4.27: Rotor slot number noise database for $Z_s = 36$, $p = 2$ (motor M1).

that many rotor slot numbers lead to a low noise level ($Z_r = Z_s \pm 4q$, $q \in \mathbb{Z}^*$). All the other possible combinations are given in the Appendix C.4.

The same database has been built for ALSTOM motors.

4.2.1.1.2 Application

Fig. 4.28 presents the acoustic measurements that were made in no-load sinusoidal case on motor M2, M3 and M4, which have the same stator, during AIT-HAMMOUDA thesis (3) whose conclusions led to motor M4 prototype manufacturing. These tests are compared in Table 4.18 to the noise database results in order to see if it properly predicts the relative noise levels of different slot combinations.

We can see that the database built with DIVA simulations correctly predicts that the 26 rotor slots is quieter than the 28 rotor slots, for which a strong resonance of order 2 occurs because $Z_r - Z_s + 2p = 28 - 36 + 6 = -2$. However, the database predicts that the 44 rotor slots, *independently of the slot shapes, and keeping all other motor parameters constant*, is nearly as noisy as the 28 rotor slots: this is because the 44 rotor slots has also a strong resonance due to

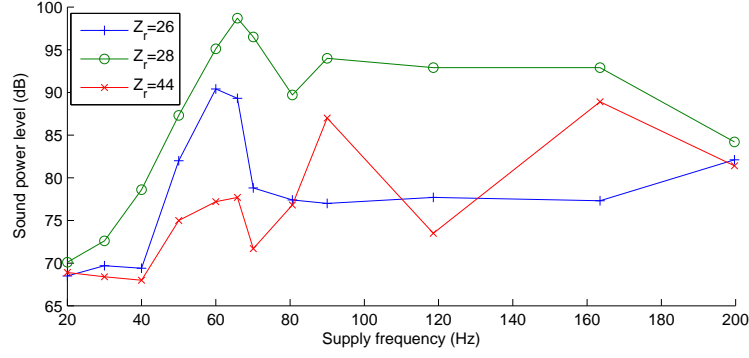


Figure 4.28: Sound power level (dB) measured on motors M2 ($Z_r = 28$), M3 ($Z_r = 26$), M4 ($Z_r = 44$) which share the same stator, but with different rotor slot numbers, rotor slot shapes, and air-gap widths.

	Measurements (SWL in dB)			Database (fictitious SWL in dBA)		
	M2 ($Z_r = 28$)	M3 ($Z_r = 26$)	M4 ($Z_r = 44$)	$Z_r = 28$	$Z_r = 26$	$Z_r = 44$
Average noise	87.7	78.3	76.2	84	74	88
Maximum noise	98.7	90.4	88.9	112	90	110

Table 4.18: Comparison between noise measurements on motors M2, M3 and M4 (having different rotor slot numbers, but also different slot shapes and air-gap widths), and fictitious noise levels simulated on the ALSTOM average motor.

a slotting force of order 2 ($Z_r - Z_s - 2p = 44 - 36 - 6 = 2$)¹.

All the motors M2, M3 and M4 elliptical modes are actually excited: for M2 and M4 it is due to the first ($k_r = k_s = 1$) pure slotting harmonic, whereas for the motor M3, it is the first saturation force harmonic ($k_a = k_r = k_s = 1$) as seen in section 4.1.3.2.3. The resonances of motor M3 and M4 occur at same supply frequencies in no-load case because their exciting force harmonics have same order and same frequency expressions ($f_s(44/3 - 2) = f_s(26/3 + 4)$).

Nevertheless, contrary to the database, the acoustic measurements made on motor M4 show that is much quieter than motor M2. In fact, the difference between motor M2 and M4 does not only come from the rotor slot number as in DIVA database: the M4 motor has a wider air-gap ($g = 1.6$ mm against $g = 1.5$ mm), and some much smaller rotor slot openings ($b_r = 1.5$ mm against $b_r = 3$ mm). The air-gap enlargement reduces in theory the global noise level of $40 \log_{10}(1.6/1.5) \approx 1.12$ dB. To estimate the impact of the slot closures b_s and b_r , the magnitude of main slotting forces F_{13} which is proportional to $A^s A^r$ in equation (4.30) has been drawn in Fig. 4.29.

¹ $Z_r = 44$ is actually the symmetric of $Z_r = 28$ with respect to $Z_s = 36$. If a rotor slot number of the form $Z_r = Z_s + q$ creates a strong magnetic force of order 2, i.e. there exist $\gamma \in [0, 1, -1]$ such as $(Z_s + q) - Z_s + \gamma 2p = q + \gamma 2p = \pm 2$, consequently $-q - \gamma 2p = \mp 2$ and there exist $\gamma' \in [0, 1, -1]$ such as $-q + \gamma' = \pm 2$, which means that the rotor slot number $Z_r = Z_s - q$ is also to avoid.

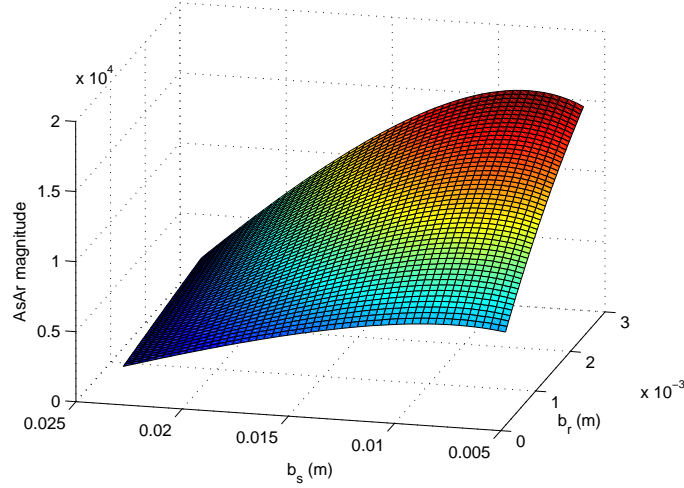


Figure 4.29: Magnitude of main slotting forces in function of stator and rotor slot opening widths b_s and b_r .

We can see that dividing b_r from 3 mm to 1.5 mm nearly reduces the magnitude of slotting forces by a factor 2, which gives a general noise reduction of $20 \log_{10}(2) \approx 6$ dB. It is therefore expected that motor M4 reduces motor M2 noise level at resonance of 7.1 dB (measurements give a 9.8 dB decrease). This shows that even with the worst slot combination ($Z_r \pm Z_s \pm 0, 2p = 2$ on this kind of motor), a motor can still be relatively quiet¹ if the slotting force harmonics magnitude is significantly reduced by acting on the slot closure or the air-gap width. Another factor that reduces the magnitude of magnetic forces when closing the slot openings is the mean flux lines entering the slots (fictitious slot depth): it can get smaller than $b_r/5$, an effect which has not been taken into account in the study of Fig. 4.29. Note that prototype M4 had however a too large slot leakage flux to be industrialised.

This slot combination database is also going to be validated for $Z_s = 48$ and $p = 2$ on the prototype defined in section 4.3.3.1.

4.2.1.2 Special slot numbers

Besides the database, another property of main slotting and saturation force spatial orders m can be used. They can be expressed as

$$m = k_r Z_r - k_s Z_s \pm 2p\gamma \quad (4.38)$$

¹Measurements of Fig. 4.28 were however made with a too low speed resolution to draw firm conclusions. For instance, the critical speed occurs near 90 Hz on motor M4, but contrary to motor M2 and M3, the region was not explored enough in order to measure noise level at resonance.

where $\gamma = 0$ or $\gamma = 1$ for slotting lines, and $\gamma = 2$ for saturation lines. If Z_r is chosen of the form $Z_r = 2pn_r$, where n_r is a positive integer, we get

$$m = k_r 2pm_r - k_s 2pq_s m_s \pm 0, 2p = 2p(k_r m_r - k_s m_s \pm 0, 1) \quad (4.39)$$

Therefore, all the pure slotting lines and saturation lines are proportional to $2p$. If $p = 2$, the main excited stator modes will be its breathing mode and its mode number 4. If $p = 3$, the expected noise reduction is greater, since the only excited modes are 0, 6, 12, etc.

As an example, the simulated sonagram of motor M6 ($p = 2$, $Z_s = 36 = 2p \times 9$, $Z_r = 28 = 2p \times 7$) is shown in Fig. 4.30: its elliptical mode natural frequency near 600 Hz to do not appear at all as no magnetic force of order 2 exist.

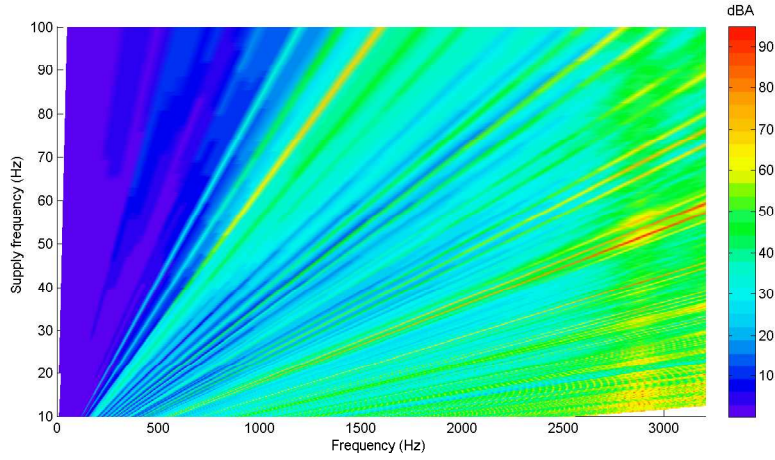


Figure 4.30: Simulated sonagram of motor M6 in sinusoidal no-load case.

This class of motors is however known to generate large synchronous parasitic torques at zero speed (31). In traction motors, these parasitic torques are however much smaller than torque pulsations due to PWM in the starting phase.

4.2.2 Slot openings width

4.2.2.1 Optimal choice

As seen in section 4.2.1.1.2, a wrong choice of slot combination can be limited by decreasing the slotting force magnitude: since $P_s P_r \propto A^s A^r$, it was done by decreasing the product $A^s A^r$, acting on stator and/or rotor slot openings as

$$\lim_{b_{s/r} \rightarrow 0} A^{s/r} = 0 \quad (4.40)$$

However, the product $P_s P_r$ is also proportional to (cf. equation (4.29))

$$P_s P_r \propto \frac{\sin(\pi k_{r0} s l_r)}{k_{r0}} \frac{\sin(\pi k_{s0} s l_s)}{k_{s0}} \quad (4.41)$$

If $sl_r = 0$ or $sl_s = 0$ (no rotor or stator teeth), the slotting harmonic is null. Another way to cancel it is to choose sl_r or sl_s according to¹

$$k_{r0}sl_r = i_0, \quad i_0 \in \mathbb{Z}^* \quad k_{s0}sl_s = j_0, \quad j_0 \in \mathbb{Z}^* \quad (4.42)$$

that is to say

$$b_r = \tau_r \left(1 - \frac{i_0}{k_{r0}}\right), \quad i_0 \in [1, k_{r0} - 1] \quad b_s = \tau_s \left(1 - \frac{j_0}{k_{s0}}\right), \quad j_0 \in [1, k_{s0} - 1] \quad (4.43)$$

The highest slotting force magnitude ($k_{r0} = k_{s0} = 1$) can only be cancelled by removing the teeth ($sl_s = 0$ or $sl_r = 0$) or closing the slots ($sl_s = 1$ or $sl_r = 1$). However, if $k_{s0} \geq 2$ or $k_{r0} \geq 2$, the slotting harmonic can be cancelled according to (4.43). The slot openings value should be chosen as small as possible in order to limit the other slotting harmonics magnitude: for the rotor, it imposes $i_0 = k_{r0} - 1$ which gives

$$b_r^{opt} = \tau_r / k_{r0} \quad (4.44)$$

Note that if b_r is chosen according to (4.44), all the rotor slotting permeance harmonics which are multiple of k_{r0} are cancelled as $sl_r k_{r0}$ is an integer.

In a same way, the smallest possible value gives $b_s = \tau_s / k_{s0}$ for stator slot openings (see Fig. 4.31).

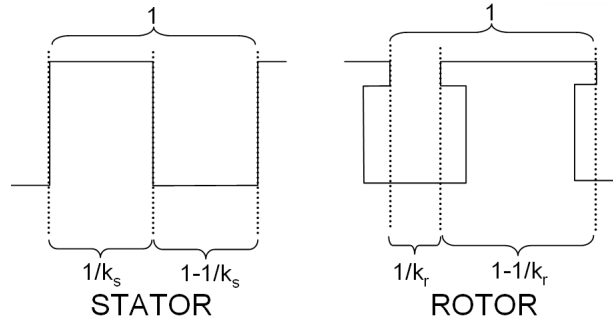


Figure 4.31: Rotor or stator slot opening smallest optimal value to cancel a slotting harmonic linked to integers k_r and k_s .

In the case of rectangular opened stator slots, the choice of their opening width is however more constrained as it has a direct influence on the available space for windings. In general,

¹ P_s is also proportional to $(-1)^{k_s+1} \sin(\pi k_s b_s / \tau_s) / k_s$. This expression is very similar to a light beam complex magnitude diffracted by a network: it is proportional to $\sin(\pi u \epsilon) / u$, where u is the wave vector magnitude, quantified by a wave number when imposing a constructive or destructive interference, and ϵ is the network hole width.

we have nearly as much air as iron in stator slotting, so the optimal value of stator slot should be given by j_0 such as

$$j_0 = \operatorname{argmin}\left\{\left|\frac{j}{k_{s0}} - \frac{1}{2}\right| \mid j \in [1, k_{s0} - 1]\right\} \quad (4.45)$$

If k_{s0} is even ($k_{s0} = 2m_{s0}$), one can easily see that the optimal value of stator slot opening can be reached by $j_0 = m_{s0}$ and gives

$$b_s^{opt} = \tau_s/2 \quad (4.46)$$

If b_s follows equation (4.46), all the stator slotting permeance harmonics with even k_s are cancelled. On the contrary, if k_{s0} is odd ($k_{s0} = 2m_{s0} + 1$), one can see that the two optimal opening width values that give a air/iron ratio the closest from the unity are

$$b_s^{opt1} = \tau_s \frac{m_{s0}}{k_{s0}} \quad b_s^{opt2} = \tau_s \frac{m_{s0} + 1}{k_{s0}} \quad (4.47)$$

Note that the slot opening optimal values are highly sensitive (see for instance Fig. 4.33), and that the theoretical values of the slots openings are modified by saturation effects and manufacturing errors. Moreover, the higher are k_{s0} and k_{r0} , the more there are some choices in the optimal slot openings values, but the lower is the magnetic noise.

The optimal value of b_s must be slightly oversized in order to take into account saturation effects: one can use for instance the analytical formulation of the slot opening increase due to saturation presented in (69).

Note that this technique can also be used to cancel a saturation, a winding or an eccentricity force harmonic as they are all linked with some air-gap reluctance harmonics. The optimal values of b_s and b_r can also be chosen independently in order to cancel two different families of harmonics associated to k_{s0} and k'_{r0} .

4.2.2.2 Application

Motor M7 rotor slot number has been chosen in order to make appear only magnetic force spatial orders proportional to $2p = 4$ (cf. 4.2.1.2). On that motor, the highest slotting lines are $f_s(4Z_r(1-s)/p+2)$ of order $4Z_r - 3Z_s + 2p = 4$, $f_s(4Z_r(1-s)/p-2)$ of order $4Z_r - 3Z_s - 2p = -4$, and $f_s(4Z_r(1-s)/p)$ of order $4Z_r - 3Z_s = 0$. These three slotting lines are linked to the permeance harmonics $k_{s0} = 3$ and $k_{r0} = 4$. They can be cancelled choosing

$$b_r = \tau_r(1 - \frac{i_0}{4}), \quad i_0 \in [1, 2, 3] \Rightarrow b_r = \frac{3}{4}\tau_r, \frac{1}{2}\tau_r, \frac{1}{4}\tau_r \quad (4.48)$$

or

$$b_s = \tau_s(1 - \frac{j_0}{3}), \quad j_0 \in [1, 2] \Rightarrow b_s = \frac{2}{3}\tau_s, \frac{1}{3}\tau_s \quad (4.49)$$

On that motor, $b_r = \frac{1}{4}\tau_r = 6.6$ mm was chosen as the smaller b_r is, the smaller slotting forces are. The initial rotor slot opening on that motor (M5a version) is $b_r = 3.5$ mm: if the

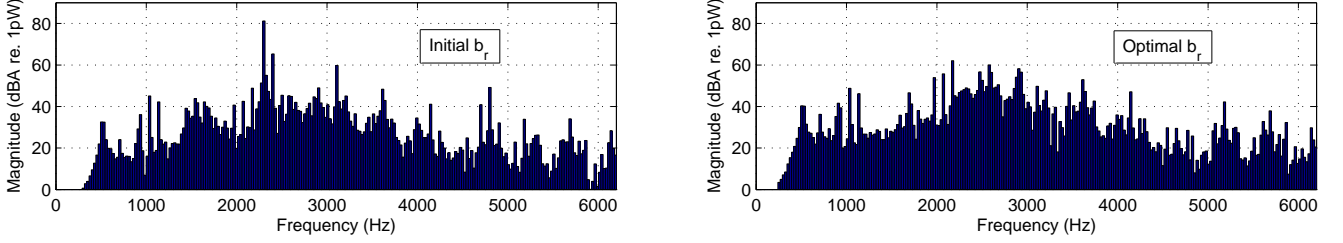


Figure 4.32: A-weighted SWL spectrum at motor M7 mode number 4 resonance ($f_s = 44.2$ Hz), for the initial rotor slot opening value (left) and the optimal value (right).

The sensitivity of the optimal b_r value is illustrated in Fig. 4.33, where the noise associated to the slotting lines $k_{s0} = 3$, $k_{r0} = 4$ has been computed in function of b_r . We can see that a 5% error on the optimal value highers the noise level from 0 to 57 dB, the maximum noise level being 73 dB. Such an error can be relativised as a magnetic noise line inferior to 60 dB may be covered by some higher magnetic lines, or other sources of noise.

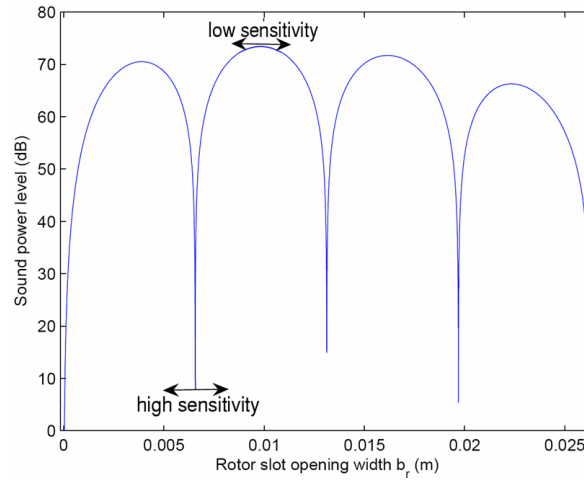


Figure 4.33: SWL radiated by the slotting lines associated to $k_{s0} = 3$ and $k_{r0} = 4$ in function of the rotor slot opening b_r varying from 0 to τ_r (motor M7). The three non zero minima correspond to the three b_r values of equation (4.48).

This technique is also going to be validated on the prototype defined in section 4.3.3.1.

4.2.3 PWM supply

In this part, some rules are proposed in order to limit the audible noise due to pure PWM lines and slotting PWM lines.

4.2.3.1 Psychoacoustic factors

Pure PWM noise is more complex than pure slotting noise: it usually involves several peaks with similar magnitude and frequency, creating a non stationary sound whose quality cannot be easily quantified in an objective way: some psychoacoustic metrics are necessary, such as tonality, roughness, loudness (which accounts for masking effects), and sharpness. KLEMENZ (93) showed in particular that the more important psychoacoustic metrics sizing the pleasantness of PWM noise were tonality (which is also important in slotting noise) and roughness. A global psychoacoustic metric, called annoyance, aggregates all these factors.

In Table 4.12, we can see that in asynchronous case with a symmetrical triangular carrier, some PWM lines occur at frequencies $2f_c$ and $2f_c \pm 2f_s$. In starting phase ($f_s \approx 0$), these lines have close frequencies, and progressively move away from one another as the supply frequency f_s increases: this is this small frequency interval that creates roughness which is measured in aspers. The frequencies $2f_c \pm 2f_s$ are characteristic of a modulation effect, created by the interaction of a high frequency f_h phenomenon with a low frequency $f_l \ll f_h$ phenomenon ($2 \cos(f_h t) \cos(f_l t) = \cos((f_h + f_l)t) + \cos((f_h - f_l)t)$). The term of stridulation, which applies to the typical sound emitted by some insects when they rub one organ to another, can also be used to qualify that particular sound: the entomologists even call the cricket organ with the smaller granularity the carrier.

At the very beginning of starting ($2f_s \leq 10 - 15$ Hz, or $4f_s \leq 10 - 15$ Hz if the line at $2f_c$ magnitude is low in on-load case, as seen in section 4.1.3.3.1.4), these three tones $2f_c$ and $2f_c \pm 2f_s$ appear fused as audible beats. As speed increases, these fused tones start to sound rough. They are then perceived as rough separate tones, and for $2f_s \geq 150$ Hz (or $4f_s \geq 150$ Hz), as smooth separate tones. Roughness is maximal when $2f_s \approx 70$ Hz (170) (or $4f_s \approx 70$ Hz), but it can be significantly decreased by switching frequency modulation strategies (93).

However, when using a random carrier frequency modulation, other psychoacoustic effects appear. A highly random sound (for instance in mixed random modulation techniques (1)) can alter the perception of a smooth motor starting, given by the correlation between the motor supply frequency and the dominant noise frequencies: when slotting noise is still audible when feeding the motor with PWM, the perception of the motor starting is present as slotting lines are proportional to the supply frequency ; however, at the very beginning of the starting phase that is necessarily asynchronous, the passenger cannot hear the motor acceleration because slotting lines have too low frequencies to be audible. If the asynchronous switching frequency

is randomly modulated, this perception of acceleration is far more degraded, and the passenger can feel a bit "disorientated". Traction applications where a synchronous phase follows the asynchronous one do not present such a problem, as PWM lines are then proportional to speed.

Besides that, random sounds can give an impression of motor poor quality (102). The perception of randomness, as well as the perception of a deterministic switching frequency modulation noise, are also strongly influenced by the frequency f_{ch} of the switching frequency change. To sum-up, the most influential parameters of a PWM spread spectrum strategy on noise are:

- the degree of randomness of the switching frequency change, and the correlation of the switching frequency with speed.
- the variation range Δf_c of the switching frequency: in random modulation techniques, a larger interval increases the probability to excite stator natural frequencies¹, but decreases the main PWM exciting forces magnitude. In deterministic modulation techniques as sinusoidal modulation, a large variation of f_c can strongly increase roughness.
- the type of switching frequency distribution in random techniques: discrete (the switching frequency takes its value in a finite set of frequencies) or continuous.
- the shape of switching frequency distribution: gaussian, uniform, etc.
- the rate of change of the switching frequency.

An exhaustive study of the influence of these parameters on the main psychoacoustic factors should be carried to design a novel spread spectrum PWM strategy, but it is not in the scope of this thesis.

4.2.3.2 Choice of the switching frequency

4.2.3.2.1 Pure PWM noise

As seen in sections 4.1.3.3.1 and 4.1.3.3.2, pure PWM lines can resonate with 0 or $2p$ stator modes, whereas combinations between slotting and PWM lines can resonate with any $k_r Z_r - k_s Z_s \pm 0, 2p$ mode. To avoid the first case in asynchronous case, the switching frequency must be chosen so that $2f_c \pm 2f_s, 4f_c \pm 2f_s, \dots$ groups do not meet the natural frequencies f_0 and f_{2p} . On the small motor M1, for which f_0 and f_{2p} are above 11 kHz, a switching frequency inferior to 5 kHz is enough to avoid these pure PWM lines resonances. For motor M5, for which f_0

¹Random modulation techniques have even been used as a way to find the motor natural frequencies (30).

and $f_{2p} = f_4$ are assumed to be close from 2900 Hz according to DIVA computations and FEM simulations (cf. Table 3.4), we should have

$$2f_c + 2f_{max} \ll f_0, f_{2p} \Rightarrow f_c \ll 1350\text{Hz} \quad (4.50)$$

or

$$2f_c - 2f_{max} \gg f_0, f_{2p} \Rightarrow f_c \gg 1550\text{Hz} \quad (4.51)$$

The meaning of \ll can be quantified more precisely using an estimation of the damping coefficient: the gap between the exciting force frequency and the natural frequency should be more than $\xi_m f_m$, which gives 60 Hz for $f_m = 3000$ Hz and $\xi_m = 2\%$. As pure PWM lines at $2f_c \pm 2f_s$ are never alone (all the current PWM subharmonics create other pure PWM lines), the condition $2f_c + 2f_{max} + \xi_m f_m < f_0, f_{2p}$ is certainly not hard enough, and one should use

$$2f_c + 2f_{max} \ll f_{0,2p} - \xi_{0,2p} f_{0,2p} \Rightarrow f_c \ll 1290\text{Hz} \quad (4.52)$$

or

$$2f_c - 2f_{max} \gg f_{0,2p} + \xi_{0,2p} f_{0,2p} \Rightarrow f_c \gg 1610\text{Hz} \quad (4.53)$$

where the use of \gg and \ll should mean at least a 100 Hz gap for a robust design. On motor M5, the current switching frequency $f_c = 1280$ Hz could therefore make pure PWM lines slightly resonate with the stator modes 0 or 4. For other traction motors with $p = 3$, $f_{2p} = f_6$ is much larger than f_0 frequency, and one must also check that the groups $4f_c \pm f_s$ does not match f_{2p} frequency. This design rule is going to be validated during the prototype tests in section 4.3.3.3.4.

4.2.3.2.2 Slotting PWM noise

We saw that on motor M1, the combination of slotting harmonics and PWM harmonics excites the stator elliptical mode during starting when the switching frequency is fixed at $f_c = 1600$ Hz. To avoid this resonance, the switching frequency must be fixed according to

$$f_c - f_{max}(Z_r(1-s)/p + 2) > f_2 \quad \text{or} \quad f_c + f_{max}(Z_r(1-s)/p + 2) < f_2 \quad (4.54)$$

It is better to respect the first inequality, as in the second one, some higher slotting PWM groups (linked to stator current harmonic $2f_c, 3f_c, \dots$) can still resonate with the elliptical mode. For motor M1, the first inequality is equivalent to $f_c \geq 3400$ Hz.

In the general case, one must find the low order slotting PWM line in Table 4.14, and according to the associated k_r value and the type of PWM strategy, the same form of inequalities as in equation (4.54) has to be applied. For motor M5 and for all traction motors, as $f_2 \ll f_c$, slotting PWM lines cannot resonate with the elliptical mode, and the switching frequency should be fixed in priority in order to avoid pure PWM lines resonance.

4.2.3.3 Current injection method

The principle of current injection method consists in adding in the PWM modulating signal a current harmonic which generates an additional magnetic force in counter-phase with a given magnetic force to cancel. Before investigating that method through the Simulink PWM model, some simulations have been run on motor M7 in order to see how an additional current harmonic in the stator phase current spectrum could effectively cancel a given slotting force harmonic.

The acoustic spectrum of motor M7 without any current injection is displayed in Fig. 4.34.

As pointed out in section 4.2.2.1, motor M7 main slotting lines are of order 4 and frequencies $f_s(4Z_r(1-s)/p \pm 2)$. These two lines have been cancelled by injecting respectively the currents

$$I_{n1} = 0.259 \cos(2\pi f_s(4Z_r(1-s)/p + 1)t + 1.375) \quad (4.55)$$

and

$$I_{n2} = 0.23 \cos(2\pi f_s(4Z_r(1-s)/p + 1)t - 0.93) \quad (4.56)$$

The resulting noise spectra are displayed in Fig. 4.35.

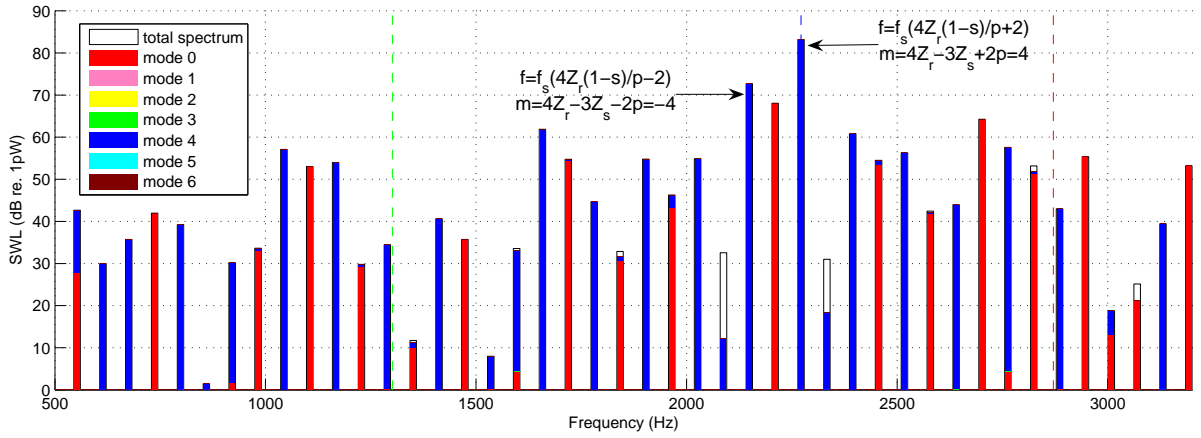


Figure 4.34: Simulated sound power level of motor M7 without current injection (no-load).

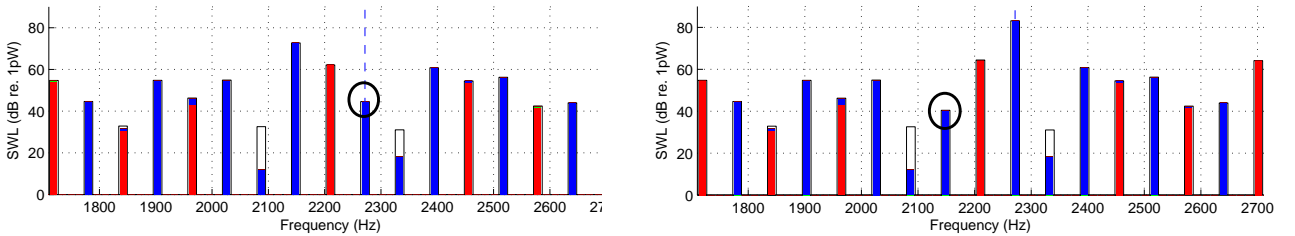


Figure 4.35: Simulated sound power level of motor M7 with current injection, cancelling the slotting force of frequency $f_s(4Z_r(1-s)/p + 2)$ and order 4 (left), and cancelling the slotting force of frequency $f_s(4Z_r(1-s)/p - 2)$ and order 4 (right).

The values of injected currents magnitude and phase angle were obtained by a trial/error method, launching several simulations in order to find which current phase and magnitude

lead to the lowest noise. The theoretical magnitude of injected current can be obtained by comparing the slotting force harmonic to the pure PWM force harmonic resulting from the additional current. The expression of the injected current to cancel a pure slotting force of spatial order $k_r Z_r - k_s Z_s + \gamma 2p$ ($\gamma = 0, -1$ or $+1$) is then :

$$I_n = \frac{\Lambda_{k_r}^r \Lambda_{k_s}^s}{4\Lambda_0^2} I_1^0 \sqrt{2} \cos(2\pi f_s (k_r Z_r (1-s)/p + \gamma) + \phi_i) \quad (4.57)$$

The phase angle ϕ_i cannot be easily expressed because it depends on the permeance harmonics phase angle, and stator mmf phase angle. The analytical expression of equation (4.57) gives a 0.16 A injected current magnitude, to be compared to the 0.23 A magnitude found in simulations. Moreover, the predicted current magnitude should be the same for both magnetic force lines, since they come from the same harmonics interaction. These differences can be explained by the fact that the force lines that we consider here do not only come from the slotting permeance harmonics $k_r = 4, k_s = 3$. For instance the combination $F_s P_0 F_s P_{sr}$ also creates a force line of order 4 and frequency $f_s (Z_r (1-s)/p + 2)$ which interferes with the pure slotting harmonic previously identified, so that a higher magnitude current is necessary to fully decrease the magnetic noise line at that frequency.

When creating this additional current by injecting a current in the PWM modulating signal, the aimed current harmonic correctly appear if the switching frequency is greater than the injected current frequency (38), that is to say

$$f_c \gg f_s (k_r Z_r (1-s)/p \pm 0, 1) \quad (4.58)$$

As annoying slotting magnetic noise appear in the same frequency range than the switching frequency in traction motors, the method is inapplicable. However, another possible way to cancel slotting force harmonics is to make them destructively interfere with pure PWM lines. This idea is more adapted to motors whose slot combinations make only appear spatial orders proportional to $2p$ (cf. section 4.2.1.2 and the example of motor M7). In asynchronous case, the highest pure PWM lines are $(2f_c - 2f_s, -2p)$, $(2f_c, 0)$ and $(2f_c + 2f_s, 2p)$ (cf. Table 4.12). Consequently, fixing the switching frequency as

$$f_c = f_s k_r Z_r (1-s)/(2p) \quad (4.59)$$

makes the frequency and orders of main pure PWM lines match the ones of main slotting harmonics. If the magnitude and phase angle of the first group of PWM current harmonics can be controlled, pure slotting and PWM forces can interfere in a destructive way. In no-load case, on motor M7, the synchronous PWM strategy defined by equation (4.59) gives a switching frequency $f_c = Z_r f_s = 36f_s$.

4.3 Noise minimisation

Once the simulation tool DIVA has been extensively validated on various motors, it can be coupled to an optimisation algorithm in order to find low-noise motors by acting on both the exciting force spectrum (through slot numbers, switching frequency, etc) and the excited structure (through the motor natural frequencies, the radiation factor, etc). Besides the noise minimisation goal, it is important to design motors that are still able to achieve requested traction performances: for instance, a motor with a very large air-gap will easily reach the low magnetic noise objective, but will result in poor efficiency ; similarly, motor M4 prototype has a relatively low magnetic noise, but had too a large slot leakage flux. Multi-objective optimisation techniques are the ideal tool to handle this kind of trade-off that cannot be analytically solved by the engineer.

4.3.1 Optimisation problem

The induction machine optimum design problem can be written as

$$\begin{cases} \min \mathbf{f}(\mathbf{X}) \\ \text{subject to } \mathbf{G}(\mathbf{X}) \leq 0 \end{cases} \quad (4.60)$$

where $\mathbf{f} = (f_1, \dots, f_M)$ is the objective function vector to minimise (magnetic noise, inefficiency, etc), $\mathbf{X} = (X_1, \dots, X_N)$ is the design variable vector (number of slots, switching frequency, etc), and \mathbf{G} is the inequality constraints vector. \mathbf{f} is also called fitness function, even though it is minimised.

4.3.1.1 Objectives

A single variable-speed noise objective function is hard to define, since a motor can have a low average noise level but a high maximum noise level (24). It was thus decided to introduce both the starting average noise level and maximum noise level in the objectives. The other objectives that can be introduced in the optimisation are:

- inefficiency (evaluated at nominal speed, where the motor runs the most)
- weight, material cost
- torque ripple

4.3.1.2 Design variables

There are more than a hundred motor and PWM supply design variables. However, some previous studies (3) have already identified the more influential variables on noise, efficiency and weight using a sensitivity analysis tool based on the evaluation of the model responses

varying the design variables of $\pm 5\%$. This method must however applied with extreme care (20), because

- the model contains some discrete variables, especially Z_r and Z_s which have a strong influence on noise: a $\pm 5\%$ variation of the slot number does not have any sense, and these design variables cannot be included in the sensitivity analysis.
- its conclusions are highly dependent of the initial value of the motor design variables, as it assumes that the model response can be developed in a polynomial function around the initial point (153): in our case, the model response contains some singularities, and some design variable values give a non differentiable noise response (cf. Fig. 4.33 where according to the slot opening value, the noise sensitivity can be very high or close to zero).
- it cannot be applied at a single supply frequency, as the influence on noise highly depends on the supply frequency: at a given speed, increasing the height of yoke can move a natural frequency closer to the exciting force, and increase the noise level ; at an other speed, it can move the natural frequency farther from the exciting force, and decrease the noise level. The sensitivity analysis must therefore be carried at variable speed, considering for instance the maximum and average noise levels during starting as responses.

The choice of the most influential design variables on the optimisation objectives therefore results from an "empirical" knowledge, considering DIVA numerical simulations as experience. For instance, some optimisations with a very high number of variables have been run, and the correlations between design variables and objectives have been quantified by averaging the correlations of all the individuals along all the generations (24): this method gives more accurate results than the sensitivity analysis one, and is also applicable to discrete variables.

The most influential variables on the objectives presented in previous section are summed up in Table 4.19, they involve both continuous variables and integer/discrete variables. The induction machine model considered in optimisations is a squirrel-cage motor with rectangular stator slots, and trapezoidal rotor slots.

4.3.1.3 Constraints

Independently of the optimisation, a full set of geometrical constraints exist. The following additional constraints can be included in the optimisation:

- maximum saturation coefficient
- maximum peak flux densities in rotor/stator teeth, and rotor/stator yokes

Design variables	Description	Type (D:discrete, C:continuous)
h_f	Frame width	C
L_s	Stator stack length	C
D_{so}	Stator stack diameter	C
h_s	Stator height of yoke	C
b_s	Stator slot opening width	C
$H1$	Stator slot isthmus height	C
$H3$	Stator slot depth under wedge	C
Z_s	Stator teeth number	D
n_s	Stator winding number of turns in series per phase	D
Y	Stator winding coil pitch	D
g	air-gap width	C
L_r	Rotor stack length	C
D_{sh}	Rotor shaft diameter	C
b_r	Rotor slot opening width	C
$B5$	Rotor slot small basis	C
$B6$	Rotor slot large basis	C
$H5$	Rotor slot depth under isthmus	C
$H4$	Rotor slot isthmus height	C
Z_r	Rotor teeth number	D
f_c	Asynchronous PWM switching frequency	C

Table 4.19: Main design variables used in the optimisations.

- maximum rotor/stator mean temperatures, when DIVA is coupled to the nodal network (21)
- maximum current densities in rotor/stator slots
- fulfilment of the specified torque/speed curve, which can be written as $\mathbf{T}_{\text{spe}}./\mathbf{T}_{\text{comp}} \leq \mathbf{1}$ ¹ where \mathbf{T}_{spe} is the vector of specified output torque at each speed, and \mathbf{T}_{comp} is the vector of computed output torque at each speed
- improvement of a given industrial design \mathbf{X}_{ref} , written as $\mathbf{f}/\mathbf{f}_{\text{ref}} \leq \mathbf{1}$ where $\mathbf{f}_{\text{ref}} = \mathbf{f}(\mathbf{X}_{\text{ref}})$

4.3.2 Optimisation method

Our optimisation problem is therefore a multi-objective, mixed-variable, constrained optimisation problem. To solve it, the Non Dominated Sorting Genetic Algorithm (NSGA-II) (45)

¹The notations ./ and .* come from Matlab language, they represent some element-wise operators which apply on matrix and vectors. This way, \mathbf{u}/\mathbf{v} is a vector of elements u_i/v_i .

has been chosen. It is based on two main notions: constrained non-domination sorting, and crowding distance.

Non-dominated order ¹ is a generalisation of the natural order of single objective problem, where individuals are simply sorted by decreasing fitness (an individual i dominates j if $f_i < f_j$, in a minimisation problem). When working with several objectives, the optimisation cannot lead to a single best individual, but to a set of "best individuals" called the Pareto front. This set is defined by splitting the population in several ranks (see Fig. 4.36) which are based on the number of individuals that each individual dominates.

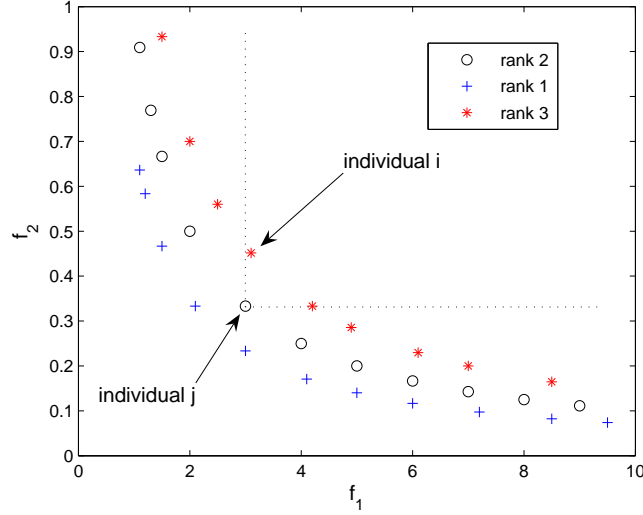


Figure 4.36: Illustration of NSGA ranking method in case of two objectives f_1 and f_2 . Individual j is non-dominated by i if there exist $k \in [1, N]$ such as $f_k^j < f_k^i$, f_k^i denoting the k -th objective function of individual i .

The domination order \succ is defined as:

$$j \succ i \quad (j \text{ dominates } i) \Leftrightarrow f_k(\mathbf{X}_j) \leq f_k(\mathbf{X}_i) \quad \forall k \in [1, M] \quad (4.61)$$

Constraints are then handled by defining a constrained non-domination relation order. A motor design \mathbf{X}_j of fitness \mathbf{f}_j is said to be constraint non-dominated by another design \mathbf{X}_i of fitness \mathbf{f}_i if

1. \mathbf{X}_j is feasible ($\mathbf{G}(\mathbf{X}_j) \leq 0$), and \mathbf{X}_i is not.
2. \mathbf{X}_j and \mathbf{X}_i are both infeasible but \mathbf{X}_j has a smaller overall constraint violation (quantified as the norm of $\mathbf{G}(\mathbf{X})$ positive values).
3. \mathbf{X}_j and \mathbf{X}_i are both feasible and $j \succ i$.

¹It is not an order relation in the mathematical sense: it is a reflexive and transitive binary relation, but it is not antisymmetric as $j \succ i$ and $i \succ i \nRightarrow i = j$.

If some optimisation methods aggregate the objective functions according to some weights fixed by the designer according to the respective importance of the different goals, and therefore lead to a single optimal solution, their main drawback is to not offer any degree of freedom left in order to include design constraints that are not included in the model.

The second notion used in NSGA-II algorithm, crowding distance, permits to uniformly spread the Pareto front individuals in the objective function space. This way, at the end of the optimisation, the designer has a wide set of solutions representing all the possible trade-offs.

NSGA-II algorithm can be summed up by the following steps:

1. *Generate a random population P_0 of size P , sort them using constraint non-domination order and compute their crowding distance.*
2. *Initialize current population $P_n = P_0$.*
3. *Create a mating pool of parents of size $P/2$ from P_n using a standard binary tournament based on Pareto-front ranking and crowding distance.*
4. *Randomly select couples from mating pool and apply bimodal crossover and polynomial mutation operators in order to generate offspring population Q_n of size P .*
5. *Combine current population P_n and offspring Q_n and sort them using constraint non-domination order relation.*
6. *Take the best individuals in terms of constraint non-domination ranking and crowding distance in order to generate new population P_{n+1} of size P .*
7. *Go to step 3. with $P_n = P_{n+1}$.*

The Matlab algorithm NSGA-II has been downloaded on the internet, but it was modified in order to handle mixed design variables by coding some discrete crossover and mutation operators. In addition, the non-domination order relation has been modified to handle constraints. A stochastic repair algorithm has been also implemented in order to "fix" the motor design which do not fulfil the geometrical constraints, making some slight random modifications in repaired individuals in order to maintain diversity.

4.3.3 Application

In this part, the optimisation algorithm is coupled to DIVA in order to design a low-noise motor reaching specified traction characteristics (output torque versus speed curve), without degrading the efficiency. The idea is to improve a given industrialised design (motor M5a) by only acting on the squirrel-cage design, as a stator manufacturing is far more expensive.

4.3.3.1 Rotor optimisation

A first optimisation has been launched on motor M5a rotor, considering the $N = 6$ design variables b_r , $B5$, $B6$, $H5$, $H4$ and Z_r . The $M = 4$ objective functions were the average noise and the maximum noise level, the efficiency and the material cost. Note that material cost is not an unrealistic objective: motor casting raw materials have become significantly more expensive in the last years, and cost reduction constraints weigh traction chains down.

The motor noise was simulated varying f_s from 5 to 105 Hz in no-load case. Some constraints were set on the maximum saturation level and the maximum flux density levels, and another constraint has been added in order to improve the initial design of motor M5a: its fitness \mathbf{f}_{ref} has been computed, and the additional constraint $\mathbf{f} \leq \mathbf{f}_{ref}$ has been set in the constraint vector. This way, all the obtained individuals necessarily improve the magnetic noise level of the current design, as well as its efficiency, and its material cost. The initial population contained $P = 30$ individuals, and was randomly generated 20 % around motor M5a design (apart from rotor slot numbers, which have been randomly generated as even numbers lying between 20 and 80), and NSGA algorithm was run during $G = 100$ generations.

Some typical results of this optimisation process can be found in (21; 22; 24; 27), as well as useful visualisations of the Pareto front multi-dimensional objectives and variables, but the results of this application will not be fully detailed here as they involve confidential ALSTOM motor geometries. As an example, a Pareto front obtained when minimising noise (average noise L_w^m and maximum noise L_w^M), inefficiency ($1/\eta$) and material cost M_c on motor M6 ($Z_s = 36$, $Z_r = 28$, $p = 2$) is displayed in Fig. 4.37 (all the individuals objectives have been projected in 2D for readability purpose, and the industrial design objectives have been marked to quickly see which individuals improve it).

The convexity of these curves are useful to identify the hardest trade-offs to make: for instance, a strong trade-off exists between efficiency and material cost, whereas average and maximum noise can clearly be minimized at the same time. The other projections show more scattered individuals, which means in particular that lowering magnetic noise does not necessarily lead to a higher material cost: indeed, a slight change of Z_r remain material cost unchanged, while it can significantly alter noise radiation.

In this final Pareto front, it is interesting to visualise the design associated to extreme values of objective functions. The lowest and highest average noise individuals are represented in Fig. 4.38. We can see that the motor with $Z_r = 32$ is the noisiest: it creates a large Maxwell force wave of order $Z_s - Z_r - 2p = 2$ which resonates with the ovalization mode of the stator, whose natural frequency is around 800 Hz. The optimisation algorithm has therefore correctly identified the noisiest motors.

In the final Pareto Front set obtained when optimising M5a rotor, the quietest designs (minimum average noise and minimum noise at resonance) were successfully compared to the

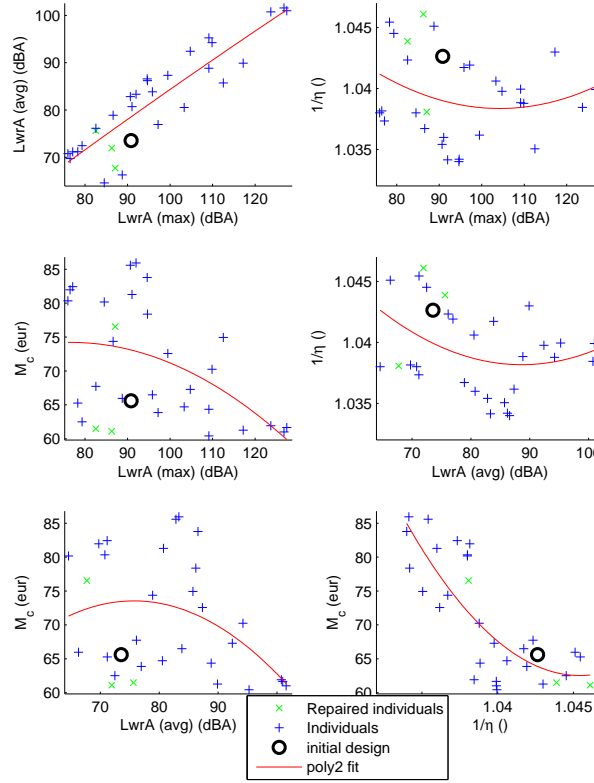


Figure 4.37: Final population (Pareto front) objectives 2-D projections (motor M6 optimisation).

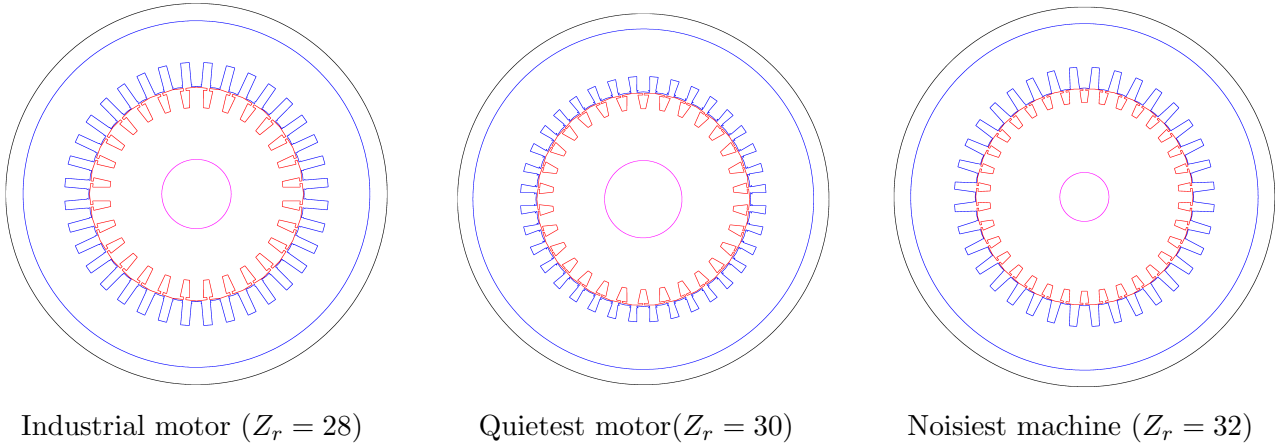


Figure 4.38: Motor sections of different individuals.

rotor slot numbers database for $Z_s = 48$ and $p = 2$. Two designs have been chosen in the final Pareto front as they did fulfil specifications: a motor with a higher number of rotor teeth ($Z_r = 60$, prototype M8), and a motor with a number of rotor teeth close from the original one ($Z_r = 36$, prototype M7). The results of the optimisation were slightly changed in order to fulfil additional mechanical constraints (reuse of motor M5a squirrel-cage rotor bars), and prototype M7 rotor slot opening value was also changed in order to apply the technique exposed in section

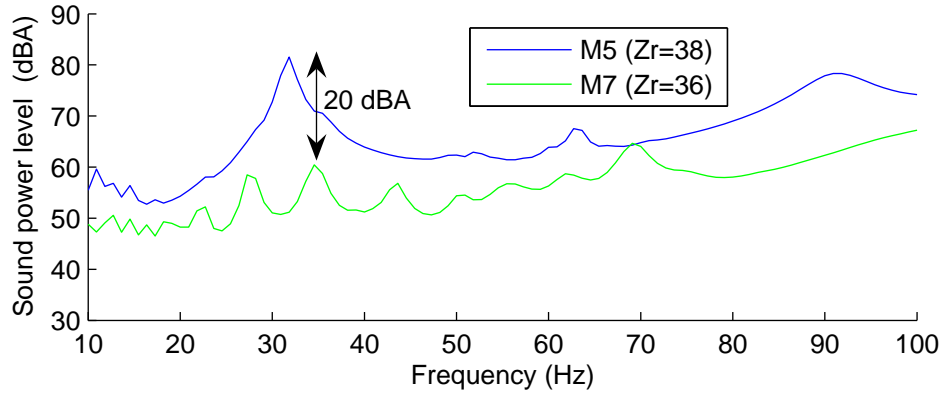


Figure 4.39: DIVA simulation of magnetic noise emitted by industrial motor M5a and prototype M7 during starting phase (no-load sinusoidal case).

4.2.2.1: the optimisation algorithm did not "find" this optimal value of rotor slot opening, as it was out of the design variable bounds.

Following these modifications, some simulations have been run in order to see if the differences between the objective functions of the individual obtained by optimisation and the final definition of the prototype is satisfactory. Prototype M7 has relatively wide rotor slot openings, so a FEM simulation has been run with the electromagnetic software OPERA in order to check if a stator tooth flux density variation with rotor rotation was acceptable: it was found that the variations were not much higher than on the initial motor M5a, and that stator iron losses by flux pulsations should not be higher. The automatic coupling between DIVA and OPERA is detailed in appendix A.4.

According to DIVA simulations, these two prototypes M7 and M8 gave respectively a reduction of 10 and 6 dB on the average noise level, and of 14 and 7 dB on the maximum noise level. At certain speeds, the decrease in magnetic noise in no-load case is expected to reach 20 dB for motor M7 (see Fig. 4.39). These predictions have to be put into perspective, since they only apply to magnetic noise. M7 theoretically gives better results than M8, but it is more risky as it relies on the slot opening optimal choice technique, whose results can be limited by local saturation effects.

4.3.3.2 PWM strategy optimisation

Motor M5a is fed with an asynchronous strategy at 1280 Hz. This default PWM pattern could not be changed, so the only degree of freedom was the switching frequency. On that motor, PWM noise is only due to pure PWM lines which are suspected to excite 0 or $2p = 4$ stator circumferential modes near 2900 Hz (cf. Table 3.4 and section 4.2.3.2.1): as shown in section 4.2.3.2.2, slotting PWM lines do not contribute to the overall PWM noise. As the optimisation focuses on the rotor design, the stator natural frequencies f_0 and f_{2p} are fixed, and including the switching frequency in the optimisation would simply lead to $2f_c \ll f_0, f_{2p}$ or $2f_c \gg f_0, f_{2p}$.

In order to decrease computational time, it was decided not to include the switching frequency in the design variables, and simulate the motor magnetic noise in sinusoidal case. The switching frequency has therefore been optimised "by hand", choosing the switching frequency $f_c = 1000$ Hz which is much inferior to $f_0/2$ and $f_{2p}/2 = f_4/2$ near 1450 Hz. Experiments will prove that this choice significantly limits PWM noise during starting.

4.3.3.3 Experimental validation

M7 rotor prototype is displayed in Fig. 4.40. The experimental set-up is presented in Fig. 4.41: four microphones record some sound pressure levels around the motor, and a clamp-on ammeter measures the motor phase current. These signals are brought to a laptop through a Bruel & Kjaer LAN data acquisition module, and treated with Pulse Labshop: some sonagrams are drawn, as well as a spectrogram of the phase current, the evolution of the sound pressure levels, and of the fundamental phase current.

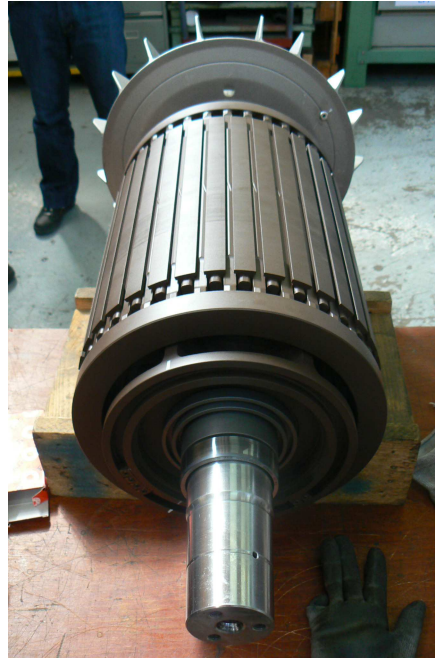


Figure 4.40: Rotor of prototype M7.

4.3.3.3.1 Traction characteristics

A first series of tests have been run in order to check if the motor electrical characteristics were unchanged. Power factor, output power and phase current were measured at several supply frequencies and voltages. The no-load starting phase current was the same (135 A), and the iron losses were even slightly lower than on motor M5a. The on-load behaviour of the prototype was also identical: the output torque 2270 Nm was correctly reached with the same current level (600 A).

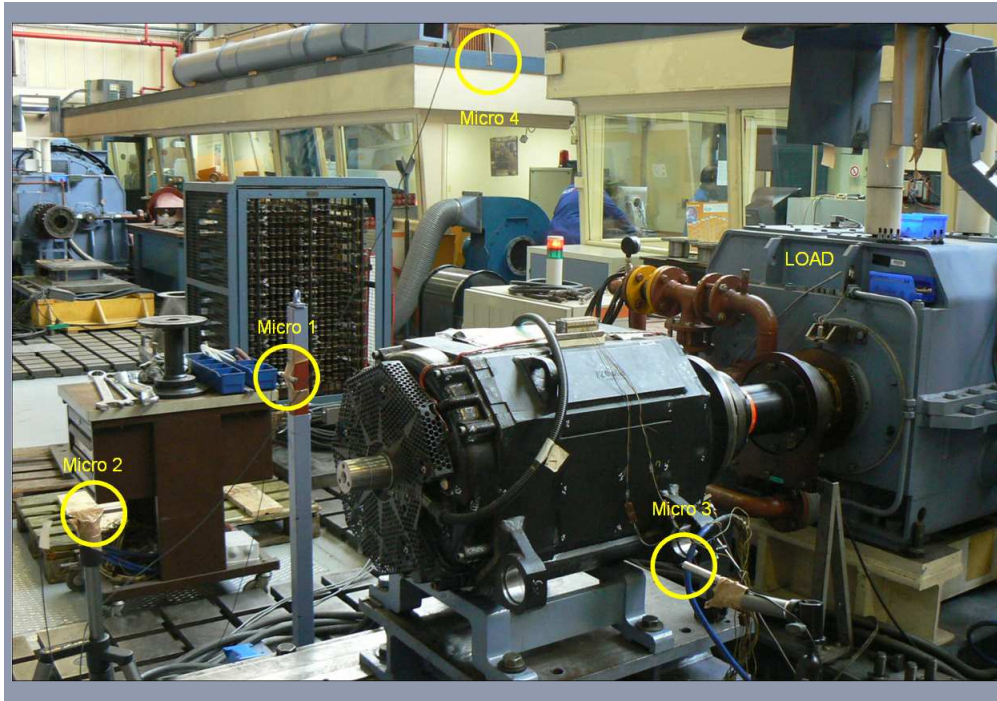


Figure 4.41: Experimental set-up.

4.3.3.3.2 No-load sinusoidal tests

In order to be able to compare the new prototype M7 noise to the industrialised motor M5a and its skewed version M5 noise, the same running conditions and noise measurements have been followed: the same current level (138 A) has been imposed at several speeds, giving the maximal air-gap flux $E_0/f_s = 4.32$, and the sound pressure level has been recorded at 1 m of the center of the motor right side. The same microphone used in previous tests on M5a and M5 has also been used to ensure the most valid comparison.

Results are displayed in Fig. 4.42. We can see that the prototype noise level is nearly linear with speed: during the tests, this was especially striking as it seemed that only the aerodynamic noise was measured.

No resonance occurred, contrary to motors M5a and M5. Near $f_s = 35$ Hz, a 15 dB decrease on global noise is obtained compared to the industrialised motor, whereas a 20 dB decrease on magnetic noise was predicted by simulation (cf. Fig. 4.39)¹: assuming that the aerodynamic noise increases the magnetic noise level of 5 dB at that speed, the correlation between simulation and experiments is excellent, although motor M5a resonance is due to a saturation harmonic of order 2 (cf. 4.1.3.2.3). This resonance of stator elliptical mode is limited by the use of a skewed rotor (motor M5), but skewing makes another noise peak appear near 50 Hz, which is especially harmful in on-load case (see Fig. 4.43) as it corresponds to a modal excitation (cf.

¹DIVA results are given in sound power L_w , whereas experiments are given in sound pressure L_p . However, a variation of sound power ΔL_w equals its variation in sound pressure ΔL_p .

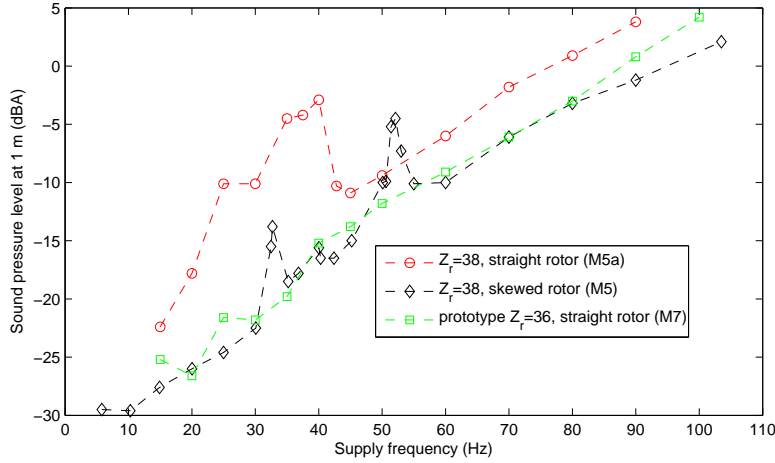


Figure 4.42: Sound pressure level of prototype M7, compared to the industrialised motor M5a, and its skewed rotor version M5 (sinusoidal no-load case).

4.1.3.2.3.3).

The new rotor has all the advantages of the skewed one (low radial magnetic forces), but without its drawbacks (excitation of stator longitudinal modes, high saturation levels due to "uncompensated" or "skewing" mmf (31), reduced magnetisation inductance and additional leakage inductance). Note that the prototype also generates a relatively high magnitude saturation wave of order 4 ($Z_r - Z_s + 4p = 36 - 48 + 8 = -4$). However, it only resonates with mode 4 near $f_s = f_4/(Z_r/p + 4) \approx 3000/32 \approx 140$ Hz which is superior to $f_{max} = 105$ Hz: even with a higher flux, the experiments showed that it was hardly visible in the sonagrams.

4.3.3.3.3 On-load sinusoidal tests

The on-load tests were carried similarly to no-load tests, except that the phase current was kept around 600 A in order to provide a 2270 Nm output torque. During the measurements, the prototype was so quiet that the gearbox (53 and 39 teeth) noise controlled the over-all sound pressure level¹. All the spectra have been post-treated in order to remove the first order gear-box harmonic and obtain the aerodynamic and magnetic noise of the motors. Results are displayed in Fig. 4.43. As in no-load tests, no resonance did occur on the prototype, and its noise linearly evolves with speed: a 10 dB decrease compared to the industrialised motor was observed at low speeds (0 to 30 km/h i.e. $f_s = 50$ Hz).

¹The noisy gearbox of the test-bench was not the one which is effectively coupled to motor M5 in the subway frame.

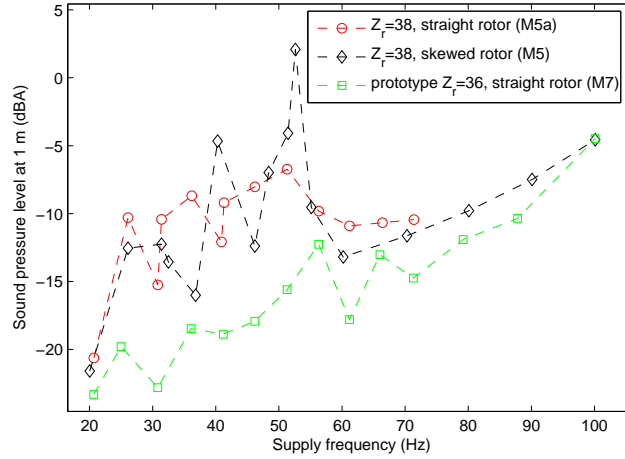


Figure 4.43: Sound pressure level of prototype M7, compared to the industrialised motor M5a, and its skewed rotor version M5 (sinusoidal on-load case).

4.3.3.3.4 No-load PWM tests

As no measurement had been done on motor M5 and M5a in PWM case, a first goal of these tests was to decrease the PWM noise by choosing another switching frequency than 1280 Hz. Another goal was to check if the first slotting lines do not add with pure PWM lines, as they have same frequencies and spatial orders.

It is noteworthy that as the prototype magnetic noise has been drastically reduced, only the PWM noise and the aerodynamic noise were then measured when supplying motor M7 with PWM. This is particularly striking in spectrum Fig. 4.44, where the three main slotting lines identified in section 4.2.2.2 only reach 55 dBA, while the three main PWM lines (cf. 4.12) reach 83 dBA. The continuous and progressively high-pitched whistle characteristic of slotting magnetic noise was totally covered by the stridulation of PWM.

As seen in section 4.2.3.2.1, the switching frequency value must be chosen in order to avoid resonance of pure PWM lines with 0 or $2p$ stator modes identified near 2900 Hz. Various switching frequencies have therefore been experimented to see if a maximum PWM noise was encountered near $f_c = 1450$ Hz (Fig. 4.45). We can see that a variation of more than 15 dB can be experimented according to the switching frequency, and that a maximum is effectively reached near $f_c = 1500$ Hz. The impact of the switching frequency is magnified by the fact that 0 and $2p$ stator modes are close in frequency (cf. section 3.2.1.3) on M5 stator. If 0 and 4 modes are also close on M2 stator, the switching frequency may have less impact as it has three pole pairs, so pure PWM lines are not able to excite both f_0 and $f_{2p} = f_6$ natural frequencies.

Note that the maximum of Fig. 4.45 is not symmetric: to the effect of getting far from the PWM lines resonance with 0 and $2p$ modes by increasing the switching frequency f_c is overlaid the effect of PWM current harmonics magnitude reduction with f_c . If the default switching

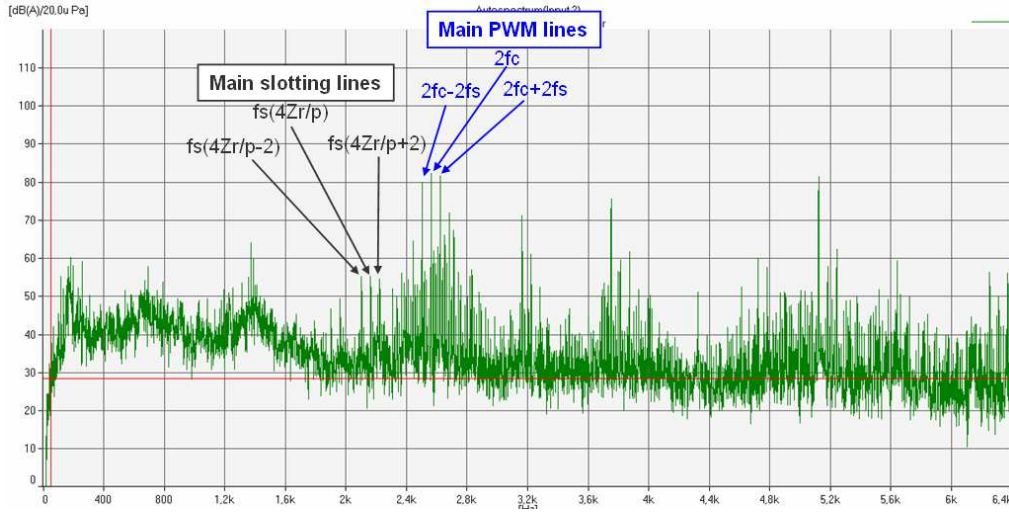


Figure 4.44: Sound pressure level spectrum of prototype M7 (asynchronous 1280 Hz PWM no-load case).

frequency on the industrialised motor M5a is 1280 Hz, a lower switching frequency (1000 Hz or 1200 Hz) can improve the noise level of 5 to 10 dB at certain speeds in starting phase, while a higher one (1900 Hz) can improve the noise level up to 10 dB during starting. Of course, the lower one is preferred as it also decreases inverter losses.

In the experimental data, one can also observe that a clear border separates the speeds affected by the switching frequency from the ones independent of the supply strategy (Fig. 4.45). This way, the phase where PWM noise dominates can clearly be identified as 10 to 50 Hz (30 km/h), whereas aerodynamic noise dominates at higher speeds (> 30 km/h).

It was shown in section 4.2.3.3 that on motor M7, the three main slotting lines spatial orders match the ones of the main asynchronous PWM lines, and that their frequency can also match at a certain speed, given by equation (4.59) :

$$f_s = \frac{2pf_c}{4Z_r(1-s)} \approx \frac{f_c}{Z_r} = 35.55 \text{ Hz} \quad (4.62)$$

At this speed, depending on the phase angle of PWM and slotting vibrations, there was a risk of constructive interference. Although no resonance was observed during no-load PWM experiments, some further tests have been run at this particular speed of 35.55 Hz in order to investigate the effect of the interference between slotting and PWM lines. Results are displayed in Fig. 4.46: nothing occurs, because PWM vibrations magnitude are much larger than slotting vibrations magnitude.

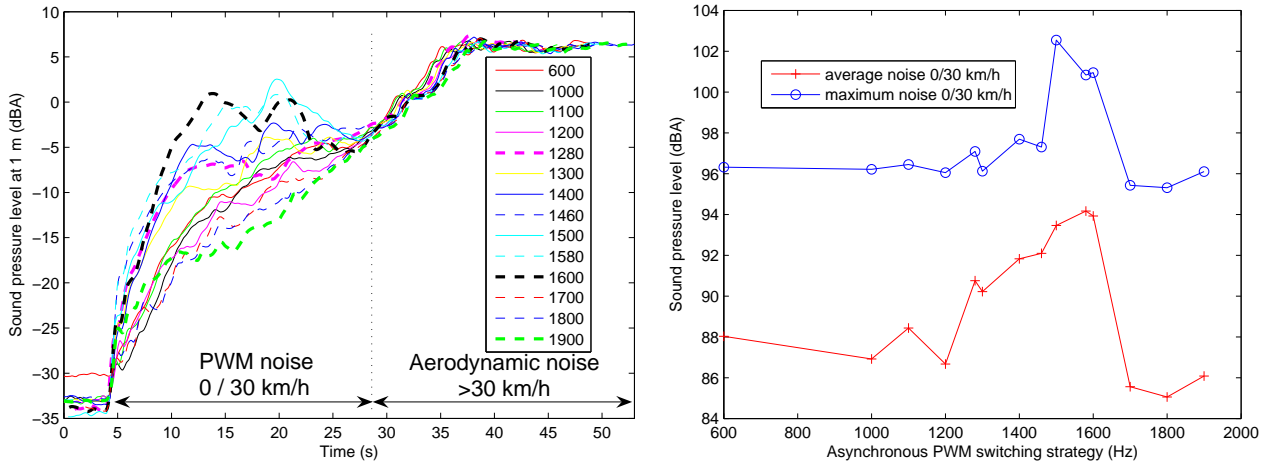


Figure 4.45: Sound pressure level of prototype M7 during starting phase, using various switching frequencies (left: noise level in function of time, right: maximum and average noise levels from 10 to 50 Hz). The default asynchronous PWM switching frequency used on the industrialised motor M5a is 1280 Hz.

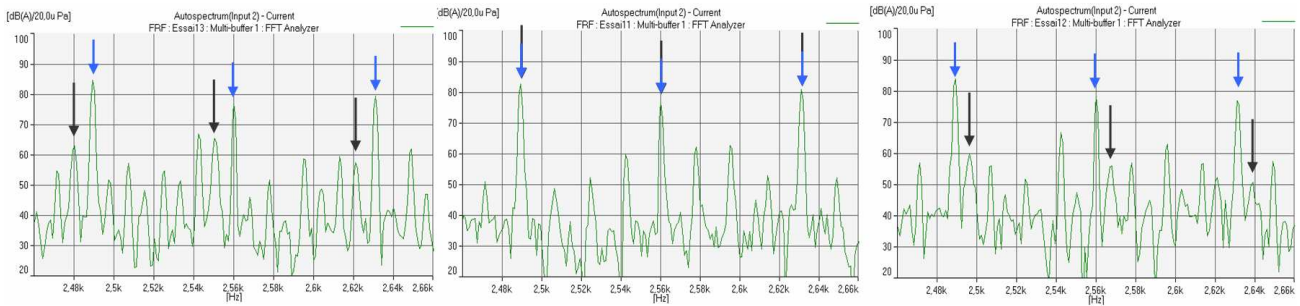


Figure 4.46: Illustration of the interference between main slotting lines (in black) and pure PWM lines (in blue), in asynchronous 1280 Hz PWM no-load case (left: $f_s = 35.43$ Hz, middle: $f_s = 35.55$ Hz, right: $f_s = 35.66$ Hz).

Chapter 5

Conclusion, future work and prospects

5.1 Conclusion

In collaboration with ALSTOM and VIBRATEC companies, and directed by LEC and L2EP laboratories, this thesis work aimed at understanding and predicting the generation of audible magnetic noise in PWM-fed induction machines, as well as establishing low-noise design rules on both the motor and its PWM strategy.

A fully analytical model of the vibro-acoustic and electrical behaviour of a PWM-fed induction machine has been elaborated. The model is able to determine the sound power level radiated by the stator vibrations due to radial Maxwell forces and the motor traction characteristics (output torque, efficiency, etc.) at variable speed. This model has been implemented in a Matlab fast simulation tool, DIVA, which contains several visualisation tools and useful output to correctly interpret the sources of magnetic noise. Numerical simulation allows in particular to virtually isolate the different sources of noise harmonics: winding harmonics can be cancelled by imposing sinusoidal mmfs, PWM harmonics can be removed by imposing sinusoidal currents, saturation harmonics by cancelling saturation permeance harmonics, slotting harmonics by imposing a smooth air-gap, etc.

The electrical model, which accounts for the influence of stepped mmf space harmonics and PWM currents time harmonics (extended equivalent circuit) and determines the air-gap radial flux density, has been successfully validated with FEM (OPERA2D, FLUX2D) and tests. The vibratory model has been also favourably compared to FEM (ANSYS, and IDEAS validations thanks to VIBRATEC) and tests, while the acoustic model based on a pulsating sphere radiation efficiency has been validated with BEM (SYSNOISE validation thanks to VIBRATEC) and tests. Some vibratory and acoustic spectra obtained by simulation have been successfully overlaid with some experimental spectra.

For further understanding of the phenomena, and to infer some low noise rules, the analytical model has been used in order to derive the exact expression of the spatial order and

frequency of the most dangerous Maxwell vibrations, including load, PWM, saturation, winding and eccentricities effects. Five main types of vibrations have been identified, namely pure slotting lines, saturation lines, winding lines, pure PWM lines, and slotting PWM lines. Their characteristics (number of nodes, velocity, propagation direction) have been validated using advanced vibro-acoustic tools (operational deflection shapes, spectrograms and order analysis).

It was proven that slotting PWM lines cannot be dangerous in medium to high power traction applications. It was also shown that saturation lines can significantly increase the magnetic noise level of a traction motor according to its slot numbers. Furthermore, it was observed that the interaction between skewing and saturation can excite some stator longitudinal modes, so that a motor whose slot combination creates a 2 order saturation vibration should not be skewed, but have its rotor slot number changed to avoid such a saturation vibration. Finally, an important effect of slip on the pure PWM line magnitude at twice the switching frequency has been observed, showing that it is necessary to make noise tests in PWM on-load case in order to measure the motor noise radiation in real running conditions.

On the ground of this analytical work, and by the aid of DIVA simulations, some new low magnetic noise design rules have been established. The old empirical laws on the rotor and stator slot numbers choice, which could not be general as they did not account for stator natural frequencies neither for the starting phase speed range, were replaced by an exhaustive database. This database has been built for a small power motor (M1 of elliptical mode near 2400 Hz), and a medium power motor representative of ALSTOM machines (elliptical mode near 600 Hz). The maximum and average noise levels from 0 to 3500 rpm, as well as the number of resonances and the order of the excited modes, are contained in these tables for $p = 2$ and $p = 3$.

A method to reduce magnetic noise due to a given slotting harmonic by choosing a relatively wide optimal slot opening value has been presented. Some design rules have also been established to limit PWM noise, and some psycho-acoustic aspects have been put in emphasis.

The analytical model has been coupled to a mixed-variable, multi-objective, constrained genetic algorithm (NSGA-II) in order to find some new induction machines achieving the specified output torque with low magnetic noise and high efficiency. This coupling has been applied to redesign the industrialised motor M5a: on the ground of some optimisation results, and of low noise rules established during the thesis, two prototypes have been designed. Only the first one, M7, was built and tested before the end of the thesis: it has reduced the noise level of motor M5a in the whole speed range, in both no-load and on-load PWM cases. While DIVA predicted up to a 20 dB reduction of the magnetic noise near 30 Hz in no-load sinusoidal case, a 15 dB reduction of the total noise (including fan noise which may have covered the prototype magnetic noise) was experienced. Similarly, up to a 10 dB decrease was experimented during on-load tests, and no resonance occurred on the prototype.

This new motor has been obtained without enlarging the air-gap, which is a strong lever for magnetic noise reduction but lowers the efficiency, and without closing the rotor slot openings, which can also strongly decrease noise (cf. section 4.2.1.1.2), but increases the slot leakage inductance: on the contrary, the low noise prototype has wide slot openings, which shows that an enlargement of the slot openings do not necessary lead to higher magnetic noise.

The effect of the asynchronous switching frequency on noise has been also investigated on motor M7, and in agreement with DIVA predictions, a resonance was found around $f_c \approx 1550$ Hz. It was shown that a bad choice of the switching frequency can increase PWM noise up to 15 dB in starting phase. A lower switching frequency has therefore been proposed, giving up to a 5 dB reduction in PWM noise, and decreasing inverter switching losses. The industrialised motor noise has therefore been improved on its whole speed range, with a 15 dB reduction at certain speeds.

5.2 Future work

DIVA simulation tool could be improved in several directions:

- the origin of non-physical lines in the PWM fractional-slot case should be further investigated.
- a reluctance network could be added in order to account for saturation more accurately (73; 128), without increasing much the computing time. In a same way, a more accurate analytical model of the mean flux line length entering into the slots could be developed based on FEM simulations or conformal transformations (129; 132) (the expression $d_{s/r}^f = b_{s/r}/5$ should change according to the whole slot shape), as well as a more accurate model of the effective slot opening widths which change with tooth tips saturation level.
- a better description of permeance function could be used. For the moment, a simple crenel function is used to express the air-gap reluctance variation, but a better analytical model could be found, for instance based on gaussian shapes (142). This new model would also change the expression of permeance harmonics magnitude obtained by BRUDNY (36), and allow to have a better analytical prediction of the exact current level to inject for active magnetic noise reduction techniques.
- the iron losses model could be extended to account for PWM time harmonics (122), and a model of inverter switching losses could be added. Indeed, depending on the supply frequency, increasing the switching frequency could decrease global losses (motor and inverter) and decrease magnetic noise radiation.

- a time/frequency analysis algorithm could be implemented (the same as in Pulse Labshop for instance) to compute sonagrams with a constant spectrum resolution on a wide speed range and frequency range. Some numerical problems could be also limited by the implementation of the mechanical response using Green's function form.

Using the psychoacoustic work of A. Leroy (105), a new spread spectrum should be designed by shaping the distribution function of the switching frequency in an optimal way, taking as objective function an aggregation of different psychoacoustic indices. The validation of the load angle computation should also be pursued by investigating the differences between FEM and DIVA rotor equivalent circuit components, and the magnetic coupling between rotor and stator when submitted to a 1 order force (unbalanced magnetic pull (10; 53)) should be further studied. Finally, the effect of slot combination on reluctant torque should be further investigated: indeed, it seems that reducing magnetic noise in traction motors generally leads to slot combinations generating a high reluctant torque.

5.3 Prospects

DIVA model could be adapted to other motor topologies (external rotor (37)) and types (permanent magnet synchronous motor, even if magnetic noise is much lower as the equivalent air-gap is larger), or to turbo-generators and switched reluctance machines (8). It could also be easily extended to transient state computations. Finally, an important application of DIVA could be fault diagnosis (the effect of a broken bar on the air-gap flux density and on vibration can be easily simulated) and non destructive control (using the external magnetic field).

Appendix A

A.1 English/French electromechanical glossary

Bore radius	Diamètre d'alésage
Coil-pitch	Pas de bobinage
Counter-phase	Antiphase
End-plate / End-shield	Flasque
Fractional-slot winding	Bobinage à pas fractionnaire
Frame	Carcasse
Shorted-pitch	A pas raccourci
Strain	Déformation
Stress	Contrainte
Shear	Cisaillement
Tooth tip	Tête de dent
Wedge	Clavette
Yoke	Culasse

Table A.1: English/French glossary.

A.2 Motor parameters and main slotting vibrations

The parameters of the different motors used during the thesis are summed up in Table [A.2](#). Motors M2, M3 and M4 have the same stator. Motors M5, M5a, M7 and M8 have also the same stator. Motor M1 is the LEC laboratory motor, the other ones are ALSTOM motors.

Variables/Name	M1	M2	M3	M4	M5	M5a	M6	M7	M8
Z_s	27	36	36	36	48	48	36	48	48
Z_r	21	28	26	44	38	38	28	36	60
p	2	3	3	3	2	2	2	2	2
Nominal Power (kW)	0.7	275	275	275	350	350	250	350	350
Skewed rotor	no	no	no	no	yes	no	no	no	no

Table A.2: Motor parameters.

The main pure slotting lines that appear on these motors are detailed in Table [A.3](#).

M1 (27/21/2)					M2 (36/28/3)					M3 (36/26/3)					M4 (36/44/3)				
m	k_s	k_r	γ	r	m	k_s	k_r	γ	r	m	k_s	k_r	γ	r	m	k_s	k_r	γ	r
0	7	9	0	0	0	7	9	0	1	0	2	3	-1	1	-2	1	1	-1	1
1	3	4	-1	1	2	1	1	1	1	-2	3	4	1	1	-2	5	4	1	1
-1	4	5	1	1	2	3	4	-1	1	-2	5	7	0	1	2	6	5	-1	1
2	1	1	1	0	-2	4	5	1	1	2	6	8	1	1	2	10	8	1	1
-2	6	8	-1	1	-2	6	8	-1	1	-2	7	10	-1	1	4	5	4	0	1
2	8	10	1	1	2	8	10	1	1	4	1	1	1	0	-4	6	5	0	1
-3	3	4	0	0	-4	3	4	0	1	4	3	4	0	1	6	4	3	1	1
3	4	5	0	0	4	4	5	0	1	4	5	7	-1	1	-6	7	6	-1	1
4	7	9	-1	0	-6	2	3	-1	0	-6	2	3	0	0					
-4	7	9	1	0	6	5	6	1	1	-6	4	6	-1	1					
-5	2	3	-1	0	6	7	9	-1	1										
5	5	6	1	0	-6	7	9	1	1										
6	1	1	0	0															
-6	6	8	0	0															
6	8	10	0	0															
M5 (48/38/2)					M6 (36/28/2)					M7 (48/36/2)					M8 (48/60/2)				
m	k_s	k_r	γ	r	m	k_s	k_r	γ	r	m	k_s	k_r	γ	r	m	k_s	k_r	γ	r
0	8	10	1	1	0	3	4	-1	1	0	3	4	0	1	0	5	4	0	1
-2	4	5	1	1	0	4	5	1	1	0	6	8	0	1	0	10	8	0	1
2	4	5	0	1	0	7	9	0	1	4	3	4	-1	1	4	5	4	-1	1
-2	7	9	-1	1	4	1	1	1	0	-4	3	4	1	1	-4	5	4	1	1
-4	3	4	-1	1	-4	3	4	0	1	4	6	8	-1	1	4	10	8	-1	1
4	8	10	0	1	4	4	5	0	1	-4	6	8	1	1	-4	10	8	1	1
6	1	1	1	0	-4	6	8	-1	1										
6	4	5	-1	1	4	7	9	-1	1										
-6	7	9	0	1	-4	7	9	1	1										
					4	8	10	1	1										

Table A.3: Highest pure slotting lines of order $m = k_r Z_r - k_s Z_s + 2p\gamma$ and frequency $f_s(Z_r(1 - s)/p + 2\gamma)$ ($\gamma=0, +1$ or -1) on motors M1 to M8 ($Z_s/Z_r/p$) ($r = 1$ indicates a resonance during starting phase).

A.3 Winding matrix filling algorithm

Let \mathbf{M}_w be the matrix representing the stator winding, representing the number of turns of each stator phase in each slot and in each layer, weighted by the current sign. It has a size of $n_l \times Z_s \times q_s$, and can be filled using the following algorithm (for shorted-pitch windings only):

```

for  $q=1$  to  $q_s$  do
  for  $k=1$  to  $p$  do
    for  $n=1$  to  $m_s$  do
       $s_1 = (k - 1)sp_s + (q - 1)m_s + n;$ 
      for  $l=1$  to  $n_l$  do
         $s_2 = \text{mod}(s_1 - (Y - sp_s)(l - 1), Z_s - 1) + 1;$ 
         $\mathbf{M}_w(l, s_2, q) = \mathbf{M}_w(l, s_2, q) + (-1)^{k+1}n_t;$ 
      end
    end
  end
end

```

This algorithm is also used in OPERA software in order to launch FEM simulations with a parametrised winding induction machine.

A.4 Diva/OPERA coupling

DIVA has been coupled to the electromagnetic software OPERA in order to validate some highly saturated cases, in which the slot opening width and depth seen by the flux distribution are strongly modified, altering the predicted magnitude of magnetic vibrations. All the models of OPERA are built following a set of instructions stored in text files, which define the motor geometry, mesh, electrical circuit and winding. All these instructions have been fully parametrised, including the description of the winding pattern as seen in section A.3: this way, DIVA motor input variables can be automatically used to generate the OPERA model of a given induction machine. Then, Matlab calls the OPERA solver, and another parametrised OPERA script is used as a post-processor to obtain the air-gap radial flux density distribution in on-load sinusoidal case.

An example of OPERA model obtained from DIVA is displayed in Fig. A.1.

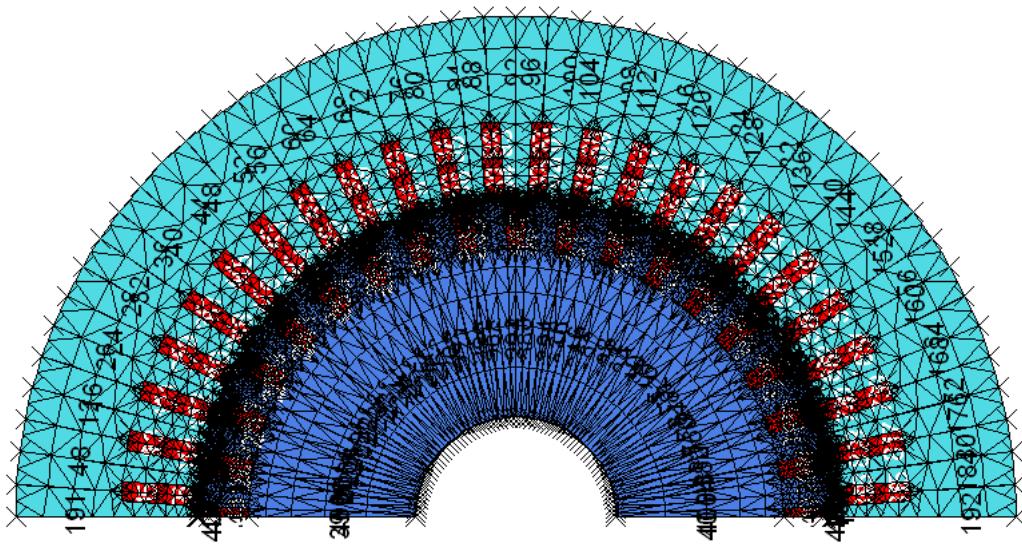


Figure A.1: FEM model of motor M7 (OPERA software).

Appendix B

B.1 Mode shapes of a finite-length cylindrical shell

Table B.1 and Fig. B.1 to B.3 show the modal base decomposition of a plate model of motor M5 equivalent cylinder using IDEAS finite element software (thanks to J. Berger, VIBRATEC company).

Mode id	Frequency	Identification	Description
1 and 2	516 Hz	Mode (2,0)	Elliptical deflection - cylinder ends in phase
3 and 4	573 Hz	Mode (2,1)	Elliptical deflection - cylinder ends in counter-phase
5 and 6	1410 Hz	Mode (3,0)	Order 3 deflection - cylinder ends in phase
7 and 8	1520 Hz	Mode (3,1)	Order 3 deflection - cylinder ends in counter-phase
9 and 10	2480 Hz		Shear deflection of cylinder ends
11 and 12	2590 Hz	Mode (4,0)	Order 4 deflection - cylinder ends in phase
13 and 14	2720 Hz	Mode (4,1)	Order 4 deflection - cylinder ends in counter-phase
15	2840 Hz		Cylinder first torsional deflection
16	2850 Hz	Mode (0,0)	Breathing deflection
17 and 18	3230 Hz	Mode (2,1) bis	Elliptical and flexural deflections - cylinder ends in counter-phase
19 and 20	3370 Hz	Mode (2,0) bis	Elliptical and flexural deflections - cylinder ends in phase
21	3440 Hz		Cylinder first flexural deflection
22 and 23	3520 Hz		Cylinder second torsional deflection
24 and 25	3530 Hz	Mode (3,0) bis	Order 3 and flexural deflections - cylinder ends in phase
26 and 27	3980 Hz	Mode (0,0)	Breathing and flexural deflection
28 and 29	3980 Hz	Mode (5,0)	Order 5 deflection - cylinder ends in phase

B.1 Mode shapes of a finite-length cylindrical shell

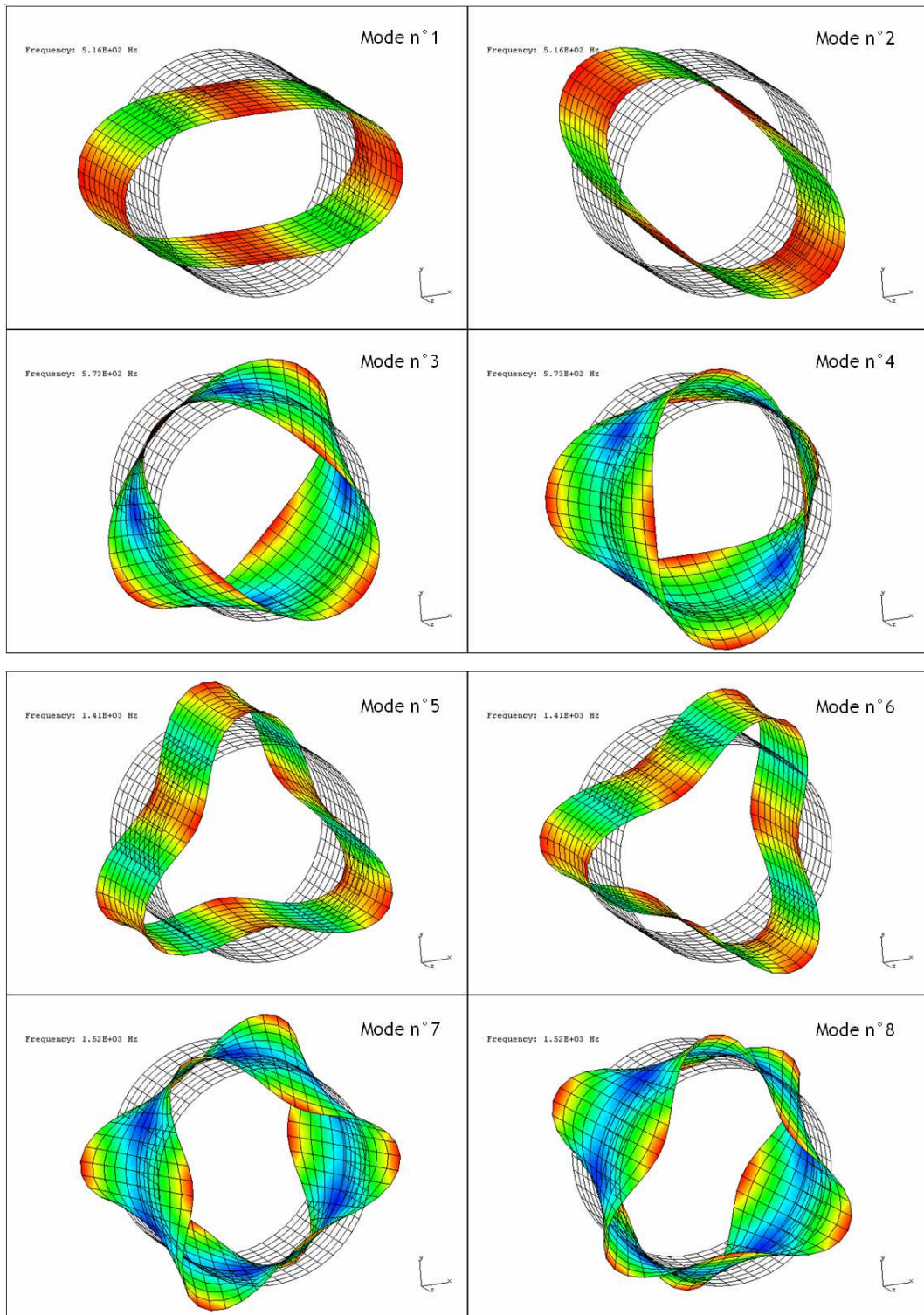


Figure B.1: Modal base of a cylindrical shell (I).

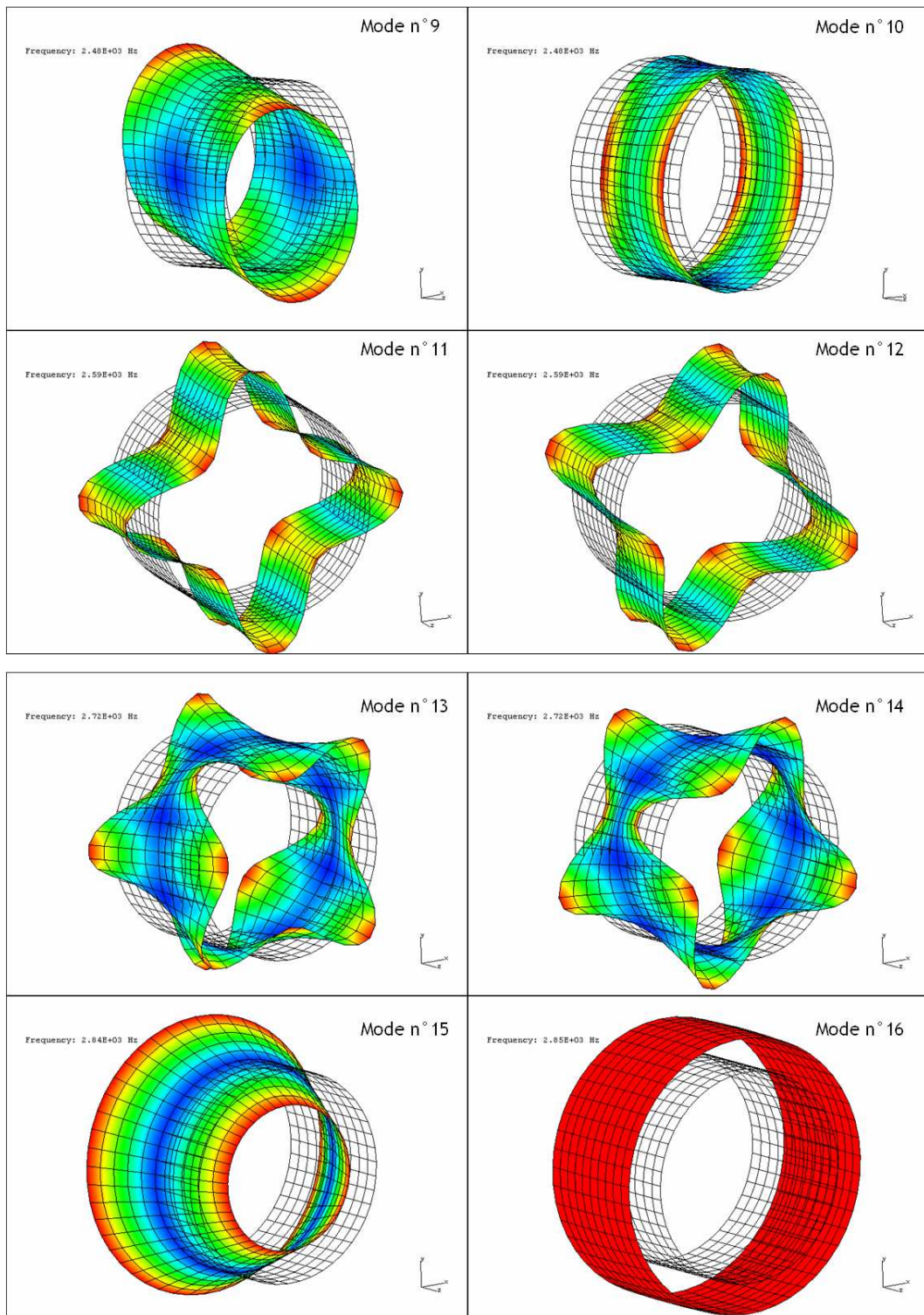


Figure B.2: Modal base of a cylindrical shell (II).

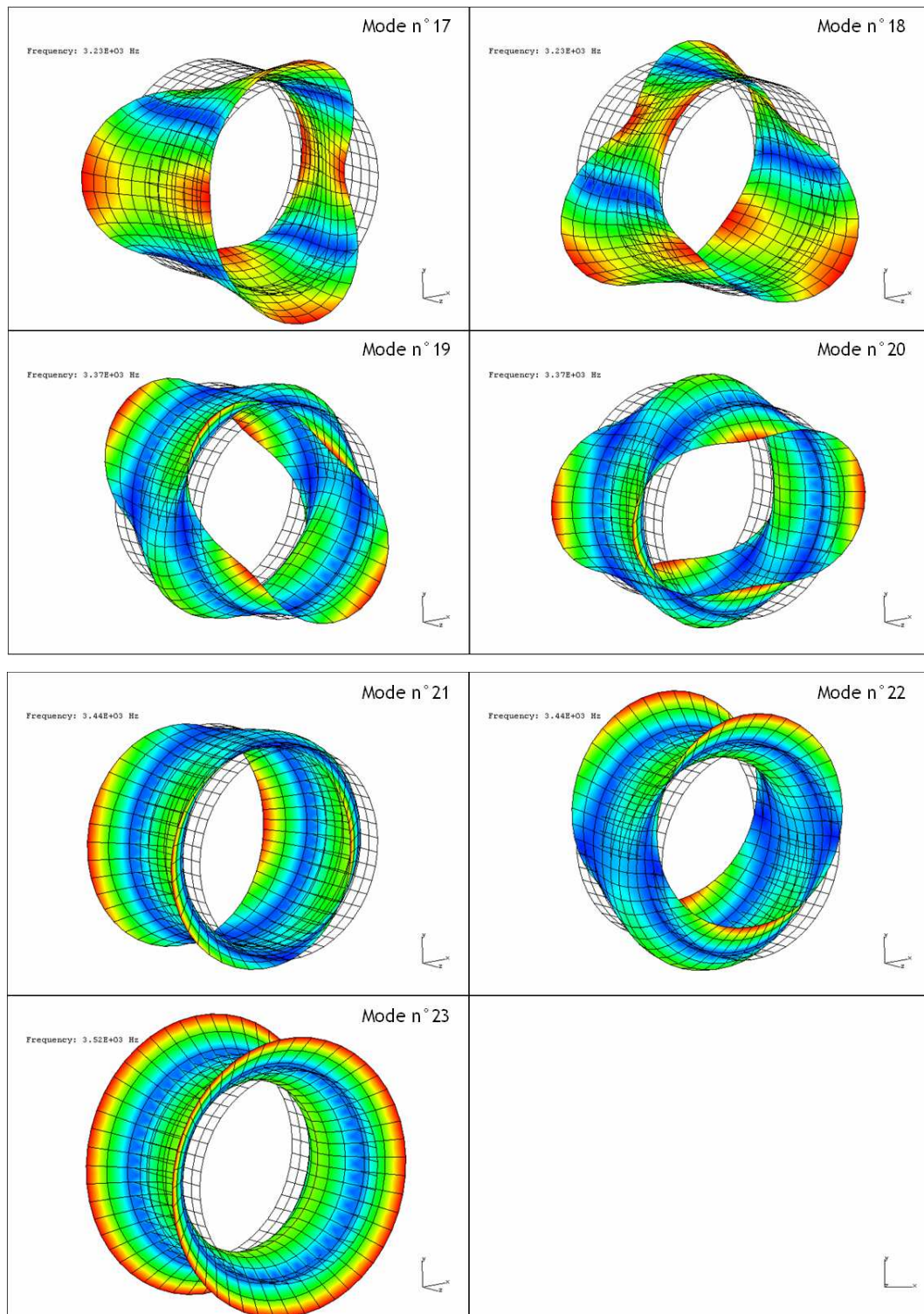


Figure B.3: Modal base of a cylindrical shell (III).

B.2 Green's function formalism

In this appendix is detailed the Green's function formalism allowing to express the vibration velocity at the surface of a cylinder in function of the internal load distribution, the exciting force and the response being both expressed in time and space domains. Two cases will be successively considered: the case of a rotating circumferential load wave on a circular cylindrical shell, and the case of a standing load wave (139).

B.2.1 Rotating circumferential load wave on a circular cylindrical shell

The radial load wave, which stands for a radial Maxwell force distribution harmonic, can be expressed as

$$q_r(\theta, t) = \frac{F}{a} \cos(q(\theta - \Omega t)) \quad (\text{B.1})$$

where $\frac{F}{a}$ is the force per unit length along the stator circumference of internal radius a . At a given time t , it has the q maxima

$$q\theta_l - q\Omega t = 2\pi l[2\pi] \Leftrightarrow \theta_l = \frac{2\pi l}{q}[2\pi] + \Omega t = \frac{2\pi l}{q} + \Omega t \quad l \in [0, q-1] \quad (\text{B.2})$$

i.e. $2q$ nodes (null force points) and anti-nodes (maximum magnitude force points). The force wave first maximum θ_0 travels with angular speed

$$\frac{d\theta_0}{dt} = \Omega \quad (\text{B.3})$$

so the force wave travels with speed $v = a\Omega$. If the form $q_r(\theta, t) = \frac{F}{a} \cos(q\theta - \Omega t)$ is used, the velocity speed becomes $v = a\frac{\Omega}{q}$.

Using dynamic influence Green's function on a steady closed circular cylindrical shell, the radial velocity response u_r can be written as (139)

$$u_r(\theta, z, t) = \int_0^t \int_0^L \int_0^{2\pi} G_{rr}(\theta, z, t; \theta^*, z^*, t^*) q_r(\theta^*, t^*) a d\theta^* dz^* dt^* \quad (\text{B.4})$$

where

$$\begin{aligned} G_{rr}(\theta, z, t; \theta^*, z^*, t^*) &= \frac{1}{\rho h} \sum_{m=1}^{\infty} \sum_{n=0}^{\infty} \sum_{p=0}^3 \sum_{n\phi=0, \pi/2} \frac{1}{N_{mnp}} U_{r,mnp}(\theta, z) U_{r,mnp}(\theta^*, z^*) S_{mnp}(t - t^*) \\ &= \frac{1}{\rho h} \sum_{m=1}^{\infty} \sum_{n=0}^{\infty} \sum_{p=1}^3 \sum_{n\phi=0, \pi/2} \frac{1}{N_{mnp}} C_{mnp}^2 \gamma_m(z) \gamma_m(z^*) \cos(n(\theta - \phi)) \cos(n(\theta^* - \phi)) S_{mnp}(t - t^*) \end{aligned} \quad (\text{B.5})$$

S_k is given for subcritical damping ($\xi < 1$) by

$$S_k(t) = \frac{1}{b_k} \exp^{-\xi_k \omega_k t} \sin(b_k t) U(t) \quad (\text{B.6})$$

U is the unit step function, and $b_k = \omega_k \sqrt{1 - \xi_k^2}$. p goes from 1 to 3 to take into account 3 natural frequencies for each mode (m, n) (the lowest is associated with the mode where the transverse component dominates (139)). γ_m is the beam function which depends on the boundary conditions (162). C_k and N_k and coefficients defined in (139; 162).

We can show that (139)

$$G_{rr}(\theta, z, t; \theta^*, z^*, t^*) = \frac{1}{\rho h} \sum_{m=1}^{\infty} \sum_{n=0}^{\infty} \sum_{p=1}^3 \frac{C_{mnp}^2}{N_{mnp}} \gamma_m(z) \gamma_m(z^*) \cos(n(\theta - \theta^*)) S_{mnp}(t - t^*) \quad (\text{B.7})$$

therefore

$$\begin{aligned} u_r(\theta, z, t) &= \frac{a}{\rho h} \sum_{m=1}^{\infty} \sum_{n=0}^{\infty} \sum_{p=1}^3 \frac{C_{mnp}^2}{N_{mnp}} \gamma_m(z) \int_0^t \int_0^L \int_0^{2\pi} \gamma_m(z^*) \cos(n(\theta - \theta^*)) S_{mnp}(t - t^*) q_r(\theta^*, t^*) d\theta^* dz^* dt^* \\ &= \frac{F}{\rho h} \sum_{m=1}^{\infty} \sum_{n=0}^{\infty} \sum_{p=1}^3 \frac{C_{mnp}^2}{N_{mnp}} \gamma_m(z) \int_0^t \int_0^L \int_0^{2\pi} \gamma_m(z^*) \cos(n(\theta - \theta^*)) S_{mnp}(t - t^*) \cos(q(\theta^* - \Omega t^*)) d\theta^* dz^* dt^* \end{aligned} \quad (\text{B.8})$$

At this point, one has to separate the variables using by developing $\cos(q(\theta^* - \Omega t^*)) = \cos(q\theta^*) \cos(q\Omega t^*) + \sin(q\theta^*) \sin(q\Omega t^*)$:

$$\begin{aligned} u_r(\theta, z, t) &= \frac{F}{\rho h} \sum_{m=1}^{\infty} \sum_{n=0}^{\infty} \sum_{p=1}^3 \frac{C_{mnp}^2}{N_{mnp}} \gamma_m(z) \int_0^t S_{mnp}(t - t^*) \cos(q\Omega t^*) dt^* \int_0^L \gamma_m(z^*) dz^* \int_0^{2\pi} \cos(n(\theta - \theta^*)) \cos(q\theta^*) d\theta^* \\ &+ \frac{F}{\rho h} \sum_{m=1}^{\infty} \sum_{n=0}^{\infty} \sum_{p=1}^3 \frac{C_{mnp}^2}{N_{mnp}} \gamma_m(z) \int_0^t S_{mnp}(t - t^*) \sin(q\Omega t^*) dt^* \int_0^L \gamma_m(z^*) dz^* \int_0^{2\pi} \cos(n(\theta - \theta^*)) \sin(q\theta^*) d\theta^* \end{aligned} \quad (\text{B.9})$$

We have

$$\int_0^{2\pi} \cos(n(\theta - \theta^*)) \cos(q\theta^*) d\theta^* = \cos(n\theta) \int_0^{2\pi} \cos(n\theta^*) \cos(q\theta^*) d\theta^* = \pi \cos(n\theta) (\delta_{n,q} + \delta_{n,-q}) \quad (\text{B.10})$$

where $\delta_{i,j}$ is the Kronecker symbol ($\delta_{i,j}=1$ if $i = j$, 0 otherwise). In a similar way,

$$\int_0^{2\pi} \cos(n(\theta - \theta^*)) \sin(q\theta^*) d\theta^* = \sin(n\theta) \int_0^{2\pi} \sin(n\theta^*) \sin(q\theta^*) d\theta^* = \pi \sin(n\theta) (\delta_{n,q} - \delta_{n,-q}) \quad (\text{B.11})$$

Assuming that $q \geq 0$ we have $\delta_{n,-q} = 0$, and the expression of the radial velocity becomes

$$\begin{aligned} u_r(\theta, z, t) &= \frac{F\pi}{\rho h} \sum_{m=1}^{\infty} \sum_{p=1}^3 \frac{C_{mqp}^2}{N_{mqp}} \gamma_m(z) \int_0^L \gamma_m(z^*) dz^* \int_0^t S_{mqp}(t-t^*) \{ \cos(q\Omega t^*) \cos(q\theta) + \sin(q\Omega t^*) \sin(q\theta) \} dt^* \\ &= \frac{F\pi}{\rho h} \sum_{m=1}^{\infty} \sum_{p=1}^3 \frac{C_{mqp}^2}{N_{mqp}} \gamma_m(z) \int_0^L \gamma_m(z^*) dz^* \int_0^t S_{mqp}(t-t^*) \cos(q(\theta - \Omega t^*)) dt^* \\ &= \frac{F\pi}{\rho h} \sum_{m=1}^{\infty} \sum_{p=1}^3 \frac{C_{mqp}^2}{N_{mqp} b_{mqp}} \gamma_m(z) \int_0^L \gamma_m(z^*) dz^* \int_0^t \exp^{-a_{mqp}(t-t^*)} \sin(b_{mqp}(t-t^*)) \cos(q(\theta - \Omega t^*)) dt^* \end{aligned} \quad (\text{B.12})$$

where $a_k = \xi_k \omega_k$.

This expression is exactly the q -th component of the response u_r in the case of a rotating point load $q_r(\theta, t) = \frac{F}{a} \delta(x - \xi) \delta(\theta - \Omega t)$ (see (139), p. 268). By identification with SOEDEL expression, we therefore have

$$\begin{aligned} u_r(\theta, z, t) &= \frac{F\pi}{\rho h} \sum_{m=1}^{\infty} \sum_{p=1}^3 \frac{C_{mqp}^2}{N_{mqp} b_{mqp}} \gamma_m(z) \int_0^L \gamma_m(z^*) dz^* \{ Y_{mqp} \cos(q(\theta - \Omega t) - \Phi_{mqp}) \\ &\quad + \exp^{-a_{mqp}t} T_{mpq}(\theta, t) \} \end{aligned} \quad (\text{B.13})$$

where

$$Y_k(q, \Omega, \omega_k, \xi_k) = \frac{\sqrt{a_k^2(\zeta_k^2 - \eta_k^2)^2 + [\eta_k(a_k^2 + \zeta_k^2) - \zeta_k(a_k^2 + \eta_k^2)]^2}}{2[a_k^4 + 2a_k^2(q^2\Omega^2 + b_k^2) + (q^2\Omega^2 - b_k^2)^2]} \quad (\text{B.14})$$

$$\Phi_k(q, \Omega, \omega_k, \xi_k) = \tan^{-1} \left(\frac{a_k(\zeta_k^2 - \eta_k^2)}{\eta_k(a_k^2 + \zeta_k^2) - \zeta_k(a_k^2 + \eta_k^2)} \right) \quad (\text{B.15})$$

$$\zeta_k(q, \Omega, \omega_k, \xi_k) = q\Omega - b_k \quad \eta_k(q, \Omega, \omega_k, \xi_k) = q\Omega + b_k \quad (\text{B.16})$$

We can see that the response steady state magnitude is proportional to Y_k , a fourth order polynomial of Ω which reaches its maximum at the following condition:

$$\begin{aligned}
 0 &= \frac{d}{d\Omega} (a_k^4 + 2a_k^2(q^2\Omega^2 + b_k^2) + (q^2\Omega^2 - b_k^2)^2) \\
 \Leftrightarrow 0 &= 4a_k^2q^2\Omega + 4q^2\Omega(q^2\Omega^2 - b_k^2) \\
 \Leftrightarrow 0 &= a_k^2 + q^2\Omega^2 - b_k^2 = \xi_k^2\omega_k^2 + q^2\Omega^2 - \omega_k^2(1 - \xi_k^2) \\
 \Leftrightarrow \Omega &= \pm \frac{w_k}{q} \sqrt{1 - 2\xi_k^2} \approx \pm \frac{w_k}{q}
 \end{aligned} \tag{B.17}$$

A rotating magnetic force wave of spatial order q and frequency f , which rotates at angular speed $\Omega = \frac{2\pi f}{q}$, therefore excites all the stator modes satisfying $w_{mqp} = 2\pi f$ independently of its rotation direction. In particular, a magnetic force wave of circumferential order $q = 2$ is expected to successively excite the modes $(m = 0, n = 2)$ and $(m = 1, n = 2)$ at variable speed.

If the rotating load resonates with mode (m', q, p') i.e. $\Omega = \frac{w_{m'qp'}}{q} \sqrt{1 - 2\xi_{m'qp'}^2}$, and considering that $Y_{m'qp'} \gg Y_{mqp}$, the steady state response becomes at resonance:

$$u_r(\theta, z, t) \approx \frac{F\pi}{\rho h} \frac{C_{m'qp'}^2}{N_{m'qp'} b_{m'qp'}} \gamma_{m'}(z) \int_0^L \gamma_{m'}(z^*) dz^* Y_{m'qp'} \cos(q(\theta - \Omega t) - \Phi_{m'qp'}) \tag{B.18}$$

which shows that the vibration waves are also rotating at angular speed Ω . As the excitation cannot be exactly rotating at the resonance frequency, the vibration wave peak may lag or lead the travelling load depending on the damping.

An order of magnitude of the characteristic time of the establishment of the steady state can be calculated considering that the natural frequencies lie between 200 Hz and 10 kHz, and damping coefficient between 0.1 and 4 % :

$$0.4\text{ms} \approx \frac{1}{2\pi 10000 \times 0.04} < \frac{1}{\omega_k \xi_k} < \frac{1}{2\pi 200 \times 0.001} \approx 0.8\text{s} \tag{B.19}$$

B.2.2 Standing circumferential load wave on a circular cylindrical shell

This time, we consider a standing (or stationary) force of the form

$$q_r(\theta, t) = \frac{F}{a} \cos(q\theta) \cos(\Omega t) = \frac{F}{2a} (\cos(q(\theta - \Omega t)) + \cos(q(\theta + \Omega t))) \tag{B.20}$$

A stationary force wave of order q is equivalent to the sum of two force waves of same magnitude rotating in opposite directions. This time, the maxima θ_l are given by :

$$\theta_l = \frac{2\pi l}{q} \quad l \in [0, q - 1] \tag{B.21}$$

They do not depend on time. The response under a standing force wave can be found by summing the responses under two rotating waves as given in previous section:

$$u_r(\theta, z, t) \approx \frac{F\pi}{\rho h} \frac{C_{m'qp'}^2}{N_{m'qp'} b_{m'qp'}} \gamma_{m'}(z) \cos(q\theta) \int_0^L \gamma_{m'}(z^*) dz^* Y_{m'qp'} \cos(q\Omega t + \Phi_{m'qp'}) \quad (\text{B.22})$$

The vibration response is also a standing wave, and we obtain exactly the same resonance condition as in the rotating wave case:

$$\Omega = \pm \frac{w_k}{q} \sqrt{1 - 2\xi_k^2} \quad (\text{B.23})$$

Note that the steady state magnitude of the circumferential response is the same whether the load wave is rotating or pulsating, whereas the sound power radiation is not (cf. [section 4.1.2](#)).

Appendix C

C.1 Exhaustive magnetic force lines characteristics

Table C.1 shows the expression of all the radial Maxwell force lines including PWM, saturation and load effects. When HO column is ticked, the exciting force harmonic has a too high order to be significant (or when it has a low order, it necessary have a very low magnitude). Column A gives a qualitative appreciation of the force harmonic magnitude.

Name	Spatial orders	Frequencies	HO
$F_{11} = P_s F_s P_s F_s$	$Z_s(k_s + \delta_{11}k'_s) + \beta_{ss}\nu_s + \delta_{11}\beta'_{ss}\nu'_s$	$\beta_{ss}\eta_s f_n^s + \delta_{11}\beta'_{ss}\eta'_s f_n^{s'}$	
$F_{12} = P_s F_s P_s F_r$	$Z_s(k_s + \delta_{12}k'_s) + \beta_{ss}\nu_s + \delta_{12}\beta_{sr}\nu_r$	$\beta_{ss}\eta_s f_n^s + \delta_{12}\beta_{sr}\eta_r f_{\nu_s n}^r$	
$F_{13} = P_s F_s P_r F_s$	$Z_s k_s + \delta_{13}Z_r k_r + \beta_{ss}\nu_s + \delta_{13}\beta_{rs}\nu'_s$	$\beta_{ss}\eta_s f_n^s + \delta_{13}k_r Z_r f_R + \delta_{13}\beta_{rs}\eta'_s f_n^{s'}$	
$F_{14} = P_s F_s P_r F_r$	$Z_s k_s + \delta_{14}Z_r k_r + \beta_{ss}\nu_s + \delta_{14}\beta_{rr}\nu_r$	$\beta_{ss}\eta_s f_n^s + \delta_{14}(\beta_{rr}\nu_r + k_r Z_r) f_R + \delta_{14}\beta_{rr}\eta_r f_{\nu_s n}^r$	
$F_{15} = P_s F_s P_{sr} F_s$	$Z_s(k_s + \delta_{15}k'_s) + \delta_{15}\epsilon_{sr}k_r Z_r + \beta_{ss}\nu_s + \delta_{15}\beta_{is}\nu'_s$	$\eta_s \beta_{ss} f_n^s + \delta_{15}\beta_{is}\eta'_s f_n^{s'} + \delta_{15}\epsilon_{sr}k_r Z_r f_R$	
$F_{16} = P_s F_s P_{sr} F_r$	$Z_s(k_s + \delta_{16}k'_s) + \delta_{16}\epsilon_{sr}k_r Z_r + \beta_{ss}\nu_s + \delta_{16}\beta_{ir}\nu'_R$	$\eta_s \beta_{ss} f_n^s + \delta_{16}(\beta_{ir}\nu_r + \epsilon_{sr}k_r Z_r) f_R + \delta_{16}\beta_{ir}\eta_r f_{\nu_s n}^r$	
$F_{17} = P_s F_s P_a F_s$	$k_s Z_s + \beta_{ss}\nu_s + \delta_{17}(\beta_{as}\nu'_s + 2k_a p)$	$\eta_s \beta_{ss} f_n^s + \delta_{17}(\beta_{as}\eta'_s f_n^{s'} + 2k_a f_s)$	X
$F_{18} = P_s F_s P_a F_r$	$k_s Z_s + \beta_{ss}\nu_s + \delta_{18}(\beta_{ar}\nu_r + 2k_a p)$	$\eta_s \beta_{ss} f_n^s + 2\delta_{18}k_a f_s + \delta_{18}\beta_{ar}(\eta_r f_{\nu_s n}^r + \nu_r f_R)$	X
$F_{19} = P_s F_s P_0 F_s$	$Z_s k_s + \delta_{19}\nu_s + \beta_{ss}\nu_s$	$\beta_{ss}\eta_s f_n^s + \delta_{19}\eta'_s f_n^{s'}$	X
$F_{110} = P_s F_s P_0 F_r$	$Z_s k_s + \delta_{110}\nu_r + \beta_{ss}\nu_s$	$\beta_{ss}\eta_s f_n^s + \delta_{110}(\eta_r f_{\nu_s n}^r + \nu_r f_R)$	X
$F_{22} = P_s F_r P_s F_r$	$(k_s + \delta_{22}k'_s)Z_s + \beta_{sr}\nu_r + \delta_{22}\beta'_{sr}\nu'_r$	$\beta_{sr}\eta_r f_{\nu_s n}^r + \delta_{22}\beta'_{sr}\eta'_r f_{\nu_s n}^{r'}$	
$F_{24} = P_s F_r P_r F_r$	$k_s Z_s + \delta_{24}k_r Z_r + \beta_{sr}\nu_r + \delta_{24}\beta_{rr}\nu'_r$	$\eta_r \beta_{sr} f_{\nu_s n}^r + (\beta_{sr}\nu_r + \delta_{24}(\nu'_r \beta_{rr} + k_r Z_r)) f_R + \delta_{24}\beta_{rr}\eta'_r f_{\nu_s n}^{r'}$	
$F_{26} = P_s F_r P_{sr} F_r$	$(k_s + \delta_{26}k'_s)Z_s + \beta_{sr}\nu_r + \delta_{26}(\epsilon_{sr}k_r Z_r + \beta_{ir}\nu_r)$	$\beta_{sr}\eta_r f_{\nu_s n}^r + (\delta_{26}\epsilon_{sr}k_r Z_r + \delta_{26}\beta_{ir}\nu_r + \beta_{sr}\nu_s) f_R + \delta_{26}\beta_{ir}\eta'_r f_{\nu_s n}^{r'}$	
$F_{28} = P_s F_r P_a F_r$	$k_s Z_s + \beta_{sr}\nu_r + \delta_{28}(\beta_{ar}\nu'_r + 2k_a p)$	$\beta_{sr}\eta_r f_{\nu_s n}^r + \beta_{ar}\eta'_r f_{\nu_s n}^{r'} + \delta_{28}(2k_a f_s + f_R(\delta_{28}\beta_{ar}\nu'_r + \beta_{sr}\nu_r))$	X
$F_{210} = P_s F_r P_0 F_r$	$k_s Z_s + \beta_{sr}\nu_r + \delta_{210}\nu'_r$	$(\beta_{sr}\nu_r + \delta_{210}\nu'_r) f_R + \beta_{sr}\eta_r f_{\nu_s n}^r + \delta_{210}\eta'_r f_{\nu_s n}^{r'}$	X
$F_{33} = P_r F_s P_r F_s$	$(k_r + \delta_{33}k'_r)Z_r + \beta_{rs}\nu_s + \delta_{33}\beta'_{rs}\nu'_s$	$(k_r + \delta_{33}k'_r)Z_r f_R + \beta_{rs}\eta_s f_n^s + \delta_{33}\beta'_{rs}\eta'_s f_n^{s'}$	
$F_{34} = P_r F_s P_r F_r$	$(k_r + \delta_{34}k'_r)Z_r + \beta_{rs}\nu_s + \delta_{34}\beta_{rr}\nu_r$	$((k_r + \delta_{34}k'_r)Z_r + \delta_{34}\beta_{rr}\nu_r) f_R + \beta_{rs}\eta_s f_n^s + \delta_{34}\beta_{rr}\eta_r f_{\nu_s n}^r$	
$F_{35} = P_r F_s P_{sr} F_s$	$(k_r + \delta_{35}\epsilon_{sr}k'_r)Z_r + \beta_{rs}\nu_s + \delta_{35}(\beta_{is}\nu'_s + k_s Z_s)$	$((k_r + \epsilon_{sr}\delta_{35}k'_r)Z_r + \delta_{35}\beta_{ir}z) f_R + \beta_{rs}\eta_s f_n^s + \delta_{35}\beta_{is}\eta'_s f_n^{s'}$	
$F_{36} = P_r F_s P_{sr} F_r$	$(1 + \delta_{36}\epsilon_{sr}k_r)Z_r + \beta_{rs}\nu_s + \delta_{36}(\beta_{ir}\nu_r + k_s Z_s)$	$((k_r + \epsilon_{sr}\delta_{36}k'_r)Z_r + \delta_{36}\beta_{ir}\nu_r) f_R + \beta_{rs}\eta_s f_n^s + \delta_{36}\beta_{ir}\eta_r f_{\nu_s n}^r$	
$F_{37} = P_r F_s P_a F_s$	$\delta_{37}2k_a p + k_r Z_r + \delta_{37}\beta_{as}\nu'_s + \beta_{rs}\nu_s$	$\beta_{rs}\eta_s f_n^s + k_r Z_r f_R + \delta_{37}(2k_a f_s + \beta_{as}\eta'_s f_n^{s'})$	X
$F_{38} = P_r F_s P_a F_r$	$\delta_{37}2k_a p + k_r Z_r + \delta_{38}\beta_{ar}\nu_r + \beta_{rs}\nu_s$	$\beta_{rs}\eta_s f_n^s + 2\delta_{38}k_a f_s + (k_r Z_r + \delta_{38}\beta_{ar}\nu_r) f_R + \delta_{38}\beta_{ar}\eta_r f_{\nu_s n}^r$	X
$F_{39} = P_r F_s P_0 F_s$	$k_r Z_r + \beta_{rs}\nu_s + \delta_{39}\nu'_s$	$\beta_{rs}\eta_s f_n^s + k_r Z_r f_R + \delta_{39}\nu'_s f_n^{s'}$	X
$F_{310} = P_r F_s P_0 F_r$	$k_r Z_r + \beta_{rs}\nu_s + \delta_{310}\nu_r$	$\beta_{rs}\eta_s f_n^s + (k_r Z_r + \delta_{310}\nu_r) f_R + \delta_{310}\eta_r f_{\nu_s n}^r$	X
$F_{44} = P_r F_r P_r F_r$	$(k_r + \delta_{44}k'_r)Z_r + \beta_{rr}\nu_r + \delta_{44}\beta'_{rr}\nu'_r$	$(\nu_r \beta_{rr} + \delta_{44}\nu'_r \beta'_{rr} + (k_r + \delta_{44}k'_r)Z_r) f_R + \beta_{rr}\eta_r f_{\nu_s n}^r + \delta_{44}\beta'_{rr}\eta'_r f_{\nu_s n}^{r'}$	
$F_{46} = P_r F_r P_{sr} F_r$	$(k_r + \delta_{46}\epsilon_{sr}k'_r)Z_r + \delta_{46}k_s Z_s + \beta_{rr}\nu_r + \delta_{46}\beta_{ir}\nu'_r$	$(\beta_{rr}\nu_r + \delta_{46}\beta_{ir}\nu_r + (k_r + \delta_{46}\epsilon_{sr}k'_r)Z_r) f_R + \beta_{rr}\eta_r f_{\nu_s n}^r + \delta_{46}\beta_{ir}\eta'_r f_{\nu_s n}^{r'}$	
$F_{48} = P_r F_r P_a F_r$	$2\delta_{48}k_a p + k_r Z_r + \beta_{rr}\nu_r + \delta_{48}\beta_{ar}\nu_r$	$(k_r Z_r - \beta_{rr}\nu_r - \delta_{48}\beta_{ar}\nu_r) f_R + \beta_{rr}\eta_r f_{\nu_s n}^r + \delta_{48}\beta_{ar}\eta'_r f_{\nu_s n}^{r'} + 2\delta_{48}k_a f_s$	X
$F_{410} = P_r F_r P_0 F_r$	$k_r Z_r + \beta_{rr}\nu_r + \delta_{410}\nu_r$	$(k_r Z_r + \beta_{rr}\nu_r) f_R + \beta_{rr}\eta_r f_{\nu_s n}^r + \delta_{410}(\nu_r f_R + \eta_r f_{\nu_s n}^r)$	X
$F_{55} = P_{sr} F_s P_{sr} F_s$	$(\epsilon_{sr}k_r + \delta_{55}\epsilon'_{sr}k'_r)Z_r + (k_s + \delta_{55}k'_s)Z_s + \beta_{is}\nu_s + \delta_{55}\beta'_{is}\nu'_s$	$(\epsilon_{sr}k_r + \delta_{55}\epsilon'_{sr}k'_r)Z_r f_R + \beta_{is}\eta_s f_n^s + \delta_{55}\beta'_{is}\eta'_s f_n^{s'}$	
$F_{56} = P_{sr} F_s P_{sr} F_r$	$(\epsilon_{sr}k_r + \delta_{55}\epsilon'_{sr}k'_r)Z_r + (k_s + \delta_{55}k'_s)Z_s + \beta_{is}\nu_s + \delta_{56}\beta_{ir}\nu_r$	$((\epsilon_{sr}k_r + \delta_{56}\epsilon'_{sr}k'_r)Z_r + \delta_{56}\beta_{ir}\nu_r) f_R + \beta_{is}\eta_s f_n^s + \delta_{56}\beta_{ir}\eta_r f_{\nu_s n}^r$	
$F_{57} = P_{sr} F_s P_a F_s$	$2\delta_{57}k_a p + \delta_{57}\beta_{as}\nu'_s + \beta_{is}\nu_s + \epsilon_{sr}k_r Z_r + k_s Z_s$	$2\delta_{57}k_a f_s + \delta_{57}\beta_{as}\eta'_s f_n^{s'} + \beta_{is}\eta_s f_n^s + \epsilon_{sr}k_r Z_r f_R$	

Name	Spatial orders	Frequencies	HO
$F_{58} = P_{sr}F_sP_aF_r$	$\delta_{58}(2k_ap + \beta_{ar}\nu_r) + \beta_{is}\nu_s + \epsilon_{sr}k_rZ_r + k_sZ_s$	$\delta_{58}(2k_af_s + \beta_{ar}\eta_rf_{\nu_{sn}}^r) + \beta_{is}\eta_sf_n^s + (\delta_{58}\nu_r\beta_{ar} + \epsilon_{sr}k_rZ_r)f_R$	
$F_{59} = P_{sr}F_sP_0F_s$	$\epsilon_{sr}k_rZ_r + k_sZ_s + \beta_{is}\nu_s + \delta_{59}\nu'_s$	$\epsilon_{sr}k_rZ_rf_R + \beta_{is}\eta_sf_n^s + \delta_{59}\eta'_sf_n^{s'}$	
$F_{510} = P_{sr}F_sP_0F_r$	$\epsilon_{sr}k_rZ_r + k_sZ_s + \beta_{is}\nu_s + \delta_{610}\nu_r$	$(\delta_{610}\nu_r + \epsilon_{sr}k_rZ_r)f_R + \beta_{is}\eta_sf_n^s + \delta_{610}\eta_rf_{\nu_{sn}}^r$	
$F_{66} = P_{sr}F_rP_{sr}F_r$	$(\epsilon_{sr}k_r + \delta_{66}\epsilon'_{sr}k'_rZ_r) + (k_s + \delta_{66}k'_s)Z_s + \beta_{ir}\nu_r + \delta_{56}\beta'_{ir}\nu'_r$	$(\beta_{ir}\nu_r + \delta_{66}\beta'_{ir}\nu'_r + (\epsilon_{sr}k_r + \delta_{66}\epsilon'_{sr}k'_r)Z_r)f_R + \beta_{ir}\eta_rf_{\nu_{sn}}^r + \delta_{66}\beta'_{ir}\eta'_rf_{\nu_{sn}}^{r'}$	
$F_{68} = P_{sr}F_rP_aF_r$	$\delta_{68}2k_ap + \beta_{ir}\nu_r + \delta_{68}\beta_{ar}\nu'_r + \epsilon_{sr}k_rZ_r + k_sZ_s$	$\delta_{68}\beta_{ar}\eta'_rf_{\nu_{sn}}^{r'} + \beta_{ir}\eta_rf_{\nu_{sn}}^r + (\epsilon_{sr}k_rZ_r + \beta_{ir}\nu_r + \delta_{68}\beta_{ar}\nu'_r)f_R + 2\delta_{68}k_af_s$	
$F_{77} = P_aF_sP_aF_s$	$2(k_a + \delta_{77}k'_a)p + \beta_{as}\nu_s + \delta_{77}\beta'_{as}\nu'_s$	$2(k_a + \delta_{77}k'_a)f_s + \beta_{as}\eta_sf_n^s + \delta_{77}\beta'_{as}\eta'_sf_n^{s'}$	
$F_{78} = P_aF_sP_aF_r$	$2(k_a + \delta_{78}k'_a)p + \delta_{78}\beta_{ar}\nu_r + \beta_{as}\nu_s$	$2(k_a + \delta_{78}k'_a)f_s + \delta_{78}\beta_{ar}\eta_rf_{\nu_{sn}}^r + \beta_{as}\eta_sf_n^s$	
$F_{79} = P_aF_sP_0F_s$	$2k_ap + \beta_{as}\nu_s + \delta_{79}\nu_s$	$2k_af_s + \beta_{as}\eta_sf_n^s + \delta_{79}\eta'_sf_n^{s'}$	
$F_{710} = P_aF_sP_0F_r$	$2k_ap + \beta_{as}\nu_s + \delta_{710}\nu_r$	$2k_af_s + \beta_{as}\eta_sf_n^s + \delta_{710}(\eta_rf_{\nu_{sn}}^r + \nu_rf_R)$	
$F_{88} = P_aF_rP_aF_r$	$2(k_a + \delta_{88}k'_a)p + \beta_{ar}\nu_r + \delta_{88}\beta'_{ar}\nu'_r$	$2(k_a + \delta_{88}k'_a)f_s + \beta_{ar}\eta_rf_{\nu_{sn}}^r + \delta_{88}\beta'_{ar}\eta'_rf_{\nu_{sn}}^{r'} + (\beta_{ar}\nu_r + \beta'_{ar}\nu'_r)f_R$	
$F_{810} = P_aF_rP_0F_r$	$2k_ap + \beta_{ar}\nu_r + \delta_{810}\nu_r$	$2k_af_s + (\beta_{ar}\nu_r + \delta_{810}\nu'_r)f_R + \beta_{ar}\eta_rf_{\nu_{sn}}^r + \delta_{810}\eta'_rf_{\nu_{sn}}^{r'}$	
$F_{99} = P_0F_sP_0F_s$	$\nu_s + \delta_{99}\nu'_s$	$\eta_sf_n^s + \delta_{99}\eta'_sf_n^{s'}$	
$F_{910} = P_0F_sP_0F_r$	$\nu_s + \delta_{910}\nu_r$	$\eta_sf_n^s + \delta_{910}(\nu_sf_R + \eta_rf_{\nu_{sn}}^r)$	
$F_{1010} = P_0F_rP_0F_r$	$\nu_r + \delta_{1010}\nu'_r$	$\eta_rf_n^r + \delta_{1010}\eta'_rf_{\nu_{sn}}^{r'} + (\nu_r + \delta_{1010}\nu'_r)f_R$	
$F_{113} = P_sF_sP_rF_sK_{se}$	$k_sZ_s + \beta_{ss}\nu_s + \delta_{113}(k_rZ_r + \beta_{rs}\nu'_s + \beta_{ser}\epsilon_{se}k_{se})$	$\beta_{ss}\eta_sf_n^s + \delta_{113}\beta_{rs}\eta'_sf_n^{s'} + \delta_{113}k_rZ_rf_R$	
$F_{114} = P_sF_sP_rF_sK_{de}$	$k_sZ_s + \beta_{ss}\nu_s + \delta_{114}(k_rZ_r + \beta_{rs}\nu'_s + \beta_{der}k_{de})$	$\beta_{ss}\eta_sf_n^s + \delta_{114}\beta_{rs}\eta'_sf_n^{s'} + \delta_{114}(k_rZ_r + \beta_{der}k_{de})f_R$	

C.2 Low order magnetic force lines characteristics

Table [C.2](#) results from the restriction of previous section Table [C.1](#) to low spatial order force harmonics.

Name	Spatial orders	Frequencies
$F_{11} = P_s F_s P_s F_s$	$Z_s(k_s - k'_s) + \beta_{ss}\nu_s - \beta'_{ss}\nu'_s$	$\beta_{ss}\eta_s f_n^s - \beta'_{ss}\eta'_s f_n^{s'}$
$F_{12} = P_s F_s P_s F_r$	$Z_s(k_s - k'_s) + \beta_{ss}\nu_s - \beta_{sr}\nu_r$	$\beta_{ss}\eta_s f_n^s - \beta_{sr}\eta_r f_{\nu_s n}^r$
$F_{13} = P_s F_s P_r F_s$	$Z_s k_s - Z_r k_r + \beta_{ss}\nu_s - \beta_{rs}\nu'_s$	$\beta_{ss}\eta_s f_n^s - k_r Z_r f_R - \beta_{rs}\eta'_s f_n^{s'}$
$F_{14} = P_s F_s P_r F_r$	$Z_s k_s - Z_r k_r + \beta_{ss}\nu_s - \beta_{rr}\nu_r$	$\beta_{ss}\eta_s f_n^s - (\beta_{rr}\nu_r + k_r Z_r) f_R - \beta_{rr}\eta_r f_{\nu_s n}^r$
$F_{15} = P_s F_s P_{sr} F_s$	$Z_s(k_s - k'_s) - \epsilon_{sr} k_r Z_r + \beta_{ss}\nu_s - \beta_{is}\nu'_s$	$\eta_s \beta_{ss} f_n^s - \beta_{is}\eta'_s f_n^{s'} - \epsilon_{sr} k_r Z_r f_R$
$F_{16} = P_s F_s P_{sr} F_r$	$Z_s(k_s - k'_s) - \epsilon_{sr} k_r Z_r + \beta_{ss}\nu_s - \beta_{ir}\nu'_R$	$\eta_s \beta_{ss} f_n^s - (\beta_{ir}\nu_r + \epsilon_{sr} k_r Z_r) f_R - \beta_{ir}\eta_r f_{\nu_s n}^r$
$F_{22} = P_s F_r P_s F_r$	$\beta_{sr}\nu_r - \beta'_{sr}\nu'_r$	$\beta_{sr}\eta_r f_{\nu_s n}^r - \beta'_{sr}\eta'_r f_{\nu_s n}^{r'}$
$F_{24} = P_s F_r P_r F_r$	$k_s Z_s - k_r Z_r + \beta_{sr}\nu_r - \beta_{rr}\nu'_r$	$\eta_r \beta_{sr} f_{\nu_s n}^r + (\beta_{sr}\nu_r - (\nu'_r \beta_{rr} + k_r Z_r)) f_R - \beta_{rr}\eta'_r f_{\nu_s n}^{r'}$
$F_{26} = P_s F_r P_{sr} F_r$	$(k_s - k'_s) Z_s + \beta_{sr}\nu_r - (\epsilon_{sr} k_r Z_r + \beta_{ir}\nu_r)$	$\beta_{sr}\eta_r f_{\nu_s n}^r + (-\epsilon_{sr} k_r Z_r - \beta_{ir}\nu_r + \beta_{sr}\nu_s) f_R - \beta_{ir}\eta'_r f_{\nu_s n}^{r'}$
$F_{33} = P_r F_s P_r F_s$	$\beta_{rs}\nu_s - \beta'_{rs}\nu'_s$	$\beta_{rs}\eta_s f_n^s - \beta'_{rs}\eta'_s f_n^{s'}$
$F_{34} = P_r F_s P_r F_r$	$\beta_{rs}\nu_s - \beta_{rr}\nu_r$	$(-\beta_{rr}\nu_r) f_R + \beta_{rs}\eta_s f_n^s - \beta_{rr}\eta_r f_{\nu_s n}^r$
$F_{35} = P_r F_s P_{sr} F_s$	$(1 - \delta_{35} k_r) Z_r + \beta_{rs}\nu_s + \delta_{35}(\beta_{is}\nu'_s + k_s Z_s)$	$(k_r - \delta_{35} k'_r) Z_r f_R + \beta_{rs}\eta_s f_n^s + \delta_{35}\beta_{is}\eta'_s f_n^{s'}$
$F_{36} = P_r F_s P_{sr} F_r$	$(1 - \delta_{36} k_r) Z_r + \beta_{rs}\nu_s + \delta_{36}(\beta_{ir}\nu_r + k_s Z_s)$	$(k_r - \delta_{36} k'_r) Z_r f_R + \beta_{rs}\eta_s f_n^s + \delta_{36}\beta_{ir}\eta_r f_{\nu_s n}^r$
$F_{44} = P_r F_r P_r F_r$	$\beta_{rr}\nu_r - \beta'_{rr}\nu'_r$	$(\nu_r \beta_{rr} - \nu'_r \beta'_{rr}) f_R + \beta_{rr}\eta_r f_{\nu_s n}^r - \beta'_{rr}\eta'_r f_{\nu_s n}^{r'}$
$F_{46} = P_r F_r P_{sr} F_r$	$(k_r - \delta_{46} k'_r) Z_r + \delta_{46} k_s Z_s + \beta_{rr}\nu_r + \delta_{46}\beta_{ir}\nu'_r$	$(\beta_{rr}\nu_r + \delta_{46}\beta_{ir}\nu_r + (k_r - \delta_{46} k'_r) Z_r) f_R + \beta_{rr}\eta_r f_{\nu_s n}^r + \delta_{46}\beta_{ir}\eta'_r f_{\nu_s n}^{r'}$
$F_{55} = P_{sr} F_s P_{sr} F_s$	$(\epsilon_{sr} k_r + \delta_{55} \epsilon'_{sr} k'_r) Z_r + (k_s + \delta_{55} k'_s) Z_s + \beta_{is}\nu_s + \delta_{55}\beta'_{is}\nu'_s$	$(\epsilon_{sr} k_r + \delta_{55} \epsilon'_{sr} k'_r) Z_r f_R + \beta_{is}\eta_s f_n^s + \delta_{55}\beta'_{is}\eta'_s f_n^{s'}$
$F_{56} = P_{sr} F_s P_{sr} F_r$	$(\epsilon_{sr} k_r + \delta_{55} \epsilon'_{sr} k'_r) Z_r + (k_s + \delta_{55} k'_s) Z_s + \beta_{is}\nu_s + \delta_{56}\beta_{ir}\nu_r$	$((\epsilon_{sr} k_r + \delta_{56} \epsilon'_{sr} k'_r) Z_r + \delta_{56}\beta_{ir}\nu_r) f_R + \beta_{is}\eta_s f_n^s + \delta_{56}\beta_{ir}\eta_r f_{\nu_s n}^r$
$F_{57} = P_{sr} F_s P_a F_s$	$2\delta_{57} k_a p + \delta_{57} \beta_{as}\nu'_s + \beta_{is}\nu_s - k_r Z_r + k_s Z_s$	$2\delta_{57} k_a f_s + \delta_{57} \beta_{as}\eta'_s f_n^{s'} + \beta_{is}\eta_s f_n^s - k_r Z_r f_R$
$F_{58} = P_{sr} F_s P_a F_r$	$\delta_{58}(2k_a p + \beta_{ar}\nu_r) + \beta_{is}\nu_s + \epsilon_{sr} k_r Z_r + k_s Z_s$	$\delta_{58}(2k_a f_s + \beta_{ar}\eta_r f_{\nu_s n}^r) + \beta_{is}\eta_s f_n^s + (\delta_{58}\nu_r \beta_{ar} + \epsilon_{sr} k_r Z_r) f_R$
$F_{59} = P_{sr} F_s P_0 F_s$	$-k_r Z_r + k_s Z_s + \beta_{is}\nu_s + \delta_{59}\nu'_s$	$-k_r Z_r f_R + \beta_{is}\eta_s f_n^s + \delta_{59}\eta'_s f_n^{s'}$
$F_{510} = P_{sr} F_s P_0 F_r$	$-k_r Z_r + k_s Z_s + \beta_{is}\nu_s + \delta_{610}\nu_r$	$(\delta_{610}\nu_r - k_r Z_r) f_R + \beta_{is}\eta_s f_n^s + \delta_{610}\eta_r f_{\nu_s n}^r$
$F_{66} = P_{sr} F_r P_{sr} F_r$	$(\epsilon_{sr} k_r + \delta_{66} \epsilon'_{sr} k'_r) Z_r + (k_s + \delta_{66} k'_s) Z_s + \beta_{ir}\nu_r + \delta_{66}\beta'_{ir}\nu'_r$	$(\beta_{ir}\nu_r + \delta_{66}\beta'_{ir}\nu'_r + (\epsilon_{sr} k_r + \delta_{66} \epsilon'_{sr} k'_r) Z_r) f_R + \beta_{ir}\eta_r f_{\nu_s n}^r + \delta_{66}\beta'_{ir}\eta'_r f_{\nu_s n}^{r'}$
$F_{68} = P_{sr} F_r P_a F_r$	$\delta_{68} 2k_a p + \beta_{ir}\nu_r + \delta_{68}\beta_{ar}\nu'_r - k_r Z_r + k_s Z_s$	$\delta_{68}\beta_{ar}\eta'_r f_{\nu_s n}^{r'} + \beta_{ir}\eta_r f_{\nu_s n}^r + (-k_r Z_r + \beta_{ir}\nu_r + \delta_{68}\beta_{ar}\nu'_r) f_R + 2\delta_{68} k_a f_s$
$F_{77} = P_a F_s P_a F_s$	$2(k_a + \delta_{77} k'_a) p + \beta_{as}\nu_s + \delta_{77}\beta'_{as}\nu'_s$	$2(k_a + \delta_{77} k'_a) f_s + \beta_{as}\eta_s f_n^s + \delta_{77}\beta'_{as}\eta'_s f_n^{s'}$
$F_{78} = P_a F_s P_a F_r$	$2(k_a + \delta_{78} k'_a) p + \delta_{78}\beta_{ar}\nu_r + \beta_{as}\nu_s$	$2(k_a + \delta_{78} k'_a) f_s + \delta_{78}\beta_{ar}\eta_r f_{\nu_s n}^r + \beta_{as}\eta_s f_n^s$
$F_{79} = P_a F_s P_0 F_s$	$2k_a p + \beta_{as}\nu_s + \delta_{79}\nu_s$	$2k_a f_s + \beta_{as}\eta_s f_n^s + \delta_{79}\eta'_s f_n^{s'}$
$F_{710} = P_a F_s P_0 F_r$	$2k_a p + \beta_{as}\nu_s + \delta_{710}\nu_r$	$2k_a f_s + \beta_{as}\eta_s f_n^s + \delta_{710}(\eta_r f_{\nu_s n}^r + \nu_r f_R)$
$F_{88} = P_a F_r P_a F_r$	$2(k_a + \delta_{88} k'_a) p + \beta_{ar}\nu_r + \delta_{88}\beta'_{ar}\nu'_r$	$2(k_a + \delta_{88} k'_a) f_s + \beta_{ar}\eta_r f_{\nu_s n}^r + \delta_{88}\beta'_{ar}\eta'_r f_{\nu_s n}^{r'} + (\beta_{ar}\nu_r + \beta'_{ar}\nu'_r) f_R$
$F_{810} = P_a F_r P_0 F_r$	$2k_a p + \beta_{ar}\nu_r + \delta_{810}\nu_r$	$2k_a f_s + (\beta_{ar}\nu_r + \delta_{810}\nu'_r) f_R + \beta_{ar}\eta_r f_{\nu_s n}^r + \delta_{810}\eta'_r f_{\nu_s n}^{r'}$
$F_{99} = P_0 F_s P_0 F_s$	$\nu_s + \delta_{99}\nu'_s$	$\eta_s f_n^s + \delta_{99}\eta'_s f_n^{s'}$
$F_{910} = P_0 F_s P_0 F_r$	$\nu_s + \delta_{910}\nu_r$	$\eta_s f_n^s + \delta_{910}(\nu_s f_R + \eta_r f_{\nu_s n}^r)$
$F_{1010} = P_0 F_r P_0 F_r$	$\nu_r + \delta_{1010}\nu'_r$	$\eta_r f_n^r + \delta_{1010}\eta'_r f_{\nu_s n}^{r'} + (\nu_r + \delta_{1010}\nu'_r) f_R$
$F_{113} = P_s F_s P_r F_s K_{se}$	$k_s Z_s + \beta_{ss}\nu_s - (k_r Z_r + \beta_{rs}\nu'_s + \beta_{ser}\epsilon_{se} k_{se})$	$\beta_{ss}\eta_s f_n^s - \beta_{rs}\eta'_s f_n^{s'} - k_r Z_r f_R$
$F_{114} = P_s F_s P_r F_s K_{de}$	$k_s Z_s + \beta_{ss}\nu_s - (k_r Z_r + \beta_{rs}\nu'_s + \beta_{der} k_{de})$	$\beta_{ss}\eta_s f_n^s - \beta_{rs}\eta'_s f_n^{s'} - (k_r Z_r + \beta_{der} k_{de}) f_R$

C.3 Low order magnetic force lines characteristics with sinusoidal supply and sinusoidal mmfs

Table C.3 results from the simplification of previous section Table C.2 in sinusoidal case, and considering sinusoidal mmfs. LF column ticks indicate a low frequency harmonic (< 400 Hz).

Name	Spatial orders	Frequencies	LF
$F_{11} = P_s F_s P_s F_s$	$2p$	$2f_s$	X
$F_{12} = P_s F_s P_s F_r$	$2p$	$2f_s$	X
$F_{13} = P_s F_s P_r F_s$	$Z_s k_s - Z_r k_r + (\beta_{ss} - \beta_{rs})p$	$-f_s(k_r Z_r(1-s)/p + \beta_{rs} - \beta_{ss})$	
$F_{14} = P_s F_s P_r F_r$	$Z_s k_s - Z_r k_r + (\beta_{ss} - \beta_{rr})p$	$-f_s(k_r Z_r(1-s)/p + \beta_{rr} - \beta_{ss})$	
$F_{15} = P_s F_s P_{sr} F_s$	$Z_s(k_s - k'_s) - \epsilon_{sr} k_r Z_r + (\beta_{ss} - \beta_{is})p$	$-f_s(\epsilon_{sr} k_r Z_r(1-s)/p + \beta_{is} - \beta_{ss})$	
$F_{16} = P_s F_s P_{sr} F_r$	$Z_s(k_s - k'_s) - \epsilon_{sr} k_r Z_r + (\beta_{ss} - \beta_{ir})p$	$-f_s(k_r Z_r/p + \beta_{ir} - \beta_{ss})$	
$F_{22} = P_s F_r P_s F_r$	$2p$	$2sf_s$	X
$F_{24} = P_s F_r P_r F_r$	$k_s Z_s - k_r Z_r + (\beta_{sr} - \beta_{rr})p$	$-f_s(k_r Z_r/p + \beta_{rr} - \beta_{sr})$	
$F_{33} = P_r F_s P_r F_s$	$2p$	$2f_s$	X
$F_{34} = P_r F_s P_r F_r$	$2p$	$2f_s$	
$F_{35} = P_r F_s P_{sr} F_s$	$(k_r - \delta_{35} k'_r)Z_r + \beta_{rs}p + \delta_{35}(\beta_{is}p + k_s Z_s)$	$-f_s((\delta_{35} k'_r - k_r)(1-s)Z_r/p - \delta_{35}\beta_{is} - \beta_{rs})$	
$F_{44} = P_r F_r P_r F_r$	$2p$	$2f_s$	X
$F_{55} = P_{sr} F_s P_{sr} F_s$	$(\epsilon_{sr} k_r + \delta_{55} \epsilon'_{sr} k'_r)Z_r + (k_s + \delta_{55} k'_s)Z_s + (\beta_{is} + \delta_{55} \beta'_{is})p$	$f_s((\epsilon_{sr} k_r + \delta_{55} \epsilon'_{sr} k'_r)Z_r(1-s)/p + \beta_{is} + \delta_{55} \beta'_{is})$	
$F_{57} = P_{sr} F_s P_a F_s$	$(2\delta_{57} k_a + \delta_{57} \beta_{as} + \beta_{is})p - k_r Z_r + k_s Z_s$	$-f_s(k_r Z_r(1-s)/p - \beta_{is} - \delta_{57}(\beta_{as} + 2k_a))$	
$F_{59} = P_{sr} F_s P_0 F_s$	$-k_r Z_r + k_s Z_s + (\beta_{is} + \delta_{59})p$	$-f_s(k_r Z_r(1-s)/p - \beta_{is} - \delta_{59})$	
$F_{510} = P_{sr} F_s P_0 F_r$	$-k_r Z_r + k_s Z_s + (\beta_{is} + \delta_{610})p$	$-f_s(k_r Z_r(1-s)/p - \beta_{is} - \delta_{610})$	
$F_{79} = P_a F_s P_0 F_s$	$2p$	$2f_s$	X
$F_{710} = P_a F_s P_0 F_r$	$2p$	$2f_s$	X
$F_{810} = P_a F_r P_0 F_r$	$2p$	$2f_s$	X
$F_{99} = P_0 F_s P_0 F_s$	$2p$	$2f_s$	X
$F_{910} = P_0 F_s P_0 F_r$	$2p$	$2f_s$	X
$F_{1010} = P_0 F_r P_0 F_r$	$2p$	$2f_s$	X
$F_{113} = P_s F_s P_r F_s K_{se}$	$k_s Z_s - k_r Z_r + (\beta_{ss} - \beta_{rs})p - \beta_{ser} \epsilon_{se} k_{se}$	$-f_s(k_r Z_r(1-s)/p + \beta_{rs} - \beta_{ss})$	
$F_{114} = P_s F_s P_r F_s K_{de}$	$k_s Z_s - k_r Z_r + (\beta_{ss} - \beta_{rs})p - \beta_{der} k_{de}$	$-f_s(k_r Z_r(1-s)/p + \beta_{rs} - \beta_{ss} + \beta_{der} k_{de})$	

C.4 Slot combination database of motor M1

In this appendix are presented the maximum and average sound power levels in dBA for all the slot combinations Z_s/Z_r from 10 to 50, including odd numbers, on motor M1 during starting phase from 5 to 90 Hz ($p = 2$). This database has been built following the method exposed in section 4.2.1.1.1, similarly to the ALSTOM database which has been partly used to design the low magnetic noise prototype M7. Note that this database can only be used for a motor whose natural frequencies are close to motor M1 ones (cf. Table 3.3).

$\begin{matrix} Z_s \\ Z_r \end{matrix}$	10	11	12	13	14	15	16	17	18	19	20	21	22	23	24	25	26	27	28	29
10	52/66	65/88	63/86	66/86	61/85	63/80	62/86	65/85	63/86	63/81	54/70	63/86	64/89	64/86	63/86	62/85	63/81	63/85	62/80	69/103
11	64/88	54/67	67/87	64/80	65/88	69/88	70/93	70/93	70/87	68/97	66/89	65/80	55/71	66/80	63/88	68/86	67/84	70/88	72/90	65/88
12	64/88	66/93	34/42	66/82	63/89	63/80	34/42	65/79	61/84	63/80	35/43	64/85	67/93	67/85	37/46	67/86	65/89	67/92	35/44	68/107
13	63/77	63/79	66/87	52/63	66/84	59/76	63/91	70/88	68/87	72/93	72/93	70/97	71/87	63/79	63/85	69/93	54/64	68/93	63/86	69/91
14	60/80	66/82	65/98	65/87	52/64	65/82	61/81	65/79	65/92	66/86	63/85	53/67	62/79	67/90	67/98	65/81	65/90	69/98	54/67	71/105
15	61/75	67/95	61/80	62/74	65/88	51/60	65/84	60/71	61/86	63/79	67/87	69/87	73/96	72/93	69/87	69/87	62/84	67/91	64/87	72/110
16	63/87	69/101	34/42	68/97	65/91	66/85	36/45	66/82	61/76	63/88	35/44	68/84	69/101	66/81	37/45	66/82	67/100	70/93	36/46	69/104
17	68/93	69/98	61/77	66/89	68/98	60/79	66/85	51/61	66/88	61/82	64/90	63/78	68/105	70/87	69/87	72/93	72/93	68/87	70/87	71/97
18	67/95	69/92	63/92	67/88	66/95	61/77	62/88	65/82	52/65	66/89	64/100	62/81	68/99	65/78	61/77	62/78	68/97	53/64	69/96	61/77
19	65/89	68/95	63/77	68/95	64/89	63/78	63/84	59/80	67/84	49/63	66/87	65/101	61/76	60/78	63/82	65/84	73/102	69/87	72/93	72/93
20	57/72	67/96	35/44	71/100	64/93	66/82	36/45	67/90	63/88	67/85	38/48	67/90	65/97	64/87	37/46	65/79	70/102	69/88	37/46	69/112
21	65/86	65/77	64/79	68/97	54/62	66/87	59/74	62/79	64/86	63/101	67/84	53/65	68/83	65/97	64/83	59/75	67/96	63/79	54/64	70/87
22	66/97	56/75	67/96	68/84	62/81	70/94	65/93	62/78	69/92	61/74	65/98	68/83	62/81	68/82	66/96	62/87	63/87	65/87	60/81	66/83
23	66/89	66/81	66/81	68/90	69/91	71/97	62/76	66/82	66/89	62/77	63/92	65/95	69/84	60/75	68/85	65/102	65/91	59/80	67/91	62/77
24	67/96	66/94	36/45	66/90	69/97	67/91	37/46	68/87	64/85	65/86	37/47	65/93	66/101	70/89	40/50	70/87	68/98	66/92	37/48	68/92
25	64/84	69/94	67/85	67/86	71/96	69/89	64/80	70/94	59/78	58/72	60/72	63/78	59/75	65/96	70/90	60/81	70/91	66/96	67/92	60/67
26	65/87	66/86	67/95	54/68	66/92	63/79	68/100	70/92	65/90	66/83	62/78	65/79	67/93	61/77	66/93	71/94	58/73	71/95	66/95	68/92
27	69/92	66/93	64/94	69/94	68/94	68/91	70/89	66/86	52/61	67/95	64/101	61/74	68/99	61/74	63/81	65/97	72/98	50/63	72/100	66/96
28	65/88	69/89	36/45	65/95	55/69	64/88	37/47	67/82	67/95	70/101	37/47	55/67	66/95	68/98	39/48	62/83	67/98	72/100	42/52	74/107
29	69/98	64/81	66/100	65/85	71/95	71/95	68/89	71/99	60/84	70/96	68/108	67/88	63/89	62/75	66/84	61/74	65/86	67/98	74/103	51/64
30	58/74	69/97	62/89	65/79	65/96	52/66	63/92	63/77	65/89	67/90	56/70	67/96	67/99	61/76	61/83	65/87	64/86	64/91	67/96	75/113
31	69/104	62/80	68/99	71/95	68/89	71/95	71/95	71/89	73/94	69/94	67/105	70/102	61/76	60/85	58/80	61/79	69/91	60/75	66/97	67/93
32	65/90	70/104	35/44	67/95	70/99	63/92	38/47	63/89	67/91	63/87	37/46	70/96	70/104	66/81	35/42	59/73	65/93	70/100	37/47	67/108
33	68/98	57/76	67/97	65/90	69/89	68/89	72/95	72/95	70/89	70/89	69/99	67/95	60/82	67/84	67/98	56/76	67/94	63/82	69/92	58/72
34	69/96	70/101	62/80	67/83	67/101	60/81	65/91	53/65	65/96	60/70	66/99	65/81	70/108	70/96	60/94	60/76	64/87	63/79	64/93	68/92
35	65/83	62/80	70/104	64/77	55/69	69/89	67/89	73/95	73/95	68/89	70/89	57/68	61/75	71/101	71/103	64/83	62/78	61/74	59/76	64/78
36	69/98	71/95	37/45	70/91	68/98	62/79	37/47	64/86	54/67	65/98	38/48	64/86	71/102	66/96	40/49	66/92	69/99	56/70	39/48	62/82
37	64/85	63/86	71/103	63/89	67/85	67/88	71/95	70/89	74/95	73/95	70/89	72/93	64/82	65/83	70/101	69/98	62/80	59/74	60/78	65/84
38	65/91	68/93	61/86	71/97	68/93	65/91	65/92	62/75	64/89	50/66	64/97	61/81	65/89	63/83	61/89	69/95	72/106	66/82	60/81	61/78
39	62/83	64/88	68/97	55/68	70/93	63/85	69/101	72/98	69/90	74/95	74/95	70/89	72/94	67/95	68/95	65/86	58/72	65/96	69/96	63/79
40	56/69	63/78	37/46	72/103	63/78	67/82	38/47	64/79	64/89	65/91	40/50	66/97	63/88	64/77	38/48	64/82	72/105	70/102	39/50	62/78
41	58/85	66/87	69/101	62/79	71/100	60/72	67/95	62/82	71/89	68/90	74/95	74/95	69/90	71/89	62/74	65/93	60/78	69/97	71/102	65/91
42	62/89	62/75	61/85	68/96	54/68	68/90	62/82	65/89	65/89	61/76	66/89	53/64	67/91	63/75	65/85	63/80	68/100	65/85	56/72	67/95
43	60/79	61/79	67/96	63/75	72/104	63/77	67/87	65/85	61/79	70/89	69/90	74/95	75/95	69/89	70/89	63/81	63/86	66/93	71/103	70/102
44	66/95	59/76	38/48	70/92	63/89	71/97	38/48	61/79	69/95	63/81	39/49	66/85	65/84	67/85	39/49	64/76	67/96	61/76	39/49	70/97
45	63/77	61/77	64/90	64/83	69/98	54/67	68/93	63/77	53/70	66/92	70/89	70/89	75/95	74/95	69/89	70/89	65/93	56/70	68/97	65/86
46	67/92	59/79	62/89	64/83	67/94	71/100	62/78	67/82	68/92	62/78	65/100	59/76	67/87	61/77	67/90	57/68	66/98	62/74	66/96	65/81
47	66/90	61/85	61/78	66/89	67/83	63/84	71/100	61/73	57/72	65/89	66/95	71/89	68/89	75/95	75/95	69/89	72/92	65/84	63/80	59/77
48	64/86	61/82	34/41	64/77	67/100	69/93	39/49	69/90	66/86	64/92	38/50	64/77	63/87	68/96	42/52	67/93	61/83	66/82	41/52	64/85
49	69/93	64/78	59/76	61/79	58/75	61/82	72/99	64/82	68/86	65/87	68/102	59/70	71/93	68/89	75/95	75/95	69/89	71/89	60/75	67/96
50	57/72	64/80	57/80	60/77	67/99	67/83	63/83	72/97	61/84	60/76	59/77	64/84	62/88	59/74	68/88	59/83	69/87	58/70	64/84	64/79

$\begin{array}{c} Z_s \\ Z_r \end{array}$	30	31	32	33	34	35	36	37	38	39	40	41	42	43	44	45	46	47	48	49	50
10	55/72	70/105	64/83	71/97	68/92	70/91	68/97	69/88	64/90	72/94	55/73	72/94	65/90	69/87	68/93	69/89	68/99	69/92	66/94	72/95	57/80
11	70/95	61/83	71/99	58/76	72/102	62/82	72/98	60/83	70/90	70/88	62/76	71/97	65/90	73/94	60/80	73/94	65/90	71/89	62/85	70/88	69/86
12	60/83	70/109	36/45	68/101	62/85	74/101	37/46	74/106	61/80	71/92	36/44	71/92	63/91	71/94	37/46	69/87	67/91	73/94	38/47	73/94	66/85
13	66/85	72/92	69/88	69/88	72/90	66/82	69/99	62/81	74/99	57/69	74/100	63/86	71/94	62/79	72/91	65/83	65/77	71/91	62/84	69/88	66/83
14	65/91	69/105	67/96	69/91	71/103	56/73	71/108	68/90	67/102	70/95	63/81	75/101	56/72	74/100	64/79	71/91	67/89	71/90	67/96	58/69	68/98
15	54/67	73/112	62/89	70/104	61/77	72/91	65/82	69/88	68/88	65/82	72/90	59/74	70/97	64/78	75/101	56/67	76/106	66/79	72/100	62/71	71/90
16	64/85	75/106	39/49	74/110	63/90	73/103	36/45	72/102	64/91	72/105	37/46	72/110	61/84	71/98	37/48	71/95	65/82	75/100	39/50	75/98	65/82
17	62/75	70/99	63/91	75/105	55/70	76/109	63/84	74/107	60/74	70/91	65/82	65/82	69/89	69/89	65/79	66/80	71/90	61/73	71/97	67/84	76/106
18	65/93	70/91	66/93	69/99	65/91	76/108	54/72	76/113	64/82	72/100	62/80	70/91	68/101	61/80	73/105	57/73	74/110	61/76	69/104	70/89	61/79
19	69/86	72/100	63/84	69/92	58/78	72/102	64/86	77/111	52/67	77/106	64/82	74/106	61/82	71/91	61/73	67/87	66/85	69/87	68/87	65/83	65/81
20	59/77	70/113	37/48	72/106	69/100	71/91	38/47	73/105	65/86	78/108	41/51	77/113	65/84	74/100	38/48	71/91	64/87	70/99	38/50	73/102	59/78
21	71/97	72/93	72/93	69/87	69/86	58/71	62/76	71/98	60/75	72/101	65/87	78/107	55/72	78/107	65/88	74/98	61/73	71/91	63/74	59/70	64/83
22	73/103	65/79	71/108	60/83	72/111	64/83	73/107	64/87	62/78	69/92	64/79	72/99	67/93	78/108	65/87	78/104	67/93	74/98	64/92	71/91	63/77
23	70/98	66/85	68/87	69/87	72/93	73/93	68/86	69/86	64/87	69/104	62/75	71/91	62/82	73/101	66/88	78/109	62/74	78/104	67/83	74/97	61/78
24	66/92	65/83	38/47	71/100	66/96	74/110	39/48	74/114	65/90	72/102	38/49	65/85	68/88	71/91	40/51	73/103	68/84	79/108	43/54	79/104	68/88
25	67/92	57/76	58/71	65/85	71/102	69/87	68/86	72/93	72/93	69/90	68/87	67/98	64/89	60/74	61/75	71/91	61/77	73/102	68/92	79/105	64/83
26	64/87	69/92	61/86	65/81	71/103	67/83	70/108	62/86	74/107	59/78	74/109	62/83	70/103	66/83	68/98	64/77	64/82	72/91	66/94	73/99	70/88
27	69/94	58/70	70/92	59/74	66/98	64/82	56/76	63/78	70/89	68/85	72/92	72/92	68/87	69/87	62/72	58/70	63/83	65/91	63/77	72/90	60/80
28	66/98	71/108	35/42	70/92	62/82	59/73	39/50	66/85	69/97	73/103	40/50	75/109	56/74	75/109	39/51	72/99	68/98	66/88	40/51	61/76	64/79
29	74/105	67/102	71/109	59/79	70/92	63/85	59/85	66/85	70/99	68/81	58/76	68/85	68/85	72/92	72/92	68/87	69/86	61/72	67/89	68/102	64/86
30	56/73	76/115	65/97	72/107	63/78	69/92	60/80	63/79	66/93	65/75	59/77	64/79	73/106	61/71	75/110	59/76	76/115	62/75	73/109	66/79	63/86
31	76/110	65/86	75/115	66/92	73/106	61/78	71/92	63/79	59/72	61/77	61/82	64/85	71/101	63/78	69/84	69/84	72/93	72/93	69/85	67/84	60/74
32	65/93	76/109	43/53	76/113	64/98	73/106	37/48	70/92	61/94	62/76	36/45	61/79	70/106	66/82	39/51	71/105	61/85	76/110	42/54	76/106	62/82
33	69/104	66/99	77/109	67/86	78/112	68/98	72/108	58/76	69/91	63/77	65/82	57/71	67/100	64/80	62/82	65/80	67/99	68/86	69/90	71/92	71/92
34	61/75	69/102	66/100	78/108	57/75	79/113	66/92	74/110	61/75	70/92	63/79	63/87	65/82	64/84	61/83	66/85	71/106	65/78	72/105	62/78	76/115
35	69/92	59/77	70/102	68/91	79/109	60/74	79/114	68/102	74/107	61/75	71/92	61/70	61/78	61/75	63/80	65/85	72/101	67/84	62/84	62/75	67/87
36	64/82	72/92	37/47	71/102	67/99	79/111	44/54	79/116	67/91	74/103	39/50	70/93	64/84	64/83	39/47	59/73	69/87	66/80	41/50	65/75	65/95
37	67/95	64/77	71/92	59/74	72/103	67/95	80/115	60/80	80/113	68/102	74/104	61/77	72/92	63/70	62/81	65/80	61/75	63/78	64/85	66/80	70/101
38	66/100	62/80	61/92	69/92	60/81	72/106	67/95	80/114	54/73	80/109	67/90	73/110	64/86	71/92	64/77	62/79	65/88	62/78	60/80	63/80	70/97
39	65/94	62/80	64/81	64/82	70/92	60/73	73/109	68/97	80/108	61/75	80/110	69/102	75/104	61/75	71/92	64/78	62/78	61/74	64/86	58/76	68/91
40	61/80	63/80	39/47	67/90	62/83	71/92	38/48	73/108	68/94	80/111	45/55	81/116	69/92	74/104	41/49	72/91	63/79	65/83	40/48	62/78	59/73
41	60/75	56/74	57/73	63/77	66/84	63/80	70/92	61/81	72/103	68/96	80/116	68/90	81/110	70/97	74/109	62/79	71/92	63/74	62/80	61/77	60/74
42	69/100	63/80	63/86	65/83	66/89	61/77	62/79	71/92	60/72	73/105	69/96	81/110	59/77	81/110	69/97	74/101	66/85	72/92	67/91	60/72	64/87
43	60/73	64/90	60/75	61/78	67/89	67/86	65/85	65/79	71/92	60/72	73/109	70/93	81/113	56/68	81/115	69/91	75/110	61/72	73/92	66/83	64/90
44	73/106	68/83	40/50	64/86	61/85	65/87	41/52	64/94	63/78	71/92	39/47	74/102	69/102	81/111	46/56	81/107	69/101	75/101	41/51	72/92	63/78
45	58/72	67/87	69/99	63/84	62/79	66/88	58/79	67/85	63/82	63/74	71/92	61/76	74/107	70/91	81/111	63/75	81/116	70/95	75/110	65/82	72/92
46	72/101	70/96	61/80	63/78	66/85	63/86	63/90	63/78	66/96	63/77	61/75	70/92	64/85	74/105	70/97	81/112	64/86	81/108	70/91	76/100	63/79
47	61/77	70/99	72/105	65/81	64/78	61/74	62/90	65/81	68/96	64/77	65/86	64/82	71/92	61/74	74/105	71/99	82/111	57/70	82/116	72/100	75/110
48	69/95	69/93	42/52	68/91	69/99	63/84	34/41	63/80	63/100	67/83	41/51	65/86	66/86	71/91	39/49	74/106	70/90	82/111	47/58	82/107	71/97
49	65/84	64/82	72/107	70/90	62/77	60/76	61/83	61/74	66/94	64/77	65/83	62/77	61/74	65/79	72/92	60/71	74/105	72/96	82/113	57/73	82/116
50	60/78	58/75	58/76	69/93	73/106	65/80	62/87	61/79	60/79	62/75	59/81	61/81	64/97	63/77	62/80	72/91	61/78	74/105	71/100	82/108	70/93

References

- [1] ACCARDO, L., FIORETTO, M., GIANNINI, G., AND MARINOG, P. Techniques of PWM space vector modulation for the reduction of magnetic acoustic noise in traction motors. In *Proceedings of SPEEDAM 2006* (May 2006). [23](#), [115](#)
- [2] AH-JACO, A. *Modélisation des moteurs asynchrones triphasés en régime transitoire avec saturation et harmoniques d'espace. Application au diagnostic*. PhD thesis, Université Claude Bernard, Lyon, France, July 1997. [29](#), [30](#)
- [3] AIT-HAMMOUDA, A. *Prédimensionnement et étude de sensibilité vibro-acoustique de machines courant alternatif et vitesse variable*. PhD thesis, Université des Sciences et des Technologies de Lille, France, Mar. 2005. [3](#), [4](#), [18](#), [30](#), [55](#), [108](#), [120](#)
- [4] ALUZRI, A., AND MOHAMMED, I. Vector optimization design of a shaded-pole induction motor. *IEEE Trans. on Energy Conversion* **7**, 3 (Sept. 2002). [25](#)
- [5] AMOR, A. H., TIMAR, P., AND POLOUJADOFF, M. Induction squirrel cage machine design with minimization of electromagnetic noise. *IEEE Trans. on En. Conv.* **10**, 4 (Dec. 1995). [25](#), [26](#)
- [6] AMOR, A. H., TIMAR, P., AND POLOUJADOFF, M. Optimum design of electromagnetic devices by the state variable method : application to transformers. In *Proceedings of the 6th International Conference on Optimization of Electrical and Electronics Equipments* (May 1998), vol. 1. [25](#)
- [7] AMRI, M. E. Measurement of magnetostriction and stress dependent magnetisation in electrical steel. In *Proceedings of 3rd international seminar on vibrations and acoustic noise of electric machinery* (2002). [14](#)
- [8] ANWAR, M., AND HUSSAIN, I. Radial force calculation and acoustic noise prediction in switched reluctance machines. *IEEE Transaction on Industry Applications* **36**, 6 (2000). [53](#), [137](#)

-
- [9] APPELBAUM, J., FUCHS, E. F., AND MHITR, J. C. Optimization of three-phase induction motor design. part I: Formulation of the optimization technique. In *IEEE Summer Power Meeting* (July 1986), no. 86. 25
 - [10] ARKKIO, A. Unbalanced magnetic pull in cage induction motors with asymmetry in rotor structure. *IEEE Proceedings of EMD* (1997). 82, 137
 - [11] ASTFALCK, A. *Analysis of electromagnetic force and noise in inverter driven induction motors*. PhD thesis, University of South Wales, Aug. 2002. 13, 21
 - [12] BANDLER, J., CHENG, Q., DAKROURY, S., MOHAMED, A., BAKR, M., MADSEND, K., AND SONDERGAARD, J. Space mapping: The state of the art. *IEEE Trans. on Microw. Theory Tech.* 52, 1 (Jan. 2004). 26
 - [13] BAO, G., ZHANG, D., SHI, J., AND JIANG, J. Optimal design for cogging torque reduction of transverse flux permanent motor using particle swarm optimization algorithm. In *4th International Power Electronics and Motion Control Conference* (2004), vol. 1. 26
 - [14] BEKEMANS, M. *Modélisation des machines électriques en vue du contrôle des efforts radiaux*. PhD thesis, Université Catholique de Louvain, Belgium, Mar. 2006. xiv, 9, 10, 53, 70
 - [15] BELAHACEN, A. *Magnetoelasticity, magnetic forces and magnetostriction in electrical machines*. PhD thesis, Helsinki University of Technology, Finland, Aug. 2004. xiv, 7, 10, 12, 13, 14
 - [16] BELHACEN, A. Vibrations of rotating electrical machines due to magnetomechanical coupling and magnetostriction. *IEEE Trans. on Magnetics* 42, 4 (Apr. 2006). 14
 - [17] BELKHAYAT, D., ROGER, D., AND BRUDNY, J. Active reduction of magnetic noise in asynchronous machine controlled by stator current harmonics. In *Proc. of EMD conference* (Sept. 1998). 25
 - [18] BELMANS, R., AND HAMEYER, K. Impact of inverter supply and numerical calculation techniques in audible noise problems. *International Seminar on Vibrations and Acoustic Noise of Electric Machinery* (1998). 19, 24
 - [19] BELMANS, R., VERDYK, GEYSEN, AND FINDLAY. Electro-mechanical analysis of the audible noise of an inverter-fed squirrel cage induction motor. *IEEE Trans. on Ind. Appl.* 27, 3 (May/June 1991). 13, 24
 - [20] BESNERAIS, J. L., FASQUELLE, A., HECQUET, M., LANFRANCHI, V., BROCHET, P., AND RANDRIA, A. A fast noise-predictive multiphysical model of the PWM-controlled induction machine. In *Proc. of the International Conference on Electrical Machines (ICEM'06)* (Chania, Greece, July 2006). 18, 121

- [21] BESNERAIS, J. L., FASQUELLE, A., LANFRANCHI, V., HECQUET, M., AND BROCHET, P. Mixed-variable optimal design of induction motors including efficiency, noise and thermal criteria. In *Proc. of the International Conference on Engineering and Optimization (EngOpt)* (Rio de Janeiro, Brazil, June 2008). [122](#), [125](#)
- [22] BESNERAIS, J. L., FASQUELLE, A., PELLE, J., HARMAND, S., HECQUET, M., LANFRANCHI, V., BROCHET, P., AND RANDRIA, A. Multiphysics modeling: electro-vibro-acoustics and heat transfer of induction machines. In *Proc. of the International Conference on Electrical Machines (ICEM'08)* (Villamora, Portugal, Sept. 2008). [125](#)
- [23] BESNERAIS, J. L., LANFRANCHI, V., HECQUET, M., AND BROCHET, P. Calcul du bruit acoustique d'une machine asynchrone a pas fractionnaire. In *Proceeding of EF'07* (Sept. 2007). [82](#)
- [24] BESNERAIS, J. L., LANFRANCHI, V., HECQUET, M., AND BROCHET, P. Multi-objective optimization of the induction machine with minimization of audible electromagnetic noise. *European Physics Journal - Applied Physics* 39, 2 (Aug. 2007). [120](#), [121](#), [125](#)
- [25] BESNERAIS, J. L., LANFRANCHI, V., HECQUET, M., AND BROCHET, P. Bruit audible d'origine magnétique des machines asynchrones. *Techniques de l'Ingénieur D6*, D 3580 (Nov. 2008). [92](#)
- [26] BESNERAIS, J. L., LANFRANCHI, V., HECQUET, M., AND BROCHET, P. Characterization of the audible magnetic noise emitted by traction motors in railway rolling stock. In *Proc. of the INTERNOISE conference* (Shanghai, China, Oct. 2008). [106](#)
- [27] BESNERAIS, J. L., LANFRANCHI, V., HECQUET, M., AND BROCHET, P. Multi-objective optimization of induction machines including mixed variables and noise minimization. *IEEE Trans. on Mag.* 44, 6 (June 2008). [125](#)
- [28] BESNERAIS, J. L., LANFRANCHI, V., HECQUET, M., BROCHET, P., AND FRIEDRICH, G. Acoustic noise of electromagnetic origin in a fractional-slot induction machine. *COMPEL* 27, 5 (Feb. 2008). [20](#), [33](#), [79](#), [81](#), [82](#)
- [29] BESNERAIS, J. L., LANFRANCHI, V., HECQUET, M., BROCHET, P., AND FRIEDRICH, G. Characterisation of the radial vibration force and vibration behaviour of a PWM-fed fractional-slot induction machine. *IET* (Nov. 2008). [24](#), [95](#), [99](#)
- [30] BLAABJERG, F., PEDERSON, J., RITCHIE, E., AND NIELSEN, P. Determination of mechanical resonances in induction motors by random modulation and acoustic measurement sinusoidal PWM drives using a randomly modulated carrier. *IEEE Trans. on Industrial Applications* 31 (July 1995). [116](#)

-
- [31] BOLDEA, I., AND NASAR, S. A. *The induction machine handbook*. CRC Press, 2002. [15](#), [20](#), [33](#), [41](#), [111](#), [130](#)
- [32] BORISOV, K., AND TRZYNADLOWSKI, A. M. Experimental investigation of a naval propulsion drive model with pwm-based attenuation of the acoustic and electromagnetic noise. *IEEE Trans. on Ind. Elec.* 53, 2 (2006). [23](#)
- [33] BOSSIO, G., ANGELO, C. D., SOLSONA, J., GARCIA, G., AND VALLA, M. A 2-D model of the induction machine: an extension of the modified winding function approach. *IEEE Trans. on Energy Conversion* 19, 1 (Mar. 2004). [14](#), [29](#)
- [34] BOUCHARD., R., AND OLIVIER, G. *Conception de moteurs asynchrones triphasés*. Editions de l'Ecole Polytechnique de Montréal, 2005. [32](#)
- [35] BOYS, J., AND HANDLEY, P. Spread spectrum switching: low noise modulation technique for PWM inverter drives. *IEE Proc. on Elec. Power Appl.* 139, 3 (May 1992). [23](#)
- [36] BRUDNY, J. *Etude quantitative des harmoniques du couple du moteur asynchrone triphasé d'induction*. Habilitation à Diriger des Recherches, Lille, 1991. [39](#), [78](#), [103](#), [136](#)
- [37] CARMELI, M., DEZZA, F. C., AND MAURI, M. Electromagnetic vibration and noise analysis of an external rotor permanent magnet motor. In *Proceedings of SPEEDAM* (2006). [137](#)
- [38] CASSORET, B., CORTON, R., ROGER, D., AND BRUDNY, J. Magnetic noise reduction of induction machines. *IEEE Trans. on Power Electronics* 18, 2 (Mar. 2003). [25](#), [104](#), [119](#)
- [39] CESTER, P. Magnetostriction as a source of noise and vibrations, design and measurement set-up on an experimental induction motor. In *Proceedings of summer seminar on Nordic Network for Multi Disciplinary Optimised Electric Drives* (June 2002). [14](#)
- [40] CHANG, S., AND YACAMINI, R. Experimental study of the vibrational behaviour of machine stators. *IEE Proc on Elec Pow App* 143, 3 (1996). [21](#)
- [41] CHAU, K., AND CHAN, S. Reduction of current ripple and acoustic noise in dual inverter pole-changing induction motor drives. In *Proceedings of the 3th annual IEEE Power Electronics Specialists Conference (PESC'00)* (2000), vol. 1. [25](#)
- [42] CHO, D., JUNG, H., AND LEE, C. Induction motor design for electric vehicle using a niching genetic algorithm. *IEEE Trans. on I. A.* 37, 4 (2001). [26](#)

-
- [43] CHO, D., AND KIM, K. Modelling of electromagnetic excitation forces of small induction motor for vibration and noise analysis. *IEE Proc. on Electr. Power Appl.* 145, 3 (1998). 20
 - [44] CORTON, R., SAWEZY, H., BELKHAYAT, D., AND BRUDNY, J. Principe of magnetic noise active reduction using three phase systems due to PWM inverter switching. In *2nd International Seminar on Vibrations and Acoustic Noise of Electric Machinery (VANEM)* (2000). 25
 - [45] DEB, K., PRATAP, A., AGARWAL, S., AND MEYARIVAN, T. A fast and elitist multi-objective genetic algorithm: NSGA-II. *IEEE Trans. on Evolutionary Computation* 6, 2 (Apr. 2002). 122
 - [46] DELAERE, K., HAMEYER, K., AND BELMANS, R. Static eccentricity as a cause for audible noise of induction motors. In *Proceedings of the international conference on Electrical machines (ICEM)* (1998), vol. 1. 20
 - [47] DELAERE, K., HEYLEN, W., BELMANS, R., AND HAMEYER, K. Finite element analysis of electrical machine vibrations caused by Lorentz, Maxwell and magnetostriction forces. *IEE Seminar on Current Trends in the Use of Finite Elements in Electromechanical Design and Analysis* (2000). 14
 - [48] DELAERE, K., HEYLEN, W., BELMANS, R., AND HAMEYER, K. Local magnetostriction forces for finite element analysis. *IEEE Trans on Magnetism* 36, 5 (Sept. 2000). 14
 - [49] DELAERE, K., HEYLEN, W., BELMANS, R., AND HAMEYER, K. Comparison of induction machine stator vibration spectra induced by reluctance forces and magnetostriction. *IEEE Trans. on Magnetism* 38, 2 (Mar. 2002). 14
 - [50] DELAERE, K., IADEVAIA, M., HEYLEN, W., SAS, P., HAMEYER, K., AND BELMANS, R. Statistical energy analysis of acoustic noise and vibration for electric motors: Transmission from air gap field to motor frame. *IEEE Proc. on Ind. Appl.* (1999). 18
 - [51] DESBIENS, G. *Machines à induction bobinées sur dents*. PhD thesis, INPG, France, Oct. 2003. 19
 - [52] DORLAND, D., FERREIRA, J., AND BLAABJERG, F. An investigation into the relation between the applied electrical waveforms and the acoustic vibrations of inverter-fed induction motors. In *Proceedings of EPE conference* (2001). 23
 - [53] DORRELL, D. The influence of rotor skew on unbalanced magnetic pull in cage induction motors with eccentric rotors. *IEE Proc on Electrical Machines and Drives*, 415 (Sept. 1995). 137

-
- [54] DORRELL, D., THOMSON, W. T., AND ROACH, S. Analysis of airgap flux, current, and vibration signals as a function of the combination of static and dynamic airgap eccentricity in 3-phase induction motors. *IEEE Trans. on Ind. Appl.* 33 (Jan./Feb. 1997). 20
 - [55] ENJETI, P., ZIOGAS, P., AND LINDSAY, J. Programmed PWM techniques to eliminate harmonics: a critical evaluation. *IEEE Trans. on Ind. Appl.* 26, 2 (Mar/Apr 1990). 25
 - [56] ERTAN, H., AND SIMSIR, N. Comparison of PWM and PFM induction drives regarding audible noise and vibration for household applications. *IEEE Trans. on Industry Applications* 40, 6 (2004). 23
 - [57] FAHY, F. *Sound and Structural Vibration Radiation, Transmission and Response*. Academic Press, 1987. 51
 - [58] FAIZ, J., AND SHARIFIAN, M. Optimal design of an induction motor for an electric vehicle. *European Trans. on Electrical Power* 16 (2006). 25
 - [59] FASQUELLE, A. *Contribution la modélisation multi-physique : électro-vibro-acoustique et aérothermique de machines de traction*. PhD thesis, Université des Sciences et Technologies de Lille, France, Nov. 2007. 46
 - [60] FEI, R., FUCHS, E., AND HUANG, H. Comparison of two optimization techniques as applied to three-phase induction motor design. *IEEE Trans. on Energy Conversion* 4, 4 (Dec. 1989). 25
 - [61] FINLEY, W., HODOWANEC, M., AND HOLTER, W. An analytical approach to solving motor vibration problems. In *Proc. of the 46th Annual Petroleum and Chemical Industry Conference* (1999). 11
 - [62] FROHNE, H. *ber die primren Bestimmungsgrößen der Lautstärke bei Asynchronmaschinen*. PhD thesis, Hannover, Germany, 1959. 15, 41
 - [63] GABSI, M. *Conception de machines spéciales et de leurs alimentations. Réduction du bruit d'origine électromagnétique*. Habilitation à Diriger des Recherches, July 1999. 25
 - [64] GARVEY, S., AND FLEM, G. L. Tangential forces matter. *Proc. 9th Int. Conf. Electrical Machines and Drives* (1999), 174–178. 11
 - [65] GARVEY, S., AND GLEW, G. Magnetostrictive excitation of vibration in machines - a modal approach. In *Proceedings of the 9th Int. Conf. Electrical Machines and Drives* (1999). 13
 - [66] GARVEY, S., PENNY, J., FRISWELL, M., AND GLEW, C. Modelling the vibrational behaviour of stator cores of electrical machines with a view to successfully predicting machine noise. *IEE Colloquium* (1999), 169–173. 11

-
- [67] GERSEM, H. D., HAMEYER, K., AND WEILAND, T. Electromagnetically excited audible noise in electrical machines. *IEEE Trans. on Magnetics* 39, 3 (May 2003). [12](#)
 - [68] GHOGGAL, A., SAHRAOUI, M., ABOUBOU, A., ZOUZOU, S., AND RAZIK, H. An improved model of the induction machine dedicated to faults detection - extension of the modified winding function approach. In *Proc. of the International Conference on Industrial Technology* (Dec. 2005), pp. 191–196. [14](#)
 - [69] GIERAS, J., WANG, C., AND LAI, J. *Noise of polyphase electric motors*. CRC Press, Dec. 2005. [17](#), [19](#), [20](#), [52](#), [53](#), [113](#)
 - [70] GRANT, D. PWM AC motor drive employing ultrasonic carrier. *Proc IEE Conf. Power Electric Variable Speed Drives* 234 (1984). [24](#)
 - [71] HABETLER, T., AND DIVAN, D. Acoustic noise reduction in sinusoidal PWM drives using a randomly modulated carrier. *IEEE Trans. on Power Electronics* 6 (July 1991). [23](#)
 - [72] HASHEMI, N., AND LISNER, R. P. A new strategy for active control of acoustic noise in converter-fed induction motors. In *Proc. of AUPEC Conference* (2002). [25](#)
 - [73] HECQUET, M. *Contribution à l'instrumentation de la démarche de conception des machines électriques*. Habilitation à Diriger des Recherches, 2005. [136](#)
 - [74] HENAO, H., RAZIK, H., AND CAPOLINO, G. Analytical approach of the stator current frequency harmonics computation for detection of induction machine rotor faults. *IEEE Trans. on Ind. App.* 41, 3 (May/June 2005). [39](#)
 - [75] HESSE, H. Air gap permeance in doubly-slotted asynchronous machines. *IEEE Trans. on Energy Conversion* 7, 3 (Sept. 1992). [78](#)
 - [76] HILGERT, T., VANDEVELDE, A., AND MELKEBEEK, J. Application of magnetostriction measurements for the computation of deformation in electrical steel. *Journal of Applied Physics* (2005). [14](#)
 - [77] HILGERT, T., VANDEVELDE, A., AND MELKEBEEK, J. Numerical analysis of the contribution of magnetic forces and magnetostriction to the vibrations in induction machines. *IET Sci. Meas. Technol.* 1, 1 (2007). [14](#)
 - [78] HIROTSUKA, I., TSUBOI, K., AND ISHIBASHI, F. Effet of slot-combination on electromagnetic vibration of squirrel-cage induction motor under loaded condition. *IEEE Proceedings of Power Conversion Conference-Nagaoka'97* (1997). [19](#)
 - [79] HUANG, H., FUCHS, E., AND ZAK, Z. Optimization of single-phase induction motor design. *IEEE Trans. on Energy Conversion* 3, 2 (June 1988). [25](#)

-
- [80] HUANG, K., LIU, Z., LI, H., YANG, J., TURNER, D., JIANG, L., AND WU, Q. Reduction of electromagnetic noise in three-phase induction motors. In *IEEE Proc. of the International Conference on Power System Technology* (2002). 19
 - [81] HUBERT, A. *Contribution à l'étude des bruits acoustiques générés lors de l'association machines électriques - convertisseurs statiques de puissances - application à la machine asynchrone*. PhD thesis, Université des Technologies de Compiègne, France, Dec. 2000. 3, 4, 20, 29, 30, 32, 33, 37, 52, 70
 - [82] HUPE, R., AND KENNEL, R. Increase of power and reduction of noise and current ripple of inverter fed induction machines. *Proc. EPE'89, Aachen, Germany* (1989), 47–50. 25
 - [83] IDIR, K., CHANG, L., AND DAI, H. Improved neural network model for induction motor design. *IEEE Trans. on Magnetics* 34, 5 (Sept. 1998). 26
 - [84] IIDA, S., OKUMA, Y., MASUKAWA, S., MIYAIRI, S., AND BOSE, B. Study on magnetic noise caused by harmonics in output voltages of PWM inverter. *IEEE Trans. on Industrial Electronics* 38 (June 1991). 23
 - [85] JOKSIMOVIC, M., DJUROVIC, M., AND PENMAN, J. Cage rotor MMF : winding function approach. *IEEE Power Engineering Review* 21, 4 (Apr. 2001). 39
 - [86] JOKSIMOVIC, M., MOMIR, D., AND ALEKSANDAR, O. Skew and linear rise of MMF across slot modeling - winding function approach. *IEEE Trans. on Energy Conversion* 3, 14 (Sept. 1999). 37, 70
 - [87] JORDAN, H. *Electric motor silencer - formation and elimination of the noises in the electric motors*. W. Giradet-Essen editor, 1950. 16, 56
 - [88] JUFER, M., AND SABONNADIÈRE, J. Conception assistée par ordinateur : moteur asynchrone. *Techniques de l'ingénieur, traité Génie Electrique D3590*, 2 (1990). 19
 - [89] JURADO, F., AND VALVERDE, M. Multiobjective genetic algorithm for three-phase PWM inverter in microturbines. *Electric Power Components and Systems* 33, 8 (Aug. 2005). 26
 - [90] KEDOUS-LEBOUC, A. *Matériaux magnétiques en génie électrique*. Hermes Sciences Publications, 2006. 13, 21
 - [91] KIM, K., JUNG, Y., AND LIM, Y. Shaping the spectra of the acoustic noise emitted by three-phase inverter drives based on the new hybrid random PWM technique. In *Record of the 37th Annual IEEE Power Electronics Specialists Conference (PESC'06)* (2006). 25
 - [92] K.KAMIMOTO, ISHIBASHI, F., NODA, S., YANASE, S., AND SASAKI, T. Magnetostriction and motor vibration. *Electrical Engineering in Japan* 123, 6 (June 2003). 14

-
- [93] KLEMENZ, M. A sound synthesis model for sound-quality optimisation of starting electric railbound vehicles. In *Proceedings of the 33rd International Congress and Exposition on Noise Control Engineering (INTERNOISE)* (2004). 23, 115
 - [94] KLOOS, G. Magnetostatic maxwell stresses and magnetostriction. *Pringer Verlag Electrical Engineering* 81 (1998). 8
 - [95] KOBAYASHI, T., TAJIMA, F., ITO, M., AND SHIBUKAWA, S. Effects of slot combination on acoustic noise from induction motors. *IEEE Trans. on Mag.* 33, 2 (1997). 19
 - [96] KRON, G. Induction motor slot combinations: rules to predetermine crawling vibration, noise and hooks in the speed-torque curve. *AIEE Transactions* 50 (1931). 19
 - [97] LAFTMAN, L. Magnetostriction and its contribution to noise in a PWM inverter fed induction machine. *Journal of Physics* 4, 8 (1998). 13, 14, 21
 - [98] LAMBERT, J. Le bruit des transports en Europe : exposition de la population, risques pour la santé et coûts pour la collectivité. *Colloque du Conseil National du Bruit* (Dec. 2000). 1
 - [99] LANFRANCHI, V. *Optimisation de la commande en vitesse variable des machines asynchrones. Conception d'une méthode de Filtrage Actif Optimisé*. PhD thesis, Université de Reims, France, Dec. 2000. 25
 - [100] LANFRANCHI, V., FRIEDRICH, G., BESNERAIS, J. L., AND HECQUET, M. Spread spectrum strategies study for induction motor vibratory and acoustic behavior. In *Proceedings of the IECON* (Nov. 2006). 23
 - [101] LANFRANCHI, V., FRIEDRICH, G., BESNERAIS, J. L., AND HECQUET, M. Using spread spectrum strategies for improvement of induction motor acoustic behavior. unpublished. 23
 - [102] LANFRANCHI, V., HUBERT, A., AND FRIEDRICH, G. Comparison of a natural sampling and random PWM strategy for reducing acoustic annoyances. In *Proceedings of European Power Electronics and drive conference (EPE 03)* (2003). 23, 116
 - [103] LEBENSZTAJN, L., MARRETTO, C., COSTA, M., AND COULOMB, J. Kriging: a useful tool for electromagnetic device optimization. *IEEE Trans. on Magnetics* 40, 2 (Mar. 2004). 26
 - [104] LECOINTE, J., ROMARY, R., BRUDNY, J., AND CZAPLA, T. Five methods of stator natural frequency determination: case of induction and switched reluctance machines. *Journal of Mechanical and Signal Processing* 18 (2004). 17

-
- [105] LEROY, A. Etude psycho-acoustique du bruit des transformateurs et des selfs. Tech. rep., ALSTOM Transport, Charleroi, Belgium, 2008. [137](#)
- [106] LIAW, L. Random slope PWM inverter using existing system background noise: analysis, design and implementation. *IEE Proc. on Electr. Power Appl.* 147 (Jan. 2000). [23](#)
- [107] LISNER, R., AND TIMAR, P. A new approach to electric motor acoustic noise standards and test procedures. *IEEE Trans. on En. Conv.* 14, 3 (Sept. 1999). [3](#)
- [108] LIWSCHITZ, M. Field harmonics in induction motors. *Electr. Eng. Trans.* 61 (Nov. 1942). [15](#), [32](#), [33](#)
- [109] LO, W., CHAN, C., ZHU, Z., XU, L., HOWE, D., AND CHAU, K. Acoustic noise radiated by PWM-controlled induction machine drives. *IEEE Trans. on Industrial Electronics* 47, 4 (Aug. 2000). [20](#), [23](#), [24](#)
- [110] LYON, R. *Statistical Energy Analysis of Dynamical Systems: Theory and Applications*. The MIT Press, Cambridge, 1975. [18](#)
- [111] MALFAIT, A., REEKMANS, R., AND BELMANS, R. Audible noise and losses in variable speed induction motor drives with IGBT inverter - influence of the squirrel cage design and the switching frequency. In *29th annual meeting of IEEE Ind. Appl. Society* (Oct. 1994), vol. 1. [24](#)
- [112] MALITI, K. *Modelling and analysis of magnetic noise in squirrel-cage induction motors*. PhD thesis, Stockholm, 2000. [15](#), [24](#), [41](#), [53](#), [57](#)
- [113] MANNA, M., MARWAHA, S., AND MARWAHA, A. Computation and analysis of end region electromagnetic force for electrical rotating machines using fem. *IEEE Proc. of PEDES* (Dec. 2006). [12](#)
- [114] MATSUSE, K., HAYASHIDA, T., KUBOTA, H., AND YOSHIDA, T. Analysis of inverter-fed high speed induction motor considering crosspath resistance between adjacent rotor bars. *IEEE Trans. Ind. Appl.* 30, 3 (May/June 1994). [34](#)
- [115] MEZANI, S. *Modélisation électromagnétique et thermique des moteurs à induction, en tenant compte des harmoniques d'espace*. PhD thesis, INPL, France, July 2004. [29](#)
- [116] MICHEL, J. *Bobinage des machines tournantes courant alternatif*. Techniques de l'Ingénieur, D 3 430. [20](#)
- [117] MININGER, X. *Réduction des vibrations des machines à réluctances variable à l'aide d'actionneurs piézoélectriques*. PhD thesis, ENS Cachan, France, Nov. 2005. [25](#)

-
- [118] MOREIRA, J., AND LIPO, T. Modeling of saturated AC machines including air gap flux harmonics components. *IEEE Trans. on Ind. Appl.* 28 (1992). 15, 41
- [119] NA, S., JUNG, Y., LIM, Y., AND YANG, S. Reduction of audible switching noise in induction motor drives using random position space vector PWM. *IEE Proceedings of Electric Power Applications* 149 (May 2002). 23
- [120] NAU, S. The influence of the skewed rotor slots on the magnetic noise of three-phase induction motors. *IEE Proc. of EMD'97* (Sept. 1997). 20
- [121] NAU, S., BORK, B., DOS SANTOS, H., SADOWSKI, N., AND CARLSON, R. The influence of the frame and windings on the natural frequencies of stator of induction motors. In *Proc. of the International Conference on Electrical Machines (ICEM)* (Sept. 2006). 17
- [122] NOVOTNY, D., AND NASAR, S. High frequency losses in induction motors. Tech. rep., NASA Lewis Research Center, Cleveland, 1991. 136
- [123] NURDIN, M., POLOUJADOFF, M., AND FAURE, A. Synthesis of squirrel cage motors : a key to optimization. *IEEE Trans. on En. Conv.* 6, 2 (June 1991). 25
- [124] OBERRETL, K. Losses, torques and magnetic noise in induction motors with static converter supply, taking multiple armature reaction and slot openings into account. *IET Proc. on Electric Power Applications* 1, 4 (July 2007), 517–531. 11
- [125] O'CONNELL, T., AND KREIN, P. A preliminary investigation of computer-aided Schwarz-Christoffel transformation for electric machine design and analysis. *IEEE COMPEL Workshop* (July 2006). 14
- [126] ONODERA, S., AND YAMASAWA, K. An evaluation of electromagnetic vibration of a squirrel-cage induction motor. *Elektrotechnicky Casopis* 44, 2 (1993). 20
- [127] PÉPIN, H. *Le bruit et les vibrations d'origine électromagnétique dans les machines tournantes à moteur électrique - Etude bibliographique*. CETIM, 2003. 19
- [128] PERHO, J. *Reluctance Network for Analysing Induction Machines*. PhD thesis, Helsinki University of Technology, Finland, Dec. 2002. 30, 136
- [129] PETRICHENKO, D. *Contribution la modlisation et la conception optimale des turboalternateurs*. PhD thesis, Ecole Centrale de Lille, France, 2006. 136
- [130] POLOUJADOFF, M., CHRISTAKI, E., AND BERGNIANN, C. Univariant search: An opportunity to identify and solve conflict problems in optimization. *IEEE Trans. on Energy Conversion* 9, 4 (Dec. 1994). 25

-
- [131] POLOUJADOFF, M., MIPO, J., AND SIARRY, P. Design p/2p windings by the simulated annealing method. In *Record of the Electric Machines and Drives Conference* (May 1997). 26
- [132] RABINOVICI, R. Magnetic field analysis of permanent magnet motors. *IEEE Trans. on Mag.* 32, 1 (Jan. 1996). 14, 136
- [133] ROBINSON, F. *Macroscopic electromagnetism*. Pergamon Press, Oxford, 1973. 8
- [134] ROYTGARTS, M., AND PRONIN, M. Reducing of induction motors vibrations at drives with semiconductor converters designing. *IEEE Trans. on Energy Conversion* 3, 2 (June 1988). 11
- [135] SALON, S., BORTOLI, M. D., BUROW, D., AND SLAVIC, C. Effects of slot closure and magnetic saturation on induction machine behavior: a study using finite element analysis. In *IEE Proc. of International Conference on Electrical Machines* (1992), vol. 2. 19
- [136] SÉGUIER, G., AND NOTELET, F. *Electrotechnique industrielle*. Editions TEC & DOC, 1994. 29
- [137] SINGH, C., AND SARKAR, D. Practical considerations in the optimisation of induction motor design. *IEE Proceedings* 139, 4 (July 1992). 25
- [138] SINGH, C., AND SARKAR, D. A research survey of induction motor operation with non-sinusoidal supply wave forms. *Electric Power Systems Research* 75 (Aug. 2005). 23
- [139] SOEDEL, W. *Vibrations of shells and plates*. Marcel Dekker, 1993. 17, 63, 77, 147, 148, 149
- [140] STANKOVIC, A., AND LEV-ARI, H. Randomized modulation in power electronic converters. *Proceedings of the IEEE* 90, 5 (May 2002). 23
- [141] STEMMLER, H., AND EILINGER, T. Spectral analysis of the sinusoidal PWM with variable switching frequency for noise reduction in inverter-fed induction motors. In *Record of the 25th Annual IEEE Power Electronics Specialists Conference (PESC)* (1994), vol. 1. 23
- [142] SUDHOFF, S., KUHN, B., CORZINE, K., AND BRANECKY, B. Magnetic equivalent circuit modeling of induction motors. *IEEE Trans. on En. Conv.* 22, 2 (2007). 30, 136
- [143] TAKAHASHI, I., AND MOCHIKAWA, H. Optimum waveforms of an inverter for decreasing acoustic noise of an induction motor. *IEEE-IAS Annual Meeting Conf. Rec.* 1 (Oct. 1985). 23

-
- [144] TIMAR, P. Effect of application of semi-conductors on vibrations and noise of slip ring induction motors. *Elektrotechnika* 70, 3 (Mar. 1977). [23](#)
 - [145] TIMAR, P. *Noise and vibration of electrical machines*. Elsevier, 1989. [16](#), [17](#), [19](#), [20](#), [24](#), [57](#)
 - [146] TIMAR, P., AND LAI, J. Acoustic noise of electromagnetic origin in an ideal frequency-converter-driven induction motor. *IEE Proc. on Electr. Power Appl.* 141, 6 (Nov. 1994). [17](#), [22](#), [61](#), [62](#)
 - [147] TSE, K., CHUNG, H.-H., HUI, S. R., AND SO, H. Analysis and spectral characteristics of a spread-spectrum technique for conducted EMI suppression. *IEEE Trans. on Power Electronics* 15, 2 (Mar. 2000). [23](#)
 - [148] UEDA, S., HONDA, K., IKIMI, T., HOMBU, M., AND UEDA, A. Magnetic noise reduction technique for an AC motor driven by a PWM inverter. *IEEE Trans. on Power Electronics* 6 (July 1991). [93](#)
 - [149] VANDEVELDE, L., AND MELKEBEEK, J. Magnetic forces and magnetostriction in electrical machines and transformer cores. *IEEE Trans. on Magnetics* 39, 3 (May 2003). [14](#)
 - [150] VERMA, S., AND BALAN, A. Determination of radial-forces in relation to noise and vibration problems of squirrel-cage induction motors. *IEEE Trans. on En. Conv.* 9, 2 (June 1994). [21](#), [41](#)
 - [151] VERMA, S., AND BALAN, A. Electromagnetic surface excitation system for the study of vibration behaviour of stator of electrical machines. In *Proceedings of ICEM 96* (1996), vol. 1, pp. 332–337. [17](#), [63](#)
 - [152] VERMA, S., AND BALAN, A. Experimental investigations on the stators of electrical machines in relation to vibration and noise problems. *IEE Proc. on Electr. Power Appl.* 145, 5 (1998). [17](#), [21](#)
 - [153] VIVIER, S. *Stratgies dOptimisation par la Mthode des Plans dExpriences Et Application aux Systmes Electrotechniques Modliss par Elments Finis*. PhD thesis, Ecole Centrale de Lille, Lille, France, 2002. [121](#)
 - [154] VIVIER, S., HECQUET, M., AND BROCHET, P. Stratégies d’optimisation basées sur la méthode des plans d’expériences pour la conception de dispositifs électrotechniques. *Revue internationale de génie électrique* (2005). [26](#)
 - [155] WACH, P. Algorithmic method of design and analysis of fractional-slot windings of AC windings. *Electrical Engineering* 81, 3 (Aug. 1998). [81](#)

-
- [156] WALLACE, A., SPEE, R., AND MARTIN, L. Current harmonics and acoustic noise in AC adjustable-speed drives. *IEEE Trans. on Industrial Electronics* 26 (1990). 24
- [157] WANG, C. *Vibro-acoustic analysis of inverter driven induction motors*. PhD thesis, The University of New South Wales, Australia, May 1998. 18
- [158] WANG, C., AND LAI, J. Prediction of natural frequencies of finite length circular cylindrical shells. *Journal of Applied Acoustics* 59 (2000). 17
- [159] WANG, C., AND LAI, J. The sound radiation efficiency of finite length acoustically thick circular cylindrical shells under mechanical excitation I: theoretical analysis. *Journal of Sound and Vibration* 232, 2 (2000). 17, 18, 51
- [160] WANG, C., AND LAI, J. The sound radiation efficiency of finite length circular cylindrical shells under mechanical excitation II: limitations of the infinite length model. *Journal of Sound and Vibration* 241, 5 (2001). 18
- [161] WANG, C., LAI, J., AND ASTFALCK, A. Sound power radiated from an inverter driven induction motor : experimental investigation. *IEE Proc. on Electr. Power Appl.* 149, 1 (Jan. 2002). 23, 24
- [162] WANG, C., LAI, J., AND ASTFALCK, A. Sound power radiated from an inverter driven induction motor II : numerical analysis. *IEE Proc. on Electr. Power Appl.* 151, 3 (May 2004). 17, 21, 148
- [163] WANG, C., LAI, J., AND PULLE, D. Prediction of acoustic noise from variable-speed induction motors: deterministic versus statistical approaches. *IEEE Trans. on Ind. Appl.* 38, 4 (2002). 18
- [164] WANG, H., AND WILLIAMS, K. Effects of laminations on the vibrational behaviour of electrical machine stators. *Journal of Sound and Vibration* 202, 5 (1997). 17, 21
- [165] YACAMINI, R., AND CHANG, S. Noise and vibration from induction machines fed from harmonic sources. *IEEE Trans. on Energy Conversion* 10, 2 (June 1995). 23
- [166] YANG, S. J. *Low noise electrical motors*. Clarendon Press, Oxford, 1981. 16, 17, 57, 106
- [167] ZHU, Z., AND HOWE, D. Effects of end-shields and rotor on the natural frequencies and modes of stator of an electrical machine. *Proc. 4th Int. Conf. Electrical Machines and Drives* (1989), 232–236. 17, 51
- [168] ZHU, Z., AND HOWE, D. Improved methods for prediction of electromagnetic noise radiated by electrical machines. *IEE Proc. on Electr. Power Appl.* 141, 2 (1994), 109–120. 17

- [169] ZHU, Z., AND HOWE, D. Influence of mounting and coupling on the natural frequencies and acoustic noise radiated by a PWM controlled induction machine. In *Proc. of the International Conference on Electrical Machines and Drives* (1999), pp. 164–168. [21](#)
- [170] ZWICKER, E., AND FASTL, H. *Psychoacoustics, Facts and Models*. Berlin Heidelberg, Germany, 1992. [23](#), [115](#)